Studies on particle production in proton-proton collisions at the LHC energies using ALICE-TOF and MC data

Pranjal Sarma

Department of Physics

Gauhati University

This thesis is submitted to

Gauhati University as requirement for the degree of

Doctor of Philosophy

Faculty of Science

December 2021

I would like to dedicate this thesis to my family …

Declaration

I hereby declare that this thesis is the result of my own research work which has been carried out under the guidance of Prof Buddhadeb Bhattacharjee of Gauhati University. I further declare that this thesis as a whole or any part thereof has not been submitted to any university (or institute) for the award of any degree or diploma.

This thesis contains less than 90,000 (ninety thousand) words excluding bibliography and captions.

Pranjal Sarma

Pranjal Sarma

December 2021

Certificate

This is to certify that the thesis titled "Studies on particle production in proton-proton collisions at the LHC energies using ALICE-TOF and MC data" is the result of research work of Pranjal Sarma, carried under my supervision, submitted to Gauhati University for the award of the degree of Doctor of Philosophy in Physics.

This thesis conforms to the standard of PhD Thesis under Gauhati University including the standard related to plagiarism and has a similarity index not more than 10% (ten percent), excluding the bibliography.

Prof Buddhadeb Bhattacharjee, Supervisor

December 2021

Professor
Department of Phys
Gauhati University

Members of the Research Advisory Committee:

28/12/2021

Prof Anurup Gohain Barua, Department of Physics, GU

Professor
Department of Phys
Gauhati University

28/12/21

Dr Kushal Kalita, Department of Physics, GU

Professor
Department of Phys
Gauhati University

Acknowledgements

I would like to express my immense gratitude to all the people who have contributed to this thesis directly or indirectly. Without their constant support and motivation, the work carried out for this thesis would have never been completed. At the outset, I would like to express my sincere appreciation and gratitude to my supervisor Prof. Buddhadeb Bhattacharjee for providing guidance and support throughout the entire period of my research. I consider myself fortunate enough for getting this opportunity to pursue my research under his guidance. I sincerely thank him for his encouragement, constant motivation to accept challenges in research thus, always pointing me in the right direction during the entire period of my research. This has helped me a lot in my research as well as my personal life. I would like to thank him for his patience whenever I commit silly mistakes and mess something up. He has also provided me with various advice and physics discussions on different aspects of research. Without his guidance and selfless support, this thesis would have never seen the daylight.

I would like to take the opportunity to thank Dr. Alexander Philipp Kalweit, co-ordinator of Physics Working Group (PWG) Light-Flavour (LF) of ALICE Collaboration for his suggestions, comments and constant support in various Physics Analysis Group (PAG), PWG meetings as well as at the CERN during my data analysis period. I also sincerely and heartily thanks other co-ordination members of the LF group, namely Dr. Francesca

Bellini, Dr. Anders Garritt Knopse, and Dr. Stefania Bufalino, for their time to time valuable comments and suggestions in my analysis with the ALICE data. Also, I take the opportunity to sincerely thank the conveners of the LF-Spectra group Dr. Antonio Ortiz Velasquez, Dr. Yasser Corrales Morales, and Dr. Giacomo Volpe, for their suggestion and comments received at various stages of my analysis. I would like to thank all the members of the ALICE Collaboration for their encouragement, various comments and suggestions that I have received at different stages of analysis and paper drafting.

I also want to thank other members of the analysis crew and the paper committee of the ALICE data analysis namely, Dr. Vytautas Vislavicius, Dr. Ivan Ravasenga, Dr. Pareskevi Ganoti and Omar Vazquez Rueda, for their continuous support at different stages of analysis and paper drafting. The intense online and offline discussions among us lead to the successful publication of the paper on the ALICE data. I am also thankful to Dr. Nicolo Jacazio for his comments, suggestions and support at the early stage of my analysis. I also express my acknowledgement to the Internal Review Committee (IRC) and Editorial Board (EB) members for their intense comments, suggestions and support during the research period.

Further, it is my privilege to acknowledge ex-Spokespersons of ALICE-India Collaboration Dr. Tapan Kumar Nayak and Dr. Subhasis Chattopadhyay of VECC, Kolkata for their support, encouragement and suggestions at various stages of my research. I would also like to thank Dr. Raghunath Sahoo of IIT, Indore for his encouragement during my research period. Moreover, I want to thank all the members of ALICE-India and the organisers of the ALICE-India Collaboration meeting for providing the scope to discuss various aspects of my analysis.

I also express my sincere thanks to all faculty members of the Department of Physics, Gauhati University, for their teaching, encouragement, and support. Also, I am thankful to all the office staff of the department for their logistics support.

My heartiest thanks goes to my senior lab-mate Dr. Nur Hussain for his constant support and help at the early stage of my research. I am also very much thankful to him for various discussions on physics and ALICE data analysis related issues. My heartiest thanks also goes to my MSc batch-mate as well as lab-mate Somen, for his support and help. Apart from the research, we have also shared many enjoyable moments in the laboratory. The joyful moments that I have shared with Nur da during our visits to the CERN, Switzerland, various ALICE-India Collaboration meetings and conferences are unforgettable. I would also like to acknowledge Dr. Kalyan Dey, Assistant Professor in Bodoland University, Kokrajhar for his support and inspiration.

It is my privilege to thank the Department of Science and Technology (DST), Govt. of India, New Delhi for providing the Junior Research Fellowship (JRF), the fund for the CERN, Switzerland visits and to attend many other national & international conferences during my research period.

I would also like to thank all my seniors, juniors and batch-mates research scholars of the Department of Physics, Gauhati University for their kind support, encouragement and cheerful company. Also, I am thankful to all the members of the VV Rao Research Scholars Hostel for their support and help during my stay at the hostel. Special thanks goes to my long term roommate Niren da for being a wonderful company in the hostel. I am also thankful to my short-term roommate, Dr. Khagen Gogoi, Assistant Professor in History, Jagiroad College for sharing hostel life with me.

I am thankful to all my school, college teachers for their guidance during the early stage of my life. Special thanks goes to my aunt Saraswati and Kabita for their teaching and guidance during my school life. Apart from my teachers, I want to thank all of my friends, i.e., starting from school to universities level for their kind moral and personal support during the research period. Special thanks goes to my MSc batch-mates Hrishikesh, Manmohan, Tonuj, Binita, Suniti, Pratima, Yoshiko for their encouragement and support. Further, I

want to express my gratitude to school/college friends Abhi, Akhil, Dambaru, Jyoti, Manoj, Nabajit for their moral support. I also joyfully thank the other ALICE-India representative committee members namely, Baidynath, Dukhishyam, Shreyashi, and Suman for different online and offline discussions at various points in time.

Last but not least, I would like to thank all my family members for their continuous support and help during the research period. Special thanks go to my sisters, Babita, Sangita and sisters-in-law, Pranjal & Dhiraj, for their support and help in ups and downs in my personal life. Also, lots of love to my niece Shriddhi and nephew Shivam. I am also grateful to my grandmother Durga and cousin brother Hemen for their encouragement and guidance. I would like to express my gratitude to Satabdee for her support, encouragement and patience. Also, thankful to Suroshree for her kind help. Moreover, I am thankful to all my relatives for their support and guidance. Finally, I apologise if someone is forgotten to acknowledge.

Thank you so much all.

Pranjal Sarma

Abstract

In the ultra-relativistic heavy-ion collisions, a de-confined state of strongly interacting quarks and gluons is expected to form. This state of matter is usually known as the Quark-Gluon Plasma (QGP) and is governed by the theory of Quantum Chromodynamics (QCD). Various experimental facilities at the Relativistic Heavy-Ion Collider (RHIC) at Brookhaven National Laboratory (BNL) and Large Hadron Collider (LHC) at the European Organisation for Nuclear Research (CERN) are realising and characterising the QGP state by studying different observables of nuclear collisions. Apart from the heavy-ion collisions, at the LHC, protons are also accelerated to the highest energies ever achieved in the laboratory. The increased energy of proton beams has opened up possibilities of producing large numbers of final-state particles (high-multiplicity events). For these events, the charged particle multiplicity becomes similar to those measured in peripheral heavy-ion collisions. Therefore, studies on the properties of the matter formed in these high-multiplicity pp collisions have become significantly important. Moreover, recent results from high-multiplicity events of p-Pb collisions at LHC energies reveal several collective behaviours reminiscent of those observed for the Pb-Pb collisions. Thus, it became important to investigate various observables of nuclear collisions in the high-multiplicity event of the pp collisions to have a deeper insight into the production mechanism of particles as well as the properties and evolution of the matter formed.

The excellent particle identification capabilities of ALICE (A Large Ion Collider Experiment) sub-detectors over a wide range of transverse momentum provide scope to study various observables of heavy-ion collisions to have a better insight into the particle production mechanism and the properties of the matter created in such collisions. The time of flight (TOF) detector of ALICE can identify various primary particles, namely, pions, kaons, and protons at the intermediate transverse momentum region. Further, the application of statistical unfolding method on TOF data enables particle identification up to higher p_{T} regions than the usual particle identification technique using TOF. Another advantage of this method is that it is independent of any Monte Carlo information and simulation for what concerns the PID efficiency and contamination from different particles. Therefore, identifications of these particles with the TOF detector as a function of p_{T}, applying statistical unfolding technique, are of immense significance. Recent results from high-multiplicity pp collisions at $\sqrt{s} = 7$ TeV and p-Pb collisions at $\sqrt{s_{NN}} = 5.02$ TeV have shown several collective behaviours similar to that observed in heavy-ion collisions. These include mass-dependent hardening of p_{T} spectra, enhanced production of baryons over mesons at the intermediate p_{T}, non-zero elliptic flow coefficients etc. In heavy-ion collisions, these results could be well explained by considering the hydrodynamic evolution of the system. However, for small systems like pp collisions, mechanisms responsible for the modification of the spectral shape of particles with mass, non-vanishing elliptic flow coefficient etc., have not been established yet. Therefore, more detailed studies on pp collisions for different multiplicity classes are crucial at the LHC energy. Moreover, previous studies on light flavour particle production were performed for different colliding systems, each at different collisions energy. In this thesis, pions, kaons and protons are identified with the Time-of-Flight (TOF) detector of ALICE in pp collisions at $\sqrt{s} = 13$ TeV using statistical unfolding technique and are studied as a function of p_{T} for different charged-particle multiplicity classes. This study will offer the unique opportunity to disentangle the effect of centre-of-mass energy from the multiplicity

dependent studies. For the complete measurement of the p_{T} spectra, results of the TOF detector are also combined with the measurements performed with other detectors/analysis techniques such as ITS, TPCTOF, rTPC, kinks, etc. The p_{T} spectra of various identified particles, namely pions, kaons and protons, are observed to become harder with increasing multiplicity, and the effect is more pronounced for heavier particles like protons. The average transverse momentum ($\langle p_{\mathrm{T}} \rangle$) of the identified particle also shows centrality and mass-dependent hardening behaviour with multiplicity similar to those observed for the p_{T} spectra. Further, the p/π ratio shows a depletion at low p_{T}, enhancement at intermediate p_{T}, and constant behaviour at high p_{T} with increased charged-particle multiplicity. These behaviour are qualitatively similar to those observed for the Pb-Pb collisions at the LHC energy, consistent with the picture of hydrodynamical evolution of the system with a common radial velocity. Moreover, the p_{T}-integrated K/π ratio increases with increasing multiplicity, whereas the p/π ratio shows no significant evolution with increasing multiplicity for the pp collisions. The increasing behaviour of the K/π ratio with multiplicity in heavy-ion collisions can be described by the enhanced production of strangeness or a reduced canonical suppression in larger freeze-out volumes. Moreover, the p_{T}-integrated yield ratios of K^0_s, Λ, Ξ, Ω to pions increases with increasing multiplicity for pp collisions and the effect is found to be more pronounced for particles having larger strangeness content. However, no significant energy dependent evolution of these ratios could be observed. These particles ratios are found to follow a common trend and scale with the charged-particle multiplicity, rather than colliding systems and collisions energies.

Understanding particle production mechanisms is yet another important motivation of nuclear collision studies. Usually, particles produced in such collisions exhibit fluctuations in number density in various phase-spaces, which are believed to occur due to different processes of particle production mechanism. This type of fluctuations is generally known as non-statistical or dynamical fluctuations and is much larger than the statistical one arising due to

finiteness in particles' yield. Dynamical fluctuations mainly arise due to correlated emission of particles, which in turn, is related to various particle production mechanisms or/and a possible phase transition that occurs during the evolution of the system. Further, it has been reported that the correlated emission of particles may also occur due to a mechanism called colour reconnection (CR) between the partons. To better understand the collision dynamics, it therefore becomes essential to disentangle and analyse these dynamical fluctuations from the mixture of statistical and dynamical one. Among various available mathematical tools, the Scaled Factorial Moment (SFM) technique is a widely accepted one that can separate the dynamical fluctuations from the mixture of the two. Previous lower energies experimental results on SFM analysis of various systems starting from the e^+e^- to heavy-ion collisions indicate a power-law growth of average scaled factorial moments $\langle F_q \rangle$ with decreasing phase-space bin width, or otherwise, with the increasing number of bins in which the phase-space is divided. Such behaviours are found to be a general characteristic of the experimental data. However, previous measurements on intermittent emission of charged particles were carried out mostly with passive detectors such as nuclear emulsion at relatively lower collisions energies for small and heavy-ion systems. No serious attempt has been made to investigate dynamical fluctuation using the scaled factorial moment technique at the LHC energies. In this investigation, an attempt has been made to explore the possibility of analysing dynamical fluctuations at the LHC energies in the light of the SFM technique with MC events generated with the PYTHIA Monash model. Further, the colour reconnection (CR) mechanism, implemented in PYTHIA, also found to explain several collective effects in the high-multiplicity pp events. Colour reconnection (CR) is a string fragmentation model, where the final partons are considered to be colour connected in such a way that the total string length becomes as short as possible, which in turn, results in correlated emission of final state particles. It is therefore very important to examine the contribution, if any, of the colour reconnection in the observed correlated emission of particle. In this present

investigation, the SFM analysis of PYTHIA generated data, which incorporates the CR, is also carried out for pp collisions at $\sqrt{s} = 2.76$, 7 and 13 TeV. An apparent increase in $\ln\langle F_q \rangle$ with increasing lnM could be observed in one-dimensional pseudorapidity (η), azimuthal angle (ϕ) and two-dimensional $\eta - \phi$ spaces of high-multiplicity pp events of $\sqrt{s} = 2.76$, 7 and 13 TeV, indicating a clear intermittent type of emission of particles. On the other hand, no such intermittent type of emission could be observed in minimum bias pp collisions. The intermittency index (α_q) is found to increase with increasing order of the moments q in all studied spaces of high-multiplicity pp events. Moreover, the strength of the intermittency index (α_q) is observed to be more in two-dimensional (2D) $\chi(\eta - \phi)$ space and least in one-dimensional $\chi(\eta)$ space. However, intermittency indices are found to independent of collisions energy. Further, studies on anomalous dimensions d_q show that it increases with increasing order of the moment q. This type of increasing behaviour of anomalous dimension with q suggests the multi-fractal nature of emission spectra and indicates the production of particle via cascading mechanism in the high multiplicity pp events. Moreover, studies on the exponent λ_q indicate that such events exhibit a non-thermal phase transition like behaviour in 2D $\chi(\eta - \phi)$ space for $q=q_c=4$. This critical value of the order of the moment q_c separates frequently occurring small fluctuations from rarely occurring large fluctuations. Further, studies with the colour reconnection (CR) mechanism in PYTHIA suggest that intermittency strength varies significantly with the variation of the strength of the CR, i.e. reconnection range (RR). With the increase of RR, a significant increase in the intermittent behaviour could be observed in comparison to default (RR = 1.8) and RR = 0.0 PYTHIA data. This increasing behaviour of intermittency is due to the fact that the increased strength of the colour reconnection produces more correlated emission of particles in these high-multiplicity pp events. A significant increase in anomalous dimensions (d_q) could be observed with the order of the moments q for RR=1.8 and 3.0, but not much variation in d_q could be observed for RR=0.0. Moreover, the position of the λ_q minimum is found to decrease to $q=q_c=3.65$

for the higher value of CR strength, i.e., RR=3.0 whereas, no minimum in λ_q is evident for RR=0.0 data sets. Therefore, it is evident that the colour reconnection mechanism in PYTHIA has a significant effect on the observed intermittency and hence on the nonthermal phase-transition like behaviour in the studied high-multiplicity pp events. Nevertheless, the colour reconnection can not solely be attributed as the cause of observed intermittency in the PYTHIA generated pp data at $\sqrt{s} = 2.76$, 7 and 13 TeV.

Table of contents

List of figures

List of tables

1

Introduction

At high-energy, Quantum Chromodynamics (QCD), the theory of strong interaction predicts a phase transition from hadronic to a de-confined state of matter, where the quarks and gluons are considered as the degrees of freedom. This state of matter is usually known as the Quark-Gluon Plasma (QGP). In the laboratory, the QGP state can be produced by colliding nuclei at the ultra-relativistic energies [1, 2]. Several accelerator programmes such as the Alternating Gradient Synchrotron (AGS) at the Brookhaven National Laboratory (BNL), the Super Proton Synchrotron (SPS) at the European Organisation for Nuclear Research (CERN) and the Relativistic Heavy Ion Collider (RHIC) at the BNL have been designed to collide various nuclei at unprecedented energies. Different mega experiments have been

set-up in these accelerator sites to realise and characterise the QGP matter formed during the collisions. Results from these experiments have already provided early indications of the formation of the QGP state [3–10]. In the year 2008, the Large Hadron Collider (LHC) at the CERN has been established to collide proton-proton (pp) as well as lead-lead (Pb-Pb) nuclei at the unprecedented energy regime of TeV. At the LHC, four dedicated experiments, namely A Large Ion Collider Experiment (ALICE), Compact Muon Solenoid (CMS), A Toroidal LHC ApparatuS (ATLAS) and Large Hadron Collider beauty (LHCb) have been developed to investigate various aspects of such collisions. The primary motivation of ALICE is to investigate and characterise the QGP state of matter by studying different observables of heavy-ion collisions. Even though the formation of the QGP state is generally investigated with heavy-ion collisions [11–14], the pp collisions, on the contrary, provide the reference measurement for the heavy-ion collisions. Apart from the reference measurement, pp collisions also provide input to constrain the fragmentation function in pQCD calculation and to constrain the soft interaction in various Monte Carlo models [15].

Recent results from the high-multiplicity p-Pb collisions at the LHC energy suggest several collective effects such as the near-side long-range two-particle angular correlation that extend over wide range of pseudorapidity (η) [16], mass-dependent hardening of the transverse momentum (p_{T}) spectra [17], (multi-)strange hadron enhancement [18] etc., reminiscent of those observed in the heavy-ion collisions. Moreover, the same study has been extended to an even smaller system like pp collisions at $\sqrt{s} = 7$ TeV. And the results of the high-multiplicity pp collisions suggest behaviours similar to those observed in the high-multiplicity p-Pb and Pb-Pb collisions [19, 20], indicating that the collective behaviours are not the features of heavy-ion collisions only. Further, the light-flavour hadrons to pions ratios show a continuous evolution from low-multiplicity pp to high-multiplicity (central) Pb-Pb collisions. Hence, it becomes important to have a better understanding of the properties of the system formed in the high-multiplicity pp collisions. However, measurement performed in

previous multiplicity dependent studies have considered different colliding systems, each at a different centre-of-mass energies [19]. It is therefore important to disentangle the effect of centre-of-mass energy from the multiplicity dependent studies and provide a more in-depth insight into the properties of the medium formed in such collisions.

Correlated emission of particles, due to a number of associated particles production mechanism, is believed to be the cause of observed non-statistical (dynamical) fluctuation in the emission spectra of charged particles of various colliding systems starting from e^-e^+ to heavy-ion collisions at different energies [21, 22]. The scaled factorial moment (SFM) technique [23–30] is found to be an effective and extensively used mathematical tool to disentangle dynamical fluctuation from the mixture of dynamical and statistical fluctuations. Previous results on SFM analysis of the lower energies experimental data of various system [21, 22] suggest that the average scaled factorial moment $\langle F_q \rangle$ follows a power-law growth with decreasing phase-space bin width, or otherwise, with the increasing number of bins M into which the phase-space is divided. Such power-law behaviour is found to be a general characteristic of the experimental data. The observed power-law behaviour of $\langle F_q \rangle$ could be interpreted in terms of intermittency in the charged particle emission spectra and is believed to originate due to a number of physical processes of particle production [23, 25, 31] or a phase transition that has occurred during the evolution of the system [32–34]. As all the previous studies have been performed at relatively lower energies, where multiparticle late stage scattering is expected to be significantly low due to relatively less number of final state particles, such studies at the LHC energies for small systems like pp collisions, may provide valuable insight about particle production mechanisms. The PYTHIA Monte Carlo (MC) model is a general-purpose event generator capable of describing pp collisions data at the LHC energies very well [35–37]. It uses a factorised perturbative expansion for the hard parton-parton interaction, combined with parton showers, and details models for hadronisation and multiple parton interactions. Further, PYTHIA also includes colour

reconnection mechanism where the final partons are expected to be colour connected in such a way that the total string length becomes minimum and thus, results in a correlated emission among the produced partons. Therefore, in this work, an attempt has also been made to find the cause of such intermittency in the high-multiplicity pp collisions with PYTHIA generated data at the LHC energies.

1.1 The Standard Model (SM) of particle physics

In the 1970s, a theoretical framework emerged to describe the interactions between all the elementary particles. In this framework, Abdus Salam, Sheldon Glashow and Steven Weinberg's electroweak force and strong force are put together to develop the famous model known as the Standard Model (SM) [38]. The gravitational force is not a part of the standard model, and therefore, it will not be discussed hereafter.

According to the standard model, the fundamental constituents of the universe are the matter particles and fields responsible for the interaction between these particles [40–42]. The matter particles are grouped into two classes: quarks and leptons; and are classified in three-generation according to their hierarchy in mass, as shown in Fig. 1.1 [43]. In case of quarks, the first generation consists of up (u) and down (d); the second generation consists of charm (c) and strange (s), and third-generation contains top (t) and bottom (b) quarks. The quarks namely u, c and t have the electric charge of +2/3 whereas, d, s and b have the charge of -1/3. Along with the electric charge, quarks also have an additional charge called colour charge. Each quark has three different types of colour charges, i.e. red, green and blue, whereas, each anti-quarks can take the anti-red, anti-green and anti-blue colour charge. The quarks can participate in all three types of interaction. In case of leptons, the first-generation particles consist of the electron (e), and electron neutrino (ν_e); muon (μ) and muon neutrino (ν_μ) are the second generations, and third-generation consist of tau (τ) and tau neutrino (ν_τ). The leptons can participate in both the electromagnetic and weak

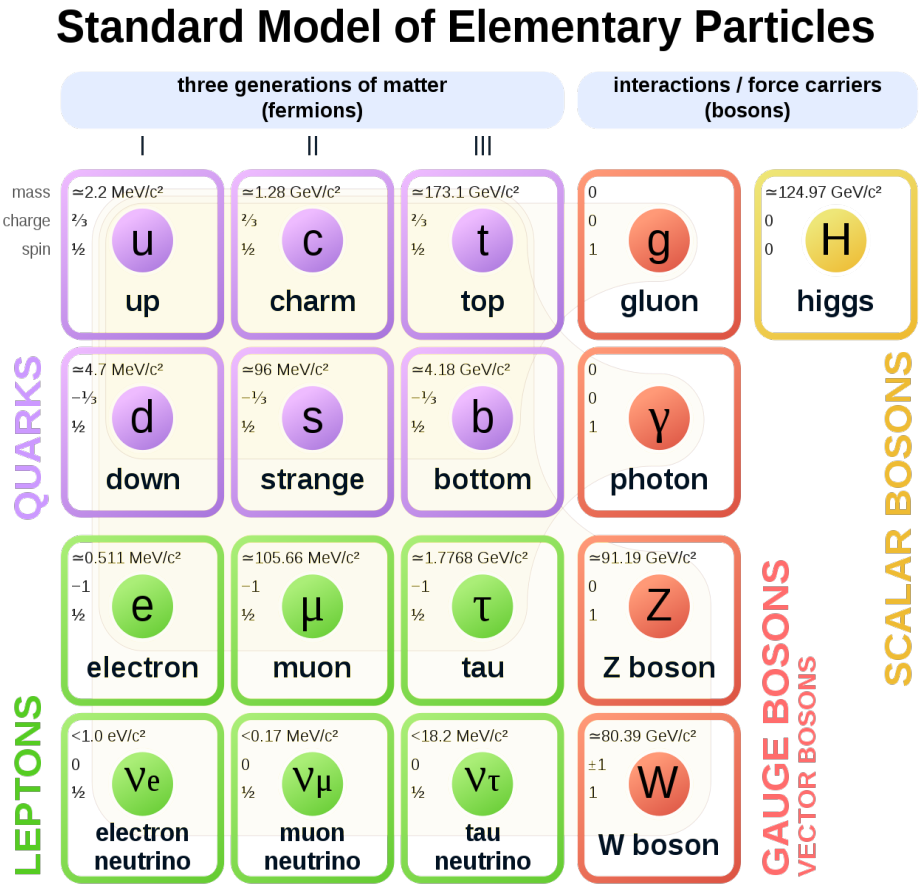

Fig. 1.1 Different generations of elementary particles in the standard model and the mediator particles of different types of forces are shown. The picture is taken from [39].

interaction except for the neutrinos, which are only weakly interacting particles. All the quarks and leptons are fermions having spin (S) = 1/2 and follow the Fermi-Dirac statistics. Apart from quarks and leptons, the field particles or the force carrier, i.e. photon (γ), $W^{\pm}$ and Z bosons, and gluon (g) are also included in the standard model. These particles are known as the Gauge bosons. The photon is responsible for the electromagnetic interaction between electrically charged particles. The $W^{\pm}$ & Z bosons are the field particles of the weak interaction, which acts between different types of quarks & leptons and the gluons are responsible for the interaction between the quarks, i.e. strong interaction. These field particles have integral spin. Photon and gluons are the massless particles having spin 1 and neutral electric charge. Gluons carry colour charges, and therefore, they can interact with each other through strong interaction and follow the Bose-Einstein statistics. The theory that can describe the interactions between the colour charge particles is known as the Quantum Chromodynamics (QCD). In nature, the leptons can exist freely; however, free quarks do not exist due to the confinement properties of the QCD. The quarks are always found to be confined in a hadron. The hadron consisting of quark-antiquark pair is known as the meson, and the bound state of three quarks or anti-quarks is known as the baryon. Both mesons and baryons are colour neutral.

Moreover, the standard model also includes a scaler boson known as Higgs, named after Peter Higgs, who proposed the Higgs mechanism along with five other scientists in 1964. According to the Higgs mechanism, particles acquire mass due to the interaction with the Higgs field [44–47]. The standard model is found to be able to explain all the experimental finding successfully and therefore, has become one of the well-tested theories in high-energy physics. Further, the search for the existence of the Higgs, which is popularly known as "God Particle", became essential to validate the Standard Model. With the primary motivation of search for the Higgs particle, different experiments such as A Toroidal LHC ApparatuS (ATLAS) and Compact Muon Solenoid (CMS) were built along with the accelerator facility

of Large Hadron Collider (LHC). In July 2012, its existence was confirmed by the results from these two experiments [48, 49]. Two of the scientists, Peter Higgs and François Englert were awarded Nobel Prize in Physics for the year 2013 for their theoretical prediction.

1.2 Quantum Chromodynamics (QCD)

The quantum chromodynamics (QCD) is a well-established theory of strong interaction, which describe the interaction between the quarks and gluons. This theory is developed in terms of elementary fields, namely, quarks and gluons, whose interactions follow the principles of relativistic quantum field theory (QFT) with a non-abelian gauge invariance SU(3). The quarks and gluons are described by a completely new quantum number known as the "colour", similar to the electric charge in the QED. For the quarks, the colour charges in the QCD are: red, green and blue; and for the anti-quarks, they are: anti-red, anti-green and anti-blue. The force between the quarks is mediated via gluon exchange, which has an unbalanced colour charge. In the SM, there are eight gluons based on the colour combination in the QCD. The quarks and gluons are generally known as the partons. The hadrons are the colour singlet particle formed either via quark-antiquark pair known as meson and by the combination of three quarks (or anti-quarks) known as baryon. The QCD has two remarkable property: confinement and asymptotic freedom, which are discussed hereafter.

1.2.1 Confinement

One of the prominent property of the QCD is the colour confinement. It is the primary mechanism due to which free colour charged particles such as quarks and gluons are not found. The strong interaction potential can well explain the confinement property of the quarks. The QCD potential for strong force is given by the following equation [50]:

$$V_s = -\frac{4}{3}\frac{\alpha_s}{\mathrm{r}} + \mathrm{kr} \tag{1.1}$$

where α_s is the strong interaction coupling constant, also known as running coupling constant, r is the distance between the colour charge, and k is the string tension between the quarks. The variation of strong interaction potential V with the distance r is shown in Fig. 1.2.

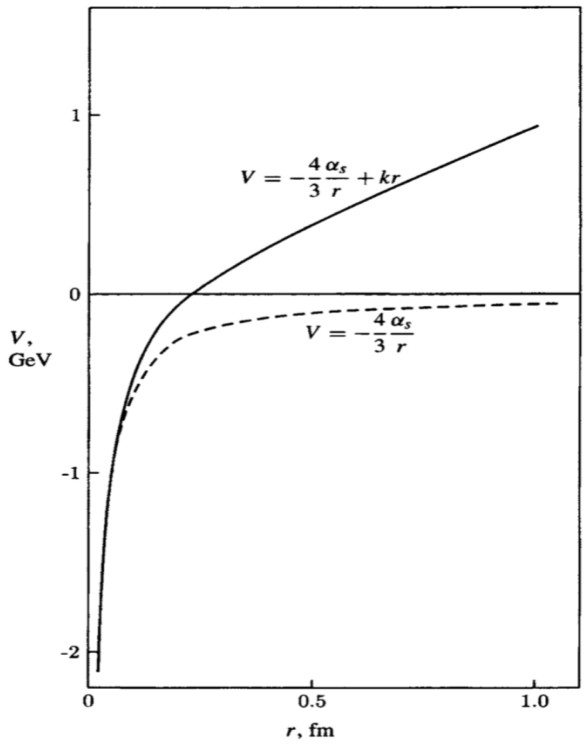

Fig. 1.2 Variation of strong interaction potential V with distance r for quark-gluon coupling α_s = 0.20 and k = 1 GeV fm^{-1} [50].

The term $\frac{\alpha_s}{\mathrm{r}}$ arises due to the single gluon exchange and dominates at small r. It is similar to the Coulomb potential between elementary charge particles. The linear term (second term) in Eq. (1.1) is associated with the confinement of quarks at large r. Due to this term, attempts to create separate quarks from hadron results in new quark-antiquarks pair, i.e. mesons. This is because the gluon-gluon interaction pulls together the lines of force of the colour field to form a string tube. Stretching the string beyond a threshold value energetically favours

creation of new $Q\bar{Q}$ pairs so that there are two short strings than one long string as shown in Fig. 1.3.

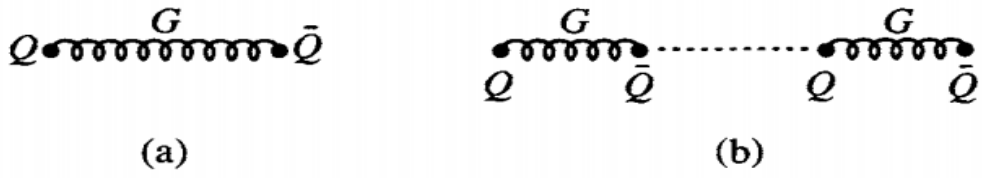

Fig. 1.3 Schematic showing (a) two quarks are connected through the gluon string and (b) formation of two new quark-antiquarks pair when the gluons string is pulled beyond the threshold value [50].

1.2.2 Asymptotic freedom

Apart from confinement, another important property of the QCD is the asymptotic freedom, which states that the interaction strength ($\alpha_S = g^2/4\pi$) between the quarks becomes smaller as the distance between them decreases. This phenomenon was first observed by Gross, Politzer and Wilczek, for which they were awarded Nobel prize in Physics for the year 2004 [51–54].

The asymptotic freedom can be well understood by recalling the force between the two charges in the vacuum in electrodynamics, which is given by the Coulomb's law:

$$F = \frac{1}{4\pi}\frac{q_1 q_2}{r^2} \tag{1.2}$$

Now, if the two charges are placed in a medium with dielectric constant $\varepsilon > 1$, the force acting on these charges will be modified according to the equation below:

$$F = \frac{1}{4\pi\varepsilon}\frac{q_1 q_2}{r^2} \tag{1.3}$$

However, in quantum field theory, the vacuum is not just an empty space and is considered as the lowest energy state of a field system having electrons of negative energies. When a

photon passes through the vacuum, it can excite an electron from negative energy to positive energy, virtually creating a pair of electron and positron, known as the vacuum fluctuation, as shown in Fig. 1.4(a). Due to this, the force between the two electrons in the vacuum modified as given in Eq. (1.4):

$$F = \frac{e_{eff}^2}{4\pi r^2} = \frac{\alpha_{em}(r)}{r^2} \tag{1.4}$$

where α_{em} is the effective fine structure constant, and it depends on the distance, r or the momentum transfer, q$\sim$1/r. If r$\rightarrow \infty$ or q $\rightarrow$ 0, the coupling thus measures the low energy photon's interaction strength and is given as $\alpha_{em}(q = 0) = 1/137$.

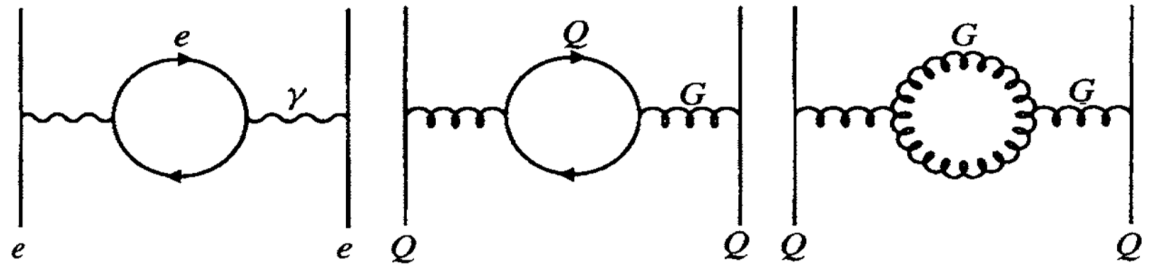

(a) (b) (c)

Fig. 1.4 The quantum vacuum polarisation which effectively changes the interactions strength. (a) In QED, the loop is shared by fermions only, (b) in QCD for a loop containing quarks and (c) in QCD for a gluon loop, involving gluon-gluon coupling, absent in QED [50].

Similar to the QED, the vacuum polarisation can also be applied to the QCD. In this case, the strong coupling constant of the QCD, α_s becomes [52–54]:

$$\alpha_s(Q^2) = \frac{4\pi}{\beta_0 ln(Q^2/\Lambda_{QCD}^2)} \tag{1.5}$$

where $\beta_0 = 11 - \frac{2}{3}n_f$, and here, n_f is the number of active quark flavour. The second term in β_0, i.e., $-\frac{2}{3}n_f$ arises due to the antiquark-quark pair effect, as shown in Fig. 1.4(b). This vacuum polarisation gives rise to stronger interaction at short distances, which is known as the screening. It scales with the number of quark flavours and is negative. However, the term

11, has the opposite sign and comes from the non-linear interaction between gluons in QCD, as shown in Fig. 1.4(c). It has an anti-screening effect, which makes the coupling weaker at short distances.

The dimensional parameter Λ_{QCD} is identical to the energy scale Q, where $\alpha_s(Q^2)$ diverges to infinity, i.e. $\alpha_s(Q^2) \to \infty$ for $Q^2 \to \Lambda^2_{QCD}$. This means that Λ_{QCD} is a constant having value of 220 MeV and therefore, correspond to the limit where the perturbation theory is no longer applicable to the QCD calculations for small energy transfers [55].

So, α_s goes to 0 as the momentum scale goes to infinity or at a distance close to 0. The peculiar behaviour of the QCD is known as asymptotic freedom. This unique behaviour of the strong coupling constant has already been verified by different high energy experiment, and the results are shown in Fig. 1.5.

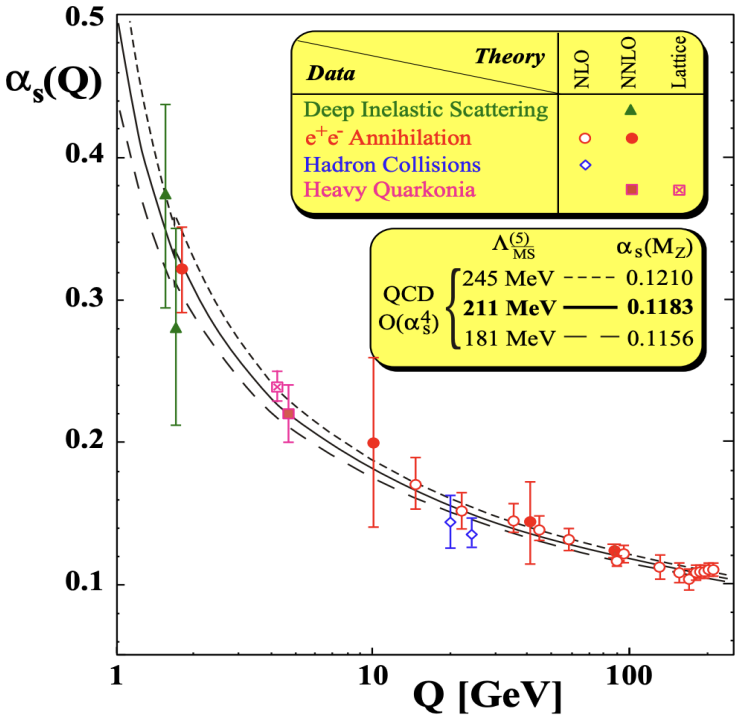

Fig. 1.5 The results of the strong interaction running coupling constant from different experiments are plotted as a function of momentum transfer and are compared with various theoretical predictions [56].

1.3 Quark-Gluon Plasma (QGP)

The concept of colour confinement is true when the matter is at normal temperature and density. However, the discovery of asymptotic freedom has opened up the question of a possible phase of matter known as the Quark-Gluon Plasma (QGP), where partons are not confined inside the hadron. In the QGP medium, the quarks and gluons can move freely over the distance larger than the typical size of the hadronic states.

The strong interaction potential, as given in Eq. (1.1) does not take account of the effect for such a medium of interacting quarks and gluons. In a plasma medium, the presence of multiple colour charges can screen the original colour in the long-range interactions. This effect is known as the Debye screening. In this case, only the short-range term of the QCD potential will be effective and therefore, it becomes:

$$V_s(T,r) \sim -\frac{\alpha_s}{r} e^{-\frac{r}{r_D}} \tag{1.6}$$

where T is the temperature of the plasma, and r_D is the Debye length. When r_D becomes smaller than the radius of a hadron, the strong force can no longer bind the quarks together, and the state dissolves. Therefore, a high-density medium of colour charges due to the excitation of vacuum or due to compression of the system, in combination with the running coupling constant at small distances can lead us to a phase of free quarks and gluons, i.e. QGP.

At first, the transition of the hadronic matter to the QGP is illustrated by considering a straightforward model. The pressure of an ideal gas of massless pions is given by the Stefan-Boltzmann form:

$$P_\pi = 3\frac{\pi^2}{90} T^4 \tag{1.7}$$

Factor 3 in Eq. (1.7) arises due to three charge states of the pion. If one considered the same behaviour for an ideal quark-gluon plasma with two flavours and three colours, then the pressure becomes:

$$P_{QGP} = \left\{ 2 \times 8 + \frac{7}{8}(3 \times 2 \times 2 \times 2) \right\} \frac{\pi^2}{90} T^4 - B = 37 \frac{\pi^2}{90} T^4 - B \tag{1.8}$$

In the above equation, the first term of the curly brackets takes care of the two spins and eight colour degrees of freedom of the gluons, the second term for the three colours, two flavours, two spins and two particle-antiparticle degrees of freedom of the quarks. The factor 7/8 is taken into account to obtain the correct statistics. The quantity B, known as the bag pressure, consider the differences between the physical vacuum and the ground state for quarks and gluons in a medium.

Since in thermodynamics, any system tries to retain in a state of lowest free energy and therefore, in highest pressure, the temperature behaviour obtained from Eqs. (1.7) & (1.8) are compared in Fig. 1.6(a). From the figure, it is observed that this model leads to a two-phase situation of strongly interacting matter, with a hadronic phase up to

$$T_c = \left(\frac{45}{17\pi^2} \right)^{1/4} B^{1/4} \simeq 0.72 B^{1/4} \tag{1.9}$$

and a QGP phase above the critical temperature T_c. From hadron spectroscopy, the bag pressure is found to be $B^{1/4} \simeq 0.2$ GeV. Therefore, one can obtain a critical temperature $T_c \simeq 150$ MeV. This critical temperature is known as the de-confinement temperature.

Further, the energy density of the two phases are given by

$$\varepsilon_\pi = \frac{\pi^2}{10} T^4 \text{ and } \varepsilon_{QGP} = 37 \frac{\pi^2}{30} T^4 + B \tag{1.10}$$

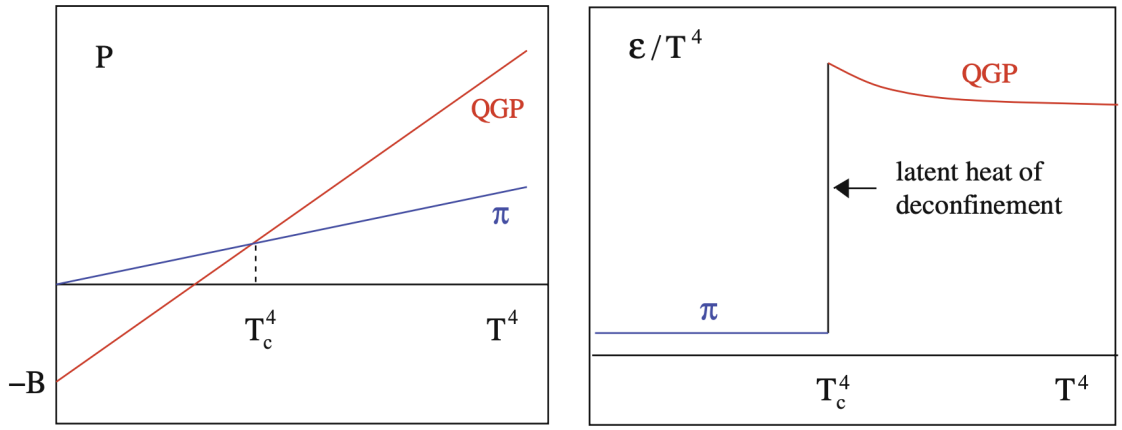

Fig. 1.6 Variation of (a) pressure and (b) energy density as a function of temperature in a two-phase ideal gas model [57].

Here, the transition is considered as the first-order. The resulting temperature dependence of energy density is shown in Fig. 1.6(b). It could be observed from the figure that the energy density increases sharply at T_c by the latent heat of de-confinement.

One of the important consequences of asymptotic freedom of the QCD is that different terms become calculable via application of the perturbation theory (pQCD) at high energies or high Q^2, as the strong coupling constant α_s become small. However, at low energies, the strong coupling constant increases and the perturbative theory breaks down. In order to calculate the properties of the QCD in the low energy region, non-perturbative numerical methods are required to be applied. The lattice gauge theory proposed by K. Wilson in 1974 provides the non-perturbative method for vector-like gauge field theory [58]. In lattice QCD, the Euclidean space-time is divided into a hyper-cubic lattice with lattice spacing a, the quarks fields placed on sites and the gauge field on the links between sites. Using the LQCD theory, the QCD phase transition is observed at critical temperature $T_c \sim 170$ MeV and energy density $\varepsilon \sim 1$ GeV/fm^3 [57]. The variations of the thermodynamic variables, pressure and energy density have been estimated using the LQCD and are shown in Figs. 1.7(a) & 1.7(b). At the critical temperature, there is a sharp increase in pressure and energy density of

the system, indicating a sudden increase in the number of degrees of freedom of the system, i.e. de-confinement from the hadron to quarks and gluons. Here, the number of quarks flavour dependence is also shown along with the Stefan-Boltzmann limit (indicated by horizontal arrows) for an ideal gas. At high temperature, it is expected that the pressure and energy density approach the Stefan-Boltzmann limit for a weakly interacting ideal gas. However, at a temperature higher than four times of critical temperature, the plots lie significantly below the Stefan-Boltzmann limit and therefore, implies that the particles present in the medium above the T_c can still interact with each other.

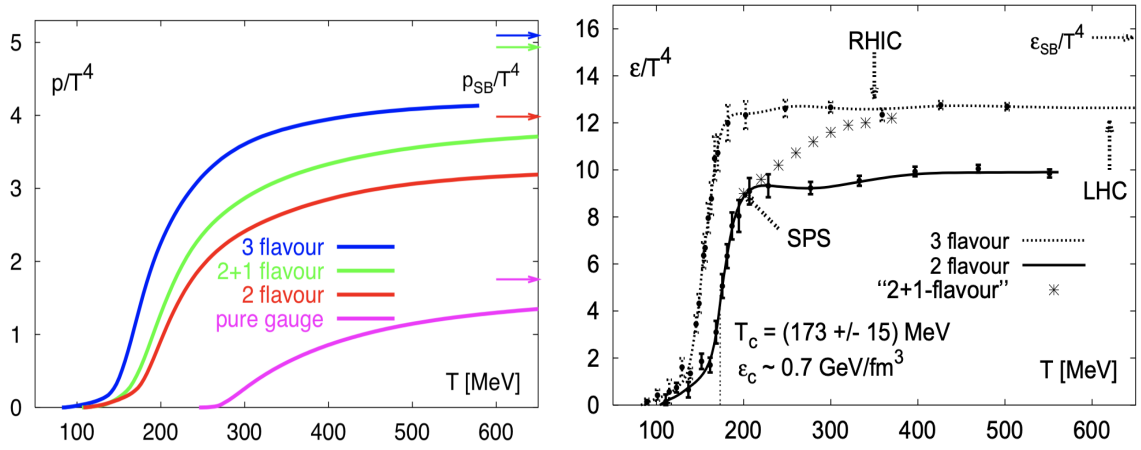

(a) (b)

Fig. 1.7 Lattice QCD calculation for (a) pressure and (b) energy density as a function of temperature for different numbers of quark flavours 2, 3 and 2+1. The Stefan-Boltzmann limits for different flavours for an ideal gas are shown by horizontal arrow. The energy density and temperature reached in SPS, RHIC and LHC heavy-ion experiments are also shown for the energy density [59–61].

In the above discussion, the transition from hadronic to de-confined partonic phase is considered as first order. However, a clear picture of the nature of the phase transition is still a conjecture. In Fig. 1.8, current understanding of the nature of phase transition is shown considering the masses of three flavour of quarks, i.e., u, d and s. The possible types of phase transition are given below:

- In the limit m $\rightarrow \infty$ for all the three quarks, the transition is first order (Pure gauge theory).
- For m $\rightarrow$ 0 of all the quarks, the Lagrangian is found to be chirally symmetric, and the phase transition will occur corresponding to chiral symmetry restoration. Therefore, the transition is also first-order.
- For $0< m < \infty$, neither spontaneous Z_3 breaking nor a chiral symmetry restoration occurs. In this case, no singular behaviour exists, apart from the transient disappearance of the first-order discontinuities on a line of second-order transition. Beyond this limit, only a "cross-over" transition from confinement to de-confinement will occur.

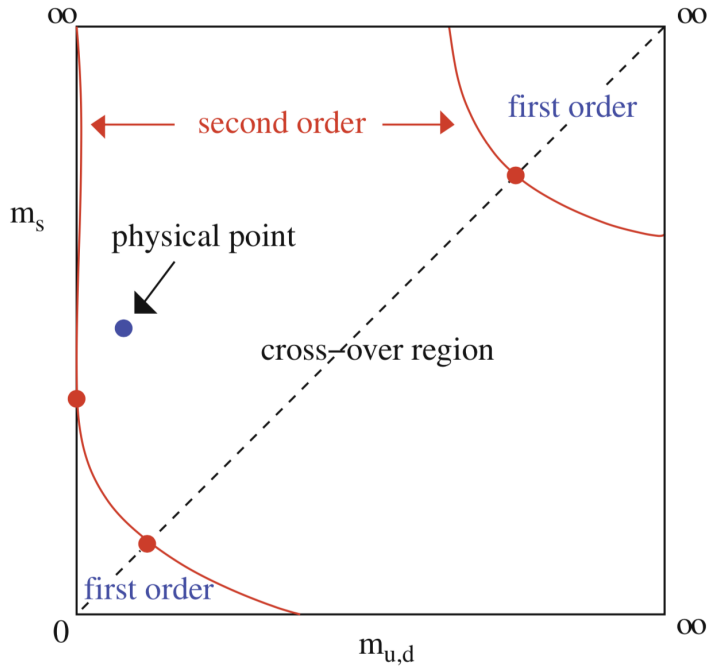

Fig. 1.8 Nature of the phase transition in the QCD for different masses of three flavours of quarks. The figure is taken from [57].

1.4 QCD phase diagram

The high-energy region of the strongly interacting matter, i.e. the de-confined phase of the quarks and gluons, can be studied by creating extreme temperature and energy density conditions. Such a matter of extreme conditions is believed to exist a few micro-second after the Big-Bang or at the core of the neutron stars. In the laboratory, the formation of such a state of matter becomes feasible by colliding nuclei at the ultra-relativistic energies. The conjectured phase-diagram of the QCD matter is shown in Fig. 1.9. The phase-diagram shows the variation of the temperature (T) with baryon chemical potential. From this figure, it is readily evident that there are at least more than one ways to attain the de-confined QGP phase.

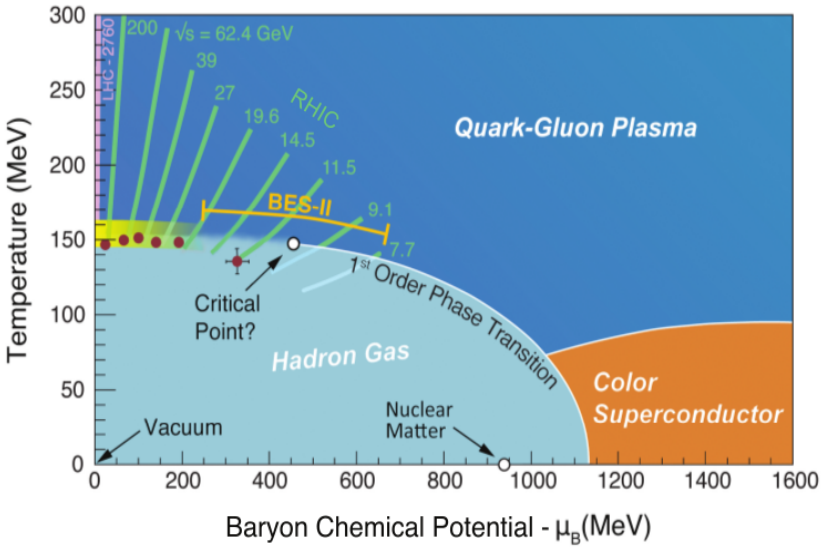

Fig. 1.9 The conjectures phase diagram of the QCD matter. The figure is taken from [62].

At high temperature and baryon chemical potential ~ 0, the phase transition from hadron gas to the QGP phase is believed to be a cross-over [63]. Lattice calculation predicts that this transition might occur at the energy density, $\varepsilon \approx 1$ GeV/fm^3 and temperature, T ≈ 170 MeV [57]. This region of the phase-diagram is being explored by the Large Hadron Collider (LHC) at the European Organisation for Nuclear Research (CERN), Switzerland and the Relativistic

Heavy-Ion Collider (RHIC) at the Brookhaven National Laboratory (BNL), USA [64]. On the other hand, the transition is believed to be the first order at the intermediate temperature and high baryon chemical potential [65, 66]. This high baryon chemical potential region of the phase-diagram will be explored by the experiment at the Facility for Antiproton and Ion Research (FAIR) at the GSI, Germany and Nuclotron-based Ion Collider fAcility (NICA) at the Joint Institute for Nuclear Research (JINR), Russia [64]. The point at which the first-order phase-transition line end and cross-over transition start is known as the critical point. The exact location of the critical point is yet to be confirmed by the experimental results and is the primary motivation of the RHIC Beam Energy Scan (BES) programme [67]. The region corresponding to the extreme high baryon chemical potential and low temperature is similar to the situation of neutron stars.

1.5 Space-time evolution of the matter formed in nuclear collisions

In ultra-relativistic nuclear collisions, two beams of nuclei are accelerated to extremely high-energy, where they travel in the opposite direction with the velocity nearly equal to that of light. In this scenario, the nuclei get Lorentz contracted along the direction of motion and appears as a "disk-like" objects as observed from the laboratory frame of reference. When two such disk-like objects collide, the collisions are classified according to the latent of overlapping zone. The overlapping nucleons of the collisions are called participants, and the nucleons that remain outside the overlapping zone & don't take part in the collisions are known as spectators. If all ($> 95\%$) nucleons of incoming beams collide, then the collisions are termed as the head-on or central collisions. On the other hand, with the variation of perpendicular distance between two beams of the nucleon, the collisions are classified as the semi mid-central and peripheral collisions. In head-on collisions, all the energy of beams

are deposited in the interaction region, and therefore, a new state of matter of extreme temperature and energy density is expected to be created. However, this is not the case for peripheral collisions, as the energy deposition will be much less than that of central collisions.

Figure 1.10 illustrates the space-time evolution of the matter formed during the heavy-ion collisions. The various possible scenarios that may arise during the collisions are discussed hereunder. One possibility is, if the energy density (ε) and temperature (T) of the system is high enough to cross the threshold value of $\varepsilon_0 \sim 1$ GeV/fm^3 and $T_c \sim 170$ MeV, a fireball of de-confined quarks and gluons will be formed as shown in the right side of the said figure [57, 68]. However, the free quarks and gluons are yet to achieve thermalisation, and the state of matter thus formed is called the pre-equilibrium state. The subsequent interaction among the free quarks and gluons may bring the system into thermal equilibrium at proper time $\tau_0 \sim$ 1 fm/c, and a new state of matter, known as the Quark-Gluon Plasma (QGP), will be formed. Further, the system will keep on expanding due to the initial pressure gradient of the collisions, and therefore, the system's temperature will decrease. At the critical temperature (T_c) and proper time $\sim$ 10 fm/c, the deconfined quarks and gluons hadronise [57]. Due to hadron's finite formation time, the system is expected to evolve through a mixed phase of hadrons and quarks & gluons. When all the quarks and gluons get confined to become hadrons, the system is known as the hadron gas. Moreover, the temperature of the system will keep on decreasing as it expands further and at the chemical freeze-out temperature (T_{ch}), the chemical compositions of the hadrons get fixed. Above the T_{ch}, the inelastic scattering between the created hadrons can take place and their energy, momentum can get modified. However, once the system crossed the T_{ch}, all the inelastic scattering between the hadrons ceases. The expansion of the system continues until the thermal freeze-out temperature (T_{Th}) is reached. Beyond that, particles can no longer interact with each other, even elastically; hence, their energy and momentum get fixed. Finally, the particles emitted from the medium after the thermal freeze-out temperature are detected at the detectors. Various experimental

observables such as charge, momentum, energy etc. of the final-state particles can be reconstructed with different detectors. The final-state particles carry information about the QGP and the various stages of the evolution of the matter formed.

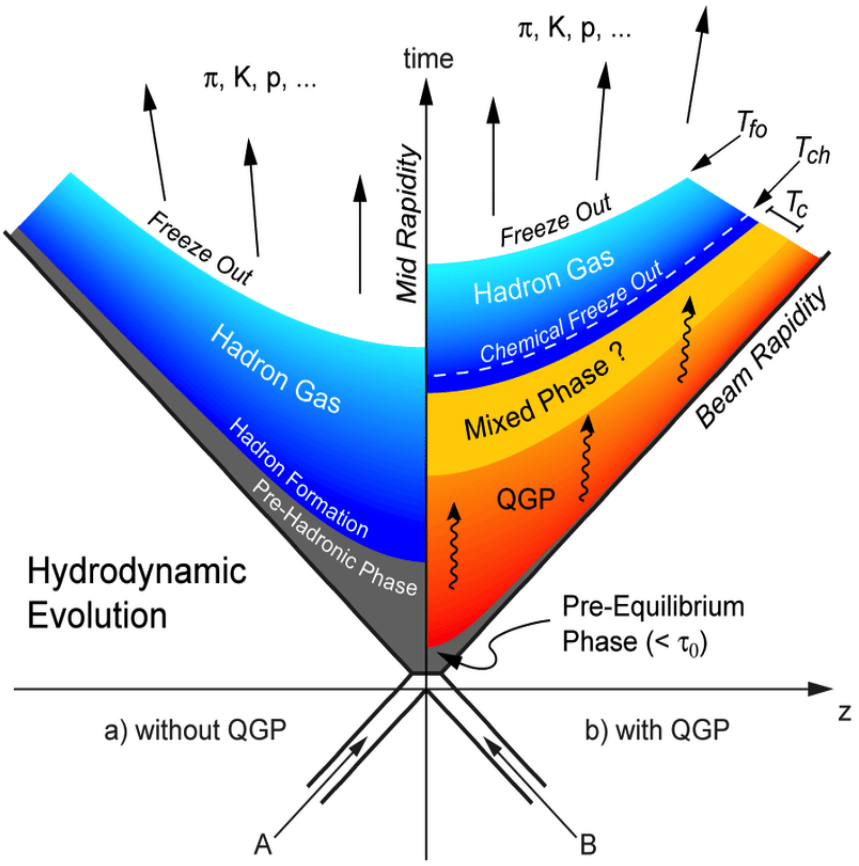

Fig. 1.10 Space-time evolution of the matter formed after the collisions of two heavy nuclei of ultra-relativistic energy. RHS of the figure shows the evolution of the system with QGP formation, and the LHS shows the evolution of the system without QGP. The figure is taken from [69].

On the other hand, if the temperature and energy density of the system are not high enough to cross the threshold value, the Quark-Gluon Plasma medium will not be formed. In this case, the system will be composed of hadrons only and will evolve as described previously after the formation of hadron gas.

1.6 Probing the ultra-relativistic nuclear collisions

The lifetime of the QGP matter formed during the collisions is expected to be $\sim 10^{-23}$ s, and the system's temperature is also very high $\sim 10^{12}$ K. It is therefore experimentally not possible to detect this state of the matter directly. Rather, one has to rely on some indirect methods or observables, which can provide reliable information about the state of the matter. Various observables of nuclear collisions can provide information about the various stages of evolution of the collisions. More detail information on different observables of nuclear collisions are given below:

1.6.1 Charged particles multiplicity

The number of charged particle produced in a collision is known as multiplicity. The multiplicity distributions of particles are general and fundamental observable of ultra-relativistic nuclear collisions that provide important information about both soft QCD processes and hard scattering. Therefore, it offers an excellent opportunity to explore interaction and correlation among them. The total number of charged particles produced in the collisions is dominated by soft processes and can give information on the medium. The hard processes are assumed to scale with the number of binary collisions (N_{coll}), whereas soft particle production is believed to scale with the number of participants (N_{part}). Moreover, as a direct measurement of the collisions event inelasticity, multiplicity contains information about different properties of the particle production mechanism and hadronisation process [70]. In heavy-ion collisions, there is a direct correlation between multiplicity and centrality [71]; however, the situation is not much clear for the pp collisions.

The number of charged particles produced at mid (pseudo)-rapidity, i.e. dN_{ch}/dy ($dN_{ch}/d\eta$) is related to energy density produced during the collisions through the Bjorken formula, which connect the energy density to the transverse energy as given below [72]:

$$\varepsilon_B(\tau_0) \geq \frac{1}{\tau_0 S_\perp}\frac{dE_\perp}{d\eta} \tag{1.11}$$

where the transverse energy is related to the charged-particle multiplicity as follows:

$$\frac{dE_\perp}{d\eta} = \frac{3}{2}\frac{1}{\tau_0 S_\perp}\langle E_\perp/N\rangle\frac{dN_{ch}}{d\eta} \tag{1.12}$$

Here τ_0 is the thermalisation time, $S_\perp$ is the transverse area of the incident nuclei and $dE_\perp/d\eta$ is the transverse energy per unit pseudorapidity. The $\langle E_\perp\rangle/N$ is the average transverse energy per produced particle.

From the measured value of the charged-particle multiplicity density at mid-pseudo-rapidity for the central Pb-Pb collisions at $\sqrt{s_{NN}} = 2.76$ TeV at the LHC [73], the energy density is estimated to be about 12.3 GeV/fm^3 at τ_0= 1 fm/c. This energy density value is about 2.3 times higher than that of the Au-Au collisions at the highest RHIC energy [4–7].

The charged-particle multiplicity density normalised to per nucleon participant pairs measured by various experiments at the RHIC and LHC energy are shown in Fig. 1.11(a). For RHIC energies, the results between the 0-6% central Au-Au collisions and Cu-Cu collisions are compared. From this comparison, it is evident that for the central collisions of symmetric nuclei, charged-particle multiplicity density per participant nucleon pair does not depend on the size of the colliding nuclei but only on the centre-of-mass energy of collisions [74, 75]. The measurement reported for the maximum RHIC energy shows that particles multiplicity density per participant nucleon pairs is 98% higher than that of SPS results at $\sqrt{s_{NN}} = 17.3$ GeV [76, 77]. Moreover, the result of the 0-5% central Pb-Pb collisions at $\sqrt{s_{NN}} = 2.76$ TeV measured by ALICE at the LHC energy suggests a significant increase, by a factor of 2.2 compared to the Au-Au collisions measurement at the RHIC. All these measurements are observed to describe by a power-law function given by Eq. (1.13).

$$f_{AA}^{Pow} = 0.78 \times (\sqrt{s_{NN}})^{0.3} \tag{1.13}$$

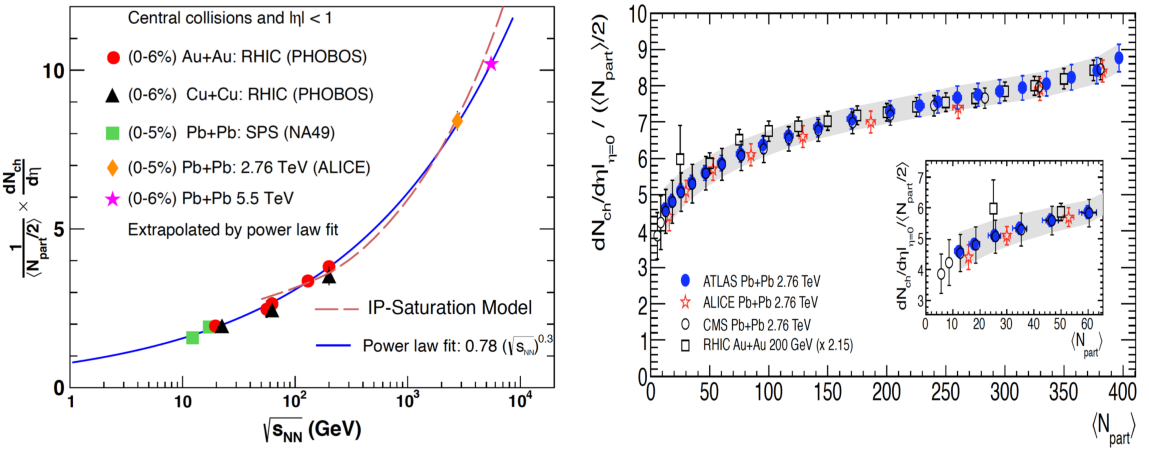

(a) (b)

Fig. 1.11 (a) Energy-dependent charged-particle multiplicity density normalised to per participant nucleon pairs in Au-Au, Cu-Cu and Pb-Pb collisions at the SPS, RHIC and LHC energies, respectively. (b) The N_{part} dependence of the multiplicity density normalised to per participant nucleon pairs from different LHC experiments is compared with the highest energy RHIC results [78].

The normalised charged-particle multiplicity density with the centrality of the collisions is shown in Fig. 1.11(b). It could also be observed that the normalised multiplicity density increases with increasing centrality, indicating that particle multiplicity at mid-rapidity increases faster than the number of participant nucleon (N_{part}). This rapid increase of multiplicity is expected due to the contribution of hard processes to particle production [79] and is quite similar to that observed for the highest RHIC energy. Moreover, normalised multiplicity density decrease by a factor of two from the most central to peripheral collisions.

Further, the unprecedented energy regime of the LHC has provided tremendous scope to study the properties and dynamics of the system formed in small systems. The numbers of particles produced in the high-multiplicity event of pp collision become similar to peripheral collisions of heavy-ion or even more prominent for p-Pb collisions. Therefore, differential analysis can be performed by considering the rare events where large numbers of particles are produced. Events of pp and p-Pb collisions can be divided according to the charged-particle multiplicity. In some cases, the high-multiplicity events produce particles 10 times larger

than the low-multiplicity events. Therefore, it becomes significantly important to investigate the rare phenomena in these events that rarely occur in low-multiplicity events.

1.6.2 Transverse momentum (p_{T}) distribution

The transverse momentum (p_{T}) spectra of the produced particles is considered as one of the most important observables of nuclear collisions. It contains information about the collision dynamics and the space-time evolution of the system from the initial to the final stage of the collisions [9, 80, 81]. Most of the particles produced in nuclear collisions are hadrons, formed via the soft interaction process. These particles then undergo several stages of evolution until they freeze-out and get detected in the detector. As discussed in section 1.5, hadron abundances get fixed at the chemical freeze-out. However, the spectral shape of particles gets modified due to elastic scattering until the kinetic freeze-out occurs. The p_{T} spectra of particles are usually investigated by calculating the invariant cross-section as given below:

$$E\frac{\mathrm{d}^3N}{\mathrm{d}p^3} = \frac{1}{2\pi p_{\mathrm{T}}}\frac{\mathrm{d}^2N}{\mathrm{d}y\mathrm{d}p_{\mathrm{T}}} \tag{1.14}$$

where E is the energy of the particle and $\mathrm{d}^2N/\mathrm{d}y\mathrm{d}p_{\mathrm{T}}$ represents an event-wise yield density.

The low p_{T} part of the spectra can be described by an exponential function having a thermal origin. In contrast, the high p_{T} part, which is dominated by hard parton-parton scattering, can be described by a power-law function. For a complete description of the identified particles p_{T} spectra, the Levy-Tsallis function is used, which has the contribution from both the exponential and power-law function. The inverse slope of the p_{T} spectra provides information about the effective temperature of the system. It contains the contribution from both the kinetic freeze-out temperature (T_{Kin}), and the collective motion of particles. The kinetic freeze-out temperature arises because of the random kinetic motion of particles. To investigate the T_{Kin} and expansion velocity of the system, the low p_{T} region

of different identified particles (π, K and p) p_{T} spectra are simultaneously fitted with the Blast-Wave (BW) model [82]. The Blast-wave model is a simplified hydrodynamical model which assumes that particles are locally thermalised at the kinetic freeze-out temperature and are coming out of the system with a common transverse velocity. Due to the common expansion velocity, the heavier particles are expected to get more momentum resulting in a change in the spectral shape.

Measurement of the p_{T} spectra in Au-Au collisions at the RHIC energies suggests a hardening behaviour with increasing collisions centrality, and the effect is more pronounced for heavier particles, like protons [83]. Similar hardening of the p_{T} spectra with increasing centrality and particles mass has also been observed in the Pb-Pb collisions at the LHC energy [11]. These mass-dependent hardening of the p_{T} spectra is usually associated with the hydrodynamic evolution of the system. A more recent measurement of the p_{T} spectra as a function of multiplicity in the p-Pb collisions at the LHC energy further suggests behaviour reminiscent of those observed in the Pb-Pb collisions [17]. At the LHC energies, the high-multiplicity pp collisions are comparable to p-Pb and peripheral Pb-Pb collisions. As the results of the p-Pb colliding system are also consistent with the hydrodynamical evolution of the matter, it becomes important to study the high-multiplicity events of pp collisions with great details. Precise investigations of the evolution of the p_{T} spectra with increasing multiplicity for such pp collisions is expected to provide significant information about the particle production and dynamics of the matter formed in these collisions.

The low p_{T} region of pions, kaons and protons p_{T} spectra are fitted with the BW model to extract different parameters, such as the kinetic freeze-out temperature and the average expansion velocity. The results of the fit are shown in Fig. 1.12 as a function of collisions energies. These measurements were performed by several experiments, namely the EOS at GSI [84], FOPI at SIS [85], NA49 at the SPS [86], STAR at the RHIC [83, 87] and ALICE at the LHC [88]. The kinetic freeze-out temperature increases with increasing collisions energy,

and then it almost shows a saturation behaviour for energy greater than $\sqrt{s_{NN}} = 10$ GeV. On the contrary, the average expansion velocity tends to increase with increasing collisions energy.

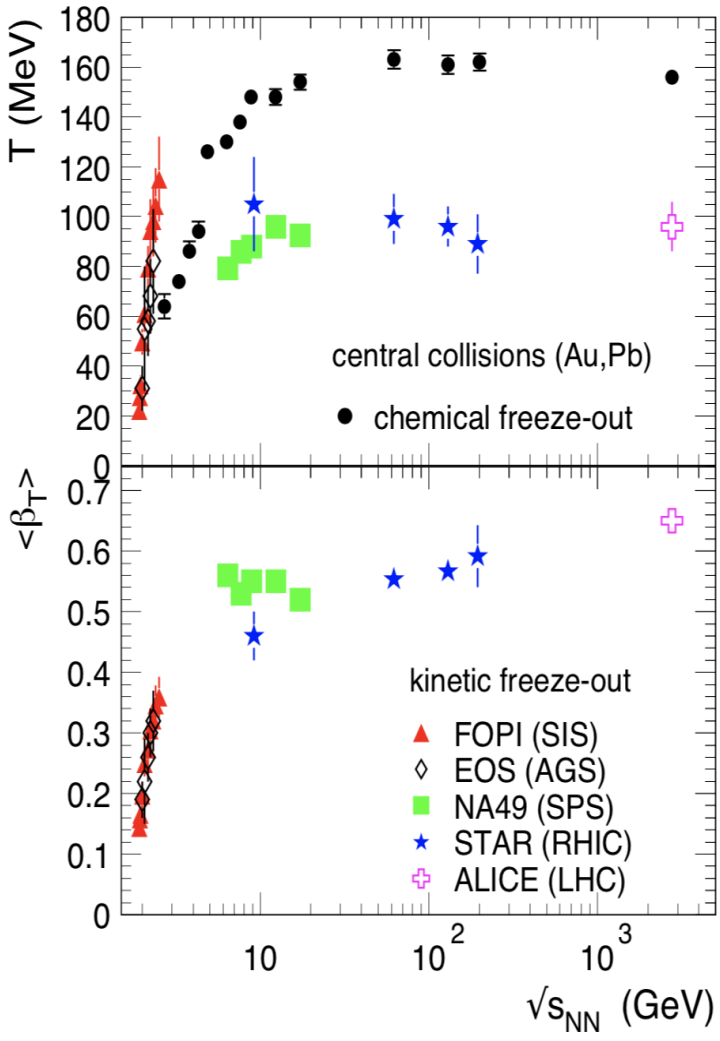

Fig. 1.12 Centre-of-mass energy dependence of the kinetic, chemical freeze-out temperature and average expansion velocity measured by different experiment at the SIS, AGS, SPS, RHIC and LHC energies [89].

The particle produced at the intermediate p_{T} region also provides valuable insight into the production mechanism. The p_{T}-differential baryon to meson ratio shows an enhancement at the intermediate p_{T} for the central collisions when studied as a function of collisions centrality and are compared with the results of small colliding systems (d-Au, pp etc.) at the

RHIC [5, 90] and LHC energies [11]. Several mechanisms, such as the recombination of quarks (coalescence model), hydrodynamic evolution of the medium with a common velocity, are observed to describe the enhanced production of baryons over mesons at the intermediate p_{T} region [91, 92]. Therefore, similar investigations for high-multiplicity pp collisions at the LHC energies are also significantly important.

The p_{T}-integrated yield of particles is a crucial observable of the nuclear collisions. The yields of particles can be calculated by combining the yields from the measured and extrapolated p_{T} spectra. The extrapolation is required for the very low p_{T} particles where detectors can't detect them. The yields of the particles provide information for a better understanding of the dynamics of the collisions. For example, particles produced in the low energy collisions are dominated by the incoming nuclei due to the stopping of the nuclei in the collisions zone, resulting in higher yields of protons. On the contrary, the incoming nuclei become transparent at higher energies and hence, the contribution from the stopping will be less. Further, a fit of different particles yields in heavy-ion collisions is performed with the statistical thermal model to extract the chemical freeze-out temperature of the system [93–95].

The yields ratios of different particles to pions are sensitive to the production mechanism [9, 80, 81, 96]. Usually, various strange particle to pions ratios indicate the enhanced production of strangeness. Similarly, the p/π ratio provides information about baryons production compared to mesons. In Fig. 1.13, the p_{T}-integrated yields ratios of light-flavour hadrons to pions as a function of multiplicity for the Pb-Pb collisions at $\sqrt{s_{NN}} = 2.76$ TeV are shown. It could be observed from the figure that both ratios follow a universal trend from the peripheral to central heavy-ion collisions. From Fig. 1.13(a), it is observed that the yields ratio of kaons to pions increases with increasing charged-particle multiplicity density, suggesting enhanced production of the strange particle [11]. A similar increase in the kaons to pions yields ratio as a function of multiplicity has also been observed for p-Pb collisions

[17]. On the other hand, the p/π ratio measured by ALICE in Pb-Pb collisions indicates decreasing behaviour for the central collisions, as observed from Fig. 1.13(b).

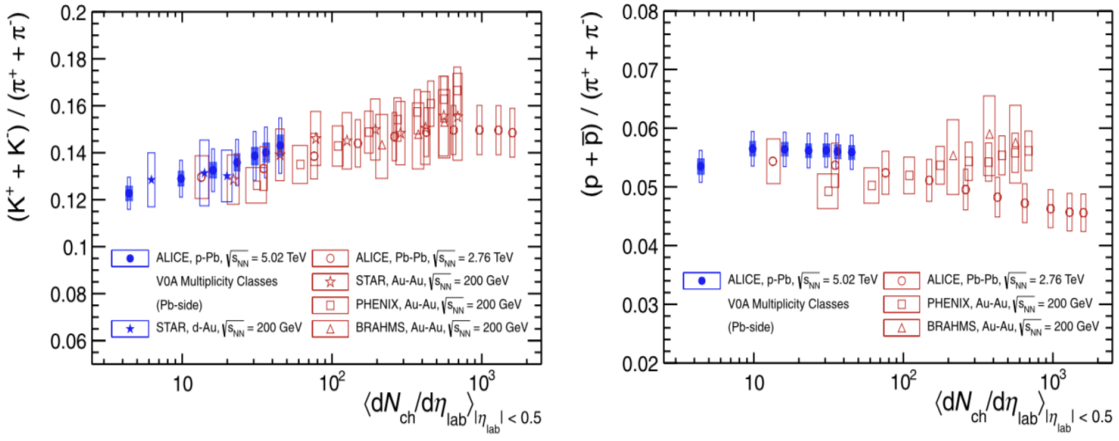

(a) (b)

Fig. 1.13 The p_{T}-integrated yield ratios of (a) K/π and (b) p/π as a function of charged-particle multiplicity in p-Pb collisions at $\sqrt{s_{NN}} = 5.02$ TeV compared with the results of the STAR, PHENIX, BRAHMS and ALICE experiment [17].

Further, any changes in the measured p_{T} spectra can be investigated by studying the average transverse momentum ($\langle p_{\mathrm{T}} \rangle$) of particles. The $\langle p_{\mathrm{T}} \rangle$ of the particle carries information about collisions dynamics and the temperature of the system at the thermal equilibrium in combination with the expansion velocity [9, 80, 81]. Studies on $\langle p_{\mathrm{T}} \rangle$ as a function of multiplicity provide information about the entropy density of the system, similar to temperature as a function of entropy for the possible formation of phase transition. Van Hove proposed that in the case of first-order phase-transition, a plateau behaviour in the $\langle p_{\mathrm{T}} \rangle$ with multiplicity could be observed, indicating the existence of latent heat of the system [32]. The variations of $\langle p_{\mathrm{T}} \rangle$ for different particles have been studied at the RHIC and LHC energies for different colliding systems [83, 11, 17]. At the RHIC energy, it has been observed that the $\langle p_{\mathrm{T}} \rangle$ increases with increasing collisions centrality and the effect is more pronounced for heavier particles. On the other hand, for Pb-Pb collisions at the LHC energy, similar behaviour in $\langle p_{\mathrm{T}} \rangle$ as seen at the RHIC could be observed which saturates at the

highest multiplicity. Further, in p-Pb collisions, the $\langle p_{\mathrm{T}} \rangle$ found to increase with increasing charged-particle multiplicity and particle mass as shown in Fig. 1.14 [83], similar to those observed in the Au-Au collisions at the RHIC and low multiplicity Pb-Pb collisions at the LHC. Therefore, studies on $\langle p_{\mathrm{T}} \rangle$ for the high-multiplicity events of small systems like pp collisions will provide information about the dynamics of the system.

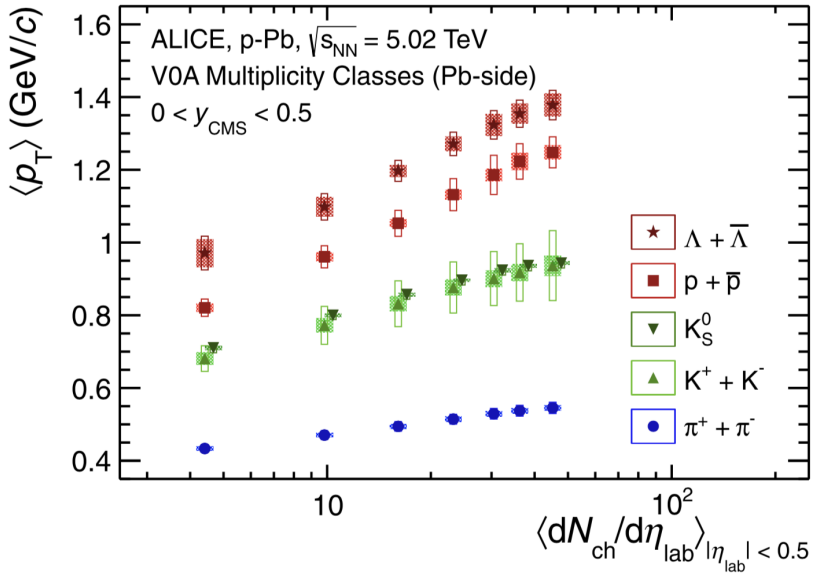

Fig. 1.14 $\langle p_{\mathrm{T}} \rangle$ of different identified charged particles as a function of charged-particle multiplicity measured by ALICE in the p-Pb collisions at $\sqrt{s_{NN}} = 5.02$ TeV [17].

1.6.3 Collective flow

The collective expansion experienced by the constituent particles of the medium formed during the collisions is known as the collective flow. The pressure gradient created during the collisions causes the system to undergoes hydrodynamical evolution. Therefore, the constituents of the medium interact with each other via momentum transfer during the evolution of the fireball to achieve thermal equilibrium. During this process, the collective motion experienced by the particles is known as the radial flow [97].

On the other hand, in non-central heavy-ion collisions [Fig. 1.15(a)], the initial spatial anisotropy of the overlapping nuclear zone, as shown in Fig. 1.15(b), is converted into momentum space anisotropy [Fig. 1.15(c)] due to anisotropy in the pressure gradient. This initial anisotropy leads to the anisotropic azimuthal distribution of particles emitted from the collisions zone and thus lead to a non-vanishing elliptic flow coefficient [97, 98]. As the elliptic flow is due to the initial anisotropy of the collisions, it is expected to be higher in semi-central collisions and vanishes in central collisions.

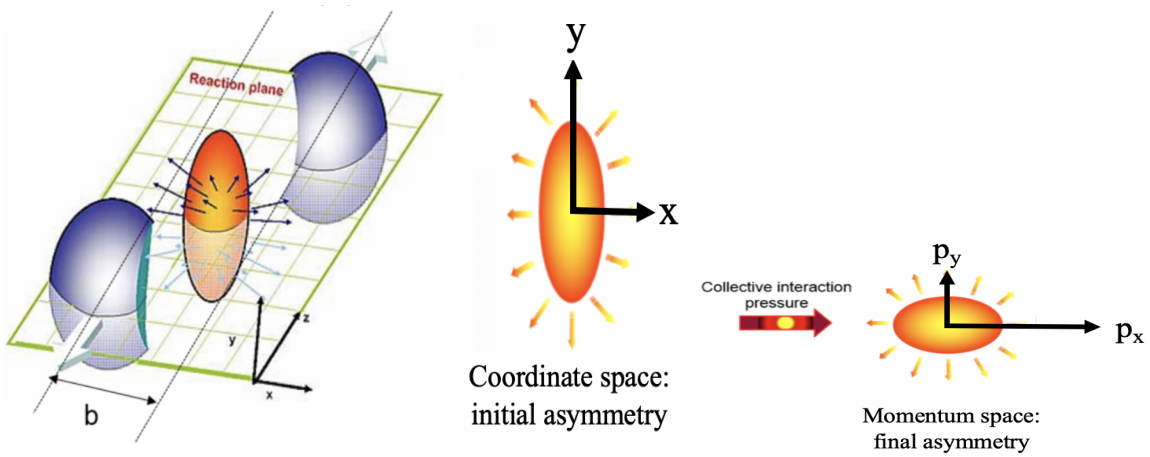

(a) (b) (c)

Fig. 1.15 (a) Schematic of the collisions overlapping zone between the incoming nuclei, (b) the initial-state anisotropy in the collisions zone that is finally converted into the final-state elliptic flow, and (c) the anisotropy in particle momentum space [99].

The anisotropic behaviour of the constituent particles can be explored by measuring the azimuthal angle distribution of particles relative to the reaction plane. The reaction plane is defined by the impact parameter (b) of the colliding nuclei and the beam direction, as shown in Fig. 1.15(a). Generally, particles anisotropic flow can be measured by the method described by Poskanzer and Voloshin [100]. The n^{th} flow parameter is given by the n^{th} Fourier coefficient of the particle azimuthal angle distribution described by Eq. (1.15).

$$\frac{dN}{d(\phi-\psi_n)} \propto \frac{1}{2\pi}\left(1+2\sum_{n=1}^{\infty} v_n cos[n(\phi-\psi_n)]\right) \tag{1.15}$$

where $v_n = \langle cos[n(\phi - \psi_n)]\rangle$ coefficients are used for a quantitative description of the event anisotropy and the angle brackets represent the average over all particles in all events. The sine terms are not present due to symmetry with respect to the reaction plane. Here, ϕ is the azimuthal angle of emission for each hadron, ψ_n is the n^{th} event plane, that varies from event-by-event. The ϕ and ψ_n are determined in a reference frame. The coefficients v_1, v_2 and v_3 are the most important observables and are known as directed, elliptic and triangular flow.

Figure 1.16(a) shows the beam energy dependence of elliptic flow of the charged particles. The measurement has been performed by different experiments such as the EOS and FOPI experiment at the GSI; E95 and E877 experiment at the AGS; CERES and NA49 experiment at the SPS; PHENIX, PHOBOS and STAR experiment at the RHIC and ALICE, ATLAS and CMS experiment at the LHC. At low fixed target energies ($\sqrt{s_{NN}} \sim 3$ GeV), v_2 is observed to be negative and is due to the fact that the spectator parts of nuclei block the matter in the direction of the reaction plane. On the other hand, at higher energies, the spectator parts moves away quickly and therefore, v_2 is positive. This behaviour is expected in hydrodynamic scenarios, in which a large pressure gradient within the reaction plane produces a more substantial expansion of the system. For the RHIC energies, the v_2 seems to continue to grow up to the highest centre of mass energies. A recent measurement of v_2 at ALICE also shows an increase of elliptic flow by about 30% compared to that are measured at the highest RHIC energy. However, this increase of elliptic flow could not be seen in the differential elliptic flow of charged particles, as shown in Fig. 1.16(b). Therefore, one can conclude that the bulk medium formed at the RHIC and LHC energies have similar properties. Further, the 30% increase of the v_2 between the two energies is due to the enlarged phase-space available for particle production and the increase in average transverse momentum of the particles between RHIC and LHC energies.

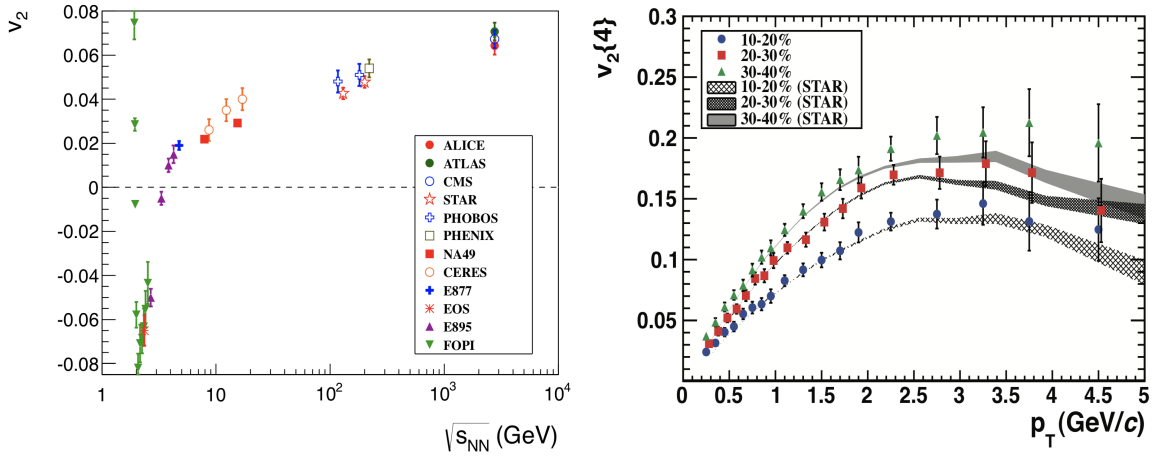

(a) (b)

Fig. 1.16 (a) The integrated elliptic flow of the charged particles as a function of the centre-of-mass energy. The results correspond to 20-30% central collisions for Au-Au or Pb-Pb collisions. (b) The p_{T}-differential elliptic flow of the charged particle measured in Pb-Pb collisions at $\sqrt{s_{NN}} = 2.76$ TeV by ALICE are compared with the STAR Au-Au collisions results at $\sqrt{s_{NN}} = 200$ GeV [78].

Moreover, the elliptic flow of various identified charged hadrons as a function of p_{T} follows two different distinct curves for mesons and baryons at the RHIC energy. The STAR experiment has also observed a non-zero elliptic flow for strange baryons (Ω, Ξ, Λ) and meson (K^0_s). Also, the v_2 scaled by the number of constituent quarks (n_q) as a function of p_{T}/n_q for different identified particles observed to follow a common curve except for the pions. These observations suggest the formation of substantial collective motion before hadronisation in the high energy nuclear collisions at the RHIC [101, 102]. ALICE has also performed a similar measurement of v_2 at the LHC. Here too, a distinct mass ordering for the low p_{T} region < 3 GeV/c could be seen, attributed to the interplay between elliptic and radial flow that modifies the v_2 according to the mass of the particle. In the intermediate p_{T}, particles v_2 tend to follow the distinct curve for mesons and baryons as observed at the RHIC. However, at the LHC, v_2 results observed to deviate from the number of constituents quarks scaling at the level of $\pm 20\%$ [103].

A similar measurement of the anisotropic flow coefficients has also been performed recently for the small systems. Charged particles anisotropic flow coefficients $v_n\{k\}$ of order n, estimated via k-particle correlation for pp collisions measured by ALICE [104] and CMS [105] Collaboration are shown in Fig. 1.17(a) and 1.17(b), respectively. For both the measurements, results show non-zero values of v_n coefficients for the pp collisions, indicating collective behaviour in the small system. Therefore, more detailed studies on v_2 and higher-order coefficients for various identified particles as a function of p_{T} and charged-particle multiplicity will provide a better understanding of collective effects in the small system.

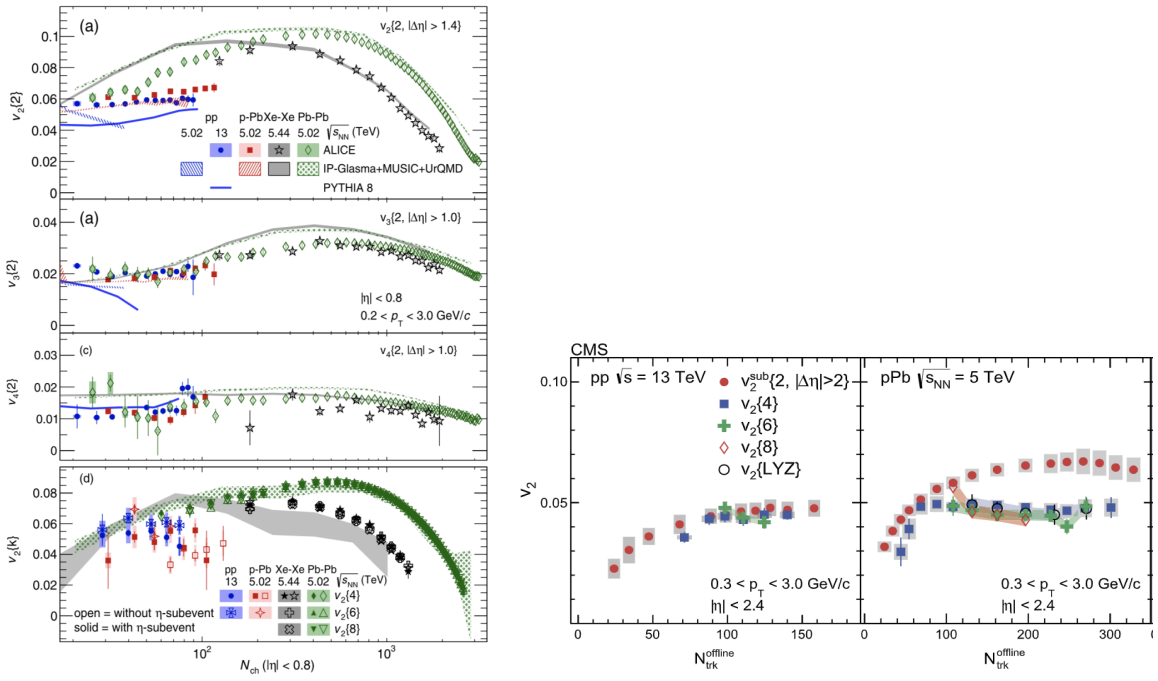

(a) (b)

Fig. 1.17 (a) $v_2\{k\}$ of charged particles as a function of charged-particle multiplicity for pp collisions at 13 TeV are compared with the results of the p-Pb, Xe-Xe and Pb-Pb collisions results [104] (b) $v_2\{k\}$ of charged particles as a function of transverse momentum in pp collisions are compared with p-Pb collisions results measured by CMS [105] .

1.6.4 Strangeness enhancement

Measurement of the strange particle production in nucleus-nucleus collisions is of immense interest as the entire visible world consists of other two light quarks i.e. up (u) and down (d). Therefore, the hadron containing strange quarks must be produced during the collisions. The production rates of strange particles are believed to increase in the QGP medium compared to a normal hadronic medium. Rafelski and Muller first suggested this as a signature of the QGP formation [106, 107]. The idea of strangeness enhancement relies on different mechanisms of strange particle production in the QGP phase and hadron gas medium. If the system produced during the collisions does not evolve through a QGP phase, the strange particle must be created via the re-scattering of the particle in the expanding hadron gas system. As the strangeness is a conserved quantity, the strange and anti-strange particle production rates should be equal. Therefore, the threshold energy required for the production of strange hadron becomes quite high. Some typical examples with lowest threshold value are given below:

$$\pi + N \rightarrow \Lambda + K \qquad E_{thres} \sim 540 \text{ MeV}$$

$$N + N \rightarrow N + \Lambda + K \qquad E_{thres} \sim 670 \text{ MeV}$$

On the other hand, the production of various strange particles is much simpler in the QGP phase. In such scenario, quark masses reduced to bare mass, resulting in lower threshold energy for strange-antistrange pair production. The threshold energy required to produce such strange-antistrange quark pair becomes just the sum of the mass of two strange quarks, i.e., $\sim$ 200 MeV. Therefore, in the QGP phase, the production rates of strange particles enhanced significantly. In the QGP phase, strange quarks are produced mainly by quark-antiquarks and gluon-gluon fusion.

$$q + \bar{q} \rightarrow s\bar{s}$$

$$g + g \rightarrow s\bar{s}$$

Strangeness enhancement was studied via the observables called strangeness enhancement factor (E), which is defined as the yield per participant in the Pb-Pb (or p-Pb) collisions normalised to yield per participant in the pBe/pp collisions. The enhanced production of the strange particle in nucleus-nucleus collisions was first observed in the WA97 and NA57 experiment at the CERN SPS [108, 109]. In Fig. 1.18, the enhancement measured by the NA57 experiment as a function of the number of the wounded nucleon is shown for hyperons and anti-hyperons. The Pb-Pb results clearly exhibit a centrality dependence strangeness enhancement for all the particles except $\bar{\Lambda}$. The STAR experiment at the RHIC has also observed a similar enhancement for the strange particles in heavy-ion collisions [110]. Further, the enhancement increases with the increase in strangeness content of the baryon. Recent results of the ALICE experiment at the LHC have also shown similar enhancement as observed in the STAR (Fig. 1.19) [111]. However, the enhancement factor is perceived to be decreased with the increase in the centre-of-mass energy. This energy-dependent decrease of strangeness enhancement is believed to occur due to the so-called canonical suppression mechanism [112, 113]. In canonical suppression, due to the unavailability of the energy levels and phase-space for $s\bar{s}$ pair production in a small system, the production rate of such processes are suppressed. Therefore, the denominator terms of the enhancement factor decrease, resulting in a higher value of strangeness enhancement for the lower energies results than LHC energy. Further, the canonical suppression increases with the increase in the strangeness content of the hadrons. Also, it is predicted to be highest at lower energy rather than the higher centre-of-mass energy.

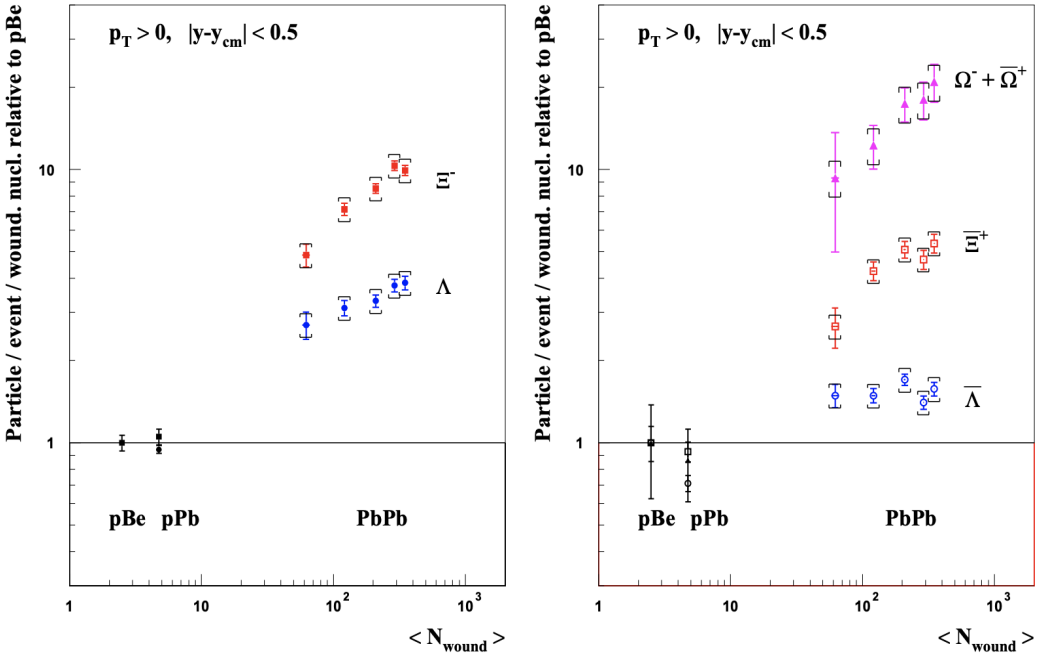

Fig. 1.18 Strangeness enhancement factor of different strange and multi-strange particles measured by the NA57 experiment as a function of the number of wound nucleon [109].

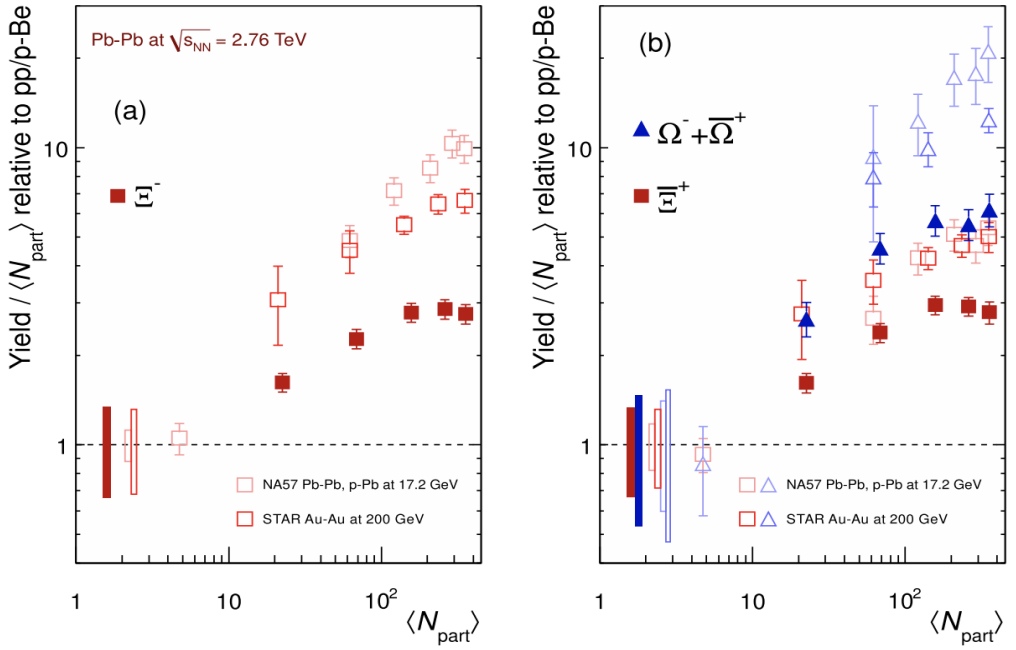

Fig. 1.19 Strangeness enhancement factor of the different strange hadron measured by the ALICE are compared with the results of the lower energies STAR and NA57 experiment [110, 111].

1.6.5 Correlation and Fluctuation

The evolution of the system formed during the collisions of heavy-ion can be studied via measurements of the momentum correlation of emitted particles. This measurement provides information about the collision geometry and its dynamics extracted from the analysis of various observables registered simultaneously. Correlated emission of particles in the region of small relative velocity arises primarily because of two effects: (i) quantum statistics (QS) and (ii) final state interaction (FSI). The QS is applicable for identical bosons and fermions, whereas, for FSI, the Coulomb interaction is applicable for charged particles and strong interaction for all types of hadrons [114]. Both effects primarily depend on the distance between the particle emission points and their relative momentum.

For the measurement of such correlated emission of particle, the two-particle correlation function C(p_1, p_2) as defined in Eq. (1.16) is generally used [114].

$$C(p_1, p_2) = \frac{d^6N}{dp_1^3 dp_2^3} \Big/ \frac{d^3N}{dp_1^3}\frac{d^3N}{dp_2^3} \tag{1.16}$$

This technique of obtaining the two-particle correlations between the emitted particles provide the method to estimate the size and lifetime of the system. Depending on the choice of study of pairs of particles, the correlation function can give information about different underlying physical processes.

The fluctuation of an experimental variable implies deviations of the quantity from its central value. Any physical quantity which is measured in an experiment is subject to fluctuation. This type of fluctuation is known as statistical fluctuation. Statistical fluctuation mainly arises due to the finiteness in sample size. On the other hand, fluctuations that arise due to the underlying physical processes that occur during the evolution of any dynamical system are known as non-statistical or dynamical fluctuation [23]. This type of fluctuations depend on the properties of the system under study and contain relevant information about

the system formed. In nuclear collisions studies, understanding the origin of dynamical fluctuations may provide new insight into the underlying mechanism responsible for particle production. One would expect a significant fluctuation in the particle multiplicities, transverse momentum etc., during the phase transition from ordinary hadronic matter to QGP [32, 33]. Moreover, a substantial fluctuation in particles multiplicity may indicate the formation of mini-jet resulting from the semi-hard parton-parton interaction or gluon bremsstrahlung [23, 24]. In nucleus-nucleus collisions, the event-by-event fluctuation of suitably chosen observables may provide information about the thermodynamic properties of the system at freeze-out. Moreover, fluctuations are very much sensitive to the nature of phase-transition. For example, the specific heat of the matter diverges for the second-order phase-transition, and therefore, fluctuations decrease significantly if the matter freezes-out at the critical temperature [115, 116].

There are several observables that can measure the dynamical fluctuation of p_{T} in high-energy nuclear collisions. The distribution of the average transverse momentum of events is one of them. It is generally defined by the following equation.

$$\langle p_{\mathrm{T}} \rangle = \frac{1}{N} \sum_{i=1}^{N} p_{\mathrm{T_i}} \tag{1.17}$$

where N is the multiplicity in a given event and $p_{\mathrm{T_i}}$ is the transverse momentum of the i^{th} particle. The $\langle p_{\mathrm{T}} \rangle$ distribution of the events is generally compared to the corresponding distributions obtained for mixed events, where particles are emitted independently from each other and follow the experimental inclusive spectra. Any deviation between these two indicates the presence of dynamical fluctuation in the system [117]. In Fig. 1.20, results of the event-by-event $\langle p_{\mathrm{T}} \rangle$ distribution for 5% most central Au-Au collisions at $\sqrt{s_{NN}} = 200$ GeV measured by the STAR experiment is shown. From the figure, it could be observed that the distribution for the data is broader compared to mixed events, suggesting the presence of dynamical fluctuations in the data. It is proposed that an increasing trend followed by

saturation in $\langle p_{\mathrm{T}} \rangle$ fluctuations, as a function of the number of participating nucleons, can provide information related to the QCD transition and onset of thermalisation [118–120]. Therefore, the measurement of dynamical fluctuations in relativistic nuclear collisions is important as it provides information about the different underlying physical process of the collisions.

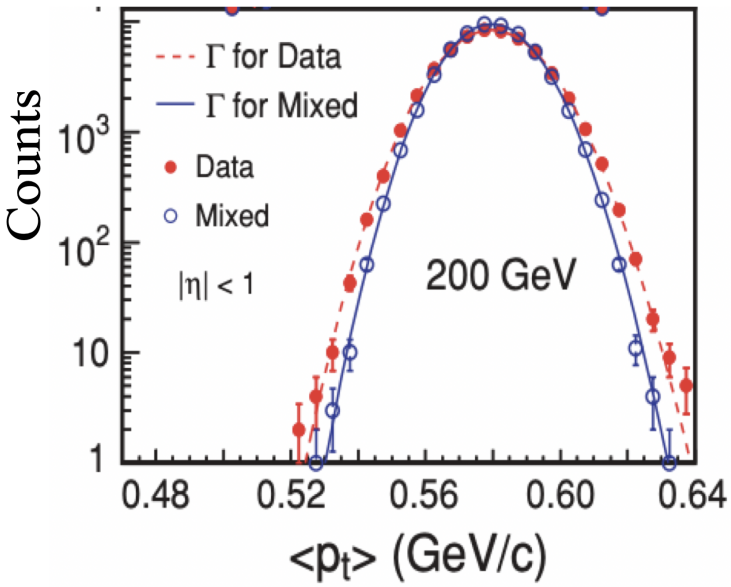

Fig. 1.20 Event-by-event distribution of average transverse momentum for 5% most central Au-Au collisions at $\sqrt{s_{NN}} = 200$ GeV [117].

The observables as mentioned above, namely, charged-particle multiplicity, transverse momentum spectra, anisotropic flow, strangeness enhancement, and correlation & fluctuation are in general known as the global observables or soft probes of nuclear collisions and independently provide information about collisions dynamics starting from chemical to kinetic freeze-out temperature.

1.6.6 Jet quenching

In high-energy nuclear collisions, the hard scattering between the incoming high energy partons results in high momentum transfer, producing high energy outgoing partons after the

interactions. These outgoing partons are then expected to undergo multiple interactions inside the collisions region before fragmenting into colourless hadrons during the hadronisation process. Such a process leads to an event with a cluster of hadrons emitted close in phase-space with high transverse energy. These types of cluster of hadrons are known as jets. In nucleus-nucleus collisions, studies on jets are important as they provide insight into the in-medium effect that can occur during the collisions, before the high energetic partons from the initial hard scattering fragments into hadrons. The effect through which such behaviour can be studied is known as the "jet quenching" effect and provides valuable information about the energy loss of the high p_{T} quarks and gluons in the medium formed in such collisions. The high energy partons are observed to lose energy via collisional energy [121, 122] and medium-induced radiative process [123–125], the latter being the most dominant in a QGP medium. The scattered partons are then expected to radiate gluons by losing its energy during its propagation, proportional to the quadrate of the in-medium path length [125, 126]. The effect of the jet quenching can be evident through the reduced production of the high-p_{T} particle. A more considerable quenching of the jet could be observed in central collisions than peripheral collisions. The emission of two back-to-back jets are not likely reconstructable as the jet with the longer path in the medium will lose much energy as shown in Fig. 1.21.

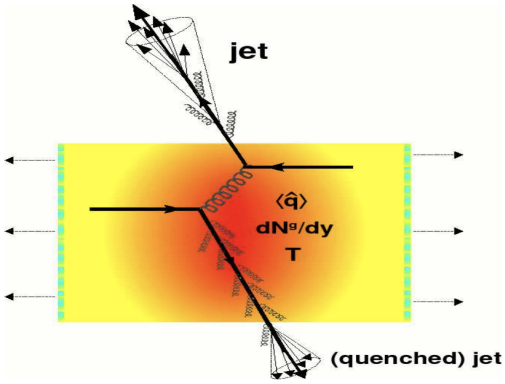

Fig. 1.21 Schematic of the di-jet moving in the opposite direction after two quarks are hard scattered in heavy-ion collisions. Jet produced near to the surface of the medium radiates gluon and then hadronises whereas, other jet produced inside the QGP medium losses energy and get quenched. The respective jets are known as near-side and away-side jets [127].

Usually, jet quenching can be quantified by the following observables:

- **Nuclear modification factor (R_{AA}):** Provide information about the modification of high p_{T} particle.
- **The centrality dependence of jet production:** Jet quenching is expected to be larger in central collisions than that of peripheral collisions.
- **Two particles azimuthal correlation:** Two di-jets with high-momentum are not likely to be reconstructed in a QGP medium.

The nuclear modification factor is defined as:

$$R_{AA} = \frac{1}{N_{coll}} \frac{d^2N_{AA}/(dydp_T)}{d^2N_{pp}/(dydp_T)} \tag{1.18}$$

where N_{coll} is the number of binary collisions in AA collisions. The possible values of R_{AA} could be:-

- $R_{AA} = 1$**:** It indicates that the AA collisions are a simple superposition of pp collisions.
- $R_{AA} < 1$**:** It indicates the effect of the strongly interacting matter in the AA collisions.
- $R_{AA} > 1$**:** Suggests the enhanced particle production in the AA collisions.

A comparison of the nuclear modification factor (R_{AA}) of inclusive charged hadrons between the central and peripheral Pb-Pb collisions measured by the ALICE experiment is shown in Fig. 1.22(a). It is evident from the figure that for central Pb-Pb collisions at high p_{T}, the R_{AA} values are much less than unity and reaches a minimum value of 0.14 at p_{T}= 6-7 GeV/c, indicating apparent suppression of the charged particles in the nuclear medium. On the contrary, for peripheral collisions, the R_{AA} value approaches to unity at high p_{T}, suggesting no suppression of charged particles [128]. In Fig. 1.22(b), the R_{AA} of inclusive charged hadrons in central Pb-Pb collisions is compared with the STAR and

PHENIX experiment results at the RHIC. It could be observed from the figure that the results from the LHC and RHIC energies show a similar pattern. However, the energy loss at the LHC is found to be much higher than RHIC energy, suggesting a denser medium at the LHC energy [128].

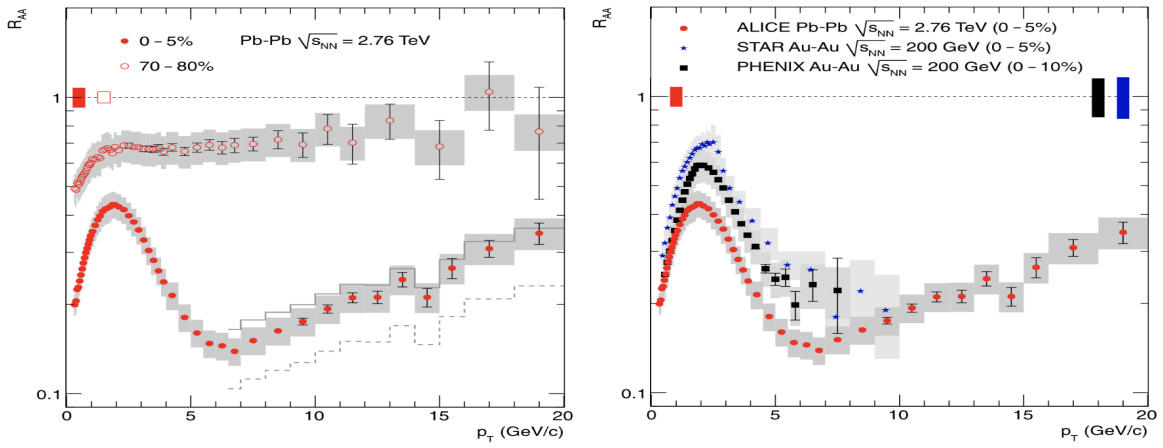

(a) (b)

Fig. 1.22 (a) R_{AA} of inclusive charged hadrons in central and peripheral Pb-Pb collisions at $\sqrt{s_{NN}} = 2.76$ TeV measured by the ALICE at the LHC. (b) R_{AA} of inclusive charged hadrons in central Pb-Pb collisions measured by ALICE is compared with lower energy STAR and PHENIX experiments results [128].

The energy loss of the partons can also be investigated by studying the two-particle azimuthal distributions. Due to the momentum conservation, the total transverse momentum of all the produced hadrons from the jets should be zero in the centre of mass frame. Therefore, if a di-hadron correlation is studied in $\Delta\phi$, it is expected that a peak at 0° in $\Delta\phi$ represents the correlation from the same side, and another peak at 180° will represent the away side correlations.

The results of the jet azimuthal distribution for pp, d-Au and Au-Au collisions at $\sqrt{s_{NN}} = 200$ GeV measured by STAR Collaboration is shown in Fig. 1.23 [129]. The top panel of the figure shows the distributions for central & minimum bias d-Au collisions and pp collisions. In the d-Au collisions, a clear near side and away-side peak could be seen, similar to those observed for pp collisions. These are generally known as jet production. In

the bottom panel of Fig. 1.23, the azimuthal distribution for the central Au-Au are shown and are compared with the results of the central d-Au and minimum bias pp collisions. For the central Au-Au collisions, the away side correlations are observed to be quenched, whereas large away side correlations are present in both d-Au and pp collisions. These results indicate the formation of a dense partonic medium in the central Au-Au collisions that suppress the away side correlations.

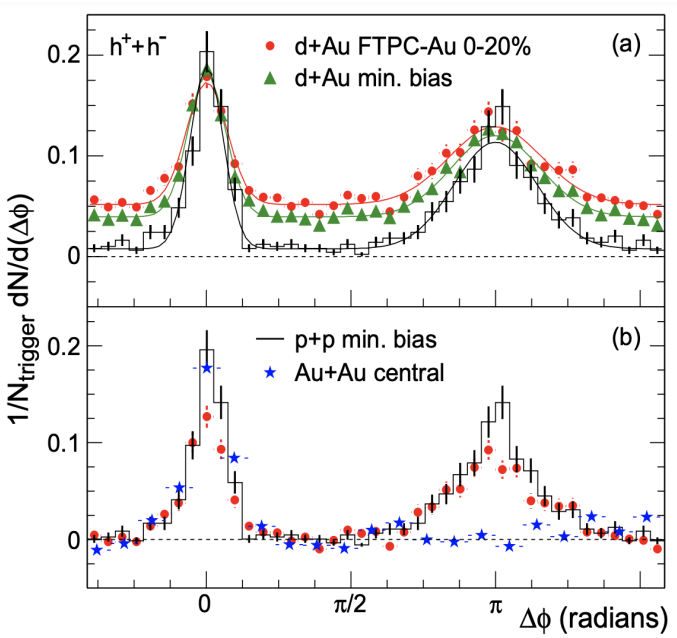

Fig. 1.23 (a) Two-particle azimuthal correlation in pp, minimum bias and central d-Au collisions and (b) comparison of two-particle azimuthal distribution for central Au-Au collisions with central d-Au and pp collisions [129].

1.6.7 J/ψ suppression

The bound state of a charm quark and anti-quark, $c\bar{c}$, is known as the J/ψ and is generally formed at a very early stage of the collisions. Therefore, the J/ψ particle expects to provide an excellent probe to study the early-stage dynamics of the medium formed in the nuclear collisions.

The potential energy required to form a $c\bar{c}$ system in free space is given by:

$$V(r) = \mathrm{kr} - \frac{\alpha_{\mathrm{eff}}}{\mathrm{r}} \tag{1.19}$$

However, in the de-confined QGP medium, the string tension k is zero and hence, the linear confining potential will vanish. Further, in the QGP medium, the c and $\bar{c}$ quarks will interact with each other through the colour-Coulomb interaction. The free space Coulomb interaction has the form e^2/r, and due to the presence of other light quarks, anti-quarks and gluons, the colour-Coulomb interaction becomes subject to Debye screening. Therefore, one obtains interaction in the form $\frac{e^{-\mathrm{r}/\lambda_{\mathrm{D}}}}{\mathrm{r}}$, where λ_D is the Debye screening radius and is inversely proportional to the charge density of the system. This type of interaction is known as colour-Yukawa interaction. The potential energy between the c and $\bar{c}$ quarks in a QGP medium is modified as given by Eq. (1.20).

$$V(r) = -\frac{\alpha_{eff} e^{-\mathrm{r}/\lambda_{\mathrm{D}}}}{\mathrm{r}} \tag{1.20}$$

The interaction between the charm and anti-charm quarks is effective only within λ_D. Beyond λ_D, the interaction potential falls off exponentially and become negligible at a large distance. The screening of the colour charge of charm and anti-charm quarks in the presence of the light quarks, anti-quarks and gluons is known as the Debye-colour screening. The Debye screening length has a dependence on the temperature of the medium. From the lowest order perturbative QCD calculations, it is found that the screening radius is related to the system's temperature as given by the equation below:

$$\lambda_D = \sqrt{\frac{2}{9\pi\alpha_{eff}}}\frac{1}{T} \tag{1.21}$$

As seen from the equation, with the increase of temperature, the Debye screening length decreases. The increased temperature of the system will also increase the light quark and gluon density around the charm and anti-charm quarks. Therefore, there are higher

possibilities of screening to diminish the c and $\bar{c}$ quarks' interaction. Thus, if the system's temperature is high enough, the attractive interaction becomes so small that the $c\bar{c}$ pair will not be formed, resulting in separate c and $\bar{c}$ quarks in the plasma. These separate charm quarks are now subsequently hadronized by combining with the light quarks/anti-quarks to form light charmonium state, e.g. $\psi^{'}$, $\psi^{"}$ leading to the reduced production rate of J/ψ. This reduced production of J/ψ is usually known as J/ψ suppression. It was first predicted by Matsui and Sats, which states that the production rates of J/ψ will be suppressed in a QGP medium compared to the state where no such medium is formed [130].

The SPS experiment at the CERN was the first experiment to observe the J/ψ suppression [131, 132]. Later it was further confirmed by experiment at the RHIC [133] and the LHC [134]. It is interesting to note that the amount of suppression observed at the LHC is less than the RHIC and SPS energies. This enhancement in the J/ψ yield at the LHC can be explained by different models, which considers the recombination of the charm quarks during the hadronisation process [134–136].

In Fig. 1.24(a), the results of the p_{T}-integrated centrality dependent nuclear modification factor (R_{AA}) of J/ψ measured via the di-muon channel by ALICE in Pb-Pb collisions at $\sqrt{s_{NN}} = 2.76$ TeV is shown [134] and are compared with the results of the PHENIX in Au-Au collisions at $\sqrt{s_{NN}} = 200$ GeV in two different rapidity interval. It is readily evident from the figure that the R_{AA} values are less than one providing clear hints of suppression in Pb-Pb collisions. As mentioned in the earlier paragraph, the R_{AA} values at the LHC is observed to be higher than that of the value measured by the PHENIX, suggesting less suppression of J/ψ particle at the LHC energy. In Fig. 1.24(b), the p_{T}-differential R_{AA} of J/ψ measured by ALICE in the central Pb-Pb collisions and PHENIX in Au-Au collisions at $\sqrt{s_{NN}} = 200$ GeV are shown. It could be observed from the figure that at higher centre-of-mass energy, the J/ψ are less suppressed in the low and intermediate p_{T}, whereas, the suppression increases with the increase of the p_{T} region.

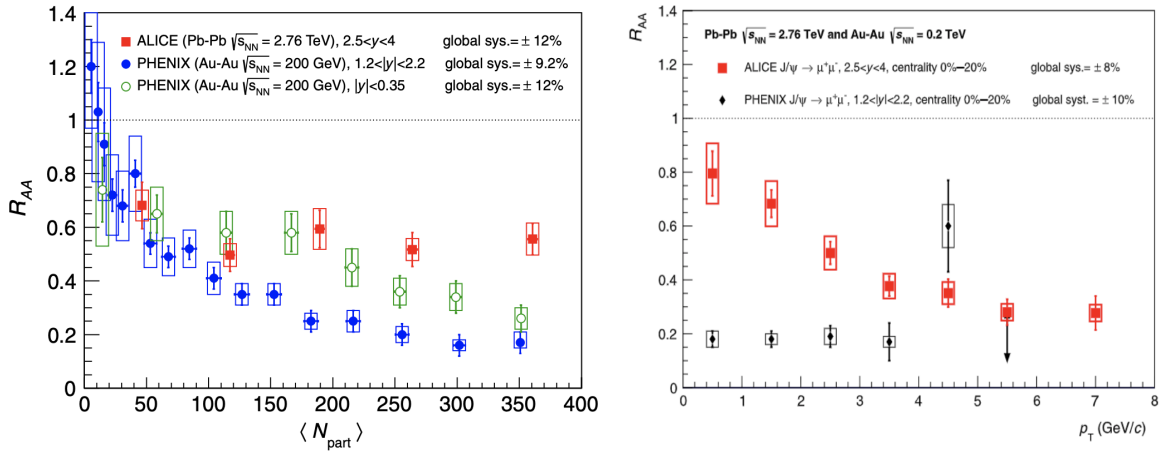

(a) (b)

Fig. 1.24 (a) Centrality dependent R_{AA} of J/ψ measured by the ALICE in Pb-Pb Collisions at $\sqrt{s_{NN}} = 2.76$ TeV are compared with the results of the PHENIX in Au-Au collisions at $\sqrt{s_{NN}} = 200$ GeV in two different rapidity interval. (b) The p_{T}-differential J/ψ R_{AA} measured by ALICE in 0-20% central Pb-Pb Collisions at $\sqrt{s_{NN}} = 2.76$ TeV are compared with the results of the PHENIX in 0-20% central Au-Au collisions at $\sqrt{s_{NN}} = 200$ GeV [134, 137].

The jet quenching and the J/ψ suppression observables are known as the hard probes of nuclear collisions as they provide information about the early hard scattering between the partons and medium modification in the QGP medium.

1.6.8 Direct photons

The photons produced during the collisions do not participate in the strong interaction with the quarks and gluons, as they interact only via electromagnetically [138, 139]. Therefore, they remain un-scattered and provide undistorted information about that particular stage of the collisions at which they were produced. The hard photons are believed to produce during the hard partonic scattering, and therefore, momentum distribution of these photons are expected to provide insight about the partonic momentum distribution.

Photons can be produced in every stage of the nucleus-nucleus collisions [140, 57]. According to their production scenario, they are mainly categorised into two group:- one is

prompt photons, and another is thermal photons. The prompt photons are produced due to the initial hard scattering between the partons, whereas, the thermal photons are produced in the pre-equilibrium stage or in the QGP medium or in the hadronic phase. Both prompt and thermal photons are known as direct photons. On the other hand, some photons may be produced in the hadronic decay after kinetic freeze-out. These are known as decay photons.

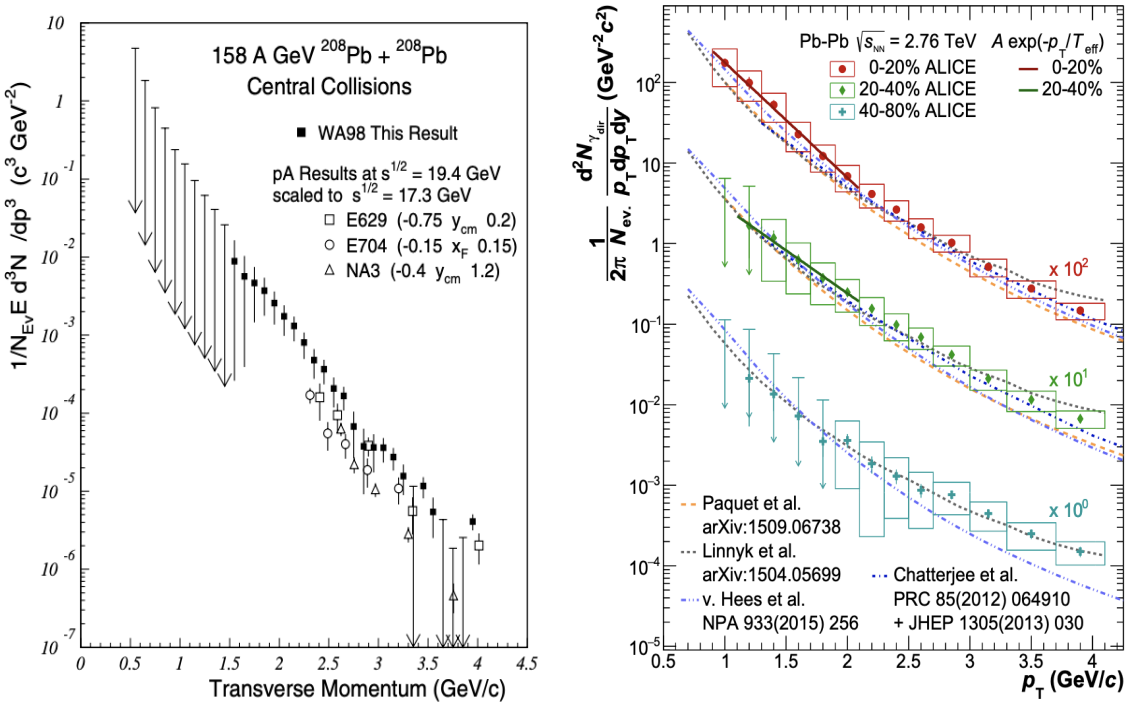

(a) (b)

Fig. 1.25 (a) Invariant direct photons multiplicity in central Pb-Pb collisions at 158A GeV compared with various direct photon measurement from proton-induced reactions. The proton-induced reactions are scaled to central Pb-Pb collisions for comparison. Data points with downwards arrows indicate unbounded 90% C.L. upper limits [141]. (b) Direct photons spectra measured by ALICE in Pb-Pb collisions at $\sqrt{s_{NN}} = 2.76$ TeV in different centrality classes are compared with various models with the assumption of formation of QGP. The fit with an exponential function is also shown [142].

Measurement of direct photons has been performed by the WA98 collaboration in Pb-Pb collisions at 158 A GeV [141]. In Fig. 1.25(a), the invariant direct photon multiplicity for central Pb-Pb collisions at 158 A GeV is shown and are compared with the proton-induced results on fixed targets at 200 GeV. The proton-induced results have been divided by the total

pp inelastic cross-section ($\sigma_{int} = 30$ mb) and by the mass number of the target to obtain the invariant direct photon yield per nucleon-nucleon collisions. They have been again multiplied by the calculated average number of nucleon-nucleon collisions (660) for the central Pb-Pb event selection for comparison with that of Pb-Pb collisions results. These results suggests an excess production of the direct photon in central Pb-Pb collisions beyond that expected from proton-induced reactions. These results suggest a modification of the prompt photon production in nucleus-nucleus collisions or an additional contribution from thermal photons.

In a recent measurement by ALICE, in the low p_{T} (<2 GeV/c) region, an excess above the prompt photon contribution has been observed in Pb-Pb collisions at $\sqrt{s_{NN}} = 2.76$ TeV [142]. In Fig. 1.25(b), the measurement of direct photons in Pb-Pb collisions at $\sqrt{s_{NN}} = 2.76$ TeV is shown along with various theoretical prediction [142]. From an exponential function fit for the most central collisions of direct photon spectra, a temperature of $\mathrm{T}_{eff} = 297 \pm 12^{stat} \pm 24^{syst}$ MeV could be obtained, after the subtraction of pQCD contribution. Those models which considered the formation of a QGP medium found to agree with the measurement within uncertainties.

1.6.9 Dilepton

Lepton pairs are produced in all stages of collisions and do not interact with quarks and gluons via the strong interaction, similar to the photon. Therefore, the measurement of leptons can provide valuable information about the stages of the collisions at which they are produced. In general, dileptons can be produced via the hard parton-parton scattering, in the QGP medium, hadronic phase, and the heavy-flavour meson's decay product. The invariant mass distribution analysis provide the opportunity to study the properties of the lepton pairs, from which they are produced. In the low-mass region ($\mathrm{m}_{inv} < 1$ GeV), thermal radiation is governed by the light vector mesons decay. At much higher mass region ($\mathrm{m}_{inv} > 3$ GeV), primordial processes such as Drell-Yen or charm decay are expected to dominate the spectra.

However, in the intermediate-mass region (IMR), extending to ϕ, the emission of the lepton pair is continuum-like with a magnitude approximately given by $q\bar{q}$ annihilation. Therefore, an increased dilepton yield in the IMR is considered among the earliest QGP formation signal [143].

Direct photon and dilepton observables are also known as the initial state observables as well as the electromagnetic (EM) probe. They both provide the information about the properties of the early state matter formed during the collisions.

1.7 Experimental facilities of high-energy nuclear collisions

The Lawrence Berkeley National Laboratory (LBNL) in Bevalac was the first facility to perform the first heavy-ion experiment in the early 1970s. In this facility, various types of nuclei were used for collisions up to the centre-of-mass energy of $\sqrt{s_{NN}} = 2.32$ GeV. It was designed with the primary purpose of dedicated studies on the equation of state (EoS) of the nuclear matter formed at a density higher than the normal state. Further, the discovery of the asymptotic freedom property of QCD has provided the opportunity to study the high-temperature phase of matter with de-confined quarks and gluons. Several experimental facilities have been built at higher centre-of-mass energy to realise and characterise such a phase of matter in the laboratory. Among them, the Alternating Gradient Synchrotron (AGS) at the Brookhaven National Laboratory (BNL) and the Super Proton Synchrotron (SPS) at the European Organisation for Nuclear Research (CERN) are such facilities, which have collided heavy-ion in fixed target mode at the centre-of-mass energy $\sqrt{s_{NN}} = 4.86$ GeV and 17.3 GeV, respectively. At the SPS, several experiments such as NA44, NA45, NA49, NA50, NA52, NA60, WA97, WA98 etc., were built to investigate different properties of the matter formed in extreme temperature and energy density. In the later year, the Relativistic Heavy-Ion Collider (RHIC) at the BNL was designed. It was the very first machine to collide two opposite beams of heavy-ions, i.e. in collider mode. Here, the Au-Au and Cu-Cu beams have been used at

$\sqrt{s_{NN}}$ = 22.4, 62.4 and 200 GeV. At the RHIC, there are four main experiments, namely STAR, BRAHMS, PHENIX and PHOBOS, mainly dedicated to realise and characterise the QGP matter. In the last decade, the Large Hadron Collider (LHC) at the CERN has been designed to collide lead (Pb) ion as the incoming beam at the centre-of-mass energies of 2.76 and 5.02 TeV. Also, at the LHC, proton beams have used to provide reference measurements of heavy-ion and their own significance at different centre-of-mass energies, i.e. $\sqrt{s} = 0.9$, 2,76, 5.02, 7 and 13 TeV. Asymmetric collisions of protons and Pb has also been performed at the LHC. There are four major experiments at the LHC: ALICE, CMS, ATLAS and LHCb, dedicated to investigate various properties of the matter formed as well as for measurements of different abundant particles produced in the collisions & study their properties.

Moreover, two new accelerator facilities are being constructed to study the properties of the QGP matter at the high chemical potential region of the phase diagram. The Facility for Anti-Proton and Ion Research (FAIR) at the GSI, Germany, will be a fixed target experiment having beam energies up to 20 GeV per nucleon. On the other hand, the Nuclotron Based Ion Collider fAcility (NICA) at the Dubna, Russia, will be a collider experiment operating at the centre of mass energy $\sqrt{s_{NN}} = 4$ GeV. Both of these experiments will use Au ion as the target and projectile.

1.8 Motivation of the thesis

Usually, the collisions between two beams of protons and collisions of a proton beam with a heavy-ion beam are known as the small colliding systems at the LHC. One of the primary motivations of studying pp collisions is that they provide the reference measurement for the heavy-ion collisions. In heavy-ion collisions, a dense and large space-time volume is expected to form. The partons produced in the collisions interact, and their properties are modified in the dense medium created in such collisions. On the contrary, in pp collisions, due to a minimal space-time volume, the produced partons do not interact much until hadronisation

occurs. And therefore, a direct comparison of heavy-ion results with pp collisions are indicative of the formation of an extreme nuclear matter, where quarks and gluons behave like free particles. Apart from reference measurement, pp collisions results are also used for providing input to constrain the fragmentation function in perturbative QCD (pQCD) calculation based on the factorisation theorem, arising out of hard scattering between partons [15]. The parton distribution functions of the proton can also be tuned by comparing results of particle production in pp collisions. Further, pp collisions results provide the input to constrain the soft interaction region in various Monte Carlo models.

However, at the LHC energies, the simple picture of particle production in small colliding systems has recently faced tremendous challenges. Due to the increase in the available centre-of-mass energy, the numbers of particles produced are expected to be large in pp and p-Pb collisions. In such high-multiplicity p-Pb collisions, the ALICE and CMS collaborations have already reported ridge-like correlations [16, 144], similar to that observed in the heavy-ion collisions at the RHIC [145–147] and LHC [148] energies. Further, the mass-dependent hardening of the p_{T} spectra, enhanced baryon to meson production at the intermediate p_{T} [17], and the enhanced production of (multi-)strange hadrons [18] have also observed in the high-multiplicity p-Pb collisions. In heavy-ion collisions, these behaviours can be interpreted as the formation of a medium that expands hydrodynamically or a de-confined medium of quarks and gluons [11, 111]. Therefore, similar studies can be extended to even a more small system like pp collisions for a better understanding of the particle productions mechanism and collisions dynamics in these systems.

The excellent particle identification capabilities of the TOF detector of ALICE provide scope to identify various primary particles, namely, pions, kaons and protons at the intermediate transverse momentum region. Further, the statistical unfolding method can be used to identify particles up to higher p_{T} regions than the usual $n\sigma$ technique of particle identification. Another important advantage of this PID method is that it is independent of any Monte Carlo

information and simulation for what concerns the PID efficiency and contamination from different particles. Therefore, identification and investigation of these particles spectra with the TOF detector are of immense significance.

Recent measurements from the lower-energy high-multiplicity pp collisions have provided significant indications of the collective behaviour similar to that observed in heavy-ion collisions [19, 20]. The p_{T} spectra of various identified particles are observed to becomes harder with increasing multiplicity, and the effect is more pronounced for particles having higher mass. Also, the average p_{T} of particles has shown mass and multiplicity dependent hardening, similar to that observed for the p_{T} spectra. Moreover, for the high-multiplicity pp events, significant enhancement in the p/π ratio at the intermediate p_{T} could be observed. All these behaviour are reminiscent of those observed for the heavy-ion collisions, where the medium is found to evolve hydrodynamically [11]. However, for pp collisions, the origin of the underlying physical process responsible for modification of particles p_{T} spectra has not been confirmed yet. As the number of particles produced in the highest energy high-multiplicity pp collisions is comparable to p-Pb and peripheral Pb-Pb collisions, measurement of these observables as a function of multiplicity in pp collisions $\sqrt{s} = 13$ TeV has become significantly important. These results are expected to provide significant information on the dynamics of the system formed.

Further, the p_{T}-integrated yields and yields ratios of different particles to pions also provide important information about collisions dynamics and particle production mechanism. Results of lower energy pp collisions have shown that yields of strange and multi-strange particles, relative to pions, increase with increasing multiplicity. In high-multiplicity pp collisions, strangeness production reach values similar to heavy-ion collisions, where a QGP medium is formed. Further, K/π, p/π and other (multi-)strange to pions yields ratios follow a common trend from low multiplicity pp to central Pb-Pb collisions, suggesting hadrochemistry of particles production is independent of colliding systems at the LHC

[19, 20]. Thus, similar studies for the highest energy pp collisions will provide scope to disentangle the effect of collisions energy from the multiplicity dependence of particle production in pp collisions, if any.

Apart from studying the properties of the matter formed, measurements on various observables of nuclear collisions are also performed to have a better insight into the particle production mechanism. Intermittency in the charged particle emission spectra has been observed on several small systems like e^+e^-, $p\bar{p}$ collisions data at lower centre-of-mass energy [21]. These types of intermittent emission of particles are found to be a general feature of the experimental data. Several causes might give rise to intermittent emission of particles. The cascading mechanism of particle production [23, 31, 25] or a phase transition that occurred during the evolution of the system [32–34] is considered the primary cause of such intermittent type of emission. Previous measurements of intermittency have been carried out at relatively lower centre-of-mass energies for both small and heavy-ion system. However, no study has been performed on intermittent emission of charged particle for small systems like pp collisions at the LHC energies. Since the numbers of particles produced during the collisions are significantly abundant in high-multiplicity pp event than that of minimum bias pp collisions at the LHC energy, these rare events provide an excellent opportunity for the systematic study of the intermittency in general and probe the particle production mechanism in particular.

The PYTHIA Monte Carlo (MC) model is a general-purpose event generator that successfully describes pp collisions data at the LHC energies [149]. Further, PYTHIA has the advantage that it can introduce and vary the effect of colour reconnection mechansim between the partons through a parameter called reconnection range (RR). The colour reconnection mechanism in PYTHIA seems to describe several collective behaviours in the high-multiplicity pp collisions [150]. Colour reconnection results in a correlated emission among the produced particle, and such emission may also give rise to intermittency in the

charged particle emission spectra. Therefore, in this thesis, studies on dynamical fluctuation in the high-multiplicity pp collisions using the PYTHIA generated data have been performed to provide better insight into the cause of such behaviour in these collisions at the LHC energies. Further, studies are also carried out by varying the strength of the colour reconnection parameter in PYTHIA to determine the dependence of intermittency and its related observables on that parameter.

1.9 Organisations of the thesis

This thesis is organised as described below: after the brief introduction about the theoretical background, available experimental results and motivation of the thesis in Chapter 1, Chapter 2 focuses on the experimental facility. Here, a detailed description of the ALICE at the LHC, its different detectors and analysis tools that are being used are discussed. In Chapter 3, the complete analysis procedure to identify pions, kaons and protons as a function of p_{T} for different charged-particle multiplicity classes using the Time of Flight (TOF) detector of ALICE are presented. Here, the estimation of different correction factors and the method of estimation of systematic uncertainties are discussed. Chapter 4 contains the analysis results obtained from Chapter 3 and the discussion on various measurement thus estimated. In Chapter 5, the studies on the dynamical fluctuation have been carried out with the Scaled Factorial Moment (SFM) technique in the high-multiplicity pp collisions data, generated with the Monte Carlo event generator PYTHIA Monash.

2

A Large Ion Collider Experiment at the LHC

A Large Ion Collider Experiment (ALICE) [151, 152] is one of the major experiments of the Large Hadron Collider (LHC) at the European Organisation for Nuclear Research (CERN). It is primarily designed to investigate the properties of the strongly interacting matter in extreme conditions of temperature and energy density, in which quarks and gluons are no longer bound inside the hadrons. The state of matter thus formed is known as the Quark-Gluon Plasma (QGP). Such a state of matter is expected to form in the nucleus-nucleus (Pb-Pb)

collisions, in the unprecedented energy regime of the Large Hadron Collider (LHC). The ALICE experiment provides an excellent opportunity for the comprehensive study of the hadrons, electrons, muons and photons produced in the collisions. It is optimised to cope with the highest multiplicity particles environment of the Pb-Pb collisions, where charged-particle multiplicity density ($\mathrm{d}N_{\mathrm{ch}}/\mathrm{d}y$) is expected to reach $\sim$ 8000 per unit of rapidity [152]. For the studies of soft observables in these environments, the ALICE detector system is designed with the lowest material budget in the mid-rapidity region. Apart from the heavy-ion system, it also studies the proton-nucleus (pA) and proton-proton (pp) collisions. The pp system provides the reference measurement for the heavy-ion collisions as well as it focuses on several physics aspects in the small system. However, both in pp and Pb-Pb collisions, the initial state gluon interaction inside the nuclei in the early stage of the collisions might survive the system evolution and affect the final state observables. For this reason, p-Pb collisions are performed to identify and characterise these so-called Cold Nuclear Matter (CNM) effects.

In the first phase of the LHC operations, i.e. from November 2009 to February 2013, ALICE has collected data at the centre-of-mass energy ($\sqrt{s_{NN}}$) of 0.9, 2.76, 7 and 8 TeV for pp collisions, 2.76 TeV for Pb-Pb collisions and 5.02 TeV for p-Pb collisions. From February 2013 to February 2015, the technical shut-down period has taken place, where different sub-detectors of the ALICE have been upgraded to collect data in a new energy regime achieved by the LHC machine. After the end of the shut-down, ALICE has collected data for pp collisions at $\sqrt{s}$ = 5.02 and 13 TeV, $\sqrt{s_{NN}}$ = 5.02 TeV for Pb-Pb collisions and $\sqrt{s_{NN}}$ = 8.16 TeV for p-Pb collisions up to December 2018. Also, ALICE has collected very limited data for the Xe-Xe collisions at $\sqrt{s_{NN}}$ = 5.44 TeV in this run.

2.1 The Large Hadron Collider

The Large Hadron Collider (LHC) is the largest and the most powerful particle accelerator in the world till date. It consists of two superconducting accelerator rings that are used to accelerate the particles. It has a circumference of approximately 27 km, situated underground at the depth ranging from 50-175 m passing through Geneva, Switzerland and Jura mountains, France. It was installed in the already existing Large Electron-Positron (LEP) collider tunnel and completes the CERN accelerator complex along with the PS and SPS, as shown in Fig. 2.1. The particles are initially accelerated up to achievable energy, and once the energy of the beams become stable, they collide at the different interaction points known as IP1, IP2, IP3 and IP4. At the LHC, four major experiments, namely, ATLAS, ALICE, CMS, and LHCb, have been set up at the four interaction points along its circumference. The ATLAS and CMS are the largest experiments having multipurpose detector system to detect the Higgs-Boson and for the study of new physics beyond the Standard Model. The ALICE is dedicated to the studies of physical properties of the Quark-Gluon Plasma (QGP) via measurement of different observables of the relativistic nucleus-nucleus collisions. Further research on proton-proton and proton-nucleus collisions are also being carried out for reference measurement of the heavy-ion collisions as well as for their own significance. The LHCb experiment, on the contrary, is dedicated to study the physics of the flavour, CP-violation using B-meson decay channels etc. The physics that the ATLAS, CMS and LHCb experiments are aiming to study, have very much low cross-sections ($\sim$ 100 pb or less) and thus, a large number of collisions are required in the LHC to full-fill the requirement for pp system. The LHC was initially built to provide collisions energy of $\sqrt{s}$ = 14 TeV for pp collisions and $\sqrt{s_{NN}}$ = 5.5 TeV for Pb-Pb collisions. However, due to the quenching of a magnet in 2008 [153], the LHC need to run at half of the designed energy, thus providing collisions energy of $\sqrt{s}$ = 7 TeV for pp collisions and $\sqrt{s_{NN}}$ = 2.76 TeV for Pb-Pb collisions.

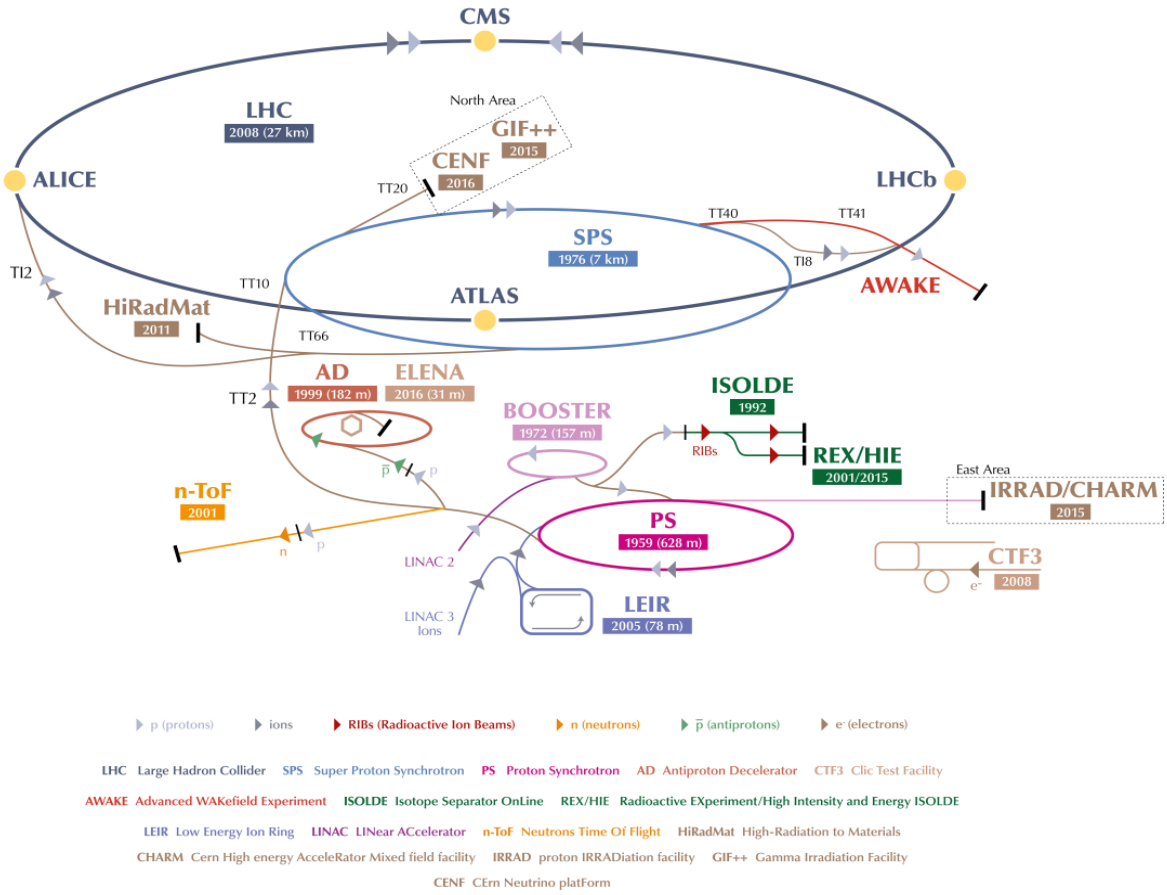

Fig. 2.1 The accelerator complex of the LHC is shown with the various accelerator such as LIER, PS, SPS etc. [154].

The particles that need to be accelerated in LHC have to go through several pre-accelerations stages before entering the LHC machine. For the pp system, at first, the electrons are stripped off from the hydrogen atoms to make it an isolated proton. Then, they are injected to the Linear Accelerator 2 (LINAC 2), which accelerate the proton beams up to 50 MeV. These injected protons are now further accelerated up to 1.4 GeV in the Proton Synchrotron Booster (PSB) before injecting them to the Proton Synchrotron (PS), where they can achieve energy up to 25 GeV. From the PS, the protons beams are injected to Super Proton Synchrotron (SPS) to further accelerate the beams up to 450 GeV. These high energy beams of protons are now injected to the beam pipes of the LHC to reach the final stable energy. Various accelerators in the CERN complex are shown in Fig. 2.1 [154].

To accelerate the Pb beam, firstly a 3 cm Pb cylinder is heated up to 500° C to vaporise a small number of atoms, which are partially ionised by a strong electric field. Then, they are accelerated in a linear device to strip off all the remaining electrons. The fully ionised Pb ions are injected to the Low Energy Ion Ring (LIER) and later injected to the PS, from which the Pb beams will follow the same injection chain as that of the protons. The Pb ions can reach beam energy of 2.51 TeV/nucleon, yielding to $\sqrt{s_{NN}}$ = 5.02 TeV or total centre-of-mass energy of 1.05 PeV (1 PeV=10^{15} eV), with the nominal magnetic field of 8.33 T.

Even though, the energy region in which the particle accelerator works is primarily considered the most significant parameter, another important accelerator parameter is the instantaneous luminosity L, i.e. the "peak" value within a fill. Luminosity is proportional to the event rate R and the interaction cross-section of the process under study (σ_{int}):

$$R = L \times \sigma_{int} \tag{2.1}$$

Instantaneous luminosity depends on the colliding beam parameters at the interaction point (IP) and can be estimated by the following equation:

$$L = \frac{N_b^2 n_b f \gamma}{4\pi\varepsilon_n \beta^*} F \tag{2.2}$$

Where,

N_b = Number of particles per bunch,

n_b = Number of bunches per beam,

f = Revolution frequency,

γ = Relativistic gamma factor,

ε_n = Normalised transverse beam emittance,

β^* = The amplitude function at the IP,

F = The geometrical reduction factor that accounts for the crossing angle at the IP

Again, the transverse beam emittance and the amplitude function are related to the bunch cross-sectional size (σ_L) by the relation:

$$\sigma_L^2 = \frac{1}{\pi}\beta\varepsilon \tag{2.3}$$

where ε provide information about the process of successful "packing" of protons into bunches during the injection. A low ε particle beam means that the particles are confined in a minimal distance and have almost the same momentum. Low ε beam is notable for keeping the particles confined in orbit along the beam direction. The parameter β determines the strength of the focusing quadruple. If the value of β is small, this means that the beam is squeezed. The quantity β^* known as amplitude function at the interaction point is also significant. For achieving higher luminosity, the value of the emittance and β^* should be kept small, depending on the capacity of the beam focusing apparatus close to the interaction point. Furthermore, to have small β^*, the β value is needed to keep large in orbit. The emittance changes with the beam momentum during the acceleration and therefore, the normalised emittance $\varepsilon_n = \gamma\beta\varepsilon$ used in Eq. (2.2), which almost remains constant during the acceleration.

The number of bunches per beam needs to be varied according to the definition of different filling schemes during LHC operations and the beam parameters ε and β^* have been optimised as a requirement of the luminosity in the different interaction points. The maximum luminosity that can be achieved in ALICE for pp collisions is limited to the value L $\sim 10^{31}$ cm^{-2}s^{-1} to avoid pile-up in the primary tracking detector. On the other hand, the luminosity value is limited to 1.0 $\times 10^{27}$ cm^{-2}s^{-1} for the Pb-Pb collisions.

2.2 The ALICE detector

The main motivation of A Large Ion Collider Experiment (ALICE) [151, 152] at the LHC is to study of properties of the strongly interacting matter known as the Quark-Gluon Plasma

(QGP) formed during the collisions of heavy-ion. The ALICE detector is located at the interaction point 2 (IP2) in the LHC ring. It has been optimised to detect particles in a very high-density particles environment. It also provides excellent particle identification (PID) for the comprehensive study of hadrons, electrons and muons produced during the collisions from very low to high transverse momentum range. The ALICE detector is also able to detect and identify photons produced during the collisions.

The schematic view of the ALICE detector is shown in Fig. 2.2. It is mainly composed of two parts: one is the central barrel, and the other is forward muon spectrometer. The central barrel detectors are located inside an L3 solenoid magnet having a magnetic field strength of 0.5 T and cover the pseudo-rapidity region $|\eta| < 0.9$ over the full azimuthal angle. The most inner detector of ALICE is the silicon-based Inner Tracking System (ITS). It is used for tacking, vertex determination and PID via specific energy loss in the detector material in the low transverse momentum region. The Time Projection Chamber (TPC) is a gaseous detector, located outside the ITS and is responsible for global tracking and PID via specific energy loss in the gas medium in the low and very high p_{T} region. Outside the TPC detector, the Transition Radiation Detector (TRD) and the Time-Of-Flight (TOF) detectors are located for identification of electrons and charged hadrons via their own technique in the intermediate transverse momentum range. Further, the High Momentum Particle IDentification (HMPID), the ElectroMagnetic CALorimeter (EMCAL) and the PHOton Spectrometer (PHOS) detectors with limited acceptance are also located inside the L3 magnet outside the TOF detector. The HMPID detector consists of Ring Imaging Cherenkov (RICH) counter and is able to identify charged hadrons with transverse momentum higher than 1 GeV/c. The EMCAL detector is a large Pb scintillator calorimeter that is being used for investigation of the properties of the jets, photons and electrons. The PHOS detector is an electromagnetic spectrometer used for the identification of the low-p_{T} photons.

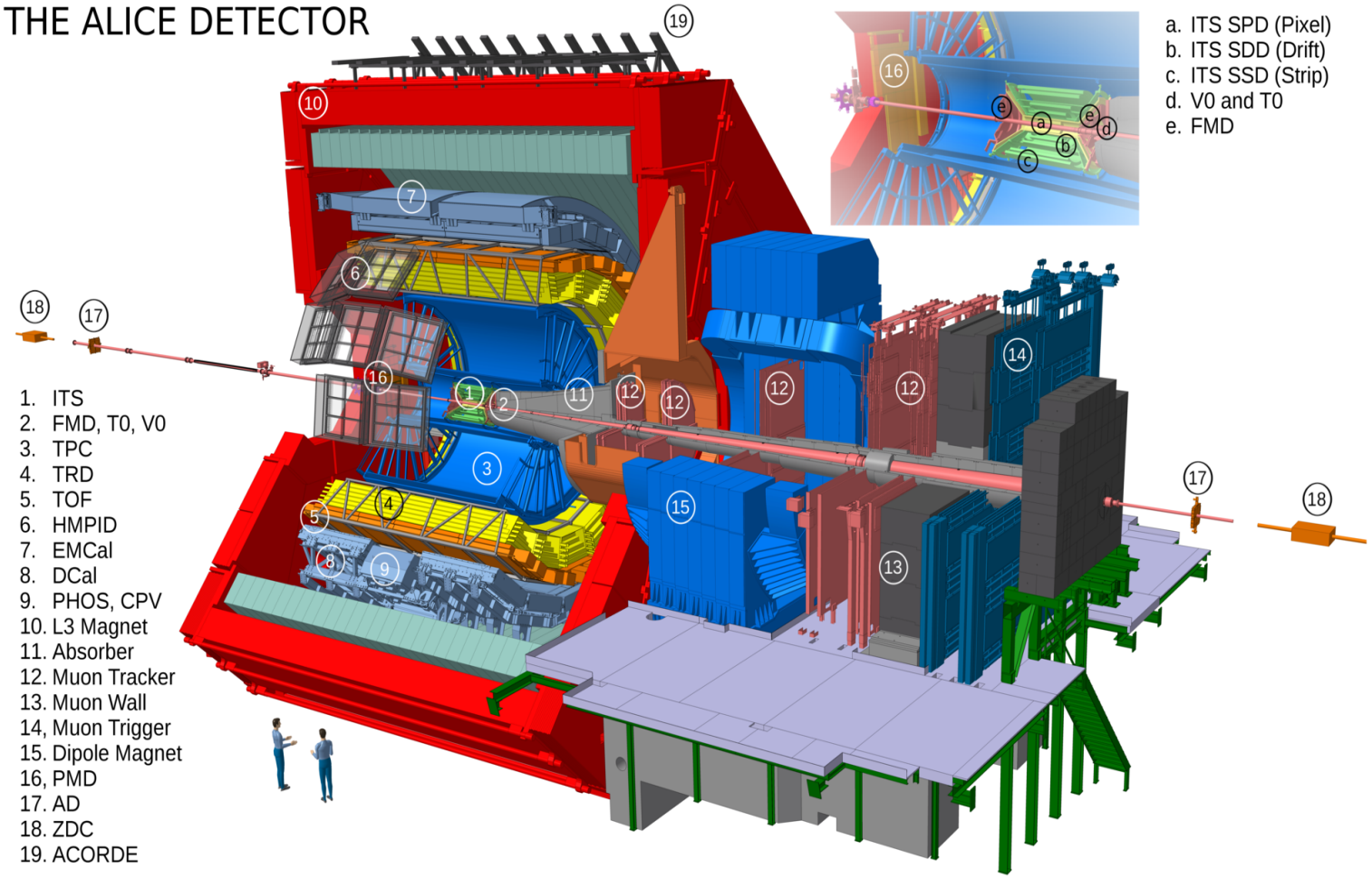

Fig. 2.2 The schematic view of the ALICE detector during the data taking period 2015 to 2018 is shown [155]. It is composed of a central barrel detector and forward muon spectrometer. The central barrel detectors are placed inside an L3 magnet.

The forward detectors consist of the single-arm muon spectrometer, the Photon Multiplicity Detector (PMD), the Forward Multiplicity Detector (FMD), T0, V0, Zero Degree Calorimeter (ZDC) detectors. The muon spectrometer covers the pseudo-rapidity range of $-4.0 < \eta < -2.5$ and is dedicated to the studies of quarkonia. The PMD is dedicated to studying the multiplicity and spatial distribution of photons in the pseudo-rapidity region $2.3 < \eta < 3.7$. The FMD detector covers the pseudo-rapidity region of $-3.4 < \eta < -1.7$ and $1.5 < \eta < 5.0$ and therefore, provides the opportunity to extend the pseudo-rapidity distribution of the charged hadrons. The T0 detector is being used for determination of the event collision time required for the time-of-flight PID, and the V0 detector is used to trigger an event, multiplicity or centrality determination as well as for background rejection. The ZDC detector is also used for estimation of the centrality of the collisions by detecting the spectator nucleon. The detail discussions on different sub-detectors of ALICE are given in the following subsections:

2.2.1 The Inner Tracking System (ITS)

The Inner Tracking System (ITS) [151, 156] detector is located near the beam pipe and covers the pseudo-rapidity range of $|\eta| < 0.9$ over the full azimuth. It is the closest tracking detector of ALICE near to the collisions point, responsible for precise measurement of primary vertex of the collisions and reconstruction of the secondary vertices from the decays of hyperons, D and B mesons. It consists of six concentric cylindrical layers having three different types of detectors, namely Silicon Pixel Detector (SPD), Silicon Drift Detector (SDD) and Silicon Strip Detector (SSD) as shown in Fig. 2.3.

As the name suggests, these detectors are based on the principle of silicon semiconductor detector. In general, semiconductor detector works as follows: a reversed bias voltage is applied to a negative-type semiconductor material. Charged particle traversing through the detector material transfer its energy to the valence electrons. The electrons are then able

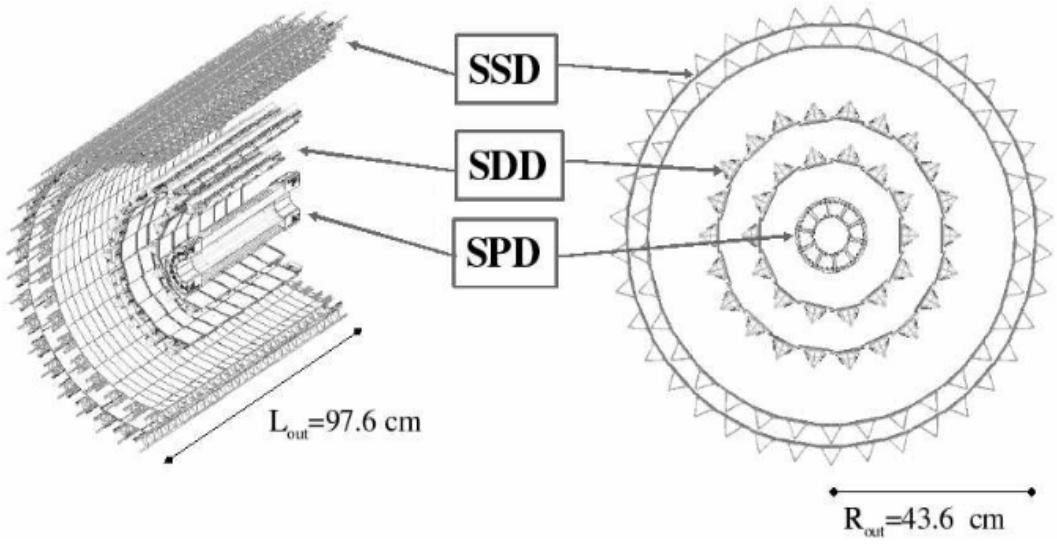

Fig. 2.3 Schematic view of the ALICE ITS detector, showing the different layers of SPD, SDD and SSD [151].

to cross the energy gap to reach the conduction band and thus, they behave like the free electrons. These free electrons are then collected at the anode, which provides a signal in the readout. Different designs of detectors were chosen depending on the particle density, which will be very large near to the interaction point and then decreases with the increase in the radius of the detector.

The layers of the SPD are located near to the beam pipe at the radial distance of 3.9 cm (first layer) and 7.6 cm (second layer). The first layer of SPD has the pseudorapidity coverage of $|\eta| < 1.98$ and therefore, it provides a continuous measurement of the charged-particle multiplicity density in combination with the FMD detector [151] in an extended pseudorapidity range. The readout of the SPD are binary, and hence, it can also be used to trigger decisions. The next intermediate two layers of the ITS are SDD and are placed at the radial distance of 15.0 and 23.9 cm. In the outermost region of SDD, SSD layers of ITS are located at a radius of 38.0 and 43.0 cm, respectively. The SDD and SSD have analogue readout and therefore, these two detectors are able to provide the magnitude of the charge

deposited. Hence, the last four layers of the ITS are used for particle identification via the measurement of the specific energy loss, i.e. dE/dx. The dynamic range of the analogue detectors are large enough to measure the dE/dx for low momentum, highly ionising particles and hence, the ITS can also be used for low p_{T} particle spectrometer, working in the non-relativistic region, where, dE/dx has the dependence of $1/\beta^2$. The energy loss in the ITS can be calculated by a hybrid parametrisation of the Bethe-Block function: a third-degree polynomial function at low p_{T} combined with the PHOBOS parametrisation for high p_{T}. The complete dependence of dE/dx is given by the equation below:

$$\frac{dE}{dX} = \begin{cases} E_0\beta^{-1}(b + 2ln\gamma - \beta^2), & (\beta\gamma > 0.7) \\ p_0 + p_1/\beta\gamma + p_2/(\beta\gamma)^2 + p_3/(\beta\gamma)^3, & (\beta\gamma \leq 0.7) \end{cases} \tag{2.4}$$

The free parameters of the Eq. (2.4), namely E_0, b, p_0, p_1, p_2, p_3 can be obtained from a fit to the mean value of the energy loss for π, K and p as a function of the p_{T}.

2.2.2 The Time Projection Chamber (TPC)

The Time Projection Chamber (TPC) [151, 157, 158] is the main detector of ALICE, whose primary purpose is to reconstruct charged particle tracks (tracking), identification of particles in the low & high p_{T} region and vertex determination with sufficient momentum resolution. The TPC is a cylindrical detector having an inner radius of 84 cm, outer radius of 247 cm and a total horizontal length of 500 cm along the beam axis. It has the pseudo-rapidity coverage of $|\eta| < 0.9$ over the full azimuthal angle. The schematic view of the ALICE TPC detector is shown in Fig. 2.4.

The active volume of the TPC is filled with 90 m^3 gas mixture of Ne:CO_2:N_2 or Ar:CO_2 in the proportion 85.7:9.5:4.8 or 88:12 at atmospheric pressure. Charged particle traversing through the active volume of the TPC ionises the gas-producing electrons and ions pairs along its path. A uniform electric field is maintained inside the TPC, which causes the electrons

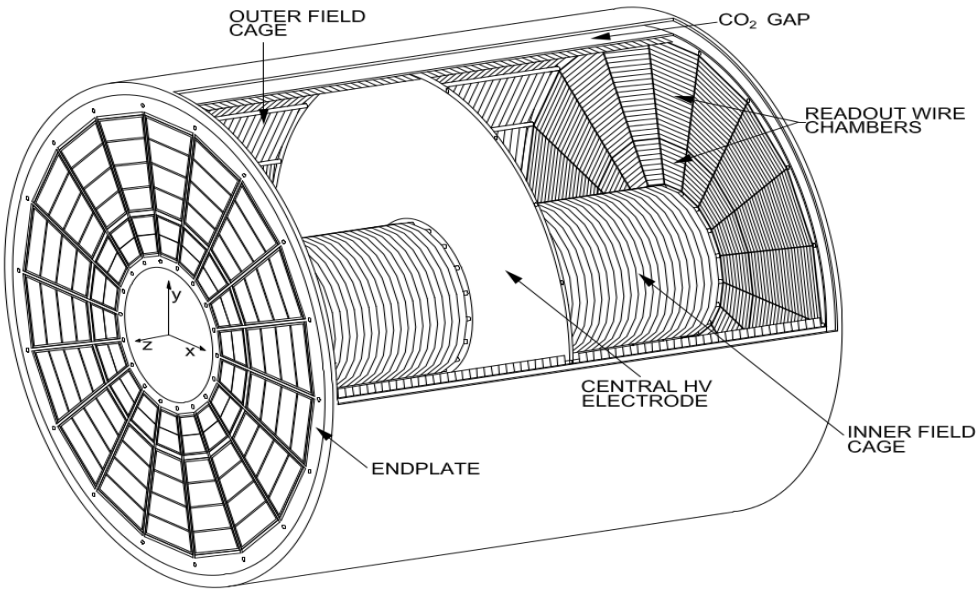

Fig. 2.4 A schematic view of the TPC detector showing the central HV electrode, end plates, readout wire chambers, inner and outer filed cage. The figure is taken from [158].

to drift towards the endplates of the TPC, where arrival point in the cylindrical plane is accurately measured. Along with the precise measurement of arrival time, the trajectory of the charged particle in space traversing through the TPC can also be determined.

In ALICE TPC, the electrode is maintained at the centre of the cylinder at a voltage of 100 kV proving an axial electric field of strength 400 V/cm. With this field, the electrons drift at a velocity of 2.65 cm/μs over 250 cm and take a maximum drift time of 94 μs.

The readout chambers of the TPC detector are Multi-Wire Proportional Chamber (MWPC) and consists of anode, cathode, and gating wire planes and a segmented cathode pad plane as shown in Fig. 2.5. In the grating wire, a negative and positive voltage can be put alternately. When a positive voltage is applied, the field lines end on the gating grid and thus drifted electrons are unable to reach the amplification region. On the contrary, when a negative voltage is applied, the electrons entered the readout chamber and drifted towards the anode wires. A positive high voltage of strength 1500 V is applied in the anode wires that lead to the amplification of the drifted electrons. In the presence of the anode wires, the electric field

evolves as 1/r and thus, the process of avalanche starts. As the TPC operates in proportional mode, the number of secondary electrons produced will be proportional to the number of primary electrons produced by the charged particle. Therefore, it will provide information about the energy loss by the incident charged particle per unit length (dE/dx). The radius of curvature in the constant magnetic field provides the measure of the momentum of the traversing particles. By measuring the dE/dx and momentum information, the particles can be identified.

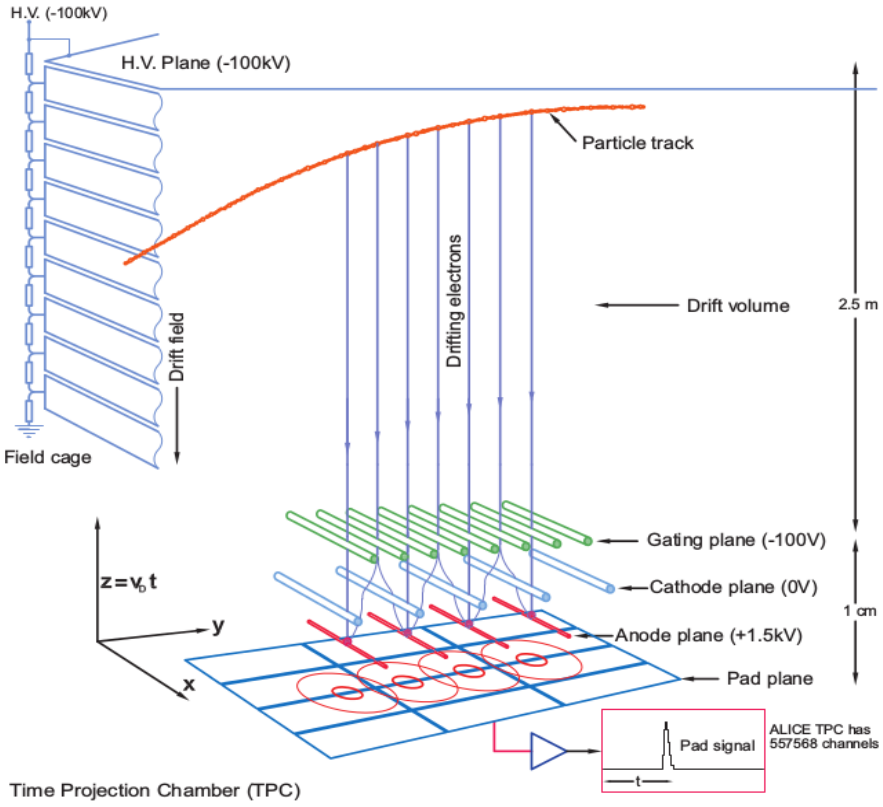

Fig. 2.5 Schematic description of the working principle of the TPC detector is shown [159].

Charged particles traversing through the gas medium of the TPC fiducial volume losses its energy in it. The mean energy loss is generally described by the Bethe-Bloch formula [158]:

$$\left\langle \frac{dE}{dx} \right\rangle = \frac{4\pi N e^4}{mc^2} \frac{Z^2}{\beta^2} \left(ln \frac{2mc^2\beta^2\gamma^2}{I} - \beta^2 - \frac{\delta(\beta)}{2} \right) \tag{2.5}$$

where N is the electrons number density in the medium, mc^2 is the rest mass energy of the electron, Z is the charge of the projectile, e is the elementary charge, β is the velocity of the particle, and I is the mean excitation energy of the atom. The $\delta(\beta)$ is the correction terms which accounts for density effect, first introduced by Fermi. The exact behaviour of $\delta(\beta)$ is material dependent.

For a given momentum, the mean energy loss of a particle depends on the charge and mass of the particle. As the $\beta\gamma$ increases, the mean energy loss decreases as $1/\beta^2$ and goes through a minimum value in dE/dx at $\beta\gamma \approx 3.6$. After that, energy loss increases with increasing $\beta\gamma$ due to the logarithmic term, which is known as the relativistic rise. The increased behaviour occurs due to two process: (i) the maximal transferable energy in each collision rises, and (ii) the cross-section for excitation and ionisation also rises due to the relativistic contraction of the electromagnetic field. A typical example of mean energy loss per unit area for positive muon in copper material is shown in Fig. 2.6.

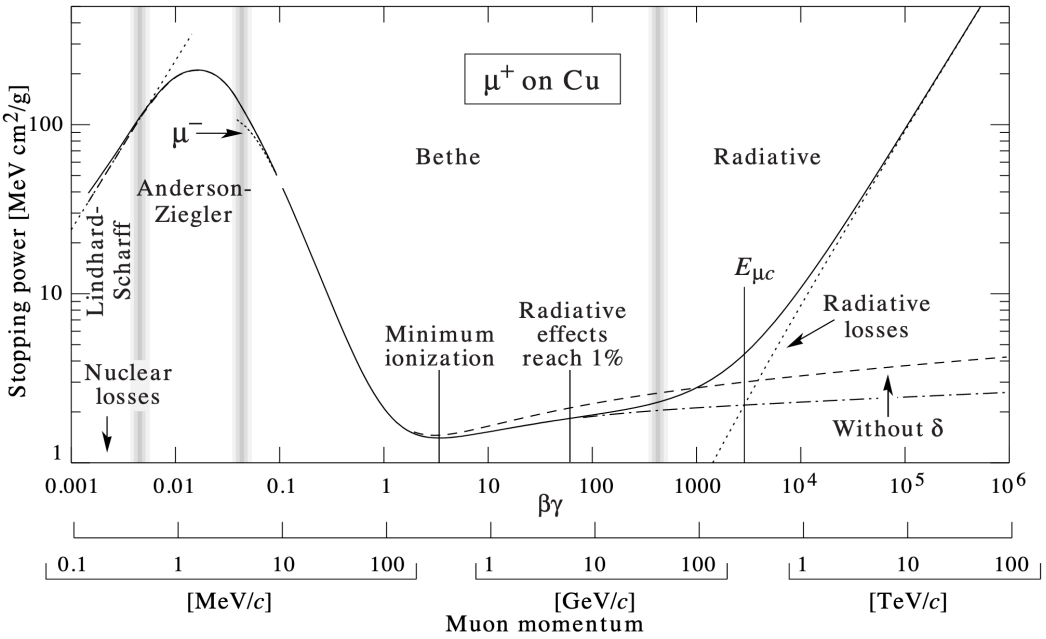

Fig. 2.6 Mean energy loss of positive muons on copper as a function of $\beta\gamma$. The figure is taken from [160].

2.2.3 The Transition Radiation Detector (TRD)

The main purpose of the Transition Radiation Detector (TRD) [151, 161] is to identify electron having $p_T > 1$ GeV/c. The low p_T electrons can be identified by the TPC detector via dE/dx measurement. The TRD is located at the radial distance of 2.90$< r <$3.68 m from the interaction point (IP). It covers the pseudo-rapidity region of $|\eta| < 0.84$ and full azimuthal angle. It is segmented along the azimuthal angle in 18 sectors, as shown in Fig 2.7. Each sector contains 30 modules arranged in five stacks along the z-axis and six layers in radius. The detector elements are made of a radiator of 4.8 cm thickness, drift section of 3 cm thickness and a multi-wire proportional chamber having gas medium Xe-CO_2. The readout of the TRD detector is consisting of pads.

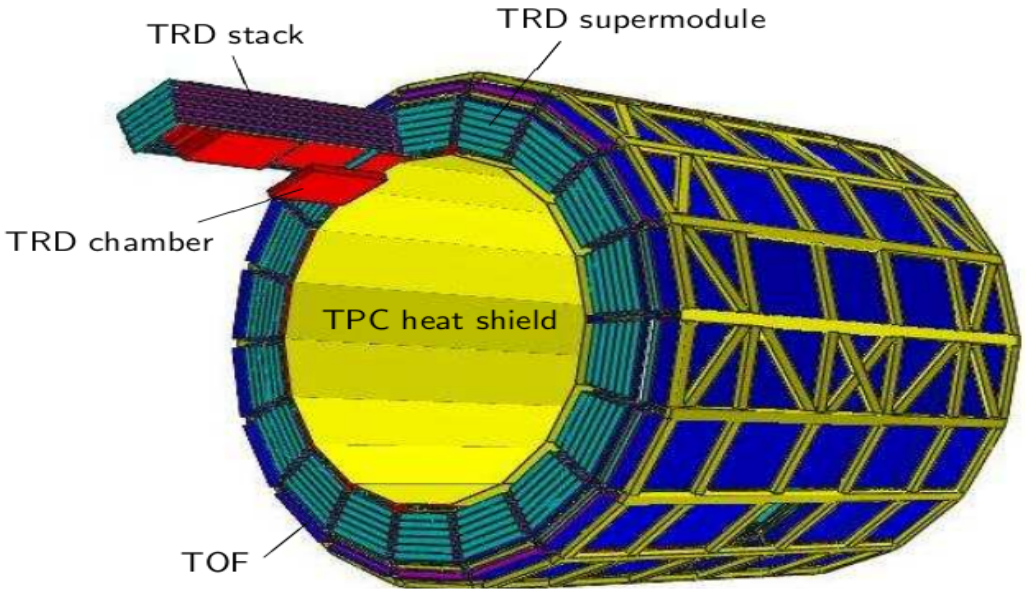

Fig. 2.7 Schematic of the TRD modules on the ALICE frame. Figure is taken from [151].

Relativistic charged particles, when traverse through the interface of two media of different dielectric constant, transition radiation is emitted with photons in the keV range. Electrons having momentum value above the threshold radiate differently than that of pions and therefore, the TRD is able to reject TPC pions up to very high momenta. The identification

of electrons is essential for the studies of electrons p_{T} spectra, for the measurement of light and heavy vector meson (J/ψ, Υ ... etc.) through their leptonic channel decay.

2.2.4 The Time of Flight (TOF)

The primary purpose of the Time Of Flight (TOF) detector [151, 162] of ALICE is to identify charged particles produced in the pseudo-rapidity range of $|\eta| < 0.9$. It identifies charged hadrons via the measurement of the particle time-of-flight from the collisions point to reach the TOF detector, combined with the momentum information provided by the TPC detector. The TOF was designed in such a way that it is able to identify charged hadrons in the intermediate transverse momentum ($0.5 < p_{\mathrm{T}} < 4$ GeV/c) range. Along with the ITS and TPC detector, the TOF can identify pions, kaons and protons by event-by-event basis.

To identify charged hadrons in the intermediate transverse momentum range, the time resolution of the TOF detector needs to be better than 100 ps, and thus, the TOF detector was built using the Multi-Gap Resistive Plate Chambers (MRPC). The intrinsic time resolution of the TOF detector is $\sim$ 50 ps, and have high detection efficiency (>99 %). The TOF detector inner layer and outer layer are located at 3.7, and 3.99 m radial distance, respectively from the interaction point and cover an area of $\sim$ 141 m^2 in the central barrel region. The TOF detector is segmented in 18 super-modules (SM) or 9.3 m long azimuthal sectors having five gas-tight modules placed along the beam axis as shown in Fig. 2.8. The two external and two intermediate modules contain 19 MRPC and the central modules contain only 15, for a total of 91 MRPC per SM. MRPCs are also called as "strips" due to their geometrical structure, and each of them composed of 96 readout pads. But, due to requirement of the PHOS [163] detector to have a lower material budget in the mid-rapidity region, the central modules of SM of 12, 13 and 14 are not installed, and this corresponds to the removal of $1440 \times 3 = 4320$ readout channel. The final TOF detector is consist of 1593 strips located in 87 gas-tight modules having a total of 152928 readout channels. The gas used in the

TOF detector is $C_2H_2F_4$ (tetrafluoroethene) and SF_6 (Sulfur hexafluoride) in the ratio of 93:7. More detailed description of the TOF detector and its particle identification technique is given in Chapter 3.

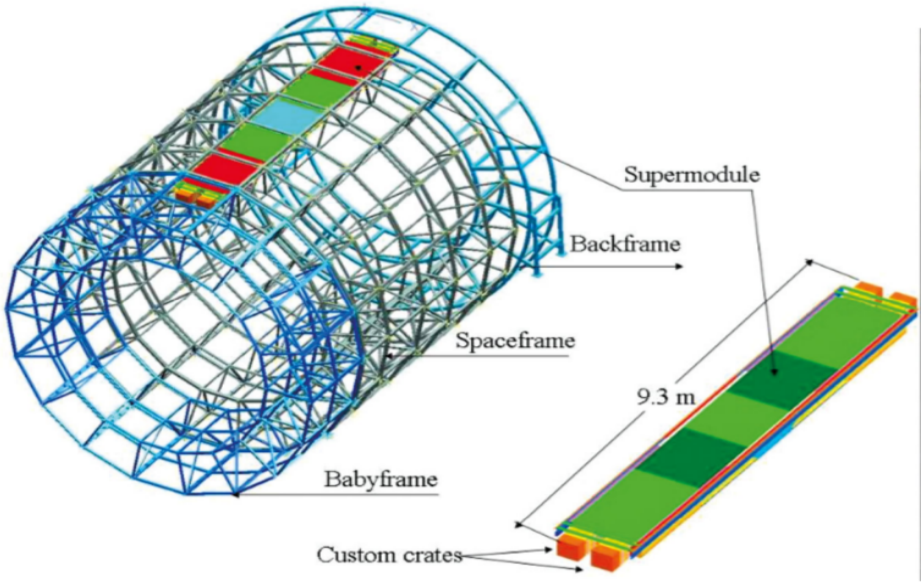

Fig. 2.8 A schematic layer of one of the 18 TOF SM inside the ALICE frame. Figure is taken from [151].

2.2.5 The High Momentum Particle IDentification (HMPID)

The High Momentum Particle IDentification (HMPID) [151, 164] detector is dedicated to the identification of the charged hadrons having transverse momentum higher than 1 GeV/c and thus provides particle identification at the intermediate p_T range. It is designed as a single-arm array having a geometrical acceptance of 5% of the central barrel. The pseudo-rapidity coverage of the HMPID detector is $|\eta| < 0.6$ and have the azimuthal coverage of $1.2^\circ < \phi < 58.8^\circ$. The HMPID detector is based on a proximity-focusing Ring Imaging Cherenkov (RICH) counters and is consists of seven modules, as shown in Fig. 2.9. The momentum range covers by the HMPID detector is determined by the radiator, which is a 15 mm thick layer of low chromaticity C_6F_{14} (perfluorohexane) liquid having a refractive

index of n = 1.2989 at wavelength = 175 nm. The Cherenkov photons produced by the fast charged particle travelling through the radiator are detected by a photon counter of Multi-wire Pad Counter (MWPC) having a thin layer of CsI in the pad cathode.

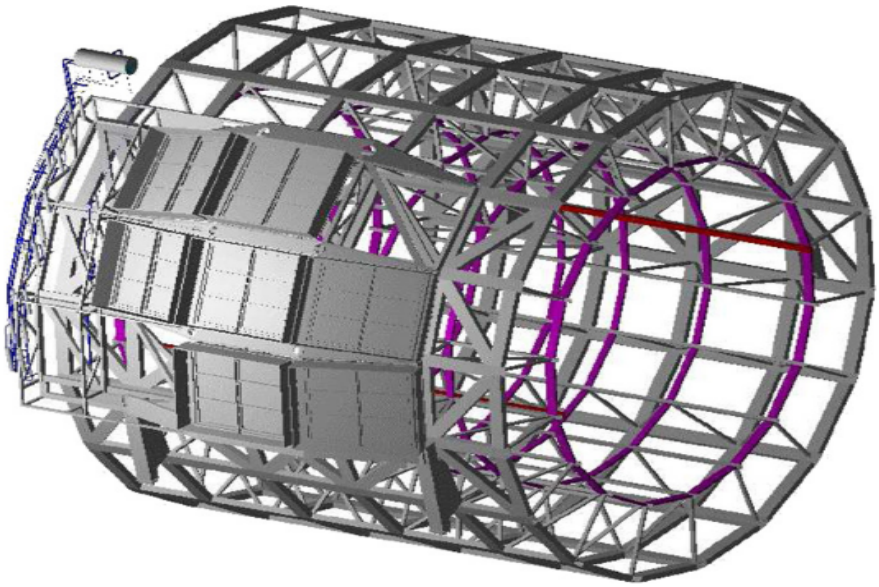

Fig. 2.9 The layout of the HMPID detector modules on the ALICE frame. Figure is taken from [165].

2.2.6 The ElectroMagnetic CALorimeter (EMCAL)

The ElectroMagnetic CALorimeter (EMCAL) [151, 166] detector is a large cylindrical scintillator sampling calorimeter made of Pb. It is located adjacent to the ALICE magnet coil at a radius of 4.5 m from the beam-line. The pseudo-rapidity coverage of the EMCAL detector is $|\eta| \leq 0.7$, with a polar angle coverage of $\Delta\phi = 107^{\circ}$, positioned approximately opposite to that of the PHOS detector in azimuth.

The electrons and photons passing through the EMCAL produce an electromagnetic shower and deposit their energy in the EMCAL towers. This deposited energy is now reconstructed by using a cluster finding algorithms. Moreover, the EMCAL detector is also used to study the properties of the jet.

2.2.7 The Photon Spectrometer (PHOS)

The PHOton Spectrometer (PHOS) [151, 163] detector is a high-resolution electromagnetic spectrometer that covers the pseudo-rapidity region of $|\eta| < 0.12$ and $\Delta\phi = 100^{\circ}$. It is dedicated to study thermal and dynamical properties of the initial phase of the collision, that can be extracted from the measurement of direct photon at low transverse momentum. Also, it is employed for the studies of the jet quenching effect, through the measurement of high p_{T} neutral π and γ-jet correlations. Direct photons can be separated from that of the decay one either through shower shape analysis at high p_{T} or through invariant mass analysis at low p_{T}.

The PHOS detector is constructed using a dense scintillator lead-tungsten ($PbWO_4$) crystal of radiation length of $20X_0$ with high photo-electron yield, which provides high energy resolution and granularity. It is composed of 5 independent modules, placed in the bottom of the ALICE setup at the radial distance of 4.6 m from the interaction point.

2.2.8 The Photon Multiplicity Detector (PMD)

The Photon Multiplicity Detector (PMD) [151, 167] is located in the forward region at a distance of 3.67 m from the IP and covers the pseudo-rapidity region of $2.3 < \eta < 3.9$ over the full azimuthal angle. It is dedicated to the measurement of the multiplicity and spatial distribution of photon in event-by-event basis. These measurements also provide an assessment of transverse electromagnetic energy and the reaction plane. The measurement of the multiplicity of photon gives important informations about limiting fragmentation, the order of the phase transition, the equation of state of matter and the formation of disoriented chiral condensates.

The PMD is a pre-shower detector, where lead (Pb) converter of the thickness of $3X_0$ (X_0=radiation length) is sandwiched between two planes of a proportional counter of high granularity. Each PMD plane consists of 24 modules, and each module contains 4608 honeycomb-shaped cells, having a total of 2,21,184 gas cells. The modules of the PMD are

of two different kinds: A-type and B-type, consisting of an array of 48 $\times$ 96 honeycomb cells configured in two different arrangements as shown in Fig 2.10. It is filled with the gas mixture of Ar and CO_2 in the ratio 70:30. Photons passing through the converter plate generates an electromagnetic shower in the pre-shower plane and produces a large-signal spread over many cells. On the contrary, the signal from charged particles is produced mostly in a single cell; thus, allows to reject such tracks from charged particles.

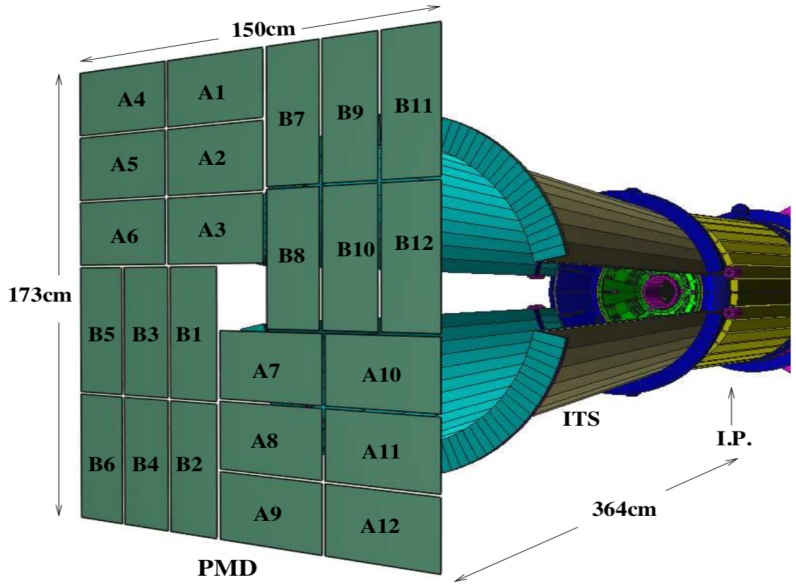

Fig. 2.10 The position of the PMD detector in ALICE is shown with respect to the ITS detector. Figure is taken from [151].

2.2.9 The Forward Multiplicity Detector (FMD)

The primary goal of the Forward Multiplicity Detector (FMD) [151, 168] is to measure the charged-particles multiplicity distribution in pseudo-rapidity region $-3.4 < \eta < -1.7$ and $1.7 < \eta < 5.0$. The combined information of the FMD and the ITS can provide a continuous measurement of the charged particles pseudo-rapidity distribution over a wide range of pseudo-rapidity. The FMD detector consists of three detector rings, namely FMD1, FMD2 and FMD3. The FMD2 & FMD3 detectors are placed on either side of the ITS detector

and are composed of both inner and outer ring made of silicon sensors. Both of the two rings have nearly the same acceptance. On the contrary, FMD1 is placed at a larger distance from IP, opposite to that of muon spectrometer to extend pseudo-rapidity coverage further. The upper limit on the η coverage is constrained due to the increased number of secondary particle contribution at the forward rapidity.

2.2.10 The Muon Spectrometer

The muon spectrometer [151, 169] detector is primarily designed for the identification of heavy flavour mesons (i.e. J/ψ, ψ', Υ, Υ' etc.) as well as ϕ meson at the forward rapidity by detecting the $\mu^+\mu^-$ leptonic pairs decayed from these particles. It is placed in the forward region covering the pseudo-rapidity range of $-4.0 < \eta < -2.5$ over the full azimuthal angle as shown in Fig. 2.11. A conic-shaped carbon absorber of length 3.5 m is placed in front of the spectrometer inside the L3 magnet. The primary function of this absorber is to absorb most of the primary and secondary particles, which are produced at the interaction point and travel towards the spectrometer. A high-granularity tracking system composed of five stations is also placed perpendicular to the beam axis. Each station is consists of two chambers plane. Two stations out of the five are placed between the L3 magnet and a large dipole, one inside the dipole and two after the dipole magnet, which has a magnetic field of 0.67 T. The muon trigger system (MTRG) consists of four planes of Resistive Plate Chamber (RPC) operating in steamer mode. An iron wall of 1.2 m thickness is also placed before the MTRG, which filter out the low p_{T} (< 4 GeV/c) muons and allow the high p_{T} muons to trigger the chamber. At last, an inner beam shield is placed to protect the spectrometer from primary and secondary particles produced at large rapidity.

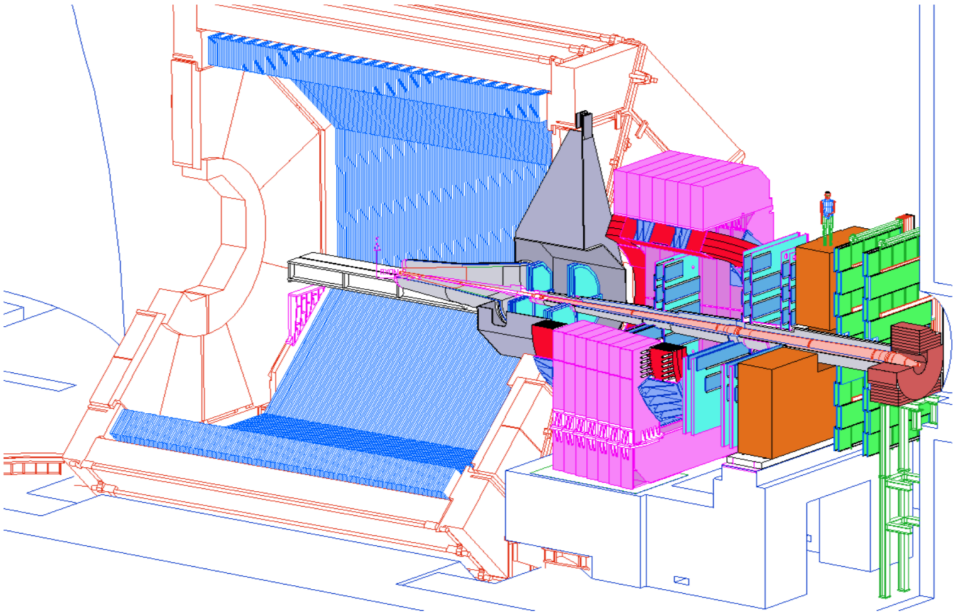

Fig. 2.11 A layout of the muon spectrometer detector is shown in the ALICE frame. Figure is taken from [151].

2.2.11 The V0 detector

The V0 [151, 168] detector is a small angle detector consisting of two arrays of scintillator counter, namely V0A & V0C and covers the pseudo-rapidity region of $2.8 < \eta < 5.1$ and $-3.7 < \eta < -1.7$ respectively. They are located on both sides of the ALICE detector in the longitudinal direction at the distance of 340 cm (V0A) and 90 cm (V0C), as shown in Fig. 2.12. Both of the arrays of the V0 detector consists of four rings in the radial direction segmented into 32 individual counters, each connected with 1 mm diameter Wave-Length Shifting (WLS) fibre, that guide the light to a photomultiplier tube. The two V0 detectors are not placed symmetrically around the IP due to the presence of the hadron absorber of the muon spectrometer.

The main objective of the V0 detector is to provide the minimum-bias trigger for the central barrel detectors along with the SPD. Also, it can be used to remove the events which are not originating from the beam-beam collisions, i.e. background events via the measurement of the V0 timing information. These events are generally occurred due to

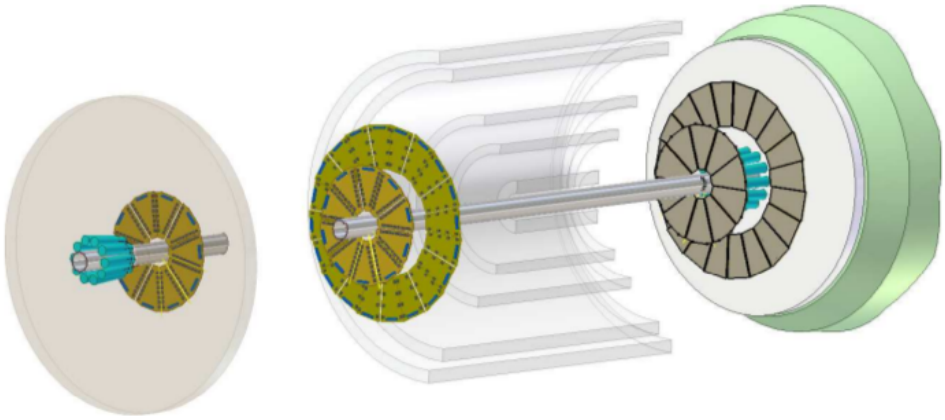

Fig. 2.12 A layout of the detectors placed at the forward-rapidity: the grey disks are the two arrays of the V0 detector. The two arrays of the T0 detector are shown in the blue cylinder around the beam pipe. The V0A (T0A) is located on the left side, and the V0C (T0C) is located at the right side of the figure. Figure is taken from [168].

the collisions of beam particles with the residual particle in the beam pipe, the so-called "beam-gas" interaction. During the second run of the LHC (Run 2), it is also used to provide the high-multiplicity trigger for pp collisions.

Charged particles traversing through the scintillator array of the V0 detector excites the material, which then emits photons during the de-excitation process. These photons are now transmitted to a photomultiplier tube (PMT) and are converted to an electrical signal. The response of the scintillator detector is fast enough to make them suitable as the trigger detectors.

The dependence between the number of impinging particles on the V0 arrays and the number of primary emitted particles is monotonic. Therefore, the V0 detector provides an estimate of the centrality of the collisions via the multiplicity recorded in the event.

2.2.12 The T0 detector

The T0 detector [151, 168] consists of two arrays of Cherenkov counters, namely, T0A and T0C located in the longitudinal direction on each side of the collisions points, as shown in

Fig. 2.13. The T0A detector is placed at a distance of 375 cm from the IP. While T0C located in front of the iron absorber of muon spectrometer at a distance of 72.7 cm from the IP. They covers the pseudo-rapidity range of $4.61 < \eta < 4.92$ and $-3.28 < \eta < -2.97$, respectively. Both T0 arrays are composed of 12 cylindrical counters, and each of them is based on a fine-mesh photomultiplier tube, optically coupled to quartz radiation with 20 mm diameter and 20 mm thickness.

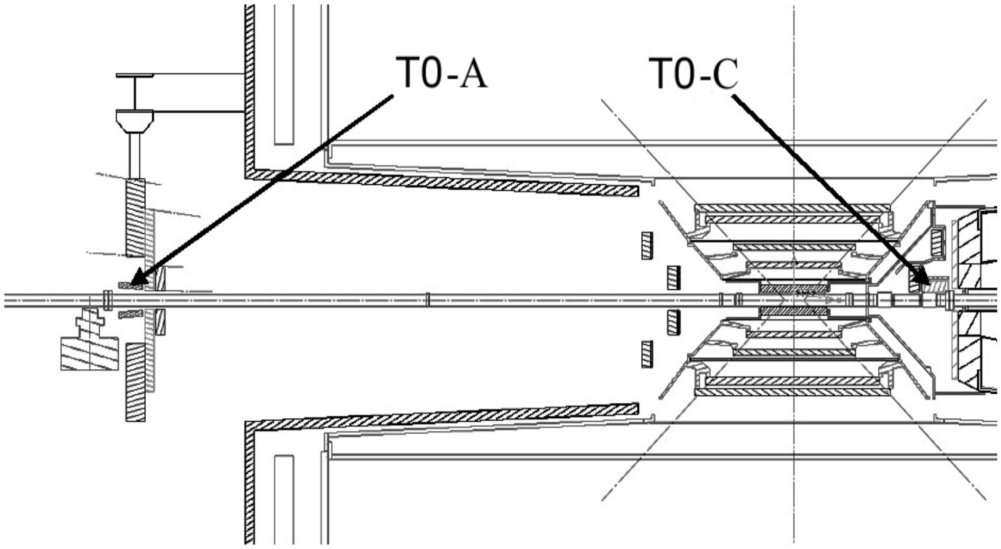

Fig. 2.13 The schematic of the two arrays of the T0 detector is shown. The figure is taken from [151].

The primary purpose of the T0 detector is to provide an accurate measurement of the event collisions time, which will serve as the start time for the time-of-flight measurement of the TOF detector. It also provides collisions trigger and monitors the luminosity providing fast feedback to the LHC accelerator team. The time resolution of the T0 detector is $\sim$ 50 ps for a single MIP event and reaches $\sim$ 25 ps for the high-multiplicity events.

2.2.13 The Zero Degree Calorimeter (ZDC)

The ZDC detector [151, 170] consists of two hadronic calorimeters placed on either side of the interaction point at a distance of 118 m. The ZDC detector is used for the estimation of collisions centrality via the measurement of the spectator nucleon that remains in the trajectory in the forward direction along the beam pipe. The ZDC is also able to estimate the reaction plane in nuclear collisions.

Due to the presence of the magnet at the LHC, the spectator protons partially separates from neutrons. And therefore, two different types of detectors, namely ZN and ZP are there to detect spectator neutrons and spectator protons, respectively in the ALICE setup. The ZN is placed between the beam pipes at zero degrees relative to the LHC axis, and the ZP is placed externally to that of the outgoing beam pipe on the side where positive particles are deflected. The ZDC is a quarts-fibre sampling calorimeter, with the passive absorber. Further, two small electromagnetic calorimeters (ZEM) are also placed at a distance of about 7 m from the IP, located at both sides of the LHC beam pipe. The ZEM detector is used primarily to distinguish between the central from peripheral and ultra-peripheral collisions [170].

2.2.14 The ALICE COsmic Ray DEtector (ACORDE)

The ALICE COsmic Ray DEtector (ACORDE) [151, 171] is a plastic scintillator detector located at the radial distance of 8.5 m at the top of the L3 magnet. There are a total of 60 arrays of such detectors and covers the pseudo-rapidity region of $|\eta| < 1.3$ over the azimuthal coverage of $-60^\circ < \phi < 60^\circ$. Each module of the ACORDE consists of two plastic scintillator paddles with an active area of 190×20 cm^2, placed on the top of each other and readout in coincidence. With this configuration, an efficiency of more than 90% over the entire length of the test module can be achieved. The ACORDE is used to provide a fast (Level-0) trigger signal, for the commissioning, calibration and alignment procedure of some of the ALICE tracking detector. It also detects single atmospheric muons and multi-muons

events in combination with the TPC, TRD and TOF detectors. It therefore provides the opportunity to study the high-energy cosmic rays in the region of the knee in the spectrum of the cosmic ray.

2.3 The ALICE Trigger System

The "trigger" system of ALICE provides the decision on whether to record the data collected by different sub-detectors. The ALICE detectors have two-level trigger systems, a low-level trigger and a high-level trigger. The low-level trigger is a hardware trigger and is known as the Central Trigger Processor (CTP). On the contrary, the high-Level Trigger (HLT) is a software trigger. The Central Trigger Processor combined inputs from different trigger detectors to optimise the event selections and readout of the detectors. The HLT allows the implementation of sophisticated logic for triggering and receives a copy of the readout from the sub-detector and then process it [172].

2.3.1 The Central Trigger Processor (CTP)

As mentioned above, it is a hardware trigger that combines the trigger signals from different sub-detectors to decide whether an event is required to accept to readout and written on the disk. In ALICE, the trigger decision is divided into three levels. The very first one is called L0 trigger and is delivered after 1.2 μs. The next trigger is known as the L1 and is delivered in 6.5 μs. The final trigger is called L2, which is delivered after 100 μs, i.e. after completion of the drift time of the TPC. The events that pass the L2 trigger are finally stored in the disk. Further, CTP is also used for producing a pre-trigger to start the TRD electronics, which is required within 900 ns after the interaction [172].

A past-future protection, which ensures that the pile-up events do not spoil the events selected for readout, is also needed to apply for different detector systems. As the readout

times of different detectors vary significantly, hence, the pile-up is recognised by considering the detectors that are part of that particular partitions as well as on the collisions system.

The rates of different trigger classes change with the type of triggers used during the data taking. The minimum-bias trigger has the highest rate. On the contrary, other triggers which look for a rare signal in an event have much lower rates, and hence, the size of the data needs to be reduced for the particular trigger classes individually. The total recording speed is limited by the maximum bandwidth of data that can be recorded to the disk and tape. The trigger classes are grouped into common triggers and rare triggers so that the precious events are not lost, and one can use proper utilisation of the disk space. If the temporary storage is above the threshold value, the rare trigger is accepted; otherwise, all triggers are accepted [172].

2.3.2 The High Level Trigger (HLT)

The HLT system of ALICE is a software trigger that consists of multiprocessor computers. It is being used to significantly reduce the size of the event by selecting the required portion (partial readout of sub-detectors) of the data. A copy of the raw data is received by the HLT and made further processing to select the relevant events and compress the data without losing the physics content.

The architectural flow of the HLT system is shown in Fig. 2.14. The data collected by different sub-detectors of ALICE are received in layer 1 through the 454 Detector Data Links (DDL). The first layer performs the basic calibration of these data, and then the second layer extracts the hits and clusters. The reconstruction of the event for each detector is performed in the third layer. After that the fourth layer combined the processed and calibrated information from all detectors to reconstruct the whole event. From these reconstructed events, layer five selects event with the physics interest. These selected data are processed further via complex data compression algorithms in layer six [172].

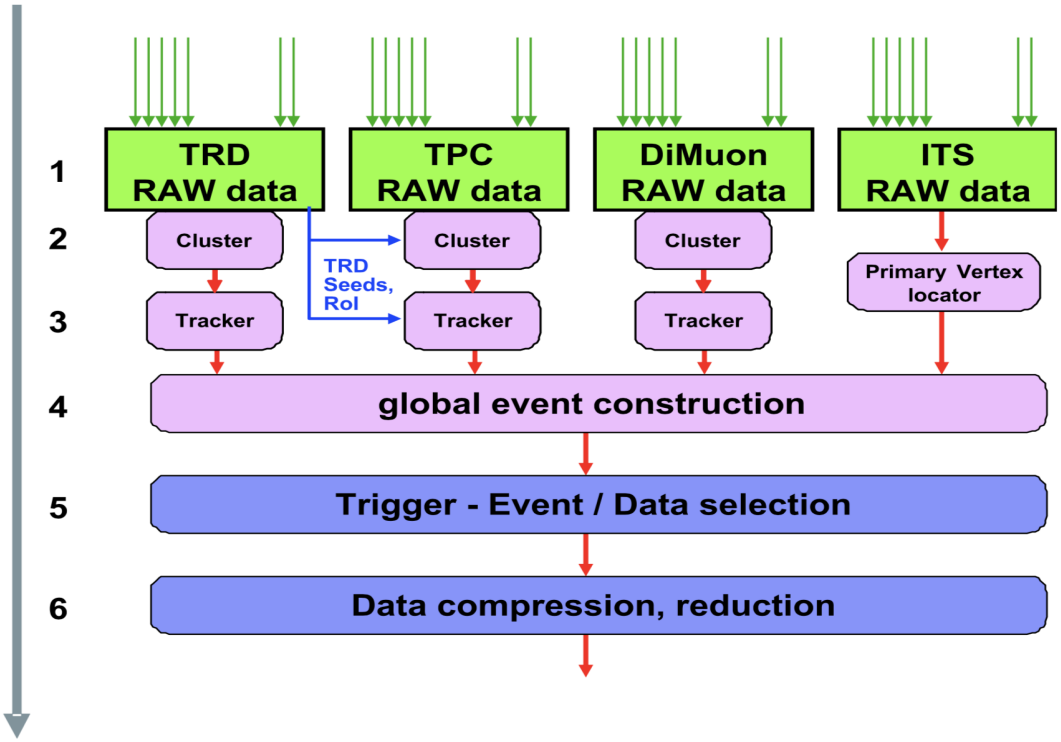

Fig. 2.14 The architectural layers of HLT are shown. Figure from [151].

2.4 ALICE Analysis Framework: AliRoot

The data recorded by the different detectors of ALICE need to be analysed to study different observables of nuclear collisions to have vital information about the particle production mechanism as well as on the state of matter formed during the collisions. The framework used for the analysis of data in the ALICE Collaboration is known as AliRoot [173], and its schematic steps of working is shown in Fig. 2.15. It is an offline analysis framework, whose main task is to perform simulation, reconstruction, calibration, quality assurance and analysis of experimental & simulated data. It contains several ALICE-specific libraries and is added to the standard open-access data analysis framework, commonly known as ROOT [174] for better performance of the framework. Analysis codes of AliRoot need to be written in C++. However, some parts of AliRoot macros are written in Fortran and are wrapped inside C++.

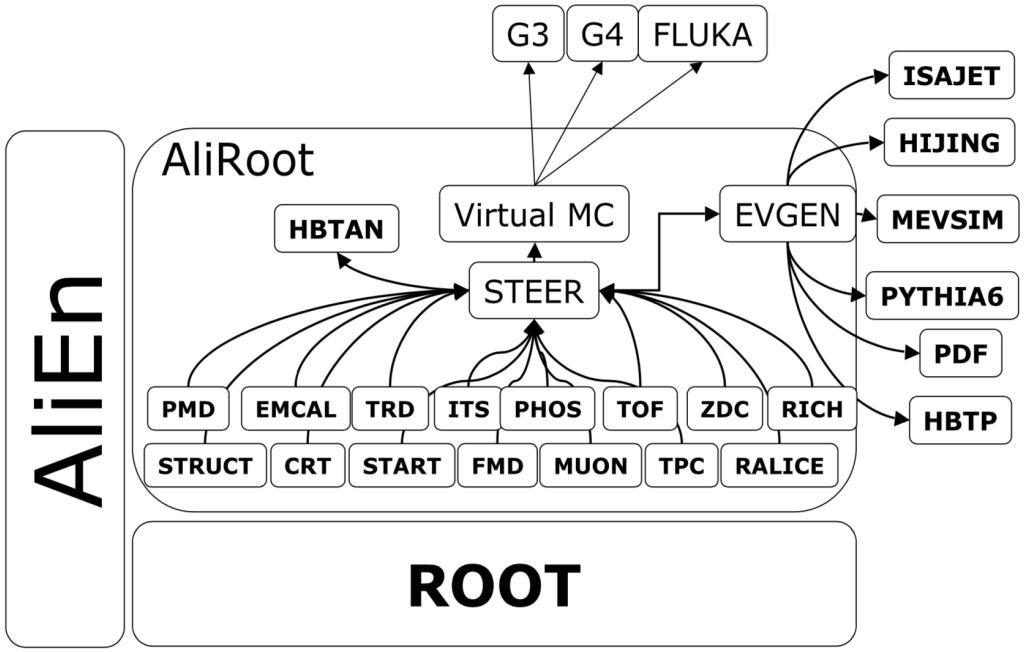

Fig. 2.15 A schematic view of the AliRoot framework of ALICE used for data analysis [151].

The data processing flow in the AliRoot framework is shown in Fig. 2.16. Monte Carlo event generators create the kinematic tree containing different physics processes at the parton level and the results of the fragmentation. These event generated data includes the relevant information such as momentum, charge, mass, type of particles of the produced particle of the generated events. Then, these particles are transported through the ALICE geometry, and the response of the detectors for particles is simulated. The energy deposited by the particle in the detector medium is known as the hits. The information about the hits is stored for each detector. These hits are then converted to digits considering the detectors response function, and finally, the digits are stored in a specific format for each of the detector as raw data. In general, detectors perform local reconstruction of the data and then a seeding procedure is used to start the Kalman filter tracking [175–177]. For comparison of the software and detector performance, the simulated events are processed through the whole cycle and then finally, the reconstructed particles are compared with the Monte Carlo generated ones.

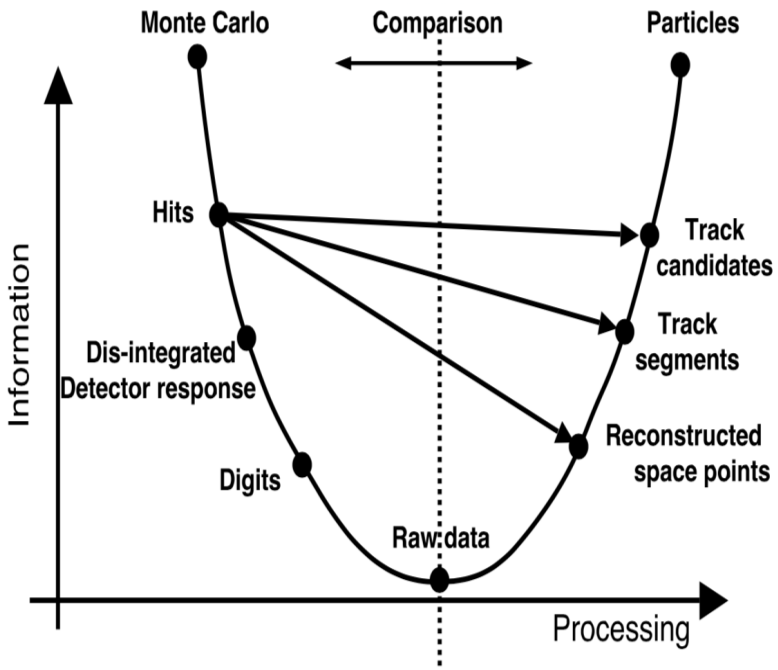

Fig. 2.16 The schematic view of the data processing in the AliRoot framework of ALICE is shown [151].

The amount of data collected by the ALICE detector is enormous. For the analysis of such a massive set of data, the computational power is required to be very high. Therefore, the worldwide Grid distributed computing system has been built up. The framework developed by ALICE Collaboration is called AliEn (ALICE Environment) [178] which is used for reconstruction and analysis of data in a distributed environment. It provides a universal file system for data storage and an interface to execute jobs on the Grid. The Grid system allows the analysis jobs to split into many identical sub-jobs that run in parallel on different computer nodes. The AliEn interface is also used to monitor the progress of the jobs on the Grid.

2.5 Summary

In this chapter, the experimental setup, usually known as the ALICE experiment at the LHC, whose data are analysed in this thesis is explained. The purpose of the LHC accelerator, the procedure for the acceleration of different types of particles, the energy range and luminosity achieved by it are also explained here. Further, discussions on different sub-detectors of ALICE used for data taking are given. In more details, those detectors, which are used in this analysis for charged particle tracking and identification, multiplicity estimation and the event time measurements, are discussed. Moreover, for data taking in ALICE, different trigger systems used and the procedure used for recoding of these collected data in the disk has also been described. AliRoot, the main framework employed in order to analyse the data collected by the ALICE experiment is also explained here. Along with all these, different data processing procedures used after the data taking has also been highlighted.

3

Identification of pions, kaons and protons with the TOF detector of ALICE

As mentioned in Sub-section 2.2.4, the Time-of-Flight (TOF) detector of ALICE is a large area, high precession gaseous detector that is used primarily for particle identification (PID) at the intermediate transverse momentum (p_{T}) region, i.e. from 0.6 to 4 GeV/c. In this p_{T} range, the particle can be identified via the measurement of travel time of the particle from the collisions point to the TOF detector. Therefore, it becomes essential for the TOF detector to have a good resolution on time-of-flight as well as on track length of the particle. In

ALICE, the TOF detector is located at the radial distance of 3.7 m from the collisions point. Thus, the particle needs to travel a considerable distance, providing excellent separation capabilities on time-of-flight between different particles having different masses. The time-of-flight information is combined with the momentum (p) of the particle, provided by the tracking detectors, namely ITS and TPC, to estimate the mass (m) of the particle following the Eq. (3.1).

$$m^2 = \frac{p^2}{v^2} = \frac{p^2}{(c\beta\gamma)^2} = \frac{p^2}{c^2}\left(\frac{(c \times t_{TOF})^2}{L^2} - 1\right) \tag{3.1}$$

where, L is the measured track length, t_{TOF} is the time measured by the TOF detector, $\beta = \frac{v}{c}$ and γ is the Lorentz factor.

The corresponding mass resolution will be:

$$\left(\frac{dm}{m}\right)^2 = \left(\frac{dp}{p}\right)^2 + \gamma^4\left[\left(\frac{dt_{TOF}}{t_{TOF}}\right)^2 + \left(\frac{dL}{L}\right)^2\right] \tag{3.2}$$

From Eq. (3.2), it could be observed that the terms contributing to the uncertainty have different weights. At high momenta, the momentum resolution can be neglected, and total uncertainty on mass estimation have the contribution from the resolution on time-of-flight and the track length. As a requirement of the ALICE experiment to provide particle identification in the extended transverse momentum range, the TOF detector was built in such a way that it can provide a timing resolution better than 90 ps [179, 114].

Furthermore, the time-of-flight difference between two particles having the same momentum and track length but having different masses m_1 and m_2 is given by:

$$t_1 - t_2 = \frac{Lc}{2p^2}\left(m_1^2 - m_2^2\right) \tag{3.3}$$

And the PID capability of the TOF detector is related to the number of the standard deviation of time difference between the two particles as given below:

$$n_\sigma = \frac{t_1 - t_2}{\delta t} \tag{3.4}$$

where δt is the total resolution of the TOF detector (δt=dt_{TOF}=σ_{TOF}) and is given by

$$\sigma^2_{TOF} = \sigma^2_{MRPC} + \sigma^2_{TDC} + \sigma^2_{Cal} + \sigma^2_{Clk} + \sigma^2_{T0} \tag{3.5}$$

where,

- σ_{MRPC} = Intrinsic resolution of the Multigap Resistive Plate Chambers (MRPC)
- σ_{TDC} = The intrinsic resolution of the readout boards due to the signal digitisation
- σ_{Cal} = The uncertainties on the calibration parameters, such as the cable lengths and path of the readout board
- σ_{Clk} = It accounts for the jitter of the clock signal distribution to the electronics
- σ_{T0} = The resolution on the measurement of the event collisions time

In this chapter, a detailed analysis performed with the TOF detector of ALICE will be discussed to identify the charged pions, kaons and protons in different charged-particle multiplicity classes in pp collisions at $\sqrt{s} = 13$ TeV. Previous studies on different observables of identified charged particles as a function of multiplicity in p-Pb collisions at $\sqrt{s} = 5.02$ TeV have shown behaviour reminiscent of those observed for the heavy-ion collisions [17, 11]. Further, a more recent multiplicity dependent study in pp collisions at $\sqrt{s} = 7$ TeV also suggests similar behaviour in the small system as observed in the p-Pb collisions providing hints that the collective behaviours are not the characteristics of heavy-ion collisions only [19]. Moreover, pions production measurement in pp collisions provide the baseline results for the studies of strangeness enhancement in the same colliding system [20] and give input to constrain different parameters in the various theoretical model [15]. However, all previous

multiplicity dependent studies were performed for different colliding systems and at different collisions energies. With the availability of the pp collisions at $\sqrt{s} = 13$ TeV data from the LHC, for the first time, it becomes feasible to disentangle the centre-of-mass energy from multiplicity dependent observables for the small system. Therefore, in this thesis, the measurements of pions, kaons and protons productions as a function of multiplicity in pp collisions at the highest LHC energy will be carried out to provide more in-depth insight into the particle production mechanism as well as on the dynamics of the collisions of the small system.

3.1 Data sample (ALICE data and Monte Carlo productions)

The datasets that are used in this analysis was recorded by the ALICE during the LHC running year 2016 for pp collisions at $\sqrt{s} = 13$ TeV. A total of 143 $\times 10^6$ events have been analysed, corresponding to the integrated luminosity of 2.47 nb^{-1}, considering the visible cross-section measured in van der Meer (vdM) scans by the T0 and V0 detectors [180]. The data sample was recorded with a magnetic field having a strength of 0.5 T inside the solenoid magnet to measure the momentum of the charged particles. The run periods used for the analysis are LHC16k & LHC16l, and corresponding reconstruction level of the datasets is the second pass, i.e. pass2. The pass2 is the most updated reconstruction period, having improved tracking information and TOF calibration. The production periods and run numbers used for this analysis are given below:

- **Period: LHC16k pass2** (**Run numbers:** 258537, 258499, 258477, 258456, 258454, 258452, 258426, 258393, 258387, 258359, 258336, 258332, 258307, 258306, 258303, 258302, 258301, 258299, 258278, 258274, 258273, 258271, 258270, 258257, 258256, 258204, 258203, 258202, 258198, 258197, 258178, 258117, 258114, 258113, 258109,

258108, 258107, 258063, 258060, 258059, 258053, 258049, 258045, 258042, 258041, 258039, 258019, 258017, 258014, 258012, 258008, 258003, 257992, 257986, 257979, 257963, 257960, 257957, 257939, 257937, 257936, 257892, 257855, 257853, 257851, 257850, 257804, 257803, 257799, 257798, 257797, 257773, 257765, 257757, 257754, 257737, 257735, 257734, 257733, 257727, 257725, 257724, 257697, 257692, 257691, 257689, 257688, 257687, 257685, 257684, 257682, 257644, 257642, 257636, 257635, 257632, 257630, 257606, 257604, 257601, 257595, 257594, 257592, 257590, 257588, 257587, 257566, 257562, 257561, 257560, 257541, 257540, 257539, 257531, 257530, 257492, 257491, 257490, 257488, 257487, 257474, 257468, 257457, 257433, 257364, 257358, 257330, 257322, 257318, 257260, 257224, 257209, 257206, 257204, 257144, 257141, 257139, 257138, 257137, 257136, 257100, 257095, 257092,257084, 257082, 257080, 257077, 257028, 257026, 257021, 257012, 257011, 256944, 256942, 256941) and

- **Period:LHC16l pass2** (**Run numbers:** 259888, 259868, 259867, 259866, 259860, 259842, 259841, 259822, 259789, 259788, 259781, 259756, 259752, 259751, 259750, 259748, 259747, 259477, 259473, 259396, 259395, 259394, 259389, 259388, 259382, 259378, 259342, 259341, 259340, 259339, 259336, 259334, 259307, 259305, 259303, 259302, 259274, 259273, 259272, 259271, 259270, 259269, 259264, 259263, 259261, 259257, 259204, 259164, 259162, 259118, 259117, 259099, 259096, 259091, 259090, 259088, 258964, 258962)

To simulate and study the performance of the detectors such as efficiency, acceptance, the fraction of primary particles, etc., Monte Carlo generated data productions are used. For pp collisions at $\sqrt{s} = 13$ TeV, the events are generated with the PYTHIA 8 Monash 2013 model [149]. The particles produced by the event generators are then transported through the different transport codes such as GEANT [181–183] and FLUKA [184] having the complete

description of the ALICE detector geometry to have the information about the interaction of the particle with the detector material. Similar data-taking conditions are applied while performing the simulation using the MC data to produce the correct detector response.

In this thesis, the MC productions LHC18f1 anchored to LHC16k pass2 and LHC18d8 anchored to LHC16l pass 2 data productions have been used. For MC data, the same run numbers as that of the experimental data have been used.

3.2 Events and vertex selection

For the selection of good quality events originating from the beam-beam collisions and not from beam-gas interactions, which are known as background events, several cuts are required to apply at the beginning of the analysis. To start with, a minimum bias trigger is applied, which requires a hit in both V0 detectors or the SPD in coincidence with the arrival of proton bunches from both directions. A selection based on the time information of the two V0 detectors, as shown in Fig. 3.1 is also applied to remove the background events. These events are located at the co-ordinate (-14.3 ns, -8.3 ns) for beam 1 and (14.3 ns, 8.3 ns) for beam 2 in the figure [185].

Background events are also rejected by considering the correlation between the SPD clusters and the number of tracks in the SPD (known as tracklets). An event is considered as the background events if the number of SPD clusters, N_{SPDClu} and number of tracklets, N_{trk} follow the Eq. (3.6) [185].

$$N_{SPDClu} \leq 65 + 4N_{trk} \tag{3.6}$$

Example plots of the events before and after application of the cut mentioned in Eq. (3.6), along with other events selection cuts used in this thesis are shown in Fig. 3.2(a) and Fig. 3.2(b), respectively.

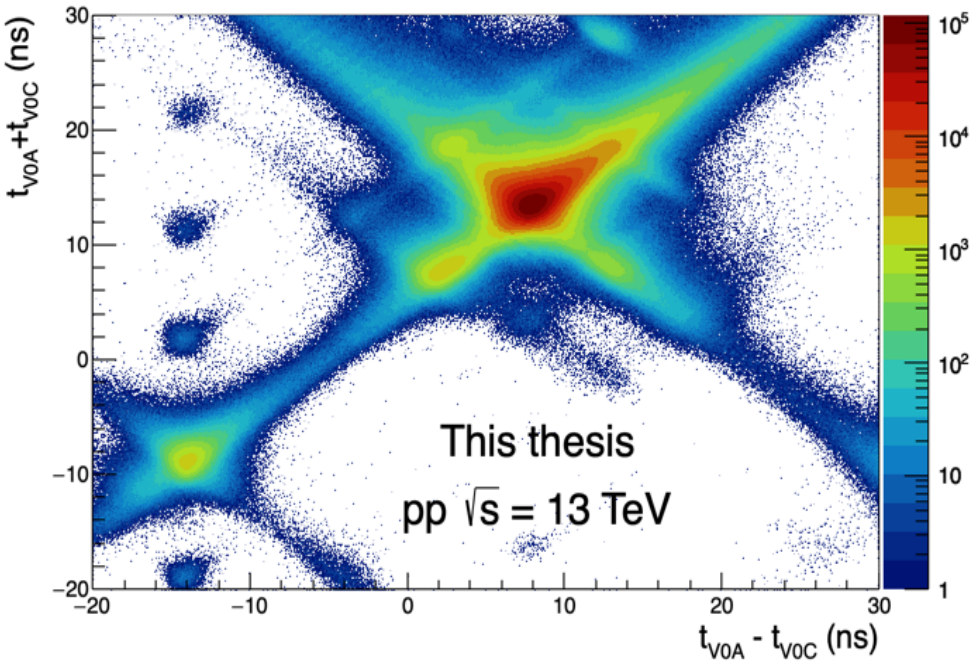

Fig. 3.1 Correlation between the sum and difference of signal times in V0A and V0C is shown. Events located at (8.3 ns, 14.3 ns) are from real collisions, whereas, the events at (-14.3 ns, -8.3 ns) and (14.3 ns, 8.3 ns) are background events from beam 1 and beam 2 respectively.

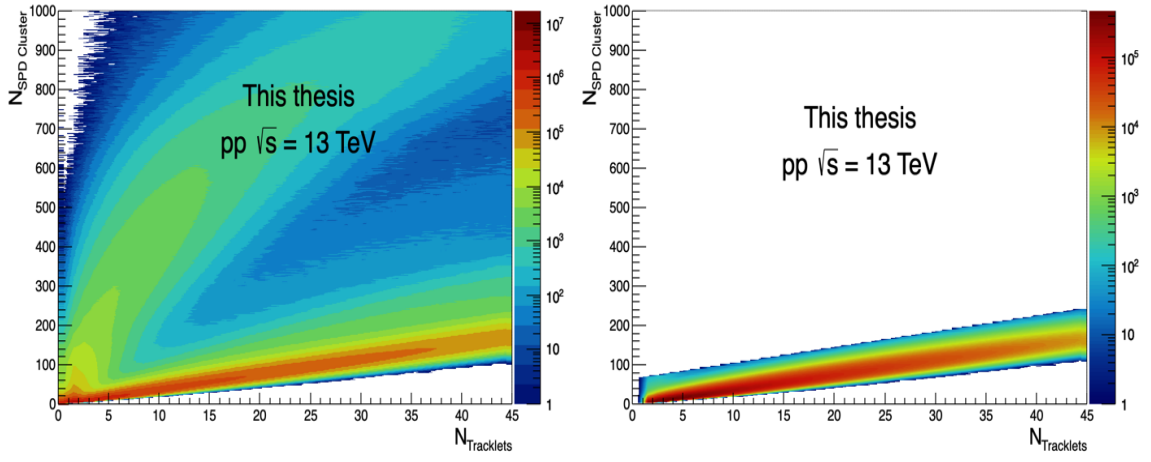

(a) (b)

Fig. 3.2 (a) Correlation between reconstructed SPD clusters and tracklets for all the events. The bands due to collisions and mean induced background is visible. (b) The same correlation is shown after application of the cut described by Eq. (3.6) and other events selection cuts that are used in this thesis.

For the rejection of in-bunch pile-up events, condition on secondary vertex reconstructed within 8 mm of the primary vertex along the beam axis is applied. The secondary vertex also requires to have at least three contributors associated with it, if the total number of tracklets in the SPD is less than 20 ($N_{Trk} < 20$) or four contributors if $20 \leq N_{Trk} < 50$ or five contributors if $50 \leq N_{Trk}$ are also needed to apply.

Those events in which data acquisition (DAQ) readout is incomplete, are also rejected. Further, the events having at least one inelastic collision are used for analyses of present work. For this, events satisfying the condition of having at least one tracklets in the two-layer of the SPD with $p_T > 0.15$ GeV/c in pseudo-rapidity region $|\eta| < 1$ is considered. In general, this condition is known as INEL>0. It is important to note that this class only corresponds to the visible cross-section, as a fraction of events will be lost due to the detector limitation and corresponds to $\sim 75\%$ of the total inelastic scattering cross-section [186].

Once the good events from the beam-beam interactions are selected, another cut on primary vertex selection is needed to apply. The primary vertices are reconstructed using the information from SPD tracklets or the global tracks (reconstructed using ITS and TPC) or both. The position of the primary vertex can be obtained from the reconstructed tracks. If this is not available, the location of the vertex is estimated from SPD tracklets. Once the reconstructed vertex is available, events whose primary vertex lies within $\pm$ 10 cm range along the z-axis from the collisions point are considered for the analysis. Further, the SPD vertex resolution along the beam axis (z_{Vtx}^{SPD}) is required to be better than 0.25 cm and SPD vertex dispersion less than 0.04. Again, if both the SPD and the track vertices exist, the displacement between the two must be less than 0.5 cm, i.e. $|z_{Vtx}^{Trk} - z_{Vtx}^{SPD}| < 0.5$ cm.

The total number of events rejected after the application of the cut mentioned above, and the final number of events used in this thesis for LHC16k and LHC16l period are shown in Fig. 3.3.

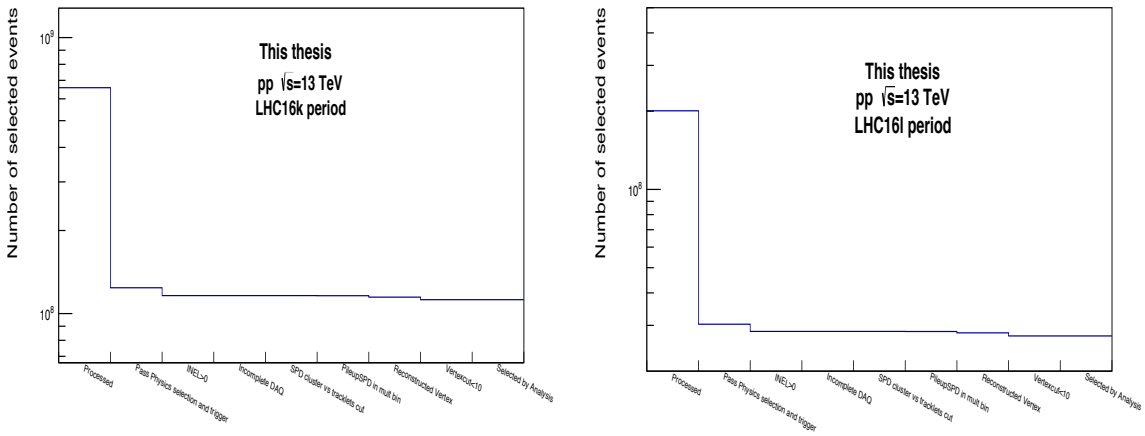

(a) LHC16k (b) LHC16l

Fig. 3.3 The numbers of events that are processed and selected for analysis for LHC16k and LHC16l period.

3.3 Multiplicity selection

The multiplicity of an event can be estimated in different ways. In ALICE, the most common method of estimating the multiplicity is to measure the charge deposited in the forward detector V0 (both V0A and V0C). The total charge deposited in the V0 detector can also be converted to V0M percentile, and one can use both the multiplicity estimators. In this thesis, the V0M percentile multiplicity estimator is used. The multiplicity classes considered for this analysis are listed in Table 3.1. And the number of selected events as a function of V0M percentile multiplicity estimator is shown in Fig. 3.4.

Table 3.1 The multiplicity classes used for the identification of π, K and p in pp collisions at $\sqrt{s} = 13$ TeV.

Multiplicity class	I	II	III	IV	V
V0M percentile (%)	0-1	1-5	5-10	10-15	15-20
Multiplicity class	VI	VII	VIII	IX	X
V0M percentile (%)	20-30	30-40	40-50	50-70	70-100

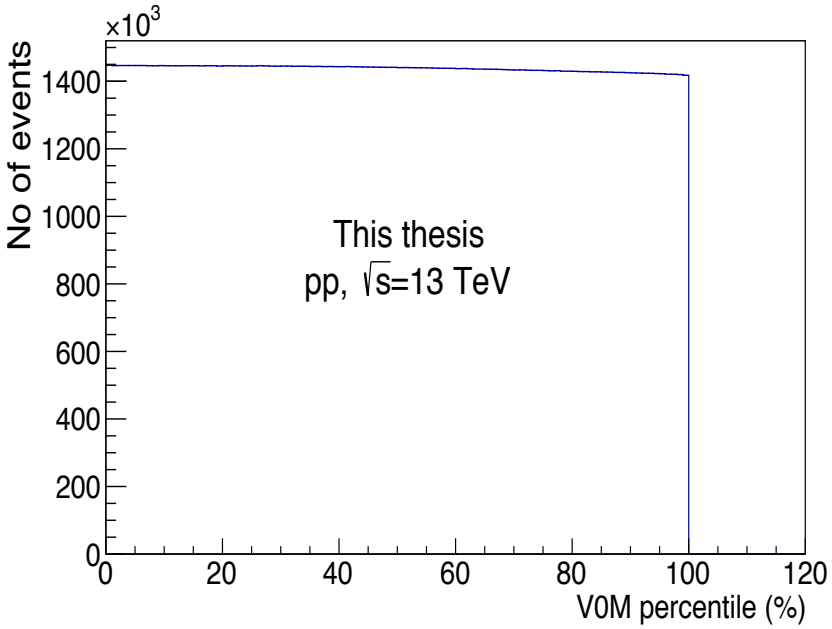

Fig. 3.4 Number of selected events as a function of V0M percentile after application of all the event selection cuts in pp collisions at $\sqrt{s} = 13$ TeV.

3.4 Tracks selection

In general, charged particles tracks can be produced at any point of the collisions. However, in this thesis, the tracks produced only from the primary vertex are selected. For the selection of such type of tracks, several pre-defined selection criteria are applied, and are required to pass all of these cuts. For this work, the cuts listed in Table. 3.2 are used to select good quality tracks.

One of the prime objectives of this thesis is to identify the light-flavour primary charged particles such as π, K, p. Particles are considered as the primary if their mean proper decay length $c\tau$ is larger than 1 cm and are produced in the collisions (including the products of strong and electromagnetic decays), but not from weak decay of other light-flavour hadrons or muons. An exception to this is the products of the weak decays, where $c\tau$ of the weakly decaying particle is less than 1 cm [187]. Primary particles are chosen on the basis of the Distance of Closest Approach (DCA) of the tracks to the primary vertex. The DCA cut is

Table 3.2 Various types of track cuts used for selection of good quality tracks. Track cuts include the reconstruction as well as the acceptance cuts.

Track cuts	Value
Minimum number of crossed row in TPC	70
Ratio of TPC crossed row to findable cluster	0.8
Maximum χ^2 per TPC cluster	4
The distance of closest approach (DCA) of the reconstructed track to the vertex in z direction (DCA_z)	2 cm
The DCA of the reconstructed track to the vertex in xy plane (DCA_{xy})	7σ
Maximum global χ^2 per ITS cluster	36
Kink Rejection	yes
Track refit in TPC	yes
Track refit in ITS	yes
Minimum number of SPD clusters	1
Pseudo-rapidity	$\|\eta\| < 0.8$
Rapidity	$\|y\| < 0.5$

considered in two directions, one along the z-direction and another in the xy plane. In the z-direction, a constant cut, as mentioned in Table. 3.2 is applied while, in the xy plane, a p_{T} dependent cut as given in Eq. (3.7) is applied.

$$\mathrm{DCA_{xy}} = 0.0105 + \frac{0.0350}{p_{\mathrm{T}}^{1.1}(\mathrm{GeV/c})} \tag{3.7}$$

The value mentioned in Eq. (3.7) correspond to 7σ in DCA_{xy} and will remove a significant fraction of secondary particles, whereas, it will not have any notable effect on the primary particles.

3.5 Track cuts specific to the TOF detector

Along with the previously mentioned track cuts, the following track cuts, specific to the TOF detector are also needed to apply.

- The track needs to have an associated hit in TOF with the measured time.

- The track length of the reconstructed particle should be greater than 350 cm.

3.6 Particle IDentification (PID) with TOF detector

3.6.1 Time-of-flight distribution in experimental data

The particle identification technique describes herewith is based on the statistical unfolding of the time-of-flight of a particle measured with the TOF detector (t_{TOF}). In this method, the time difference distribution between the measured time-of-flight and the expected time-of-flight are fitted with four template time-of-flight distribution, three for pions, kaons and protons; and one for the background particles.

The time-of-flight information measured by the TOF detector is combined with the event collisions time t_{ev} measured by the T0 detector to estimate the correct time-of-flight (tof) of the particles. Therefore, the correct tof is generally defined as follows:

$$tof = t_{TOF} - t_{ev} \tag{3.8}$$

For identification of particles, the separation time-of-flight between the tof obtained from data and the expected time-of-flight of a particle ($t_{exp,i}$) is considered. The time difference distributions for different particles are obtained from the following time difference:

$$tof - t_{exp,i} \tag{3.9}$$

The $t_{exp,i}$ are computed for each particle by considering the track length and energy loss in the medium. The $tof - t_{exp,i}$ distributions for π, K and p are shown in Fig. 3.5.

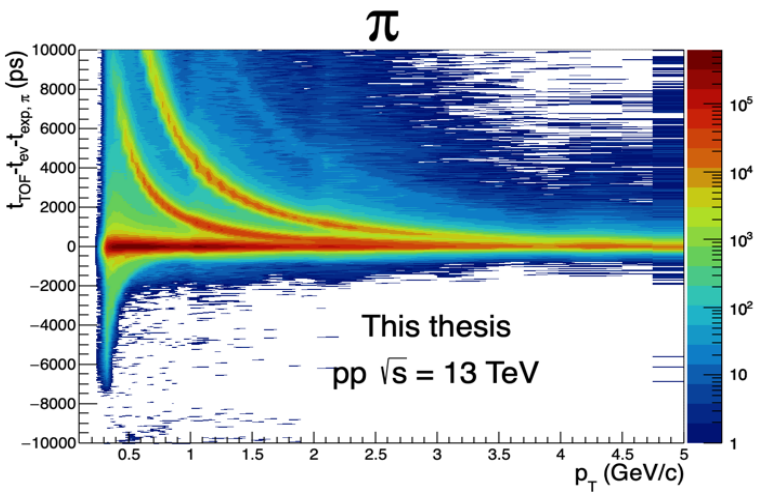

(a)

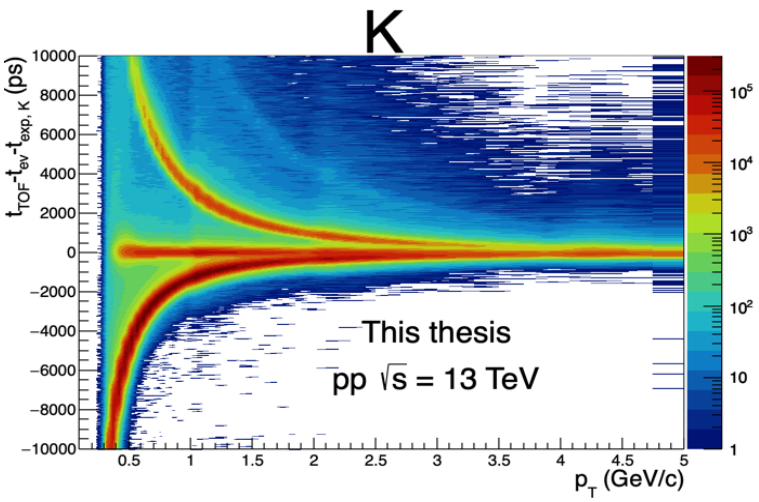

(b)

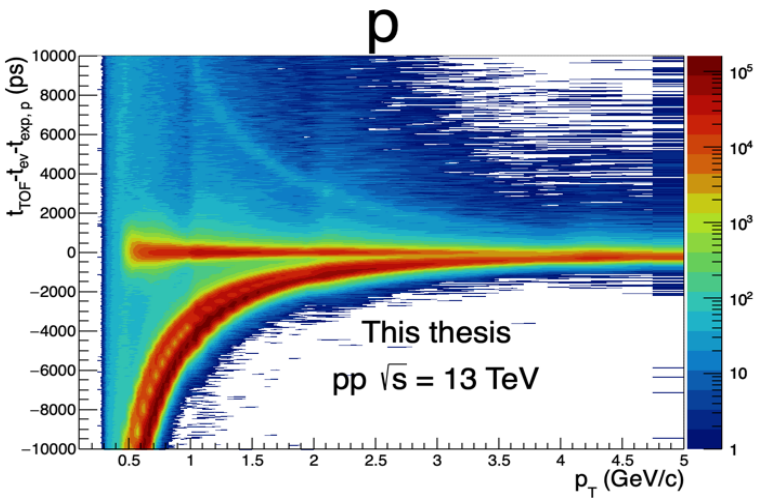

(c)

Fig. 3.5 $t_{TOF} - t_{ev} - t_{exp,i}$ distribution as a function of p_{T} for (a) pions, (b) kaons and (c) protons in MB pp collisions at $\sqrt{s} = 13$ TeV.

3.6.2 TOF signal description

For the identification of particles with the TOF detector, the response of the detector needs to be parametrised properly. In an ideal case, the TOF signal is a simple Gaussian function with the mean at zero and the standard deviation equal to the resolution of the TOF detector. However, excess counts in the right-hand side of the time distribution could be observed. The exact reason for such excess counts in the data can not be explained adequately. And therefore, for the proper description of such excess counts in the experimental data and correct estimation of raw yields of the particle, an exponential tail function is convoluted with the gaussian function on the right-hand side. For pp collisions, the TOF signal is given by the function f(x) as described in Eq. (3.10).

$$f(x) = \begin{cases} Gaus(x, \mu, \sigma) & x \leq \mu + \tau \\ Gaus(\mu + \tau, \mu, \sigma).e^{-s(x-\tau-\mu)} & x > \mu + \tau \end{cases} \tag{3.10}$$

The function f(x) is described by four parameters namely mean (μ), sigma (σ) of the Gaussian part, the tail (τ, the point where the exponential tail starts) and its slope (s). A representative plot, showing the TOF signal function describes by the Eq. (3.10) is shown in Fig. 3.6. Also, the effect of variation of the σ and slope parameter of the TOF signal function is shown in Fig. 3.7(a) and 3.7(b), respectively.

3.6.3 TOF PID performance

The identification of the particle with the TOF detector relies on the time resolution of the TOF. An idea about the time resolution can be obtained by fitting the $tof - t_{exp,\pi}$ distribution with a Gaussian function for all the tracks in the transverse momentum range 0.9 to 1.1 GeV/c, which satisfy the standard events and track selection cuts. As the separation between pions, kaons and protons are good enough in the p_{T} range mentioned above; therefore, the particles are assumed to be pions in that region. The performance distribution is shown in Fig. 3.8.

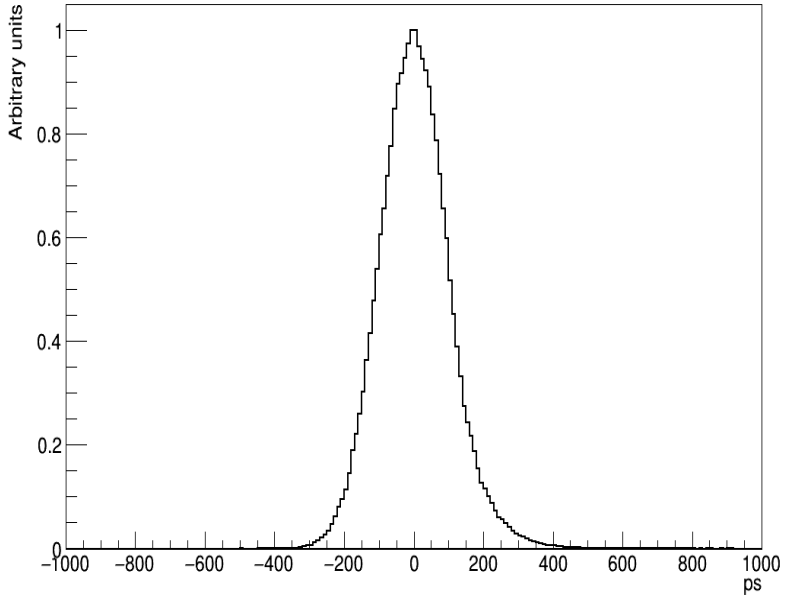

Fig. 3.6 Representation of the TOF signal function as described in Eq. (3.10).

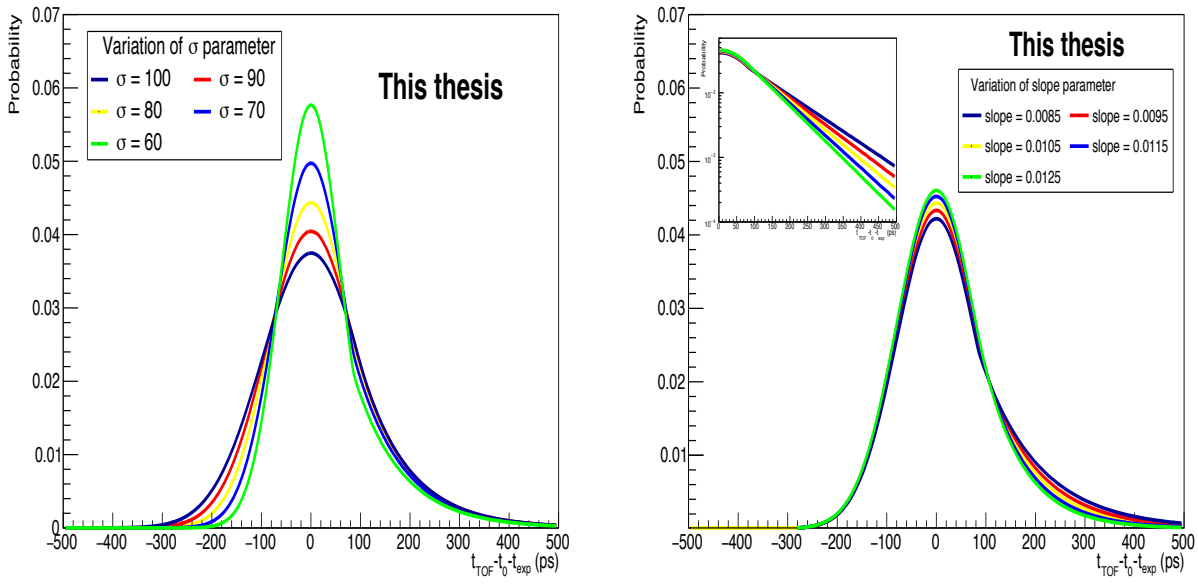

(a) σ variation

(b) Slope variation

Fig. 3.7 Variations of the TOF signal function with the variation of σ and slope parameter are shown. Inset in (b) shows the zoom version of the slope variation in higher positive time difference.

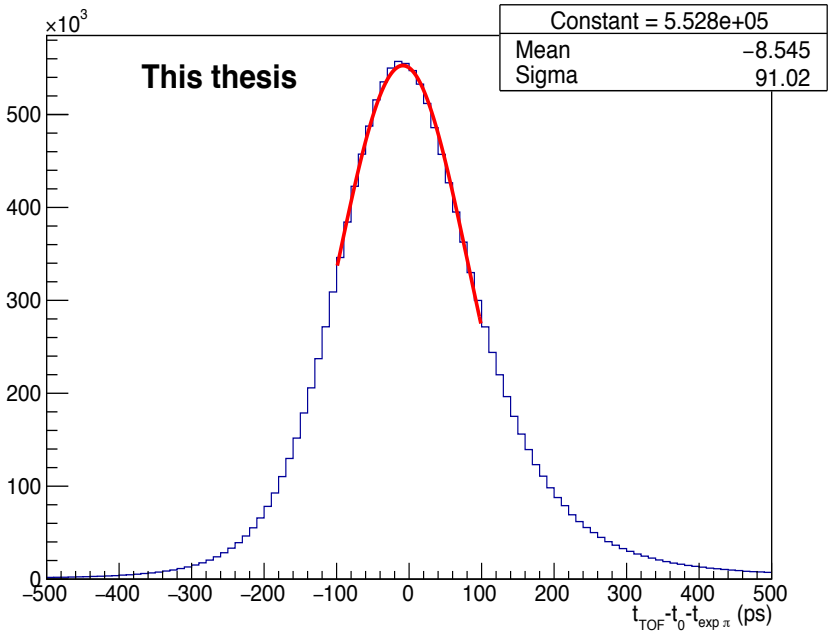

Fig. 3.8 The $t_{TOF} - t_{ev} - t_{exp,\pi}$ distribution of all the tracks in the p_{T} range 0.9 to 1.1 GeV/c is fitted with the gaussian function.

The total time resolution of particle identification has several contributions and is given by Eq. (3.11).

$$\sigma^2_{PID} = \sigma^2_{t_{TOF}} + \sigma^2_{t_{ev}} + \sigma^2_{t_{exp,i}} \tag{3.11}$$

where the $\sigma_{t_{ev}}$ is the uncertainty in resolution due to the event collisions time determination and is dependent on the method used. The $\sigma_{t_{exp,i}}$ is the resolution uncertainty due to the tracking and reconstruction, which depend upon the transverse momentum and the particle type [188].

In this thesis, event collisions time is estimated by a combination of both TOF and T0 detectors and the method is usually known as t^{Best}_{ev}. If it is estimated by only TOF detector then the t^{Best}_{ev} corresponds to t^{TOF}_{ev}, and if it is provided by T0 detector, then it corresponds to t^{T0}_{ev}. If both the measurements are available for event time calculation, then t^{Best}_{ev} is estimated by the weighted mean of the two methods. Further, if both of them are not available, then the

t_{ev}^{Best} fails and the event collision time is defined by t_{ev}^{Fill}, which has the worst resolution of $\sim$ 200 ps [188].

The resolution of the event collisions time estimation varies from 20 to 80 ps with track (high to low) multiplicity, as shown in Fig. 3.9 [188]. During the analysis, this can be overcome by estimating the event collisions time resolution on track by track basis for each event. For this, the resolution of TOF detector is taken from ALICE OADB for LHC16k and LHC16l run periods and is found to be 80 ps. The T0 and tracking resolutions are estimated by considering a random sampling in the gaussian distribution, where σ of the gaussian distribution is considered as the squared difference between the resolution measured in data for each particle and the one measured for TOF.

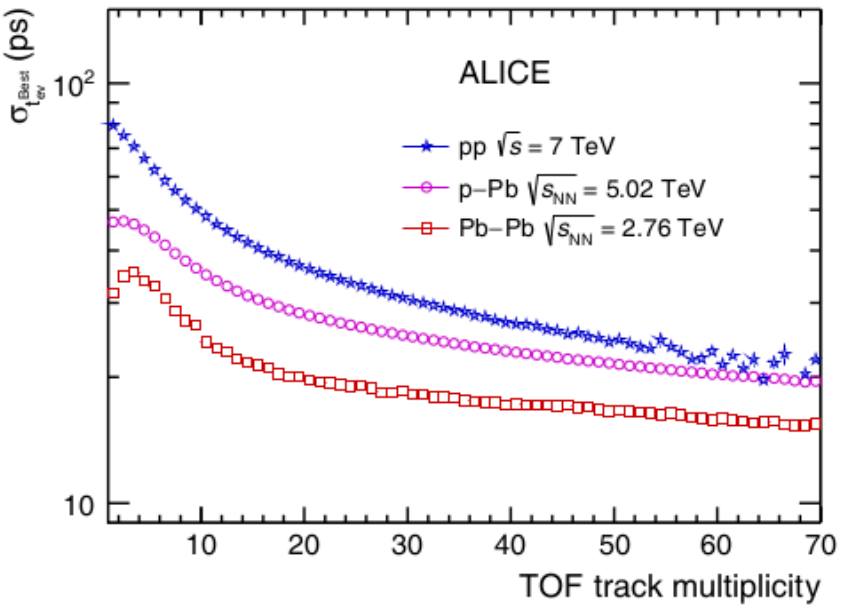

Fig. 3.9 Resolution of the t_{ev}^{Best} as a function of track multiplicity in different colliding systems and energies [188].

An idea about different parameters of the TOF signal can be gained by fitting the time difference distribution for the tracks in the p_{T} range 0.9 to 1.1 GeV/c with the TOF signal

function as described by Eq. (3.10). The fitted distribution with different parameters of the TOF signal function is shown in Fig. 3.10.

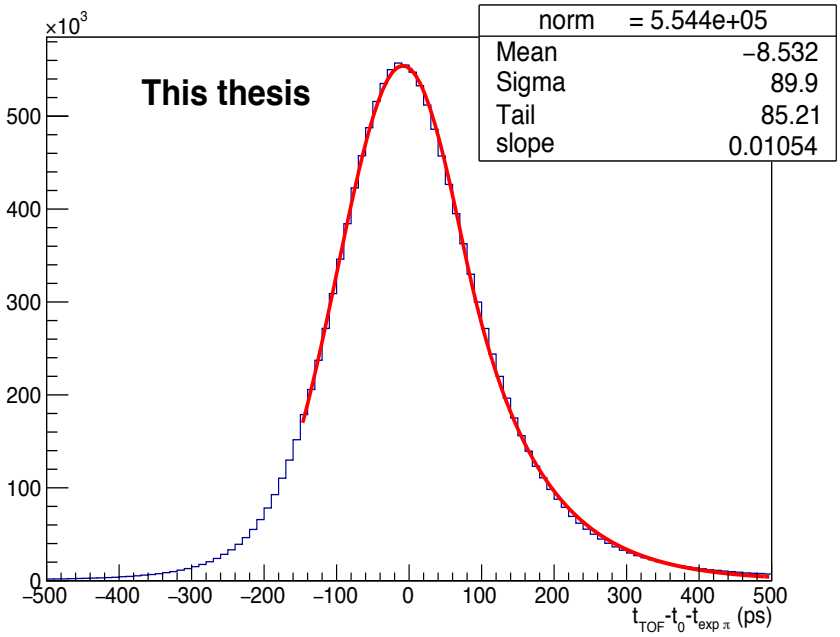

Fig. 3.10 The $t_{TOF} - t_{ev} - t_{exp,\pi}$ distribution of all the tracks in the p_{T} range 0.9 to 1.1 GeV/c is fitted with the TOF signal function to have an idea about different parameters of the function.

3.6.4 Mismatch parameterisation

To identify particles with the TOF detector, the track reconstructed in the TPC needs to propagate to the TOF. In a high-multiplicity environment as well as for low p_{T} particle, there is some probability that a track reconstructed in TPC may be wrongly matched to a track of TOF. This type of mismatch happens mainly due to propagation of a track from TPC to TOF detector and gets mixed with the track produced by some other particle and the combinatorial background produced in the collisions. This type of backgrounds are known as a mismatch and need to be taken into account during the yield extraction procedure to identify the π, K and p correctly. In this thesis, the mismatch tracks time distributions are obtained by

considering the random value of TOF PID response function as a function of pseudo-rapidity. The class used in the AliRoot to obtain such time is given in Eq. (3.12).

$$t_{mismatch} = AliTOFPIDResponse :: GetMismatchRandomValue(\eta); \tag{3.12}$$

The time difference between the mismatch track and the expected one for each type of particles are used to construct the mismatch distribution. The distributions are obtained from the data itself using the time difference $t_{mismatch} - t_{exp,i}$

3.6.5 Raw yields extraction

The raw yields of the particles are obtained by using the template fits method on the time difference distribution between the TOF time and the theoretical time-of-flight for each type of particle. First of all, for a particular kind of track, the rapidity is calculated by considering a mass hypothesis and the track selected within the rapidity interval of $|y| < 0.5$ are considered for analysis for that particular mass hypothesis. Then, the difference between the measured time-of-flight and the expected time-of-flight distributions are obtained for each p_{T} and multiplicity bins. The mass hypothesis is only correct for some of the track and therefore, the time difference distribution in data is composed of three sub-distributions correspondings to π, K and p. The sub-distribution corresponding to zero time difference is for the correct mass hypothesis, and the rest of the two distributions are for background particles. The time difference distribution is then fitted with the TFractionFitter class of ROOT [189] with the help of four templates, three corresponding to π, K and p and one for the mismatch. The signal template will be the one for which the mass hypothesis is considered during the rapidity estimation and therefore, the fitted results will provide raw yields of that (single) particle only. Thus, the same procedure needs to be repeated for three

times considering each particle mass hypothesis, i.e. pions, kaons and protons, to estimate the raw yields of these particles correctly.

Procedure for template generation

As mentioned in the above section, extraction of raw yield from the time difference distribution of data for a particular type of particle relies on the templates for both signal and backgrounds particles. These templates are generated for each of the particle considering the equation given below:

$$t_{template,i,j} = t_{exp,i} - t_{exp,j} + \text{TOFSignal} + \text{ExtraSmearing} + \text{SecondaryTail} \tag{3.13}$$

In the above equation, for the signal template, one needs to consider i = j and for background particles, i $\neq$ j. This method is repeated for each particle type with i = π, K, p and j = π, K, p.

The TOFSignal term in Eq. (3.13) takes account of the TOF detector response and need to be considered for each type of particles. It is generated by randomly sampling the TOF signal function in the data. The ExtraSmearing term takes account of the uncertainty due to the tracking and t_{ev} determination and is obtained by gaussian sampling in data as given below:

$$\text{ExtraSmearing} = Gaus(0, \sigma_{Extra}) \tag{3.14}$$

where the σ_{Extra} parameter is obtained for each track considering the equation given below:

$$\sigma_{Extra} = \sqrt{\sigma^2_{t_{exp,i}} - \sigma^2_{TOF}} \tag{3.15}$$

Furthermore, in the time difference distribution of data, it could also be observed that there exists a second-order tail which extends up to large arrival time. The source of this tail was found to be the particles which suffer decay just before arrival at the TOF detector. These are correlated mismatch tracks that differ from the uncorrelated mismatch and result in a delayed arrival time of the particles, thus contributing to the right-hand side of the TOF signal. In this thesis, a secondary tail contribution obtained from the Monte Carlo GEANT simulation has been added in the template generation process to describe the experimental time of flight distribution correctly and to get an accurate description of the signal. Here, the secondary tail contribution for genuine signal formed by the primary tracks of pions has been considered. An example plot of such a secondary tail is shown in Fig. 3.11.

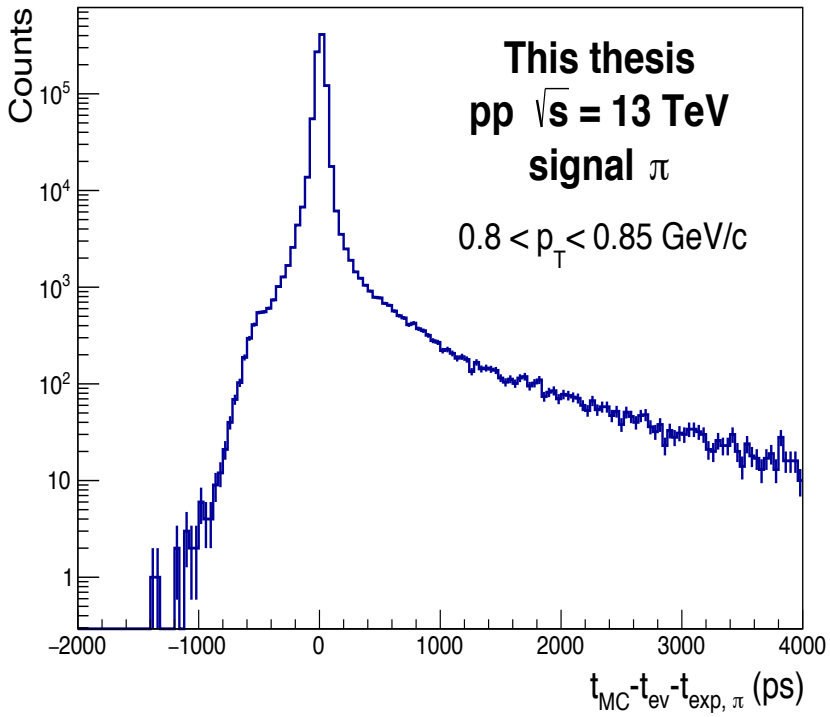

Fig. 3.11 An example plot of pions secondary tail obtained from the MC GEANT simulation.

The $t_{TOF} - t_{ev} - t_{exp,\pi}$ distribution fitted using the templates without and with having the secondary tail contribution for pions mass hypothesis in a selected p_{T} range are shown in Figs.

3.12(a) & 3.12(b), respectively for pp collisions at $\sqrt{s} = 13$ TeV. From Fig. 3.12(a), it could be observed that when no secondary tail contribution is there in the templates, an apparent deficit of the template and fit results than that of the data distribution is clearly visible. This deficit of particles in the templates can be corrected by including the secondary tail contribution during the template generation process, and the fit result is shown in Fig. 3.12(b).

Some examples of the template fits performed in different p_{T} bins for the extraction of raw yield of π, K and p in minimum bias pp collisions at $\sqrt{s} = 13$ TeV are shown in Figs. 3.13, 3.14 and 3.15, respectively. Similar fits have also been performed in other p_{T} bins for different charged-particle multiplicity classes to extract raw yields of the particles.

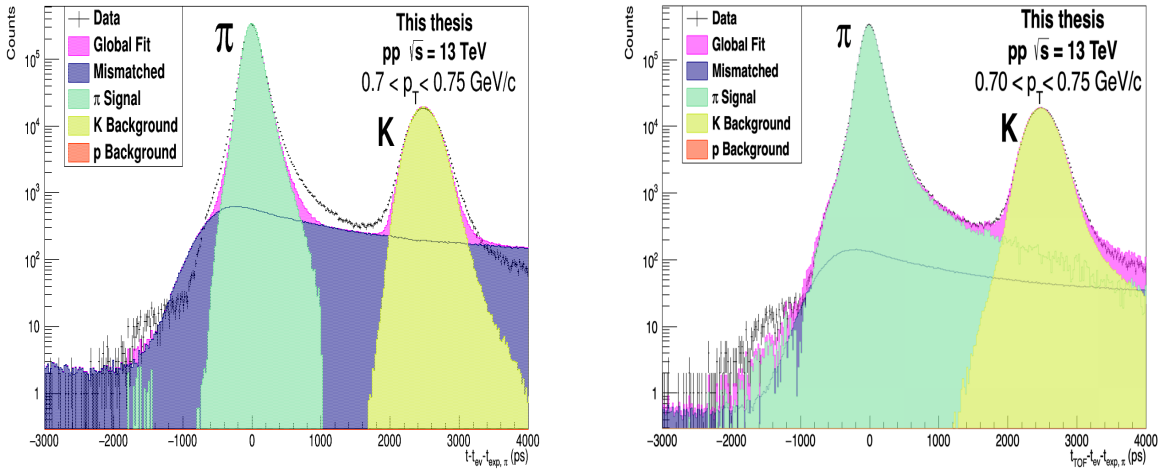

(a) (b)

Fig. 3.12 Comparison of time difference distribution fit of pions (a) without the secondary tail and (b) with the secondary tail contribution in the templates. A clear description of data with the secondary tail contribution could be observed compared to the results without the secondary tail in the templates.

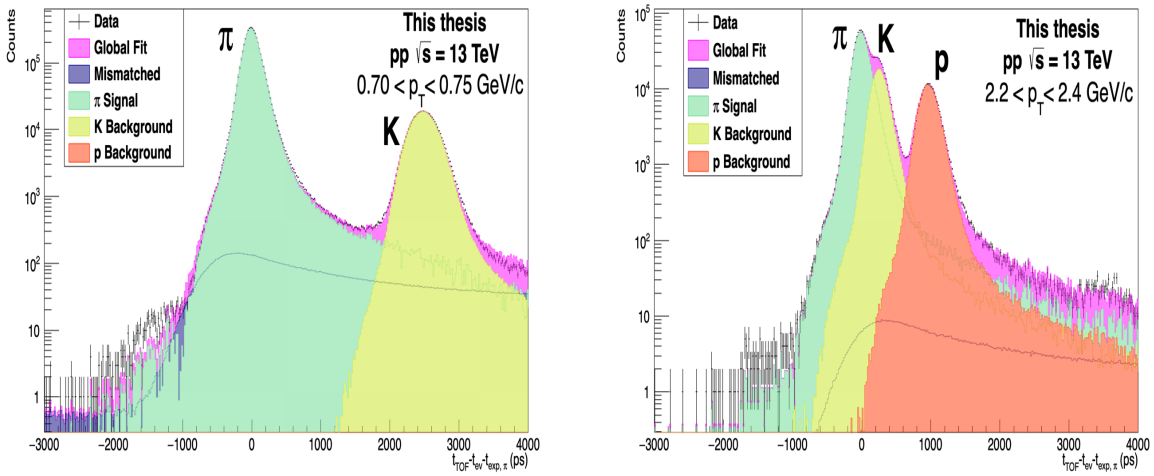

(a) (b)

Fig. 3.13 Fit examples of π to extract the raw yields of the particles in (a) low and (b) intermediate p_{T} bins in minimum bias pp collisions. The templates for the three type of particles are shown in a different colour. The mismatched template is shown in the blue line, and the total fit is represented by magenta colour.

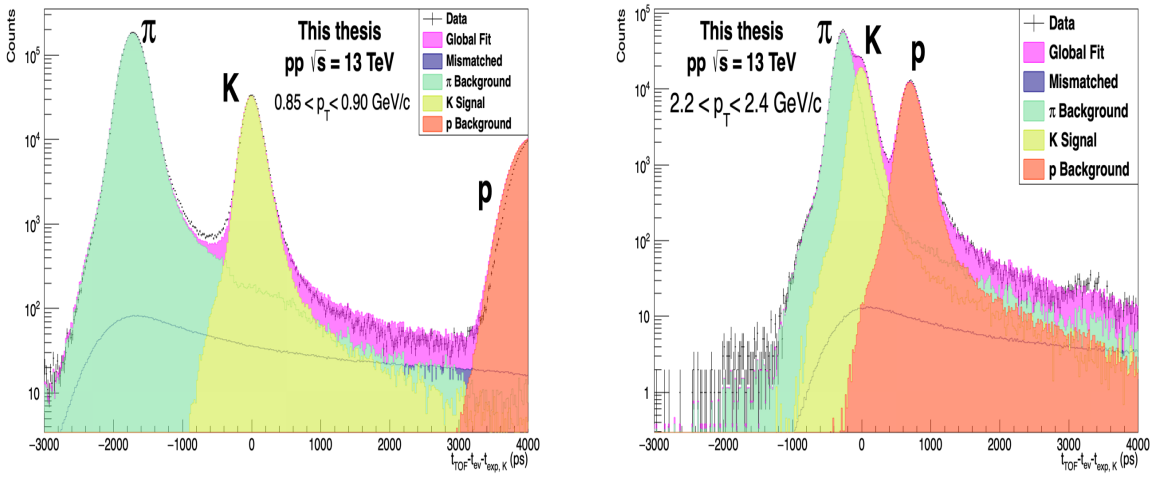

(a) (b)

Fig. 3.14 Fit examples of K to extract the raw yields in (a) low and (b) intermediate p_{T} bins in minimum bias pp collisions. The templates for the three type of particles are shown in a different colour. The mismatched template is shown in the blue line, and the total fit is represented by magenta colour.

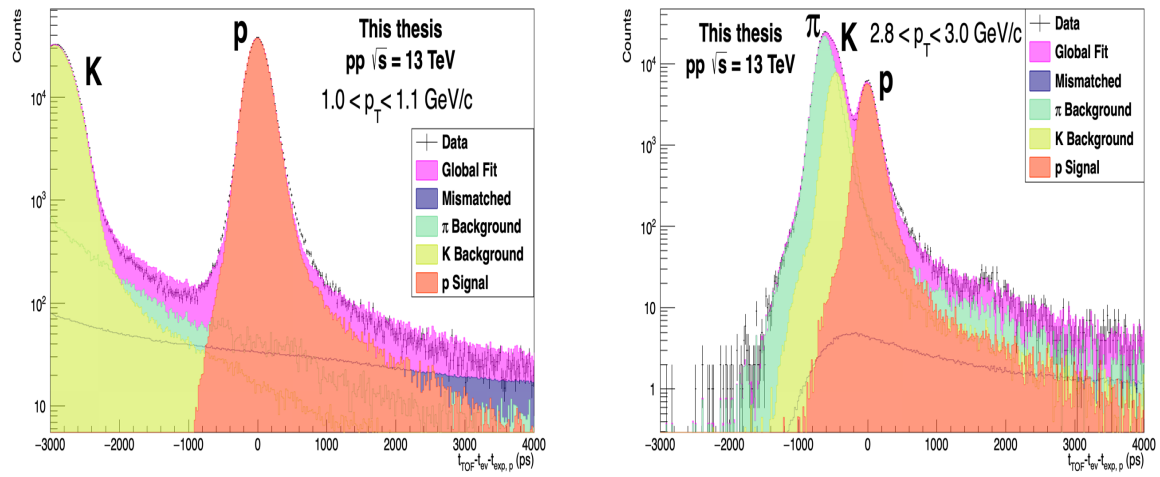

(a) (b)

Fig. 3.15 Fit examples of p to extract the raw yields in (a) low and (b) intermediate p_{T} bin in minimum bias pp collisions. The templates for the three type of particles are shown in a different colour. The mismatched template is shown in the blue line, and the total fit is represented by magenta colour.

3.6.6 Efficiency correction

As already seen in the previous chapter that each detector of ALICE has certain limitations, and hence, it is not possible to detect all the particles produced during the collisions. Further, as the interactions of the particles with the detector medium are stochastic, all the particles that pass through the detector may not create a signal for reconstructable tracks with all necessary track cuts. Therefore, several correction factors are needed to apply that can take care of these limitations to obtain the final corrected spectra of the particle. The efficiency corrections discussed hereunder takes into account of the detector response during the data taking condition as well as the track reconstruction conditions of the particles from the initial to final hits in different detectors. These correction factors are estimated after the application of the track cuts discussed in Table. 3.2. The correction factors are determined from the Monte Carlo simulation and take care of the detector's acceptance as well.

Tracking Efficiency

The tracking efficiency takes into account the fact that all the primary charged particles pass through the TPC detector can't be reconstructed. It is estimated from the Monte Carlo (MC) simulation and is defined as the ratio of the number of primary charged tracks reconstructed to the number of generated primary charged particles within the rapidity region of $|y| < 0.5$ as given in Eq. (3.16). As the reconstruction is done for tracks, that propagate through ITS and TPC detectors, a pseudo-rapidity cut of $|\eta| < 0.8$ also needs to be applied. Further, the tracking efficiency has some dependence on the track cuts used for the analysis, and therefore, the reconstructed tracks for MC simulation have to propagate through the same track cuts as that applied during the reconstruction of the data.

$$Tracking_{efficiency} = \frac{\text{Reconstructed Track}_{\textit{Primary, MC PID, } |\eta| < 0.8, \, |y| < 0.5}}{\text{Generated Particles}_{\textit{Primary, MC PID, } |\eta| < 0.8, \, |y| < 0.5}} \tag{3.16}$$

Along with the track selection cuts mentioned above, the Monte Carlo truth information on the identity of the particles also has to be satisfied for both the generated particles and reconstructed tracks, as the raw spectra are to be corrected for a fraction of primary particles estimated with a data-driven approach as described in Sub-section 3.6.6. The tracking efficiencies, thus obtained, are shown in Fig. 3.16 for $\pi^{\pm}$, $\mathrm{K}^{\pm}$ and $\mathrm{p}(\bar{p})$ for minimum bias (INEL>0) pp collisions at $\sqrt{s} = 13$ TeV. No significant difference could be observed in the tracking efficiency for both positive and negative π & K, whereas for proton and anti-proton, a significant difference could be observed at low momentum ($p_{\mathrm{T}} < 2$ GeV) due to anti-proton absorption in the detector material.

In the thesis, the $\pi^{\pm}$, $\mathrm{K}^{\pm}$ and $\mathrm{p}(\bar{p})$ spectra have been obtained for different V0M multiplicity classes, and hence, the efficiencies also need to be estimated for different multiplicity classes. The p_{T} dependent tracking efficiencies in different multiplicity classes for pions,

kaons and protons are shown in Fig. 3.17. And their ratio to minimum bias pp collisions are shown in Fig. 3.18. From these plots, it is evident that the tracking efficiencies are independent of multiplicity class considered and therefore, multiplicity integrated efficiency has been applied in the raw spectra to obtain the finally corrected spectra with reduced statistical uncertainties.

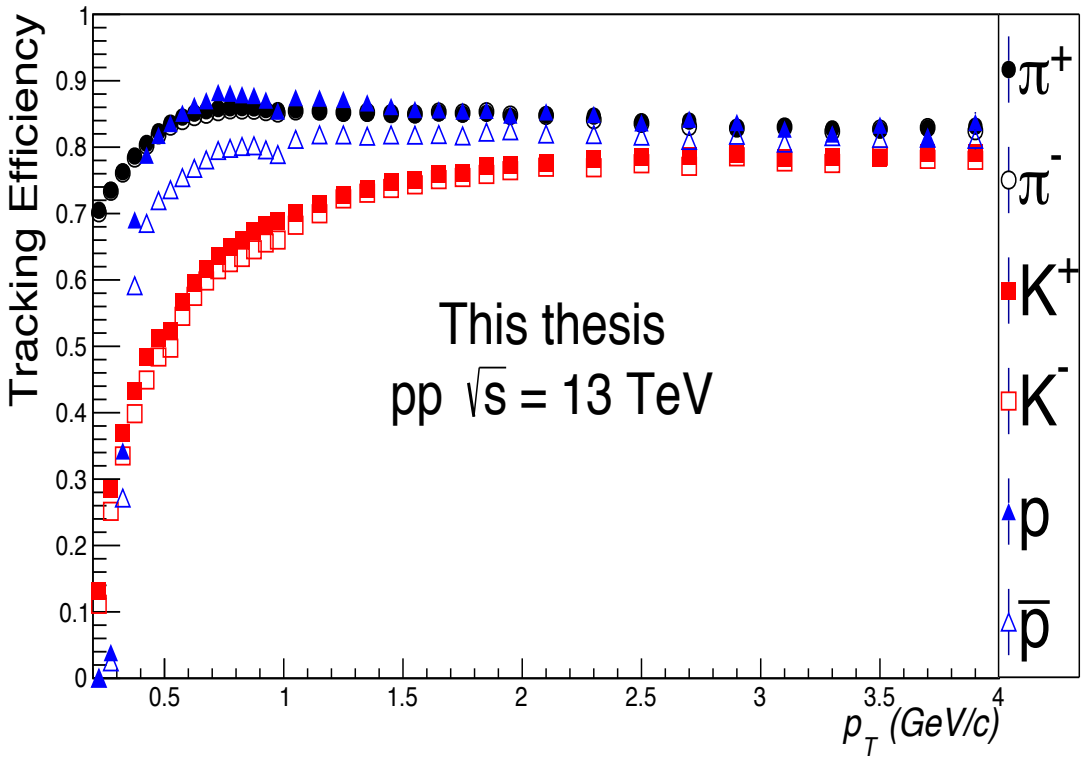

Fig. 3.16 p_{T} dependent tracking efficiencies for pions, kaons and protons in MB (INEL>0) pp collisions at $\sqrt{s} = 13$ TeV.

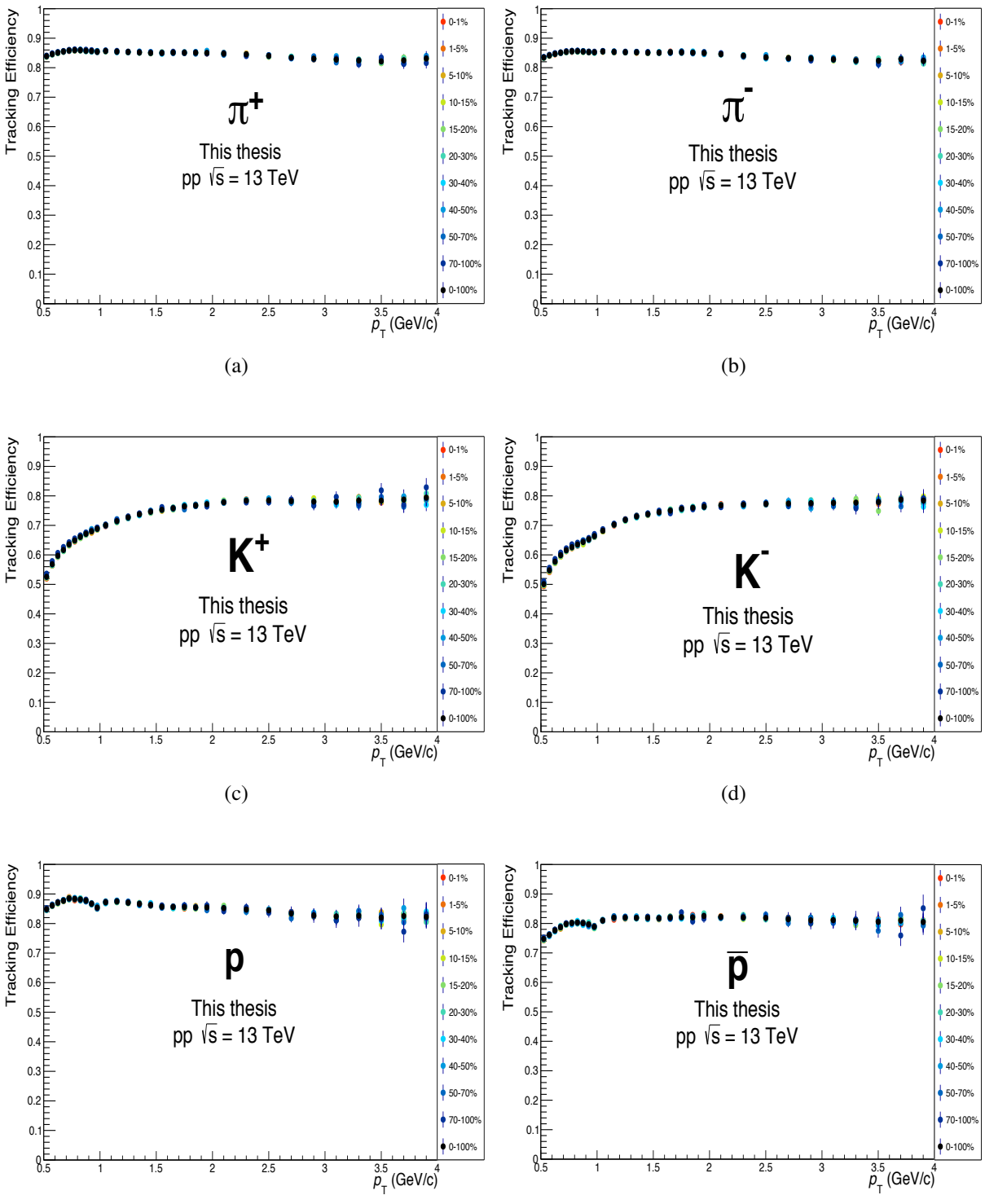

Fig. 3.17 p_{T} dependent tracking efficiencies in different multiplicity classes for (a) π^+, (b) π^-, (c) K^+, (d) K^-, (e) p and (f) $\bar{\mathrm{p}}$ in pp collisions at $\sqrt{s} = 13$ TeV.

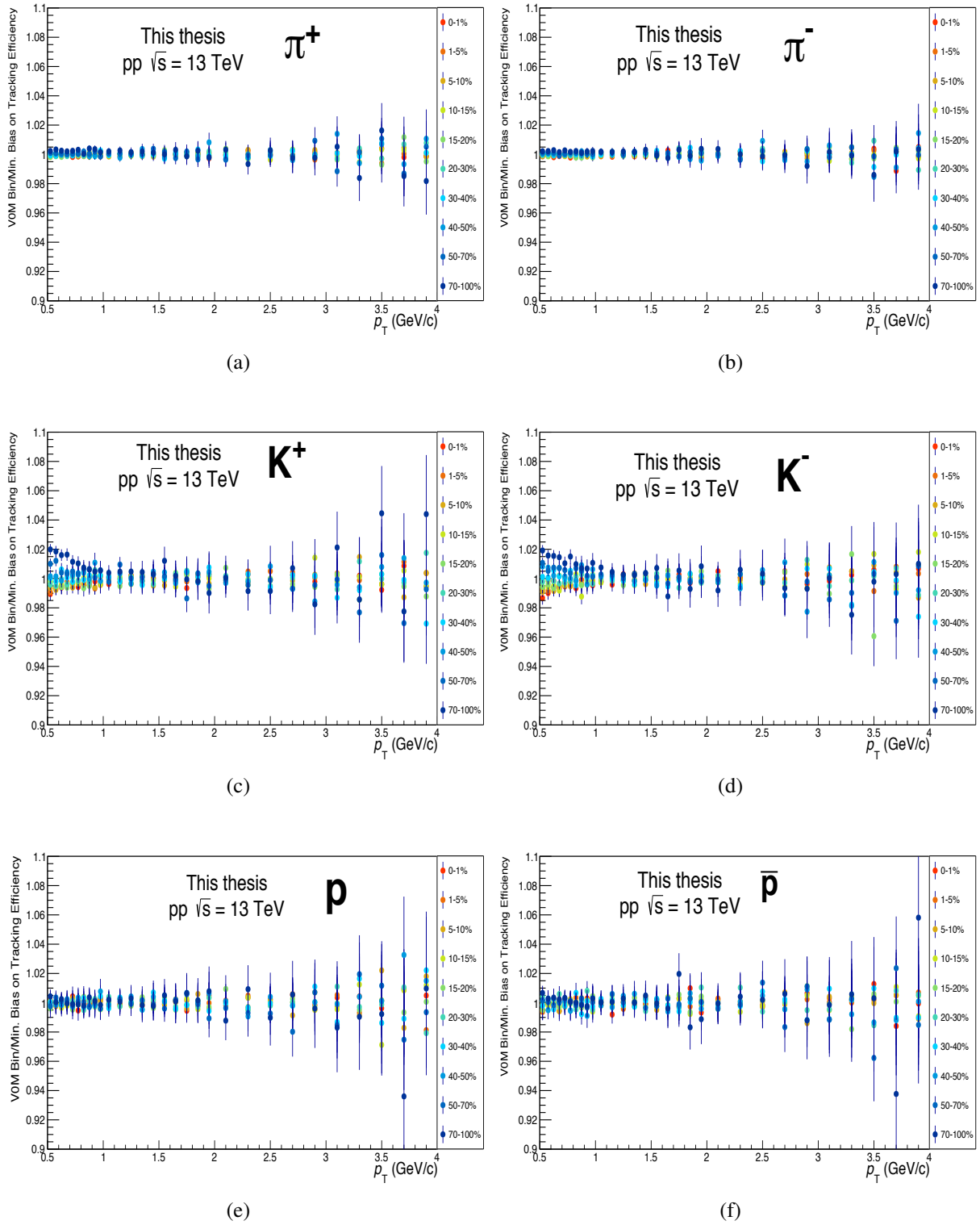

(a) (b)

(c) (d)

(e) (f)

Fig. 3.18 Ratio of V0M bin to the MB tracking efficiency for (a) π^+, (b) π^-, (c) K^+, (d) K^-, (e) p and (f) $\bar{p}$ in different V0M multiplicity classes in pp collisions at $\sqrt{s} = 13$ TeV.

Matching Efficiency

The matching efficiency takes account of the fact that all the reconstructed track in the TPC can't be matched with the corresponding tracks of TOF detector. It is estimated by considering the ratio between the tracks matched with the TOF detector to the total number of reconstructed tracks in the TPC detector and is given by Eq. (3.17).

$$Matching_{efficiency} = \frac{\text{Tracks matched with TOF}_{\textit{Primary, MC PID, } |\eta| <0.8, \, |y| <0.5}}{\text{All reconstructed track}_{\textit{Primary, MC PID, } |\eta| <0.8, \, |y| <0.5}} \tag{3.17}$$

During propagation of particle from the TPC to TOF, some particles tracks get lost due to the geometrical acceptance of the detector, weak decay of unstable particles and interaction of the particles with detector material. Further, the tracks reaching the TOF detector should have an associated TOF signal. The matching efficiency takes account of all these facts, and the estimated efficiencies for different types of particles are shown in Fig. 3.19. The matching efficiency is observed to be similar for positive and negative pions whereas, for positive & negative kaons and protons, it seems different at low p_{T} due to the absorption of the particle in the detector material located between the TPC and TOF detector. Further, the matching efficiency increases with the increase of p_{T} and at high p_{T}, the matching efficiency of all light flavoured particles are found to be more or less same.

The p_{T} dependent matching efficiencies in different multiplicity classes for pions, kaons and protons are shown in Fig. 3.20 and their ratios to minimum bias pp collisions are shown in Fig. 3.21. The multiplicity integrated matching efficiency has been applied in the raw spectra to obtain the finally corrected spectra with reduced statistical uncertainties as the dependence of matching efficiency on the multiplicity is also quite small.

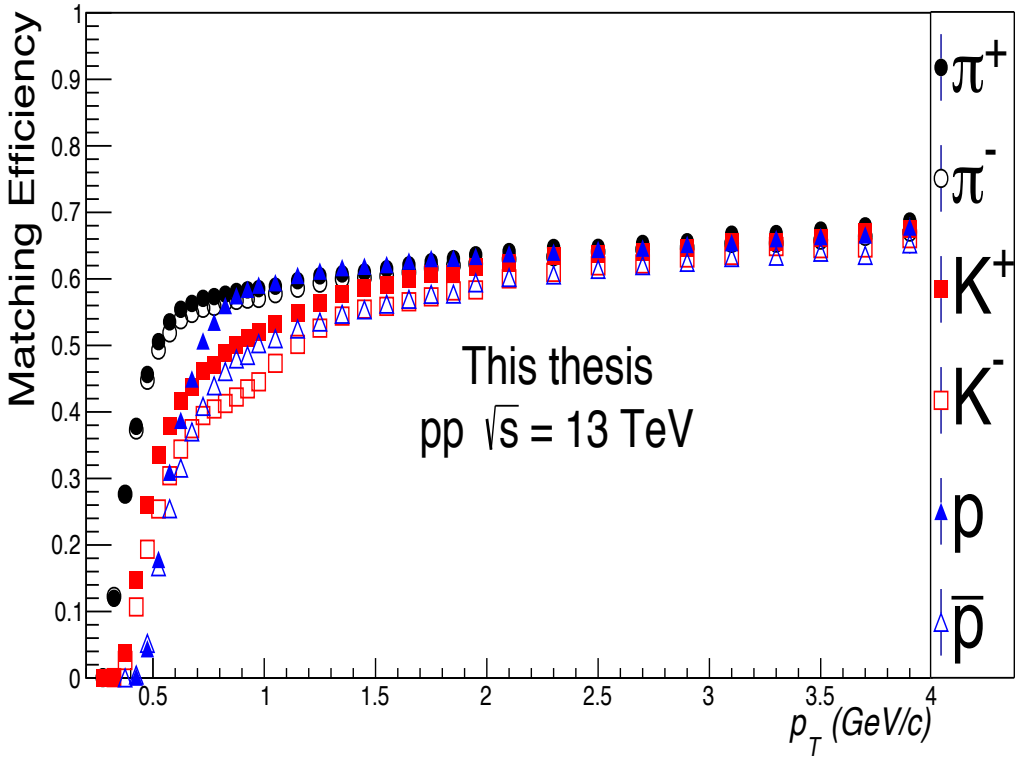

Fig. 3.19 p_{T} dependent matching efficiencies for pions, kaons and protons in MB (INEL>0) pp collisions at $\sqrt{s} = 13$ TeV.

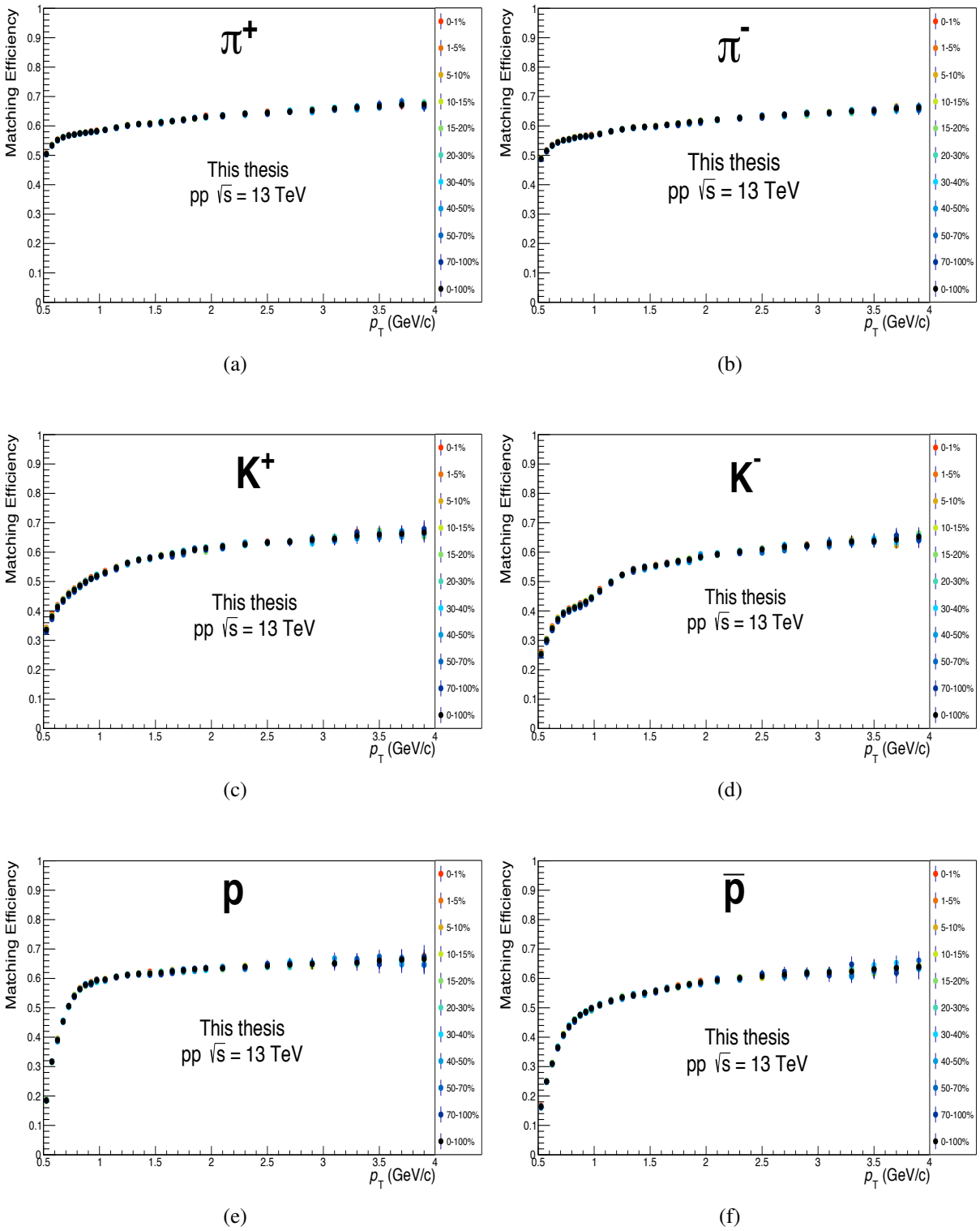

(a) (b)

(c) (d)

(e) (f)

Fig. 3.20 p_{T} dependent matching efficiencies in different multiplicity classes for (a) π^+, (b) π^-, (c) K^+, (d) K^-, (e) p and (f) $\bar{\mathrm{p}}$ in pp collisions at $\sqrt{s} = 13$ TeV.

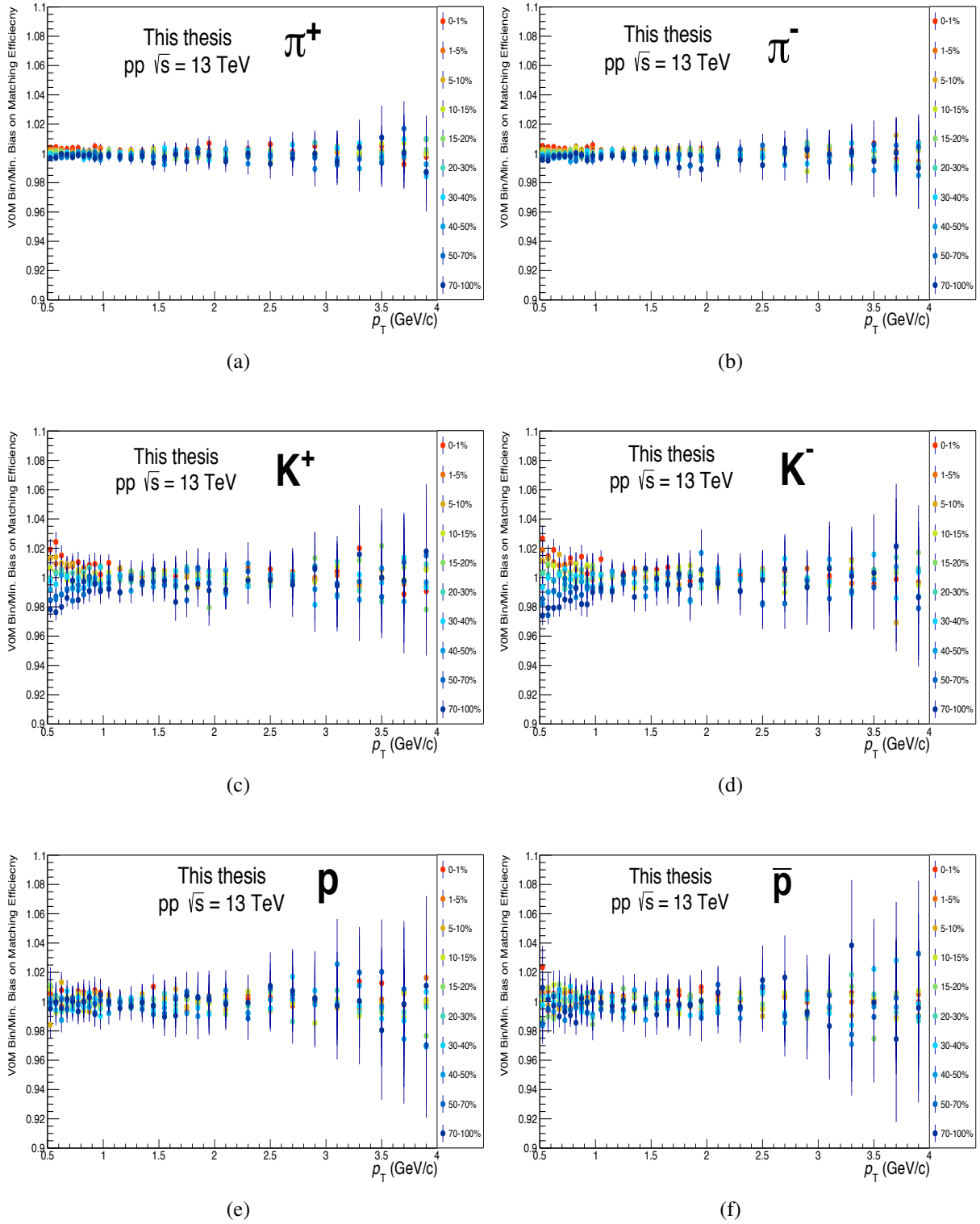

(a) (b)

(c) (d)

(e) (f)

Fig. 3.21 Ratio of V0M bin to the MB matching efficiency for (a) π^+, (b) π^-, (c) K^+, (d) K^-, (e) p and (f) $\bar{p}$ in different V0M multiplicity classes in pp collisions at $\sqrt{s} = 13$ TeV.

Geant Fluka correction

It could be observed from the tracking and matching efficiencies that the GEANT3 transport code use in the AliRoot analysis framework is unable to reproduce the correct description of the interactions cross-section with the material for anti-proton and negative kaons at the low transverse momentum. Therefore, GEANT3 provide an inaccurate parameterisation of the energy loss in the material. However, it is possible to overcome the incorrect parameterisation of the tracking and matching efficiency by using a comparison between GEANT3/FLUKA for K^- and GEANT3/GEANT4 for $\bar{p}$ to describe the interaction of particle accurately. Various types of correction factors used in this thesis are shown in Fig. 3.22. The correction factor for the tracking efficiency of anti-protons is parameterised by a function 1- 0.0129$\times$ Exp(-$p_T\times$ 0.676) and for negative kaons, it is described by the function 0.97 + 0.011 $\times p_T$. The matching efficiency correction factor for K^- is taken from a previous analysis [190].

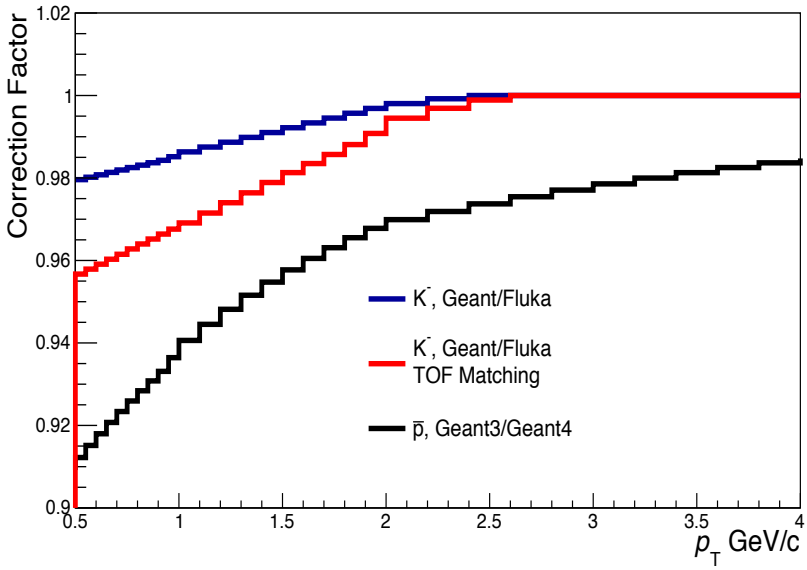

Fig. 3.22 GEANT/FLUKA correction factors for K^- and $\bar{p}$.

Primary fraction (Feed-down correction)

To measure the spectra of the primary charged particles, tracks whose primary vertex lies inside the distance of the closest approach in the xy plane (DCA_{xy}) as mentioned in the Eq. (3.7) are only selected. This DCA_{xy} cut can remove most of the tracks of secondary particles; however, non-zero contributions from these particles still remain in the raw spectra. The contamination from secondary particles such as weak decay and material knock out particles which are not removed by the application of the DCA_{xy} cuts are eliminated by estimating the fraction of the primary particles and using these factors to correct the spectra. A data-driven method has been used to calculate the fraction of primary particles. At first step, the DCA_{xy} cut is removed from the standard track selection cuts, and the DCA_{xy} distributions are obtained for data in each p_{T} bins. A similar procedure is also applied for the Monte Carlo reconstructed tracks to get the template distributions for primary particles as well as for secondary particles from weak decay and material knock out particles. In the case of pions, the template distribution of material knock out is not required as the number of such particles will be negligible. The contribution of the material knock-out particles is significant for protons, and the effect is more pronounced for low p_{T} particles. After obtaining the template distributions, in each p_{T} bin, the DCA_{xy} distribution of data is fitted with the 2 or 3 component global fit to estimate the fraction of primary particles in each bin. The 2 component fits are performed of $\pi^{\pm}$, $\bar{p}$ and the 3 component fits are performed for p at low p_{T}. The primary fraction correction factor for $\mathrm{K}^{\pm}$ is negligible and therefore, is not considered in the thesis.

The DCA_{xy} distributions of identified particles in data are obtained by applying a cut of 2σ for each particle on the combined TPC and TOF signal as given by Eq. (3.18).

$$\sigma_{TPC-TOF,i} = \sqrt{\sigma^2_{TPC,i} + \sigma^2_{TOF,i}} \tag{3.18}$$

Some example plots of the combined TPC and TOF signal for pions and protons in two different p_{T} bins with and without $\sigma_{TPC-TOF,i}$ cuts are shown in Figs. 3.23 and 3.24, respectively.

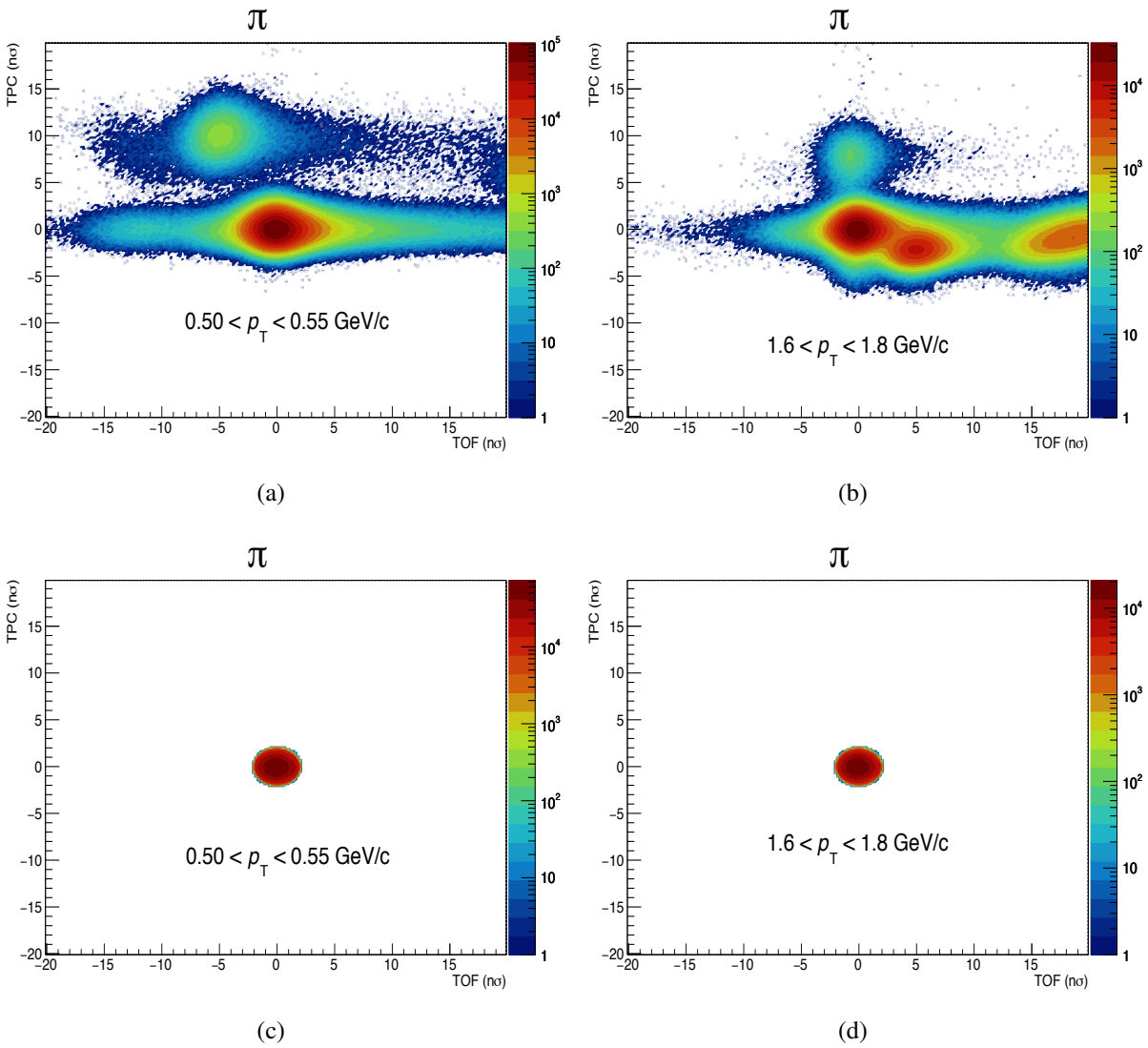

Fig. 3.23 The combined TPC and TOF particle identification separation power for pions in two different p_{T} bins. (a), (b) without any cut on $\sigma_{TPC-TOF,\pi}$ and (c), (d) with a 2σ cut on $\sigma_{TPC-TOF,\pi}$.

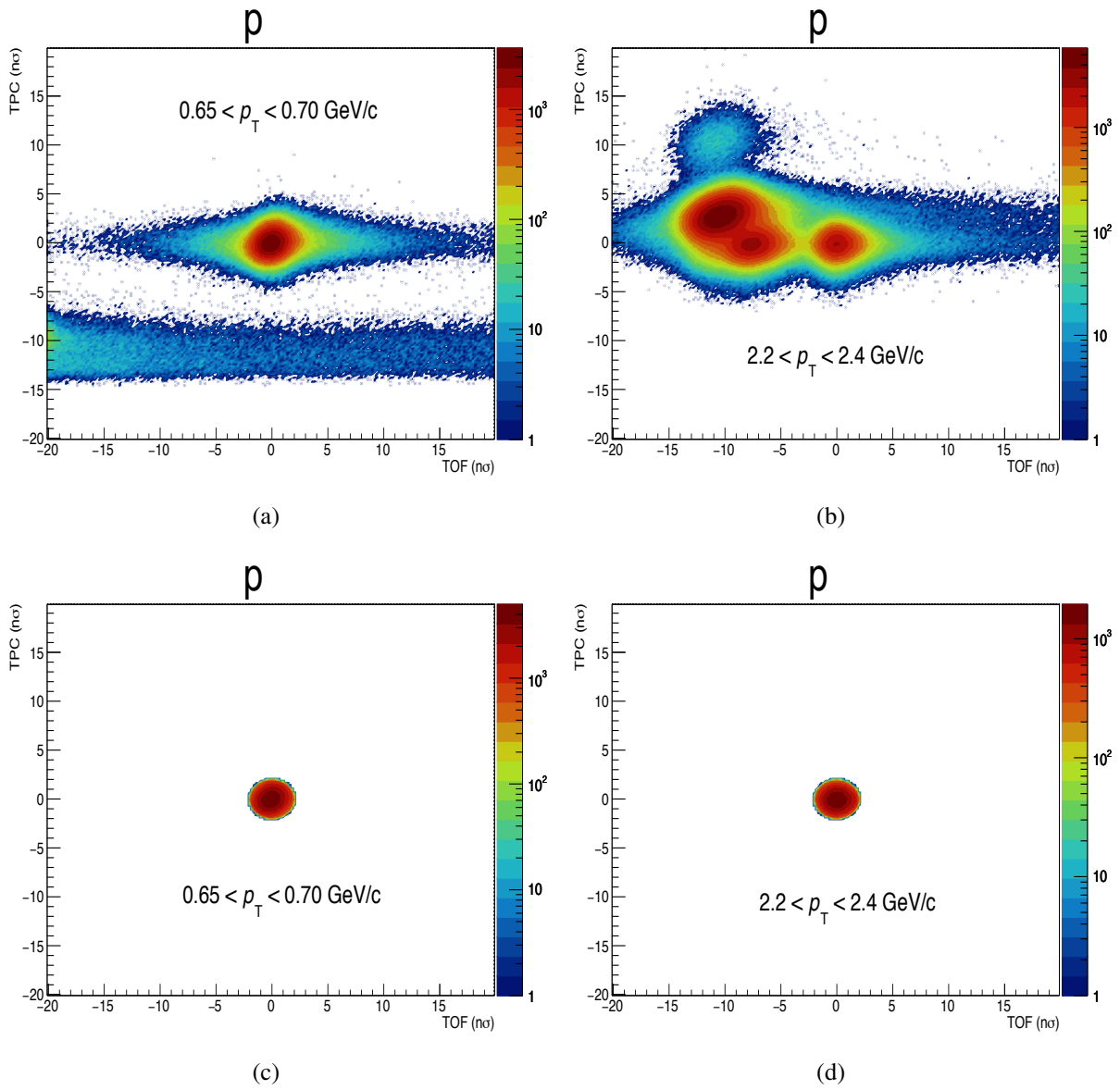

Fig. 3.24 The combined TPC and TOF particle identification separation power for protons in two different p_{T} bins. (a), (b) without any cut on $\sigma_{TPC-TOF,p}$ and (c), (d) with a 2σ cut on $\sigma_{TPC-TOF,p}$.

On the other hand, for MC templates, the distributions are obtained by applying pure MC truth information on the particles. The fractions of primary particles are obtained by fitting the data and template DCA$_{xy}$ distributions with the help of the TFractionFitter class to unfold various components of the distributions. And then, the relative fraction of primaries are estimated by integrating the fit results to the region of primary tracks selection criteria, i.e. DCA$_{xy} < 7\sigma$.

The example plots of the DCA$_{xy}$ distributions of particles in data, the templates for primary, secondary particle and the fit results are shown in Figs. 3.25, 3.26 and 3.27 for π^+, p and $\bar{\text{p}}$, respectively. As the π^+ and π^- results are similar hence the fit results for π^+ are only shown in the figure.

The fractions of primary for pions and protons estimated from the fits are shown in Fig. 3.28.

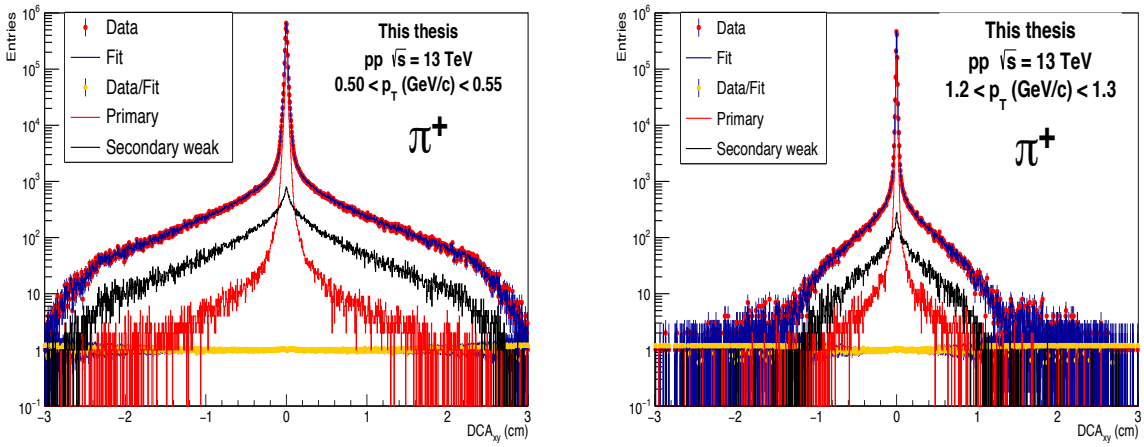

(a) (b)

Fig. 3.25 Examples of DCA$_{xy}$ distributions of pions for data, primary particles and secondary particles from weak decay are shown in two different p_{T} bins. The fit result for π^+ is also shown.

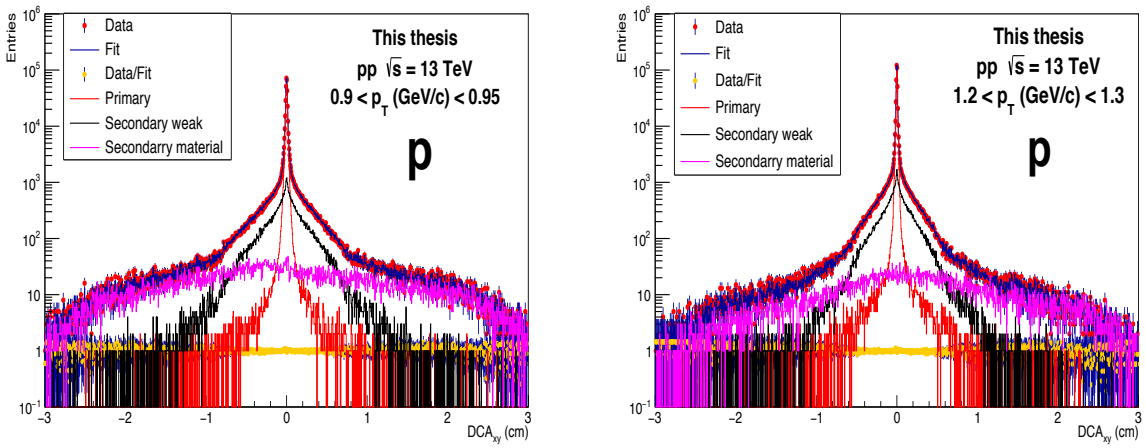

(a) (b)

Fig. 3.26 Examples of DCA$_{xy}$ distributions of protons for data, primary particles, secondary particles from weak decay and material knock-out are shown in two different p_{T} bins. The fit result for p is also shown.

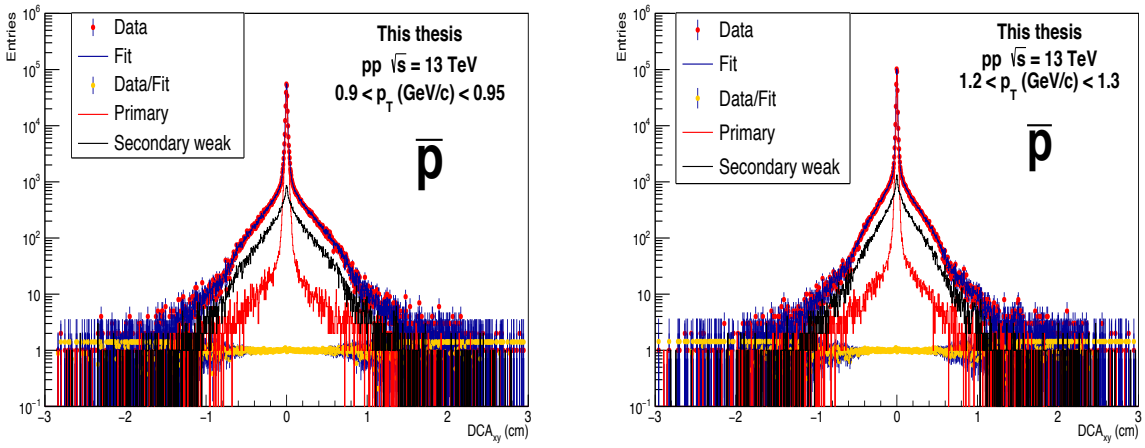

(a) (b)

Fig. 3.27 Examples of DCA$_{xy}$ distributions of anti-proton for data, primary particles and secondary particles from weak decay are shown in two different p_{T} bins. The fit result for $\bar{\mathrm{p}}$ is also shown.

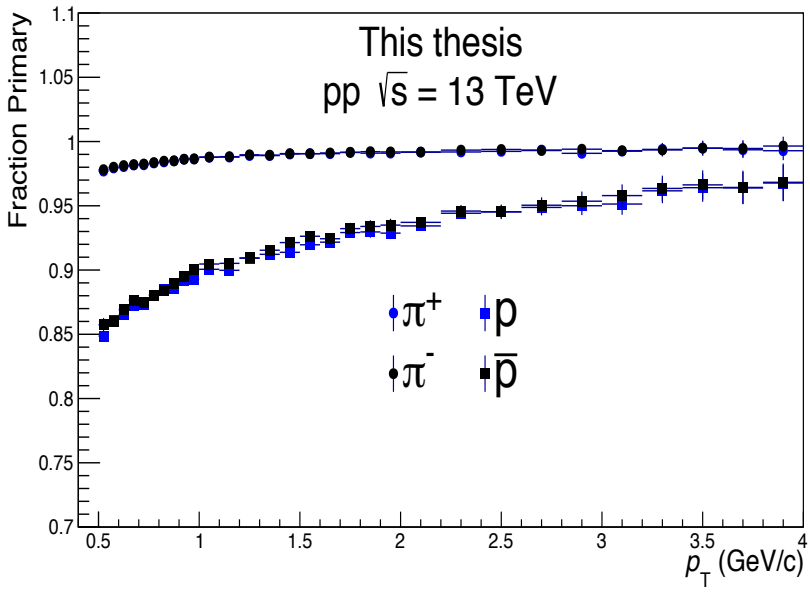

Fig. 3.28 The fraction of primary particles for pions and protons obtained from the fit results of the DCA_{xy} distributions.

3.6.7 Corrected p_{T} spectra

The final p_{T} spectra of different identified particles are estimated by correcting the raw yields obtained from the template fits with various correction factors such as tracking efficiency, matching efficiency, feed-down correction and GEANT/FLUKA correction as discussed above. Further, the p_{T} spectra are also normalised to the number of events analysed in each multiplicity class. These correction factors are applied as given in Eq. (3.19).

$$\frac{\mathrm{d}^2\mathrm{N}}{\mathrm{d}y\mathrm{d}p_{\mathrm{T}}} = \frac{1}{N_{ev}} \times \frac{\text{Raw Yield}}{Tracking_{Efficiency} \times Matching_{Efficiency}} \times \text{Fraction Primary} \tag{3.19}$$

The obtained corrected p_{T} spectra for pions, kaons and protons in different charged-particle multiplicity classes are shown in Fig. 3.29.

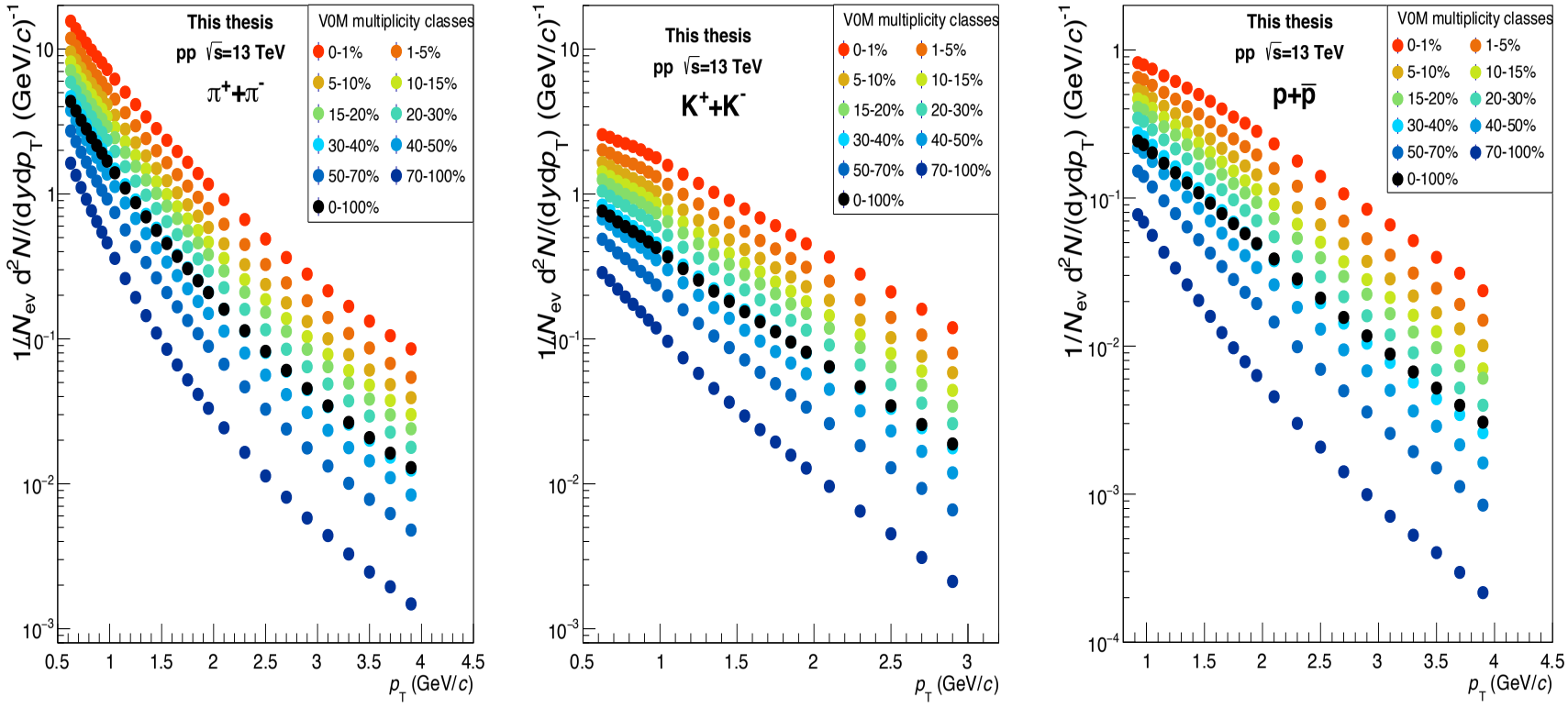

(a) (b) (c)

Fig. 3.29 Final corrected p_{T} spectra of (a) pions, (b) kaons and (c) protons in different V0M multiplicity classes identified with TOF detector.

3.6.8 Systematic uncertainty

A systematic uncertainty in measurement or quantity derived from the set of measurement is the possible unknown variation, that does not randomly vary from point to point. These uncertainties arise mainly due to the imperfects modelling or simulation, lack of understanding of the experiment, uncertainty associated with different correction and parameter involved etc. in the experiment or during the data analysis.

In this thesis, the systematic uncertainty of pions, kaons and protons are originated from the sources given below:

- Track cut
- Particle identification (PID) technique
- Pile-up selection cut
- TPC-TOF matching

Systematic uncertainty due to track cuts (σ_{sys}^{track}):

To estimate the systematic uncertainty for the track selection criteria, a particular parameter of the standard track cut listed in Table. 3.2 is varied to a higher and lower values for both data, and Monte Carlo reconstructed tracks. Then the raw yields from the data and different correction factors from the MC simulation are obtained. At last, the final corrected spectra are estimated for each particle type for both higher and lower values of the track cuts. The difference between the ratio of spectra of higher to standard and lower to the standard are considered as systematic uncertainty for that particular type of track cuts. The same method has also been applied for other track selection parameters. The track cuts used for the systematic uncertainty study are listed in Table 3.3.

Table 3.3 Track cut variation used for the studies of systematic uncertainty.

Track cuts	Default value	Higher value	Lower value
Min. no of TPC Crossed rows	70	80	60
Track χ^2/TPC$_{Cluster}$	4	5	3
DCA$_Z$ (cm)	2	3	1
DCA$_{XY}$ (cm)	7σ (given by eq (3.7))	8σ	6σ

The variation of spectra due to the variation of different track cut parameters to the standard one in multiplicity integrated class for pions, kaons and protons are shown in Figs. 3.30, 3.31 and 3.32, respectively.

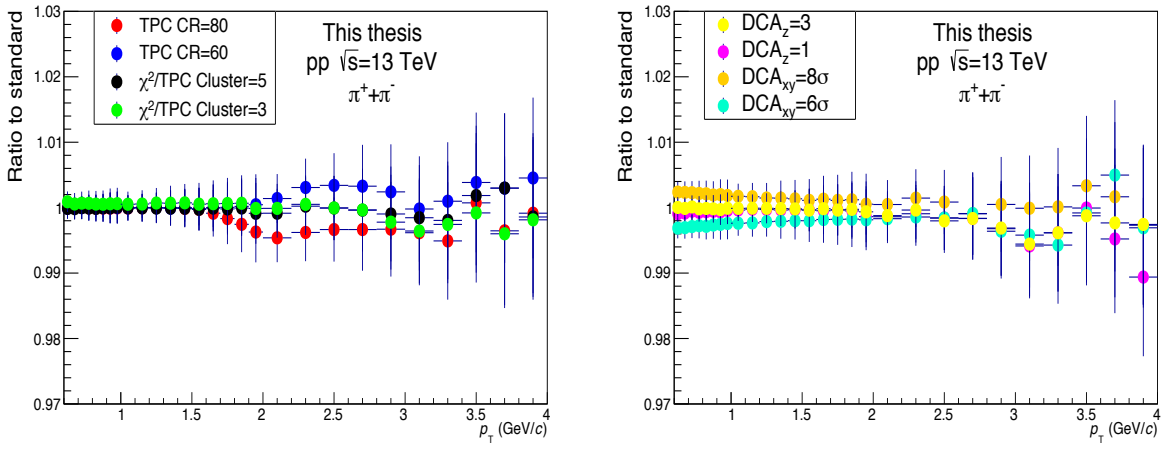

(a) (b)

Fig. 3.30 Ratio of the pions p_{T} spectra obtained with varied track cuts parameters to that of the standard track cuts selection in minimum bias pp collisions at $\sqrt{s} = 13$ TeV.

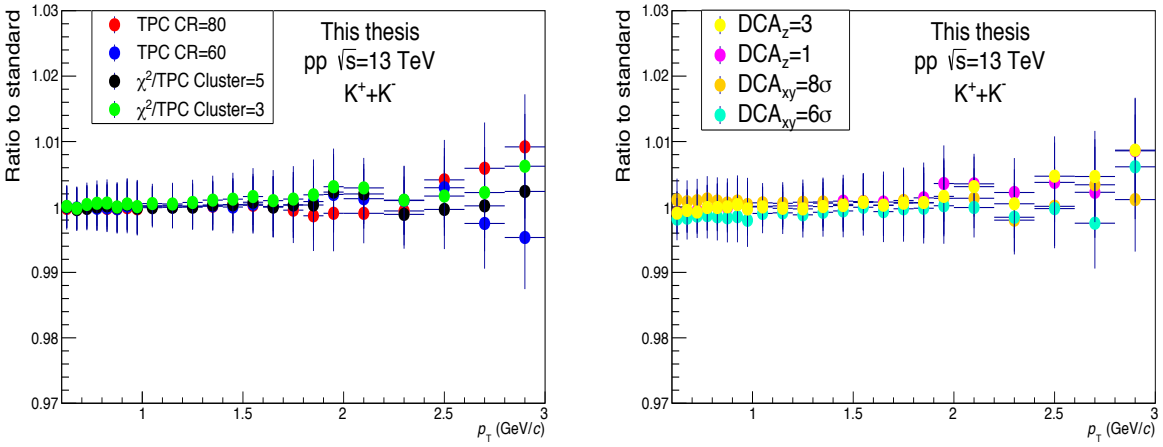

(a) (b)

Fig. 3.31 Ratio of the kaons p_{T} spectra obtained with varied track cuts parameters to that of the standard track cuts selection in minimum bias pp collisions at $\sqrt{s} = 13$ TeV.

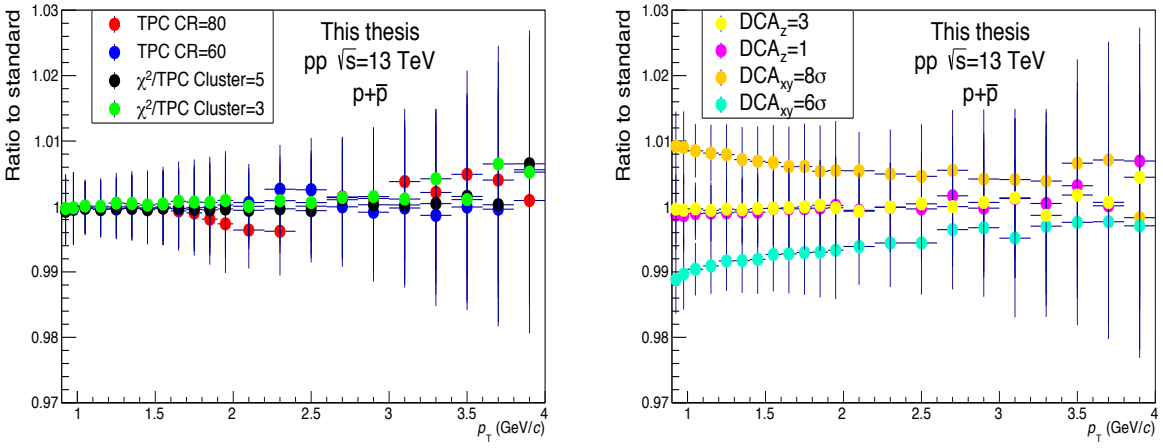

(a) (b)

Fig. 3.32 Ratio of the protons p_{T} spectra obtained with varied track cuts parameters to that of the standard track cuts selection in minimum bias pp collisions at $\sqrt{s} = 13$ TeV.

Systematic uncertainty due to particle identification (PID) with TOF detector (σ_{sys}^{PID}):

The uncertainty arises due to the particle identification with the TOF detector, affect only the raw spectra. To estimate the systematic uncertainty for PID, parameters such as standard deviation (σ) and slope (s) of the standard TOF signal function as given in Eq. (3.10), are varied simultaneously by $\pm$ 10% to construct the templates. The obtained templates are then used to fits the data time-of-flight difference distributions and to extract the raw yield of the particles. The highest variations of spectra due to the variation of different PID parameters to the standard one are considered as the systematic uncertainty. Some representative plots on the variation of the spectra with the variation of different PID parameters in multiplicity integrated classes for pions, kaons and protons are shown in Figs. 3.33(a), 3.34(a) and 3.35(a), respectively.

Systematic uncertainty due to pile-up events (σ_{sys}^{pileup}):

In this thesis, the systematic uncertainty arising due to the pileup events are also taken into account. In the standard pileup events selection, the multiplicity dependent pileup events selection cuts are used which have different no of SPD vertex contributors depending on the number of tracks. For the estimation of systematic uncertainty, the no of primary vertex contributions in the SPD are varied to fixed values 5 & 3, and their difference to the standard one is considered. The ratio of the varied pileup parameter spectra to the standard one in multiplicity integrated class for pions, kaons and protons are shown in Figs. 3.33(b), 3.34(b) and 3.35(b), respectively.

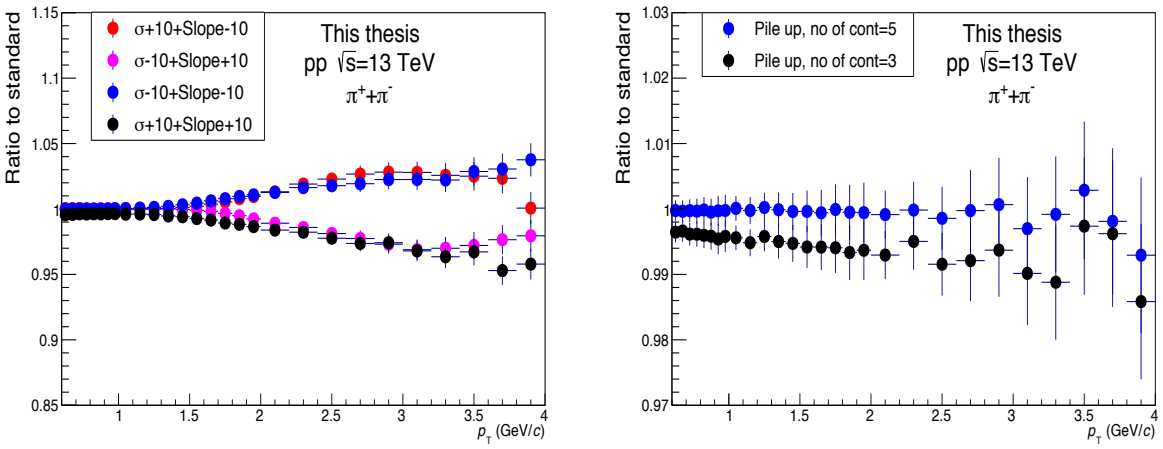

(a) (b)

Fig. 3.33 The ratio of the pions p_{T} spectra obtained with varied (a) PID parameters and (b) pile up selection cuts to standard one in minimum bias pp collisions at $\sqrt{s} = 13$ TeV.

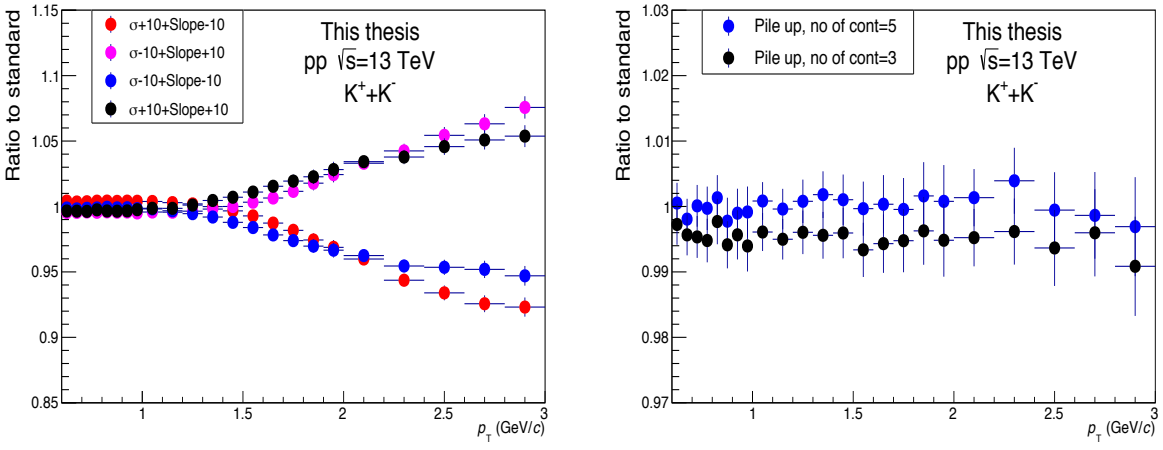

(a) (b)

Fig. 3.34 The ratio of the kaons p_{T} spectra obtained with varied (a) PID parameters and (b) pile up selection cuts to standard one in minimum bias pp collisions at $\sqrt{s} = 13$ TeV.

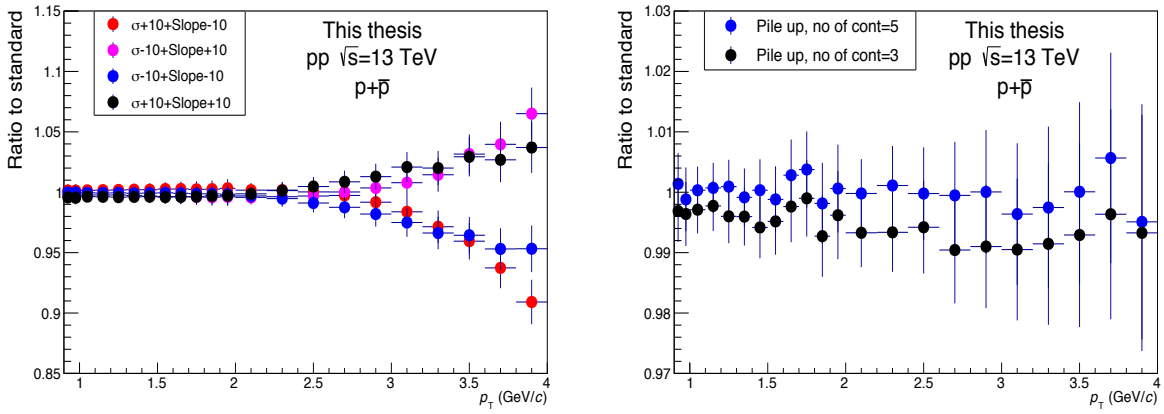

(a) (b)

Fig. 3.35 The ratio of the protons p_{T} spectra obtained with varied (a) PID parameters and (b) pile up selection cuts to that of the standard one in minimum bias pp collisions at $\sqrt{s} = 13$ TeV.

Systematic uncertainty due to TPC-TOF matching efficiency ($\sigma_{sys}^{match\ eff}$):

The matching of the track from TPC to TOF cluster during the track reconstruction process is also considered as another source of systematic uncertainty. As the procedure for the estimation of this uncertainty is much complicated and does not vary with colliding energy, the uncertainty for TPC-TOF matching for pions, kaons and protons are taken from previously obtained results at pp collisions at $\sqrt{s} = 7$ TeV [191]. The systematic uncertainties are 3, 6 and 4% for pions, kaons and protons, respectively and are constant over the studied p_{T} range.

Total systematic uncertainty (σ_{sys}^{total}):

The contributions of the systematic uncertainties as described above, are added in quadrature as given by Eq. (3.20) to obtain the total systematic uncertainty. The total systematic uncertainty as well the contributions from other sources for pions, kaons and protons in some selected multiplicity classes are shown in Figs. 3.36, 3.37 and 3.38, respectively.

$$\sigma_{sys}^{total} = \sqrt{(\sigma_{sys}^{track})^2 + (\sigma_{sys}^{PID})^2 + (\sigma_{sys}^{pileup})^2 + (\sigma_{sys}^{match\ eff})^2} \tag{3.20}$$

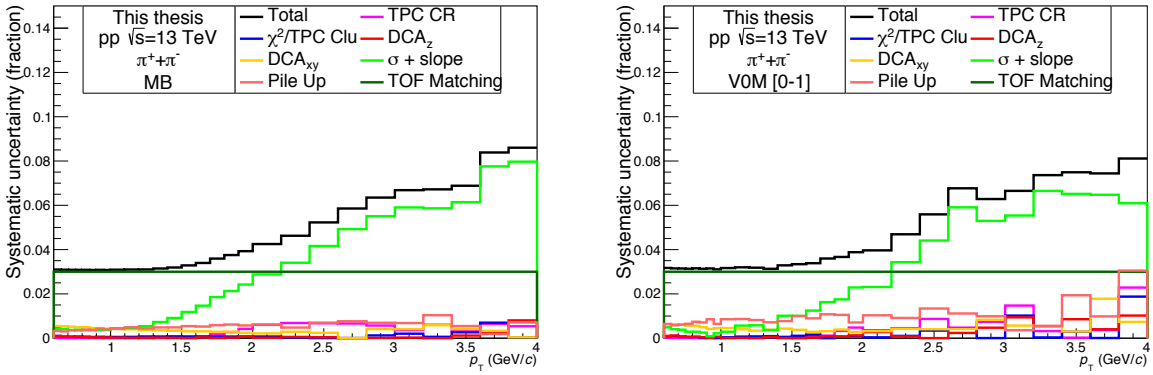

(a)

(b)

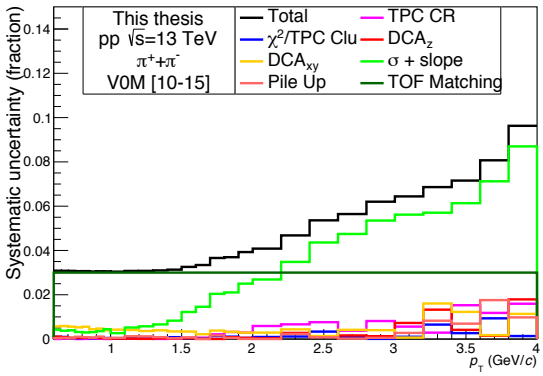

(c)

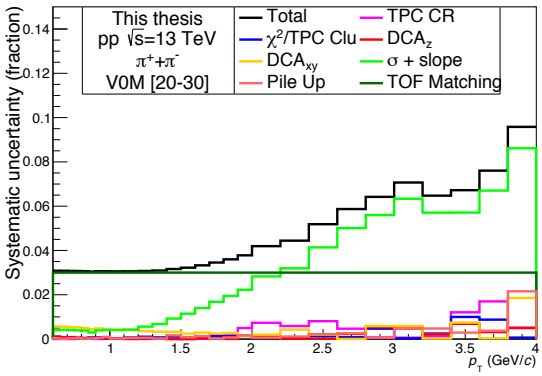

(d)

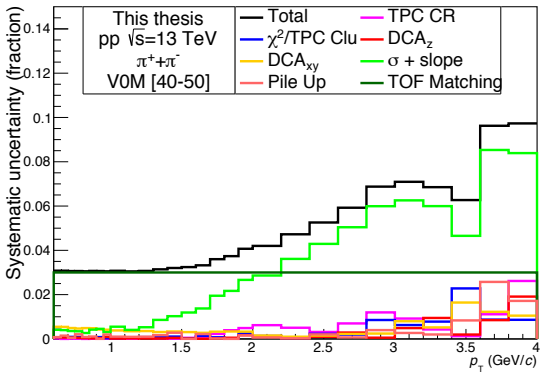

(e)

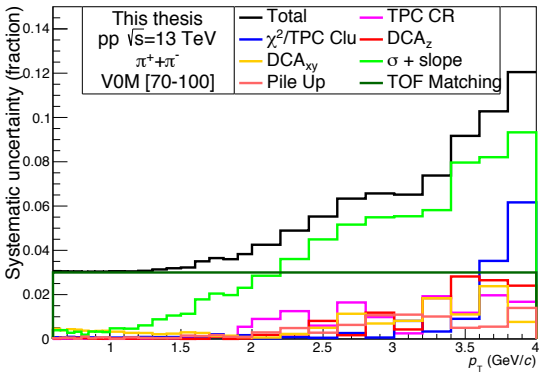

(f)

Fig. 3.36 Systematic uncertainty from different sources as well as the total uncertainties are shown for pions in (a) MB, (b) 0-1%, (c) 10-15%, (d) 20-30%, (e) 40-50% and (f) 70-100% V0M multiplicity classes.

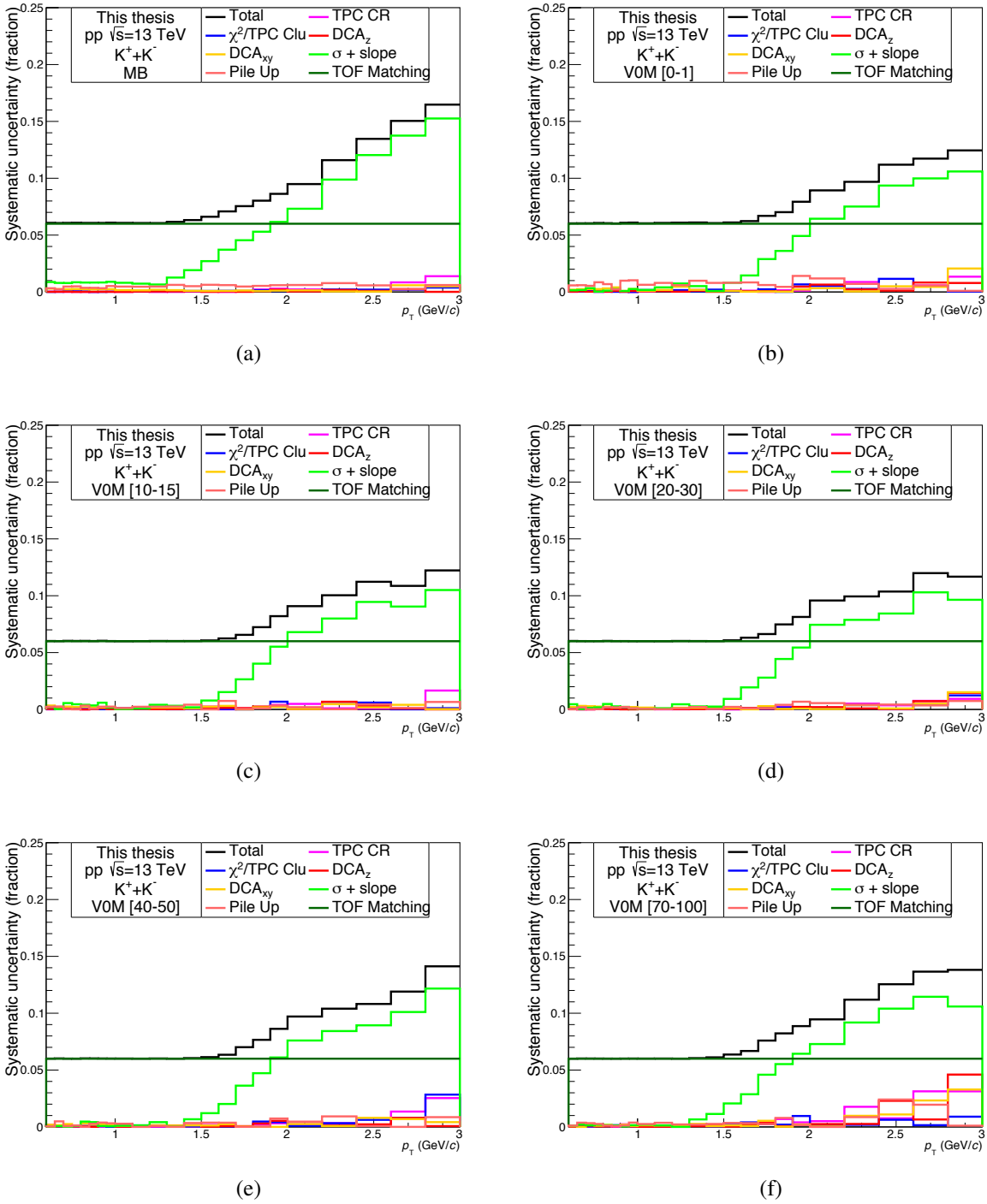

Fig. 3.37 Systematic uncertainty from different sources as well as the total uncertainties are is shown for kaons in (a) MB, (b) 0-1%, (c) 10-15%, (d) 20-30%, (e) 40-50% and (f) 70-100% V0M multiplicity classes.

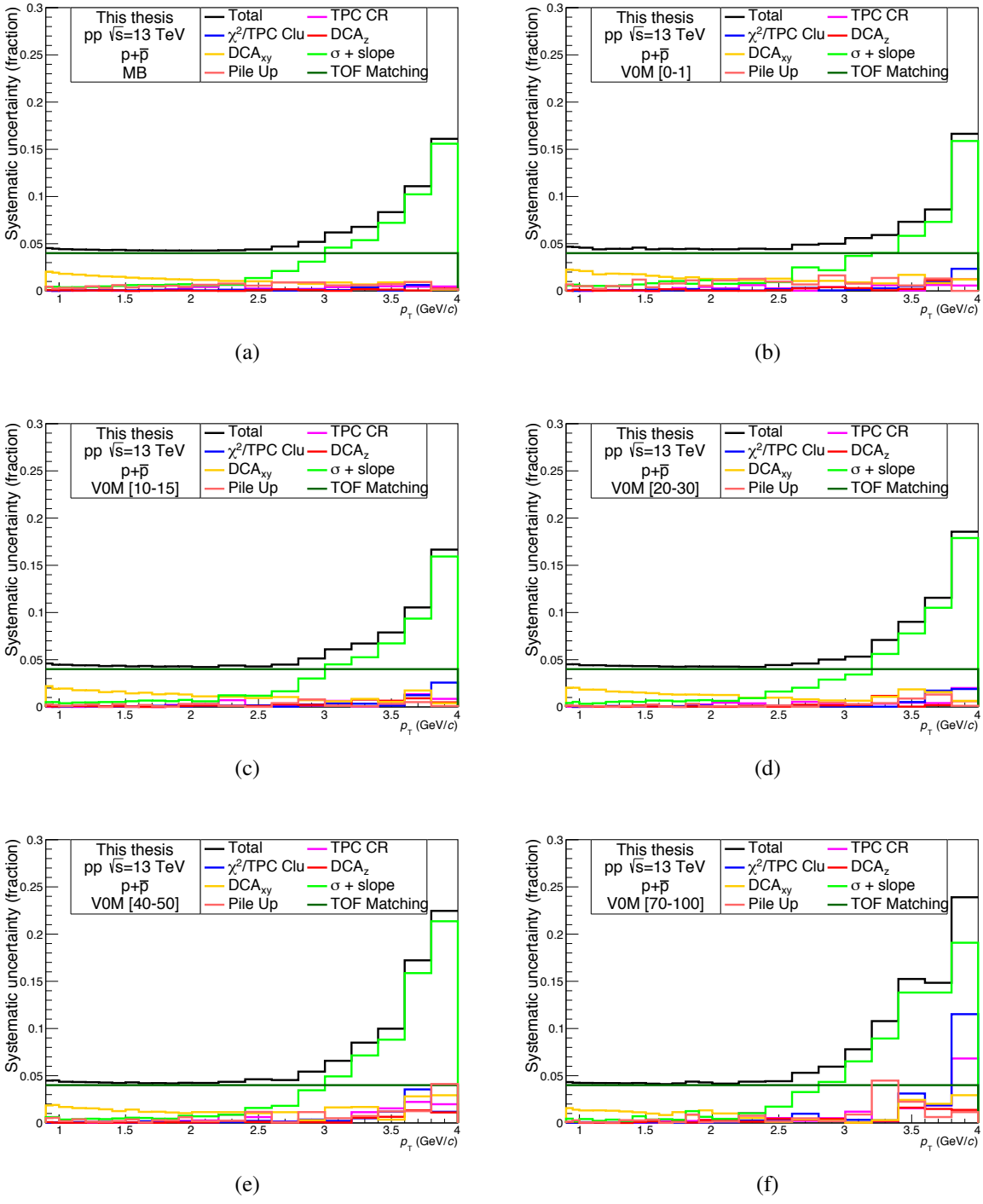

Fig. 3.38 Systematic uncertainty from different sources as well as the total uncertainties are shown for protons in (a) MB, (b) 0-1%, (c) 10-15%, (d) 20-30%, (e) 40-50% and (f) 70-100% V0M multiplicity classes.

Furthermore, some other sources of systematic uncertainty which are more or less common to other detectors/techniques analysis and the uncertainty values are standard for pp collisions at $\sqrt{s} = 13$ TeV are also added (in quadrature) in the final combined p_{T} spectra. The following common sources of systematic uncertainty are considered in this analysis.

- Material budget (TPC-TOF): p_{T}-dependent (low$-$high p_{T} values):- (0.5$-$0.2%) for π, (1.5$-$0.4%) for K and (2.9$-$0.1%) for p.
- Hadronic interaction: p_{T}-dependent (low$-$high p_{T} values):- (2$-$2.4%) for π and (2.7$-$1.8%) for K; p_{T}-independent:- 1 (3.6)% for p ($\bar{\mathrm{p}}$).
- ITS-TPC matching efficiency: p_{T}-dependent (low$-$high p_{T} values):- (0.7$-$2.9%) for π, K and p
- Signal loss correction: p_{T}-independent:- 0.2% for π, 1% for K and 3.3% for p.

Uncorrelated systematic uncertainty

As this thesis focuses on the p_{T} spectra as a function of event multiplicity, it is crucial to study the amount of uncorrelated systematic uncertainty across different multiplicity classes. The uncorrelated systematic uncertainties are estimated by taking the difference between the spectral ratio (V0M multiplicity class to minimum bias) after the variation of the parameter to the standard one. Different sources of uncorrelated systematic uncertainty for π, K and p in some selected multiplicity classes are shown in Figs. 3.39, 3.40, & 3.41, respectively for pp collisions at $\sqrt{s} = 13$ TeV.

3.6.9 Systematic uncertainty on K/π and p/π ratios

The particle ratios are estimated by dividing the final corrected p_{T} spectra of kaons and protons, by pions in each multiplicity class. The systematic uncertainties related to particle ratios are evaluated by considering the differences of the particle ratio between the varied

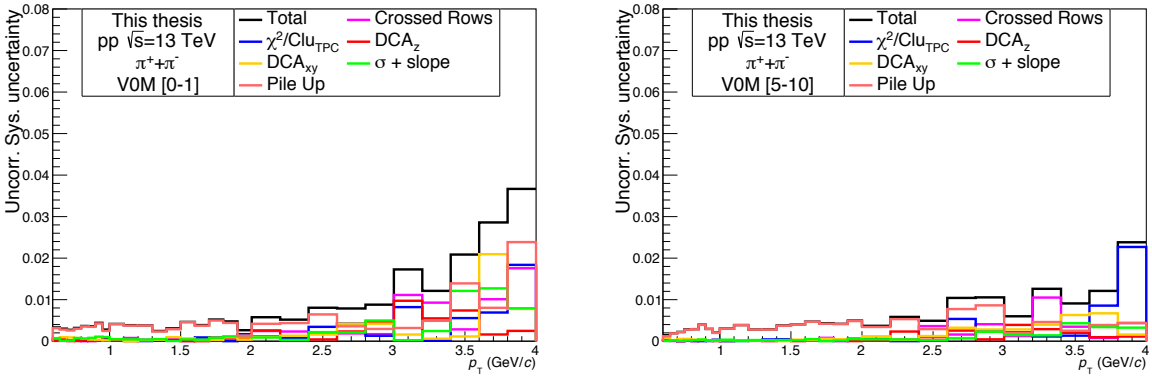

(a)

(b)

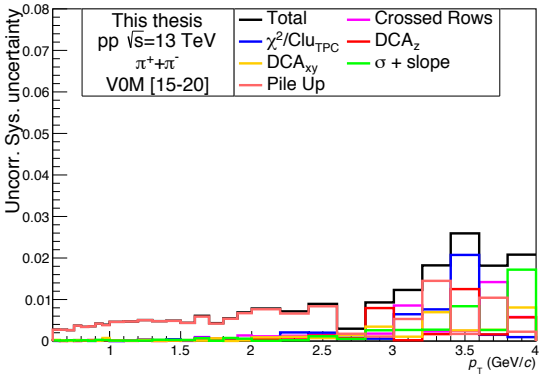

(c)

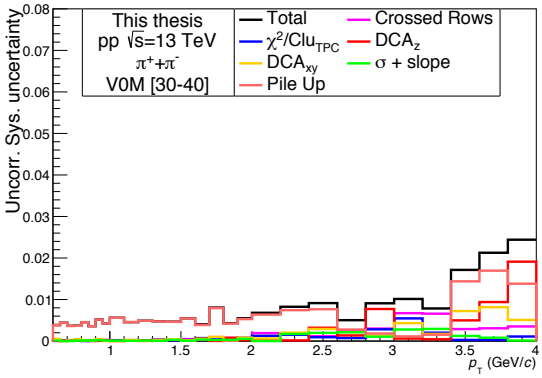

(d)

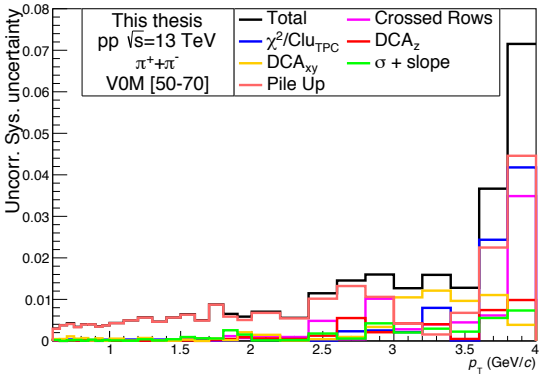

(e)

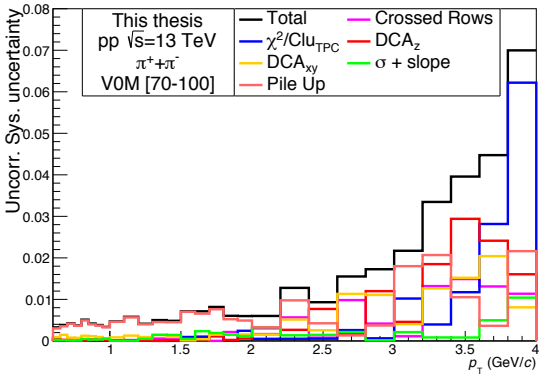

(f)

Fig. 3.39 Uncorrelated systematic uncertainty from different sources as well as the total uncorrelated uncertainties are shown for pions in (a) 0-1%, (b) 5-10%, (c) 15-20%, (d) 30-40%, (e) 50-70% and (e) 70-100% V0M multiplicity classes.

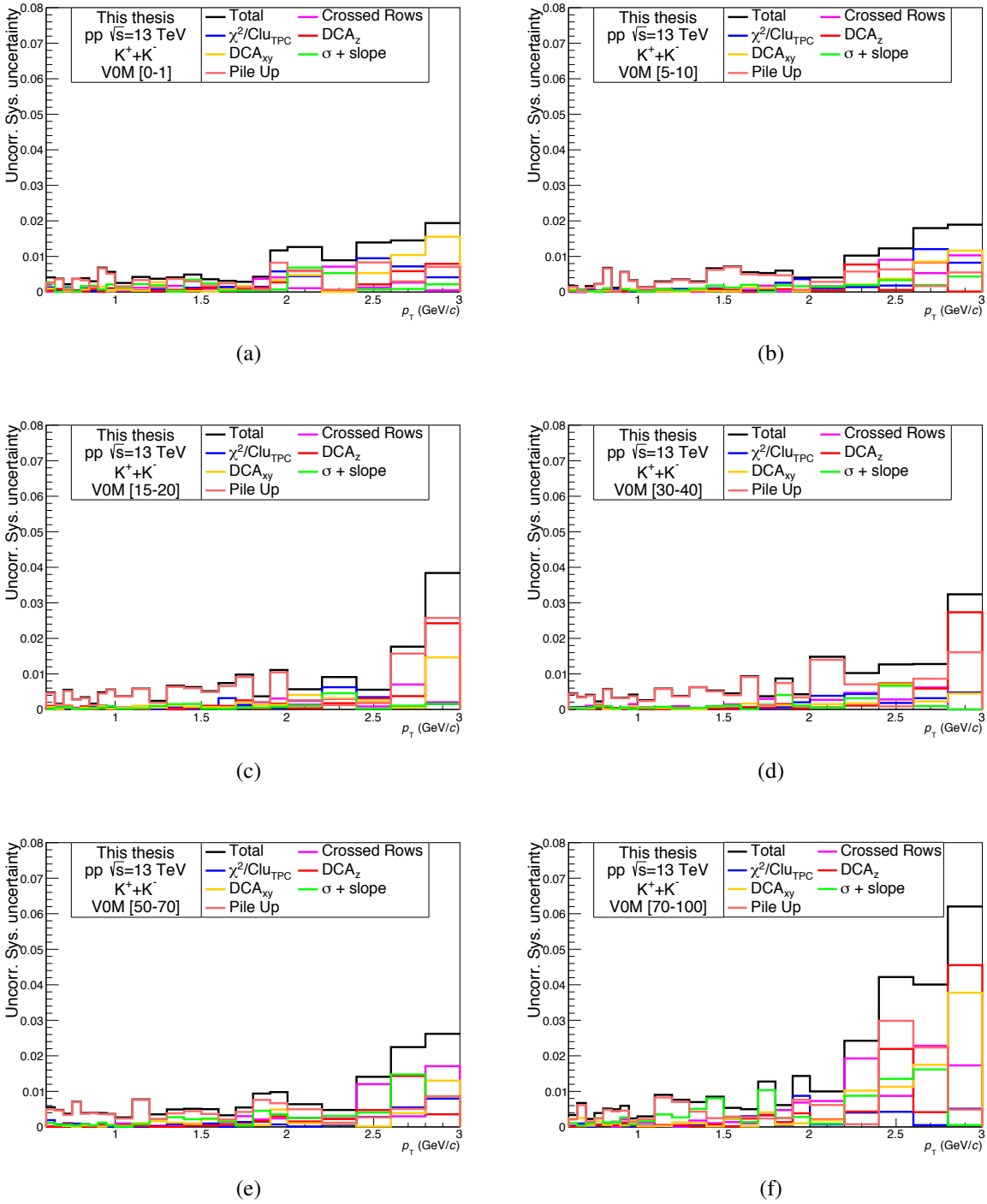

Fig. 3.40 Uncorrelated systematic uncertainty from different sources as well as the total uncorrelated uncertainties are shown for kaons in (a) 0-1%, (b) 5-10%, (c) 15-20%, (d) 30-40%, (e) 50-70% and (e) 70-100% V0M multiplicity classes.

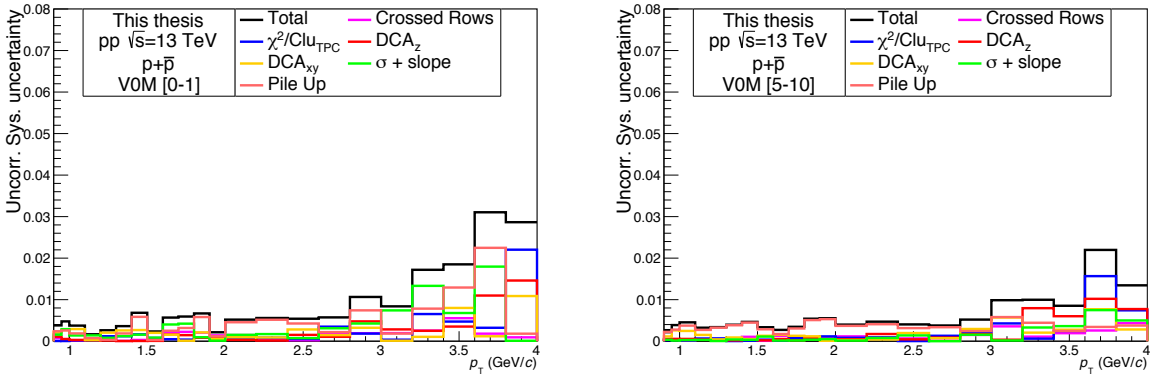

(a)

(b)

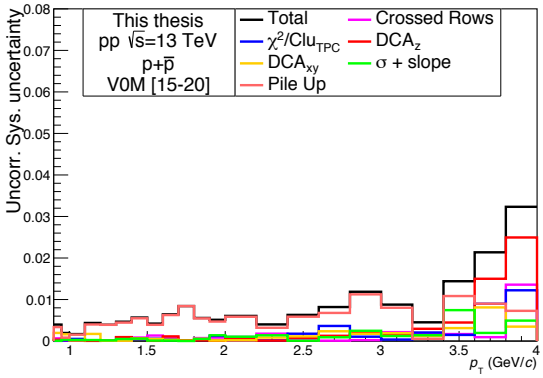

(c)

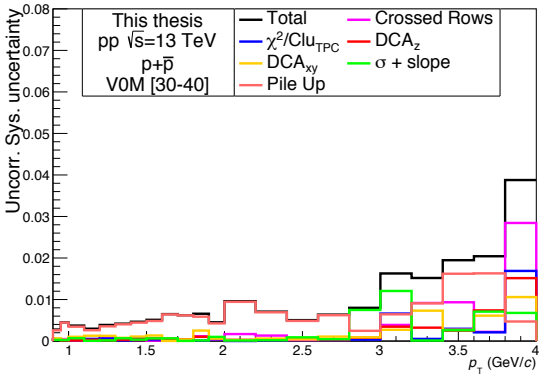

(d)

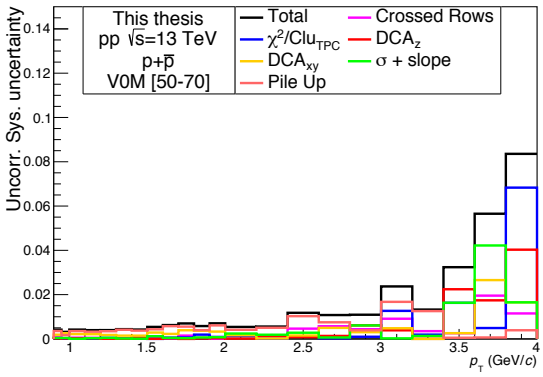

(e)

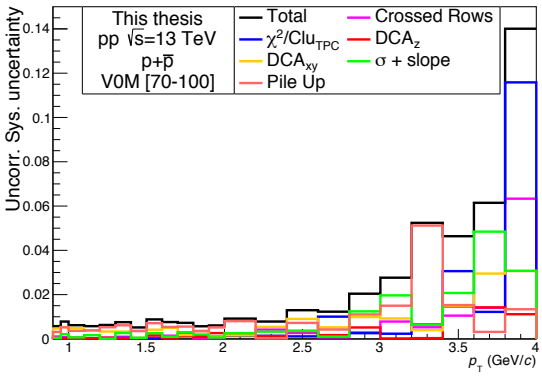

(f)

Fig. 3.41 Uncorrelated systematic uncertainty from different sources as well as the total uncorrelated uncertainties are shown for protons in (a) 0-1%, (b) 5-10%, (c) 15-20%, (d) 30-40%, (e) 50-70% and (e) 70-100% V0M multiplicity classes.

parameters to the standard one. The total uncertainty, along with different sources of systematic uncertainties, are shown in Figs. 3.42, 3.43. The systematic uncertainties related to the TPC-TOF matching efficiencies are obtained by propagating the single-particle uncertainty to the particle ratios and are found to be 6.7 and 5% for K/π and p/π ratios, respectively. Further, for estimation of the uncorrelated systematic uncertainty in the particle ratios, the same procedure as that of the uncorrelated systematic uncertainty estimation for p_{T} spectra have been used, and the results are shown in Figs. 3.44 and 3.45.

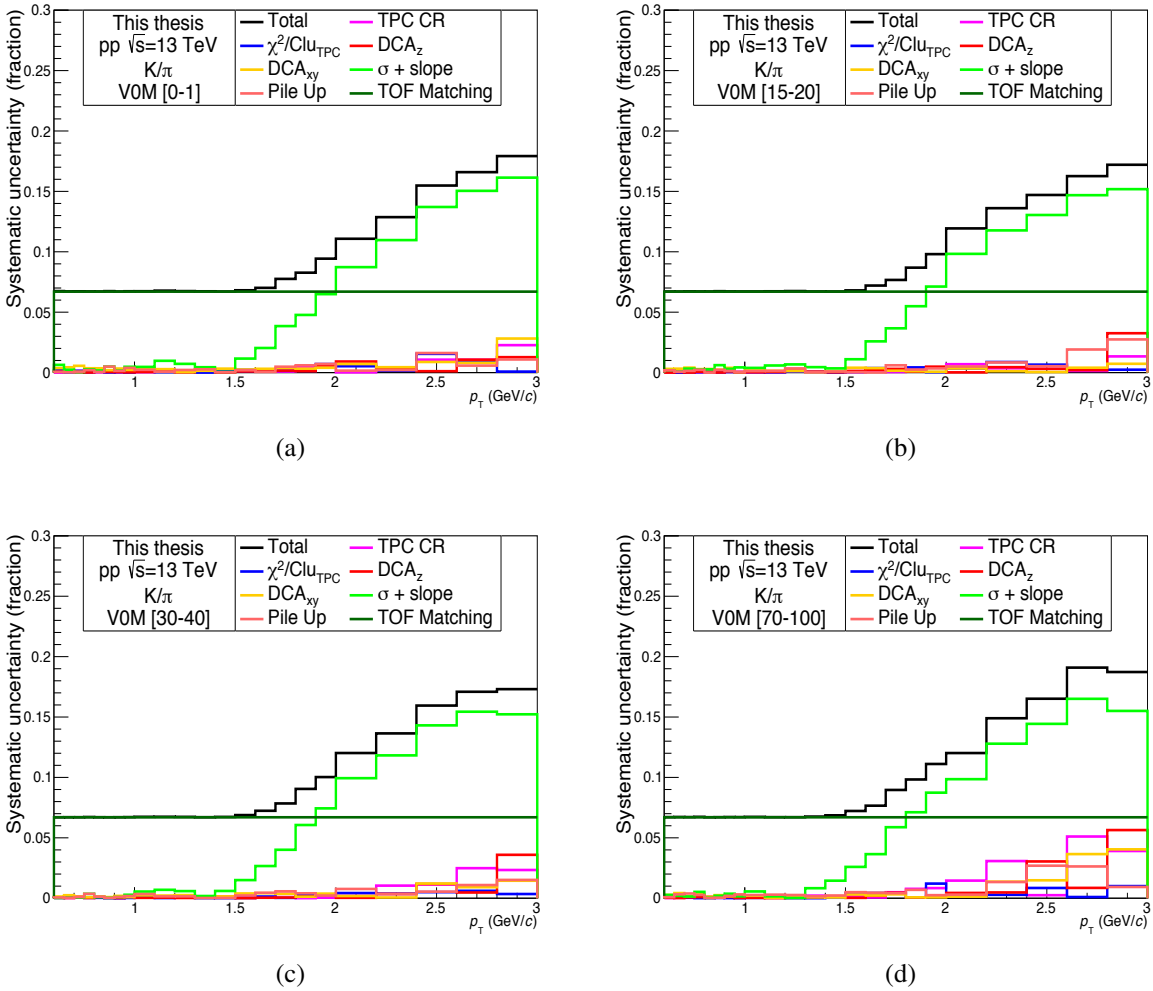

Fig. 3.42 Systematic uncertainties from different sources and the total one are shown for K/π ratio in (a) 0-1%, (b) 15-20%, (c) 30-40%, and (d) 70-100% V0M multiplicity classes.

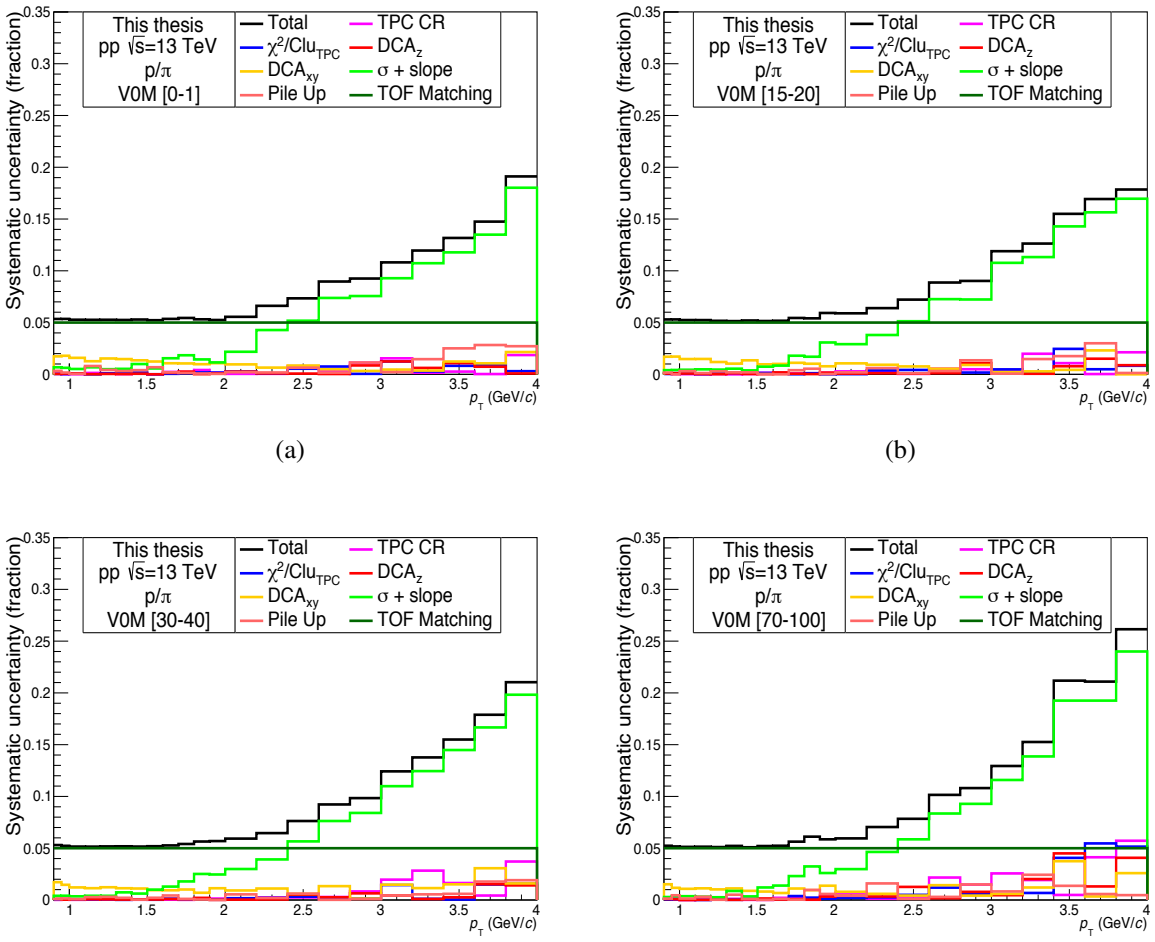

Fig. 3.43 Systematic uncertainty from different sources as well as the total uncertainties are shown for p/π ratio in (a) 0-1%, (b) 15-20%, (c) 30-40%, and (d) 70-100% V0M multiplicity classes.

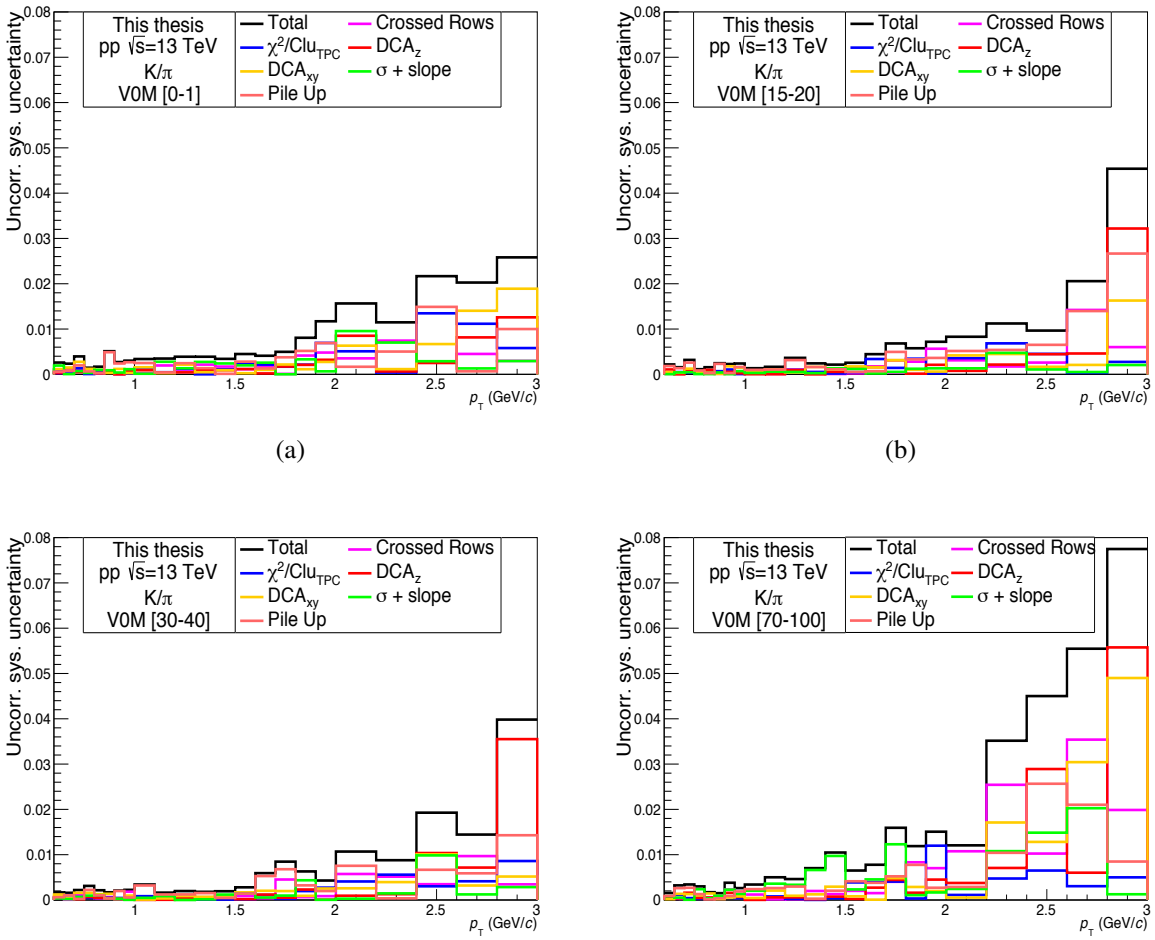

Fig. 3.44 Uncorrelated systematic uncertainty from different sources as well as the total uncertainties are shown for K/π ratio in (a) 0-1%, (b) 15-20%, (c) 30-40%, and (d) 70-100% V0M multiplicity classes.

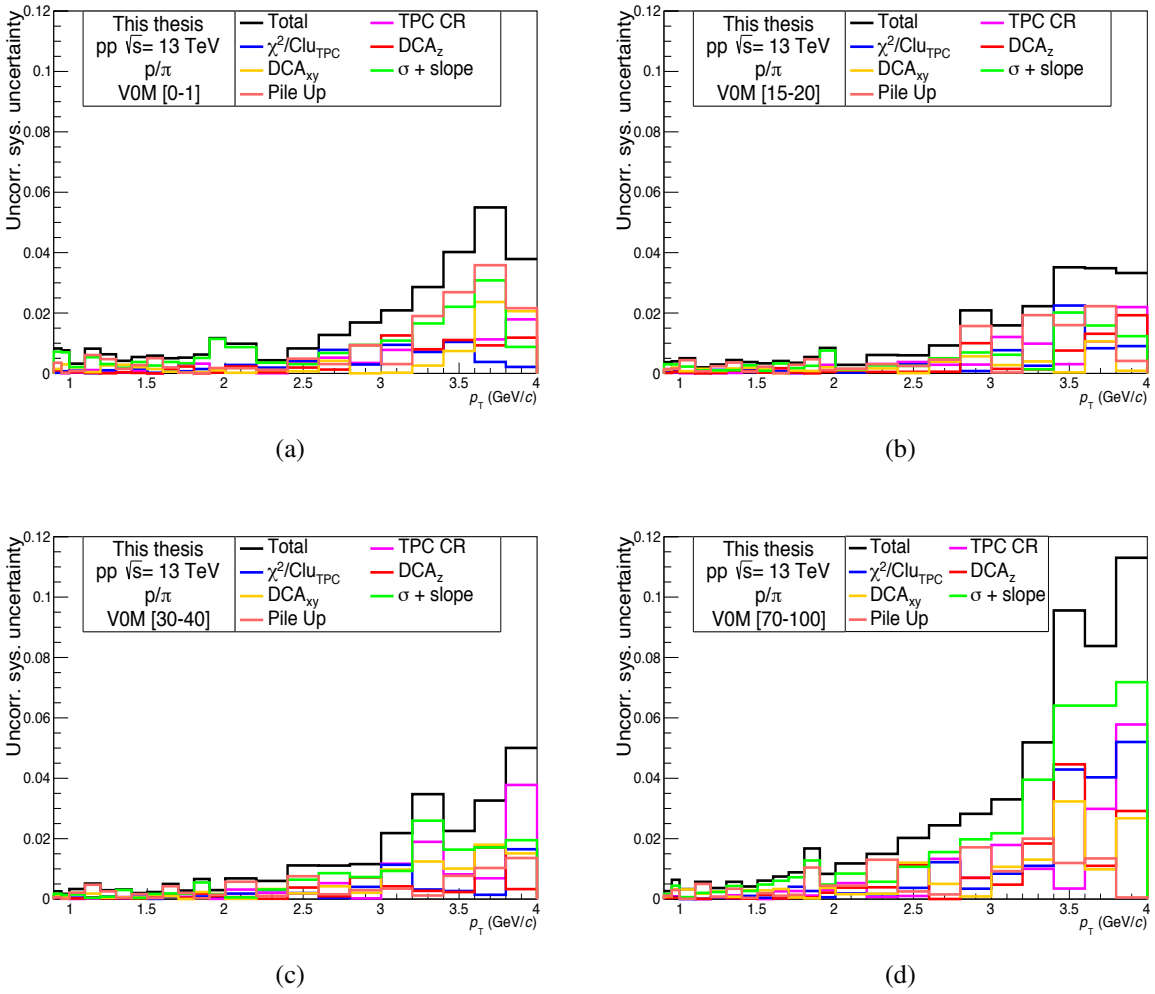

Fig. 3.45 Uncorrelated systematic uncertainty from different sources as well as the total uncertainties are shown for p/π ratio in (a) 0-1%, (b) 15-20%, (c) 30-40%, and (d) 70-100% V0M multiplicity classes.

3.7 Summary

In this chapter, a comprehensive study has been performed to analyse the ALICE data and identify the primary charged particles, namely pions, kaons and protons. The primary pions, kaons and protons, are identified with the Time-of-Flight (TOF) detector of ALICE via measurement of their time of flight from the collisions point to the detector. At first, the

performance of the TOF detector of ALICE in pp collisions at $\sqrt{s} = 13$ TeV is discussed. Then, a statistical unfolding method has been applied, where the time-difference distribution between the TOF time in data and the expected time of flight of a particle are fitted with the four template distributions, three for the charged pions, kaons & protons; and an additional template which take care of the background arising due to wrongly associated tracks in the TOF detector. This procedure is repeated in p_{T} bins for the multiplicity-integrated class as well as for all charged-particle multiplicity classes to identify them. Using the TOF detector, pions, kaons and protons are identified in the p_{T} range 0.7 to 4 GeV/c, 0.6 to 3 GeV/c and 0.9 to 4 GeV/c, respectively.

Further, the track reconstruction efficiency and TPC-TOF matching efficiency estimated from the Monte Carlo simulation are applied in the raw spectra of identified particles to obtain the final corrected p_{T} spectra. Moreover, for the estimation of primary pions and protons spectra, the raw p_{T} spectra are required to correct for a fraction of primary particles estimated with data-driven DCA_{xy} fits.

Finally, various sources of systematic uncertainty related to the p_{T} spectra measurement and their estimation procedure are discussed in this chapter. The primary source of systematic uncertainty is observed to be the TOF particle identification uncertainty. The systematic uncertainties related to the track reconstruction procedure are also estimated in this thesis. The total systematic uncertainties are obtained by adding individual contributions from different sources in quadrature. The systematic uncertainties are observed to be multiplicity dependent, which is large for the lowest multiplicity and small for the highest multiplicity class. Further, the multiplicity uncorrelated systematic uncertainties are also estimated and observe to be multiplicity dependent similar to that of systematic uncertainty. Moreover, various types of systematic uncertainty estimated for the K/π and p/π ratios are also presented.

4

Production of π, K and p as a function of charged-particle multiplicity in pp collisions at $\sqrt{s} = 13$ TeV

In this chapter, multiplicity dependent pions, kaons and protons production results in pp collisions at $\sqrt{s}$ = 13 TeV are presented. The results obtained from the TOF detector analysis described in the previous chapter are discussed hereunder. The p_{T} spectra of particles identified with the TOF detector are combined with the results of the analysis performed

by other detectors or methods of particle identification such as the ITS stand-alone, TPC-TOF, the relativistic rise of TPC, and kinks topology for complete measurement of the p_{T} spectra from very low to high p_{T} range. The combined results are then compared with the measurement available for lower energy pp, p−Pb and Pb−Pb collisions. These results are also compared with the results of different Monte Carlo event generators for a better insight into the particle production mechanism and collisions dynamics of pp collisions.

In this thesis, as mentioned earlier, the V0M percentile multiplicity estimator has been used to obtain the p_{T} spectra in different charged-particle multiplicity classes. The charge deposited in the two V0 detectors: V0A and V0C are combined to get the total charge on the V0M. The total charge on V0M is then converted to V0M percentile to provide a relative measure of the multiplicity. For relating the charged-particle multiplicity for different V0M multiplicity classes, the mean charged-particle multiplicity density ($\langle \mathrm{d}N_{\mathrm{ch}}/\mathrm{d}\eta \rangle$) are estimated in the pseudo-rapidity range $|\eta| < 0.5$. The mean charged-particle multiplicity estimated in different multiplicity classes for pp collisions at $\sqrt{s} = 13$ TeV is given in Table. 4.1.

Table 4.1 Mean charged-particle multiplicity density $\langle \mathrm{d}N_{\mathrm{ch}}/\mathrm{d}\eta \rangle$ measured in different charged-particle multiplicity classes and their corresponding V0M percentile class.

Mult. class	I	II	III	IV
V0M perccentile (%)	0-1	1-5	5-10	10-15
$\langle \mathrm{d}N_{\mathrm{ch}}/\mathrm{d}\eta \rangle$	26.02 ± 0.35	20.02 ± 0.27	16.17 ± 0.22	13.77 ± 0.19
Mult. class	V	VI	VII	VIII
V0M perccentile (%)	15-20	20-30	30-40	40-50
$\langle \mathrm{d}N_{\mathrm{ch}}/\mathrm{d}\eta \rangle$	12.04 ± 0.17	10.02 ± 0.14	7.95 ± 0.11	6.32 ± 0.09
Mult. class	IX	X		
V0M perccentile (%)	50-70	70-100		
$\langle \mathrm{d}N_{\mathrm{ch}}/\mathrm{d}\eta \rangle$	4.50 ± 0.07	2.55 ± 0.04		

4.1 The p_{T} spectra of pions, kaons and protons identified with the TOF detector

As described in the previous chapter, the final corrected p_{T} spectra of the identified particles are estimated by correcting the raw p_{T} spectra of the particle by different correction factors. Among them, the correction factors corresponding to the detection probability of a particle by various detectors need to be taken into account. The correction factors contain tracking efficiency which takes care of the reconstruction probability of tracks within the detector acceptance, matching efficiency due to the propagation of a track from the TPC to TOF. Moreover, the raw p_{T} spectra have the contributions from secondary particles, and therefore, corrections for fractions of primary particles in the data sample is required to apply to obtain the final corrected yields of the primary particles. These correction factors are applied as given in Eq. (4.1).

$$\frac{\mathrm{d}^2\mathrm{N}}{\mathrm{d}y\mathrm{d}p_{\mathrm{T}}} = \frac{1}{N_{ev}} \times \frac{\text{Raw Yield}}{Tracking_{Efficiency} \times Matching_{Efficiency}} \times \text{Fraction Primary} \tag{4.1}$$

It could be observed from results of the previous chapter that the different corrections factors estimated are independent of the multiplicity classes considered and therefore, the multiplicity integrated correction factors are used to obtain the final p_{T} spectra with reduced statistical uncertainty.

The final corrected p_{T} spectra of pions, kaons and protons identified with the TOF detector with their corresponding systematic uncertainty are shown in Figs. 4.1(a), 4.1(b) and 4.1(c), respectively for different charged-particle multiplicity classes and minimum-bias (INEL>0) pp collisions at $\sqrt{s}$ = 13 TeV. From the figures, particles p_{T} spectra are observed to become harder with increasing charged-particle multiplicity. It is also observed that the

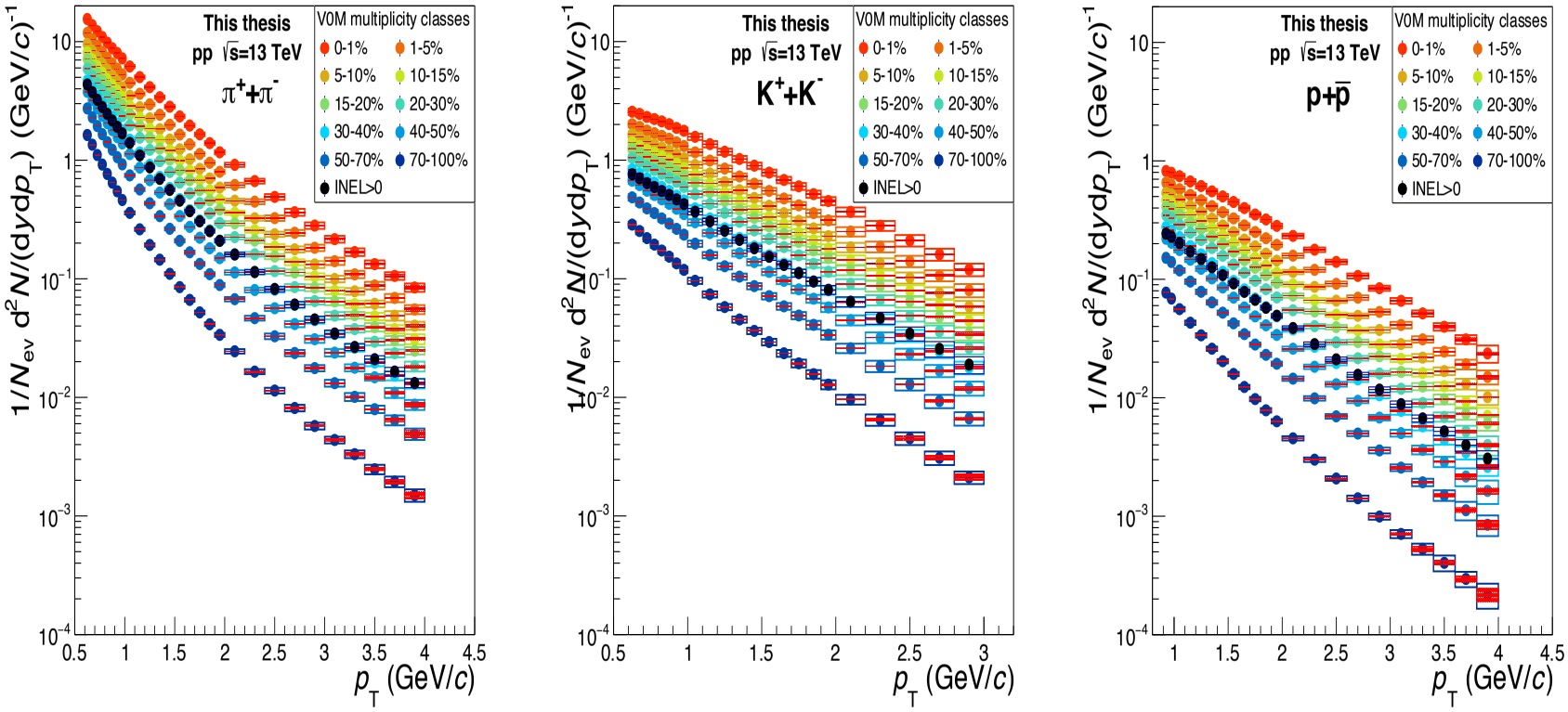

(a) (b) (c)

Fig. 4.1 The p_{T} spectra of the pions, kaons and protons in different V0M multiplicity classes identified with the TOF detector. The statistical uncertainties are represented by lines and are within the marker. The open boxes represent systematic uncertainty, and the shaded boxes represent uncorrelated systematic uncertainty.

hardening of the p_{T} spectra with increasing multiplicity is more pronounced for higher mass particles, i.e. for proton.

The p_{T} spectra ratio of positive to negative particles for π, K and p are shown in Figs. 4.2(a), 4.3(a) and 4.4(a), respectively. These figures show that the ratios are within unity in the studied p_{T} range. Further, the positive to negative particles ratios in V0M multiplicity class to INEL>0 events class are also shown in Figs. 4.2(b), 4.3(b), 4.4(b). It could be observed from these figures that those ratios are flat for all the studied multiplicity classes of all the identified particles. From the above observations, one can conclude that particles and anti-particles production rates are the same in pp collisions at $\sqrt{s} = 13$ TeV and is independent of the multiplicity class considered.

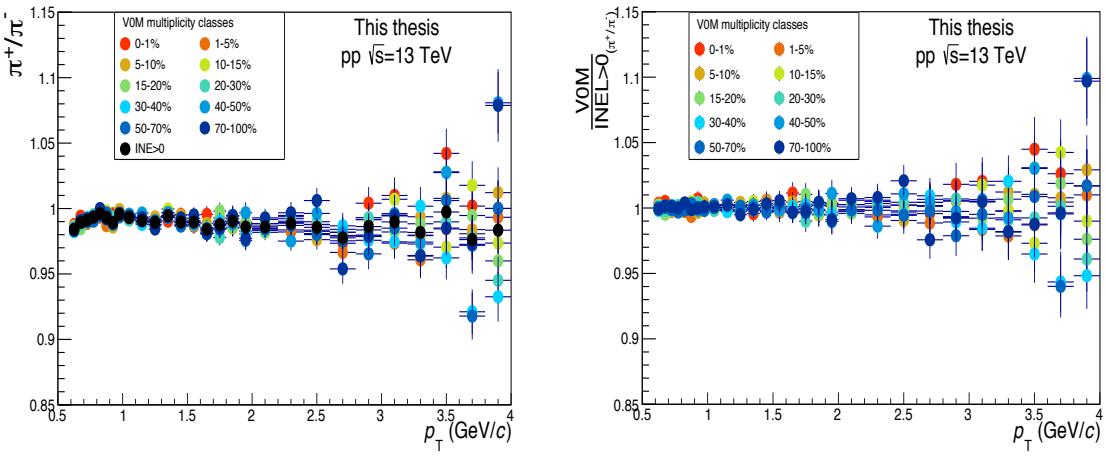

(a) (b)

Fig. 4.2 p_{T} spectra ratio of (a) positive to negative pions and (b) the same ratio in V0M multiplicity class to that of INEL>0 events class.

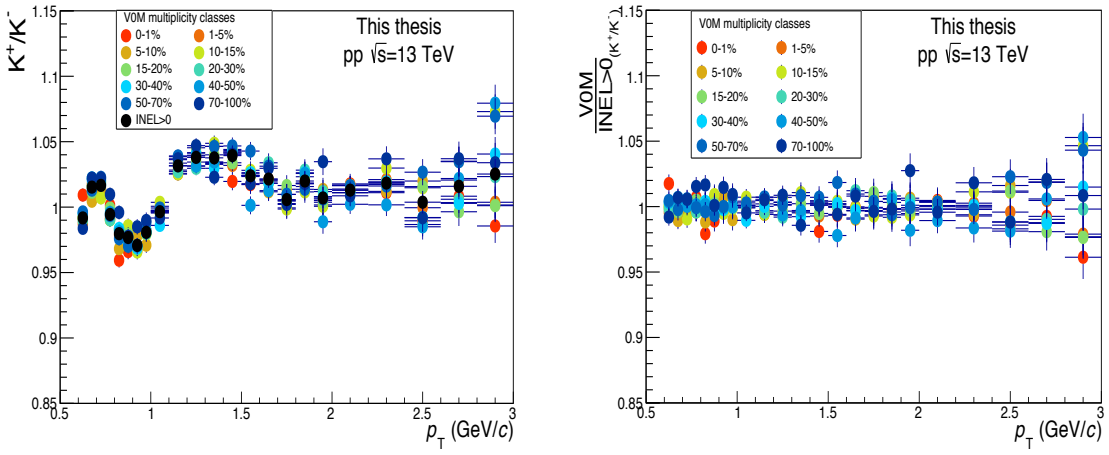

(a) (b)

Fig. 4.3 p_{T} spectra ratio of (a) positive to negative kaons and (b) the same ratio in V0M multiplicity class to that of INEL>0 events class.

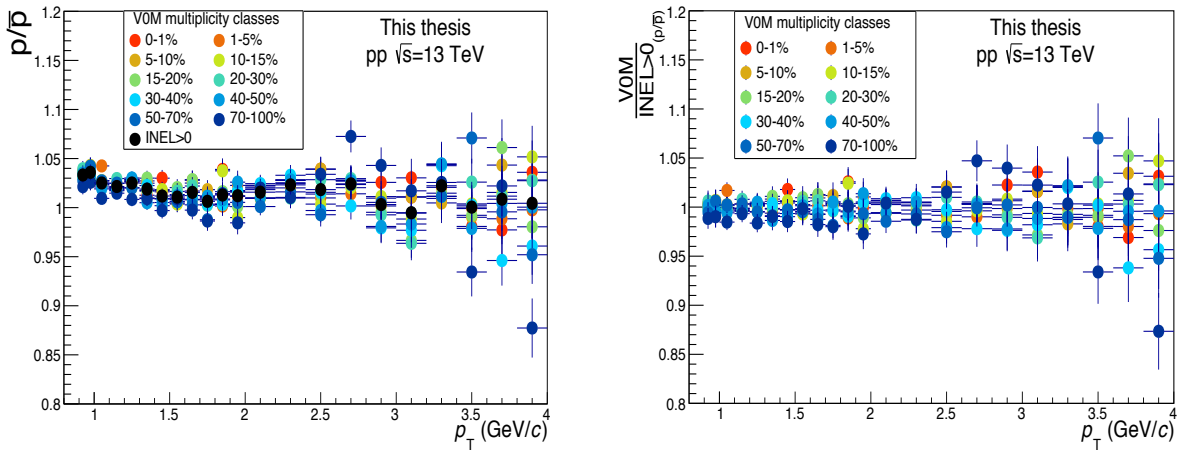

(a) (b)

Fig. 4.4 p_{T} spectra ratio of (a) positive to negative protons and (b) the same ratio in V0M multiplicity class to that of INEL>0 events class.

4.2 Kaons to pions and protons to pions ratios

The kaons to pions and protons to pions ratios identified with the TOF detector in various charged-particle multiplicity classes with their corresponding systematic uncertainty are shown in Figs. 4.5(a) and 4.5(b). No significant evolution in the K/π ratio with the charged-particle multiplicity could be observed from Fig. 4.5(a). On the contrary, the p/π ratio, as shown in Fig. 4.5(b), exhibits a considerable evolution with increasing charged-particle multiplicity in the studied p_{T} range of the TOF detector. In the high-multiplicity pp collisions, the p/π ratio shows a depletion at low p_{T} and an enhancement at intermediate p_{T}.

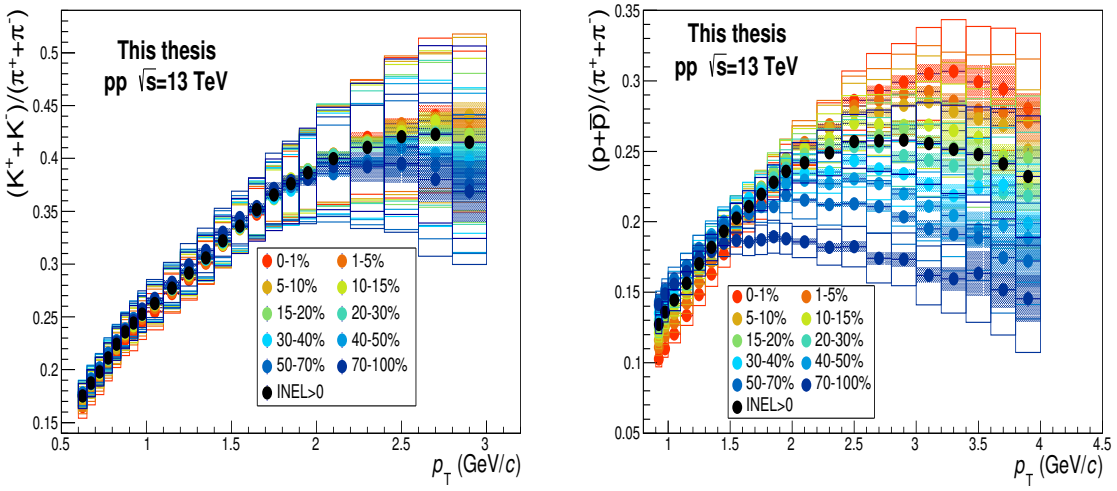

(a) (b)

Fig. 4.5 (a) Kaons to pions and (b) protons to pions ratios with systematic uncertainties in different charged-particle multiplicity classes as well as in minimum bias pp collisions at $\sqrt{s} = 13$ TeV.

4.3 Combined p_{T} spectra of pions, kaons and protons

The measurement of the p_{T} spectra of identified charged particles over a wide momentum range provides the complete picture of particle production in ultra-relativistic nuclear collisions. For the measurement of the complete p_{T} spectra from very low to high transverse

momentum, the TOF PID results are needed to combine with the results of ITSsa, rTPC and TPC-TOF particle identification techniques. In addition to these, for kaons, the results obtained with kink topology analysis are also included in the combined spectra.

The p_{T} spectra obtained from different analyses are combined by considering a weighted average of the spectra in the overlapping region of p_{T} bins. The combined p_{T} spectra are estimated following the procedure given below:

1. At first, the TPC-TOF and TOF PID spectra are combined using the inverse square of the systematic uncertainty as weight. Here, the TOF matching efficiency and tracking systematic uncertainties are considered correlated, and hence, these are removed from the weight (in quadrature) during the combination. Once the combination is performed, the same systematic uncertainty is added again in quadrature to the combined p_{T} spectra.

2. The combined spectra of the TPC-TOF and TOF PID are combined with the rTPC spectra using the inverse square of the systematic uncertainty as the weight. After combination, the tracking systematic uncertainty is again added in quadrature in combined p_{T} spectra for each type of particle.

3. The systematic uncertainty related to the material budget of TPC-TOF is added in quadrature before combining the spectra with ITSsa.

4. In the case of kaons, the kinks spectra are also needed to add in the combining procedure. Here, the inverse square of the systematic uncertainty is considered as weights and the spectra of kink and combined one from TPC-TOF, TOF and rTPC are added. For kink analysis, the tracking systematic uncertainty is considered correlated to the TPC-TOF, TOF and rTPC PID technique. Therefore, these are removed during the combination procedure and are added later after the combination (in quadrature).

5. Finally, the ITSsa p_{T} spectra are combined, considering the inverse square of statistical and systematic uncertainty as weights.

6. A global systematic uncertainty of 2.1% is added in quadrature to the whole p_{T} spectra taking into account the MC imprecisions.

7. Then, the ITS-TPC matching efficiency systematic uncertainty is added in quadrature in the spectra [192].

8. The systematic uncertainties for the hadronic cross-section (arising due to Geant3-Geant4 corrections) are added in quadrature before combining with the ITSsa analysis, which has a separate uncertainty.

9. Then the signal loss correction systematic uncertainty is applied in quadrature to the spectra.

To have a clear view regarding the agreement between different analysis, the p_{T} spectra's ratio from the individual PID method to that of the combined p_{T} spectra are estimated and are shown in Figs. 4.6, 4.7, 4.8 for pions, kaons, and protons, respectively in highest and lowest multiplicity classes. It could be observed from the figures that the agreement between different analyses are very good and are well within the systematic uncertainties. For TOF PID at high p_{T} and lowest multiplicity class, due to the worsening of the event time resolution, as expected, a little deviation from the combined spectra is evident. However, within systematic uncertainty, the results are observed to agree well with each other. Furthermore, due to the worsening of the event time resolution, the systematic uncertainty for the TOF PID method also increases in the high p_{T} region.

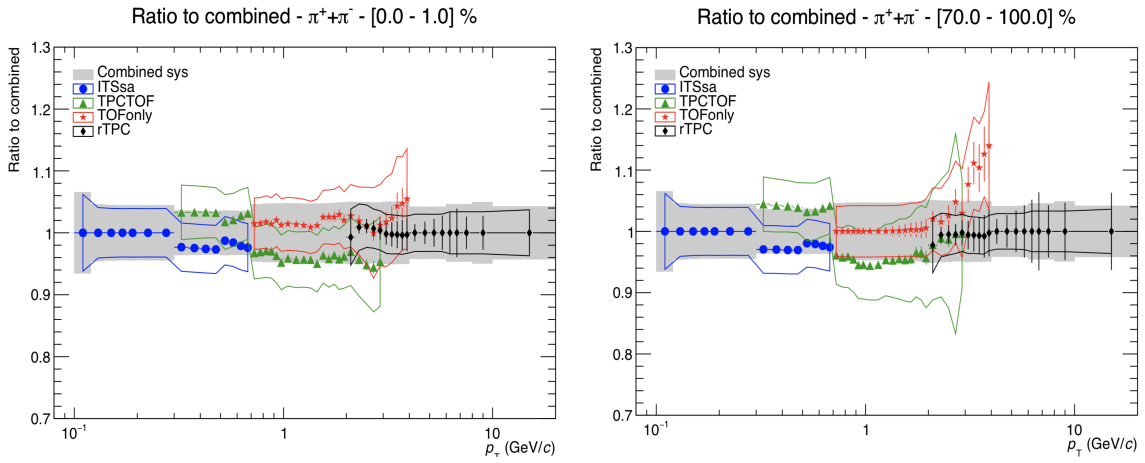

(a) (b)

Fig. 4.6 Ratio of individual PID p_{T} spectra to the combined one for pions in V0M multiplicity class (a) 0-1% and (b) 70-100%. The coloured bands represent the total systematic uncertainty.

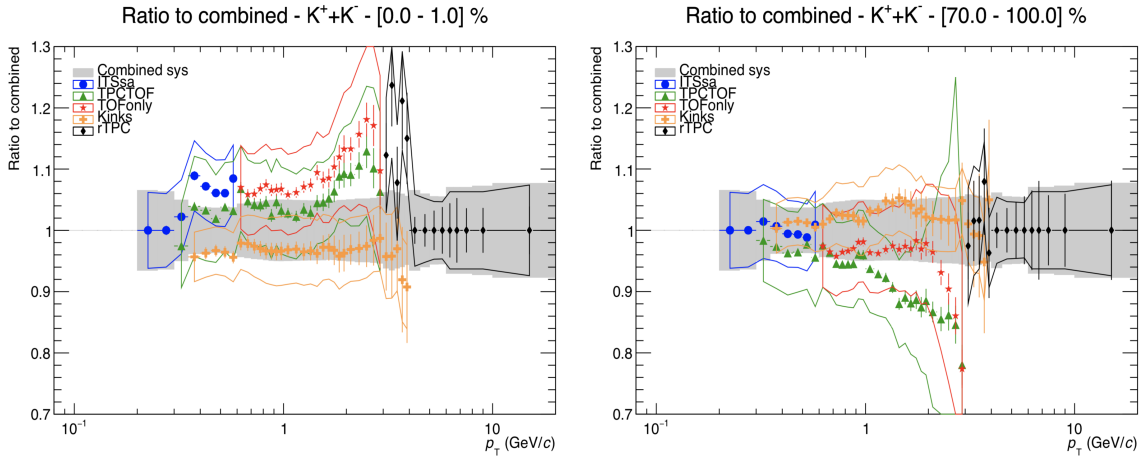

(a) (b)

Fig. 4.7 Ratio of individual PID p_{T} spectra to the combined one for kaon in V0M multiplicity class (a) 0-1% and (b) 70-100%. The coloured bands represent the total systematic uncertainty.

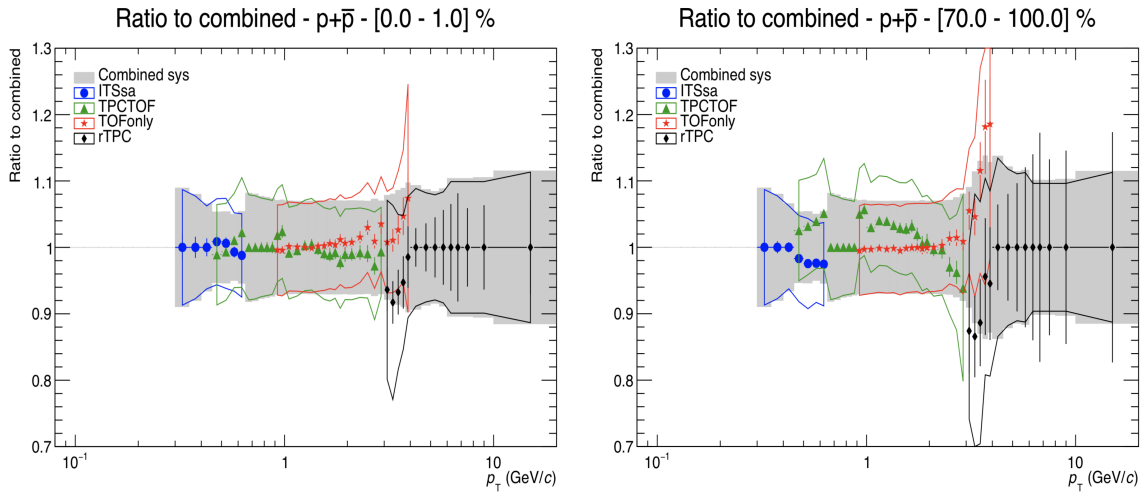

(a) (b)

Fig. 4.8 Ratio of individual PID p_{T} spectra to the combined one for proton in V0M multiplicity class (a) 0-1% and (b) 70-100%. The coloured bands represent the total systematic uncertainty.

The combined p_{T} spectra of different identified charged particles, namely pions, kaons and protons are shown in Figs. 4.9(a), 4.9(b) and 4.9(c) respectively. It could be observed from the figures that the measured p_{T} spectra become harder as the charged-particle multiplicity increases and the effect is more pronounced for heavier particles like proton, suggesting a mass-dependent hardening of the p_{T} spectra. Similar hardening of the p_{T} spectra with increasing multiplicity for pp collisions has also been observed for the inclusive charged-hadron [193], where various models with multi-parton interaction (MPI) were observed to describe the behaviour. The lower panel in each of the figures shows the p_{T} spectra's evolution in V0M multiplicity class to the INEL>0 event class. It is evident from the figures that the ratios are identical for π, K, and p, indicating a common mechanism at work that depends solely on the final-state multiplicity. The multiplicity and mass-dependent hardening of the p_{T} spectra for various identified particles have also been observed for lower energy pp and p-Pb collisions, and are considered a regular feature of the Pb-Pb collisions at the LHC energies [17, 19, 194]. In Pb-Pb collisions, the mass-dependent modifications of the p_{T} spectra are considered due to the hydrodynamical evolution of the system [11]. In the

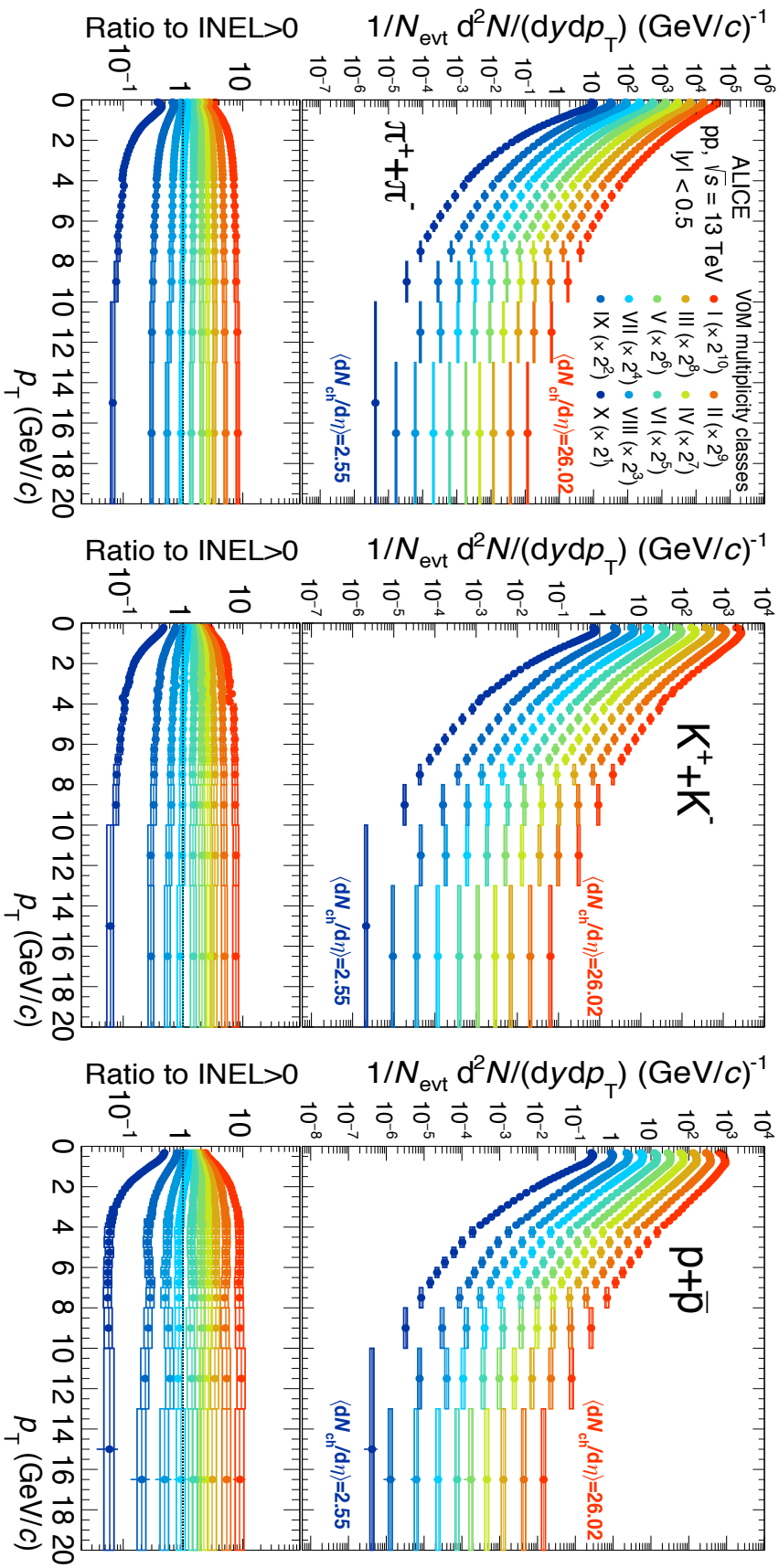

Fig. 4.9 Final combined p_T spectra of (a) pions, (b) kaons and (c) protons in different V0M multiplicity classes. Spectra are scaled by powers of 2 for better visibility. The corresponding ratios to INEL>0 spectra are shown in the bottom panels of each figure.

high p_{T} ($>$ 4 GeV/c) region, the slope of the particles spectra becomes independent of the multiplicity class considered. Here, the particles are mainly produced via the fragmentation process [195].

The p_{T}-differential K/π and p/π ratios in some selected V0M multiplicity classes are shown in Figs. 4.10(a) and 4.10(b), respectively. It could be observed from Fig. 4.10(a) that the K/π ratio shows no evolution with increasing charged-particle multiplicity. On the contrary, it is readily evident from Fig. 4.10(b) that the p/π ratio shows a depletion at low p_{T} ($<$ 2 GeV/c) and a significant enhancement at the intermediate p_{T} ($2 < p_{\mathrm{T}} < 4$ GeV/c) in the highest multiplicity class. At the high p_{T}, the p/π ratio shows constant behaviour and becomes independent of the multiplicity class considered. Similar enhancement at intermediate p_{T}, depletion at low p_{T}, and a constant behaviour at high p_{T} have also been reported in the lower energy pp, p-Pb and Pb-Pb collisions [19, 17, 11]. In central Pb-Pb collisions, the mass-dependent enhancement in the p/π ratio at the intermediate p_{T} can be well described by a collectively expanding source or due to the consequence of hadronisation via recombination of quarks in the plasma phase [11, 91, 92].

Moreover, the K/π and p/π ratios at low, intermediate and high p_{T} as a function of charged-particle multiplicity are shown in Fig. 4.11 and are compared with the results of the lower energy pp collisions at the LHC. Here also, the K/π ratio seems independent of multiplicity class considered and remains flat from low to high-multiplicity pp collisions. On the other hand, the p/π ratio shows a decreasing trend at low p_{T}, an increasing trend at the intermediate p_{T} and a constant behaviour at the high p_{T} with increasing charged-particle multiplicity. The results also follow a similar pattern, as observed in the pp collisions at $\sqrt{s} = 7$ TeV [19].

For comparison of the data results with various Monte Carlo models, the generated events are classified according to the number of particles simulated at the forward and backward pseudo-rapidities covered by the V0 detector, in a similar way the event classification is

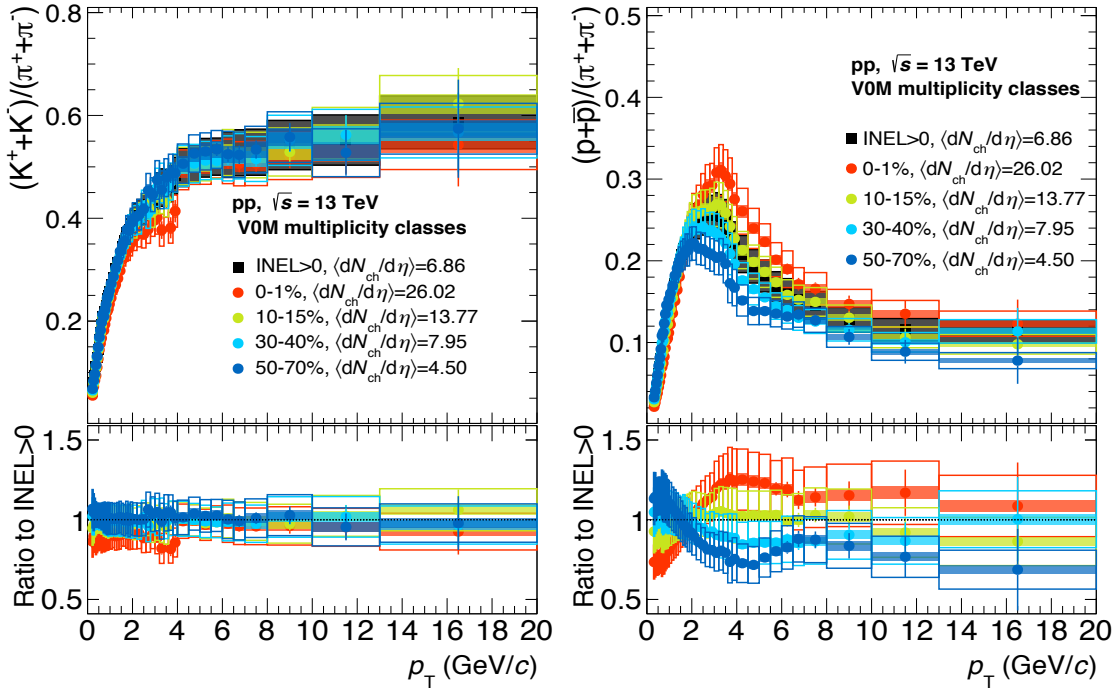

(a) (b)

Fig. 4.10 p_{T}-differential (a) K/π and (b) p/π ratios in some selected V0M multiplicity class with systematic uncertainty.

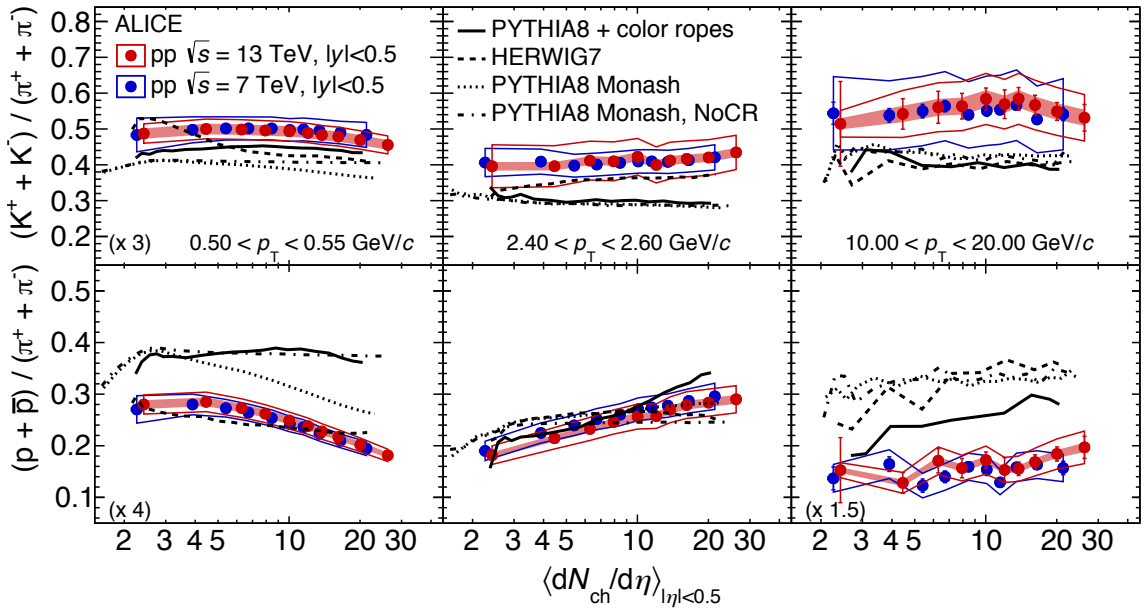

Fig. 4.11 K/π and p/π ratios as a function of charged-particle multiplicity at low, intermediate and high p_{T} bins are compared with the lower energy pp collisions. Predictions from various Monte Carlo event generators are also shown.

performed for the data. The average charged-particle multiplicity density is then estimated in the mid pseudo-rapidity region. The HERWIG7 model [196, 197], in which hadronisation process occurs via the mechanism of cluster formation, is able to provide a good description of the evolution of the K/π, and p/π ratios with increasing charged-particle multiplicity in the low and intermediate p_{T} ranges and the results are consistent with the measured ratios within 1-2 standard deviations. The PYTHIA 8 model [149], which includes the mechanism of colour reconnection (CR), produces only a qualitative description of the evolution of the p/π ratio against multiplicity and overestimates the values of the ratio in low and high p_{T}. The evolution of both the K/π and p/π ratios with increasing charged-particle multiplicity cannot be described by the PYTHIA 8 model when CR mechanism is switched off.

Further, in a completely new version of PYTHIA [198–200], the hadronisation mechanism includes overlapping colour string, which then forms colour ropes with a higher string tension between quarks and is allowed to interact with each other, resulting in enhanced production of strange and di-quark. This PYTHIA model can provide a qualitative description of the K/π and p/π ratio at low and intermediate p_{T}, respectively; but, overestimate the p/π ratio at low p_{T}. This behaviour could be well understood considering that larger effective string strength is mostly translated to hadronic mass and thus feeds down the low p_{T} part. Therefore, the p/π ratio is overestimated at high p_{T} and the K/π ratio is underestimated at intermediate and high p_{T} region.

4.3.1 p_{T}-integrated yields, particle yields ratios and average p_{T}

The p_{T}-integrated yields (dN/dy) and average transverse momentum ($\langle p_{\mathrm{T}} \rangle$) of the identified particles are estimated for various multiplicity classes from the final combined p_{T} spectra using an extrapolation to $p_{\mathrm{T}} = 0$. The extrapolation procedures are performed after fitting the measured p_{T} spectra with the Levy-Tsallis function given by Eq. (4.2) [201, 202, 191].

$$\frac{\mathrm{d}^2N}{\mathrm{d}p_\mathrm{T}\mathrm{d}y} = p_\mathrm{T}\frac{\mathrm{d}N}{\mathrm{d}y}\frac{(n-1)(n-2)}{nC(nC+m_0(n-2))}\left(1+\frac{m_\mathrm{T}-m_0}{nC}\right)^{-n} \tag{4.2}$$

where $m_\mathrm{T} = \sqrt{p_\mathrm{T}^2+m_0^2}$, m_0 is the particle rest mass and C, n and the yields dN/dy are the free parameters of the fits. The Levy-Tsallis function describes the p_T spectra of the identified particle rather well from very low to high p_T region.

The extrapolated fractions of the yields for pions at low p_T are 8 and 10% for the highest and lowest multiplicity classes, respectively. The fraction is 6 and 13% for kaons, and for protons, it is 7 and 20% for the highest and lowest multiplicity classes, respectively. Several other functions such as Bose-Einstein, Fermi-Dirac, p_T-exponential at low p_T and Hagedorn, Bylinkin at high p_T are used to estimate systematic uncertainties associated with the extrapolation procedure. The systematic uncertainties on the yields due to the extrapolation procedure are 2, 2 and 3% for π, K and p, respectively at the lowest multiplicity class and are observed to become smaller at highest multiplicity. In the case of $\langle p_\mathrm{T}\rangle$, for all the three particles, the extrapolation's systematic uncertainties are 2% for the lowest multiplicity class.

The statistical uncertainties on the yields and mean p_T are estimated by shifting the central values of each spectra point through the fraction of the statistical uncertainty. The fraction is randomly drawn from Gaussian distribution and new values of the integrated yields and means p_T are calculated. This procedure is repeated 1000 times to calculate the standard deviation of the yields and mean p_T and later used as the statistical uncertainty. For estimation of the systematic uncertainty related to the p_T-integrated yields, the spectra points are shifted to the higher and lower values of the systematic uncertainty associated with each p_T bin, and the fit procedures are repeated. For $\langle p_\mathrm{T}\rangle$, each point of the spectra is shifted to the upper/lower edge of the corresponding p_T bin to obtain the hardest/softest particle distribution. The largest difference to the nominal yields and $\langle p_\mathrm{T}\rangle$ values are combined with the extrapolation uncertainties to calculate the total systematic uncertainties.

The p_{T}-integrated yields of π, K and p as a function of charged-particle multiplicity for pp collisions at $\sqrt{s} = 13$ TeV are plotted in Fig. 4.12, and the results are compared with the measurement available at lower energy pp collisions [19]. It is observed from the figure that the yields of the particles increase linearly with increasing charged-particle multiplicity. It is also observed that as expected, the yields of pions are much higher than that of kaons and protons since pions are the most abundant particle produced in the ultra-relativistic nuclear collisions. Moreover, when similar charged-particle multiplicities are considered, the yields of the particles are observed to be similar at both the measured centre-of-mass energies.

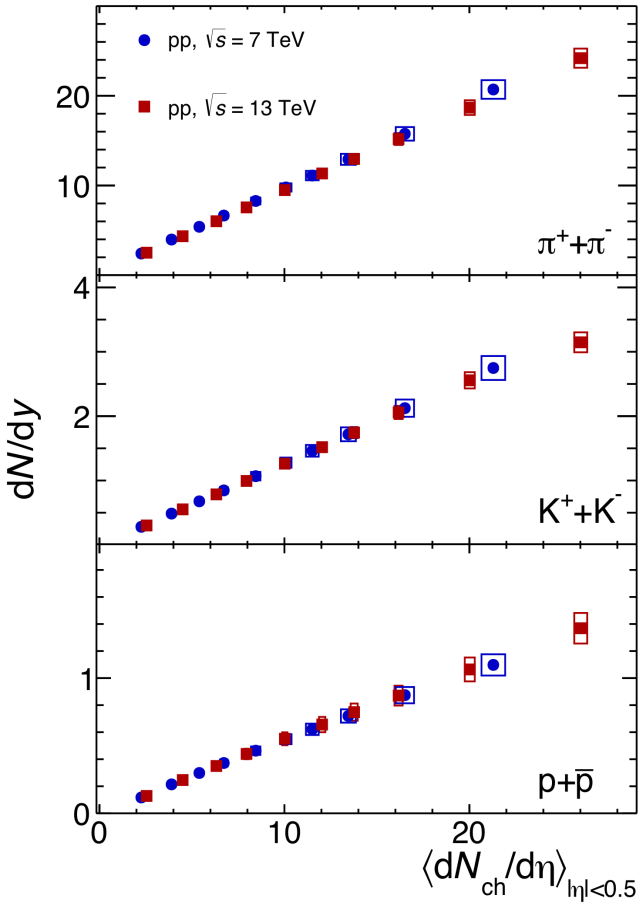

Fig. 4.12 The p_{T}-integrated yields of π, K and p as a function of multiplicity in pp collisions at $\sqrt{s} = 13$ TeV are compared with the results of lower energy pp collisions.

The $\langle p_{\mathrm{T}} \rangle$ of π, K and p estimated as a function of multiplicity in the pp collisions at $\sqrt{s} = 13$ TeV are plotted in Fig. 4.13 and are compared with the already published results

of pp collisions at $\sqrt{s} = 7$ TeV [19]. It could be observed from the figure that the $\langle p_{\mathrm{T}} \rangle$ becomes harder with increasing charged-particle multiplicity, and the hardening is more pronounced for heavier particles like proton. Similar mass-dependent hardening of the $\langle p_{\mathrm{T}} \rangle$ with increasing charged-particle multiplicity and particle mass has also been observed at the lower energy pp, p-Pb and Pb-Pb collisions [19, 17, 11]. In heavy-ion collisions at the LHC energies, such mass-dependent effect are considered as the consequence of evolution of the system with common radial flow velocity. For a better comparison of $\langle p_{\mathrm{T}} \rangle$ in small system, the results of the pp collisions at $\sqrt{s} = 13$ TeV are fitted with the function $a - \frac{b}{(\langle \mathrm{d}N_{\mathrm{ch}}/\mathrm{d}\eta \rangle + c)}$ represented by the solid red line. In the lower panel of the figure, a comparison between the data ratios in different collisions energies to pp 13 TeV fitted line are shown. These results indicate a little increase in $\langle p_{\mathrm{T}} \rangle$ for pions at the highest centre-of-mass energy, while for protons, it is similar at the two centre-of-mass energies.

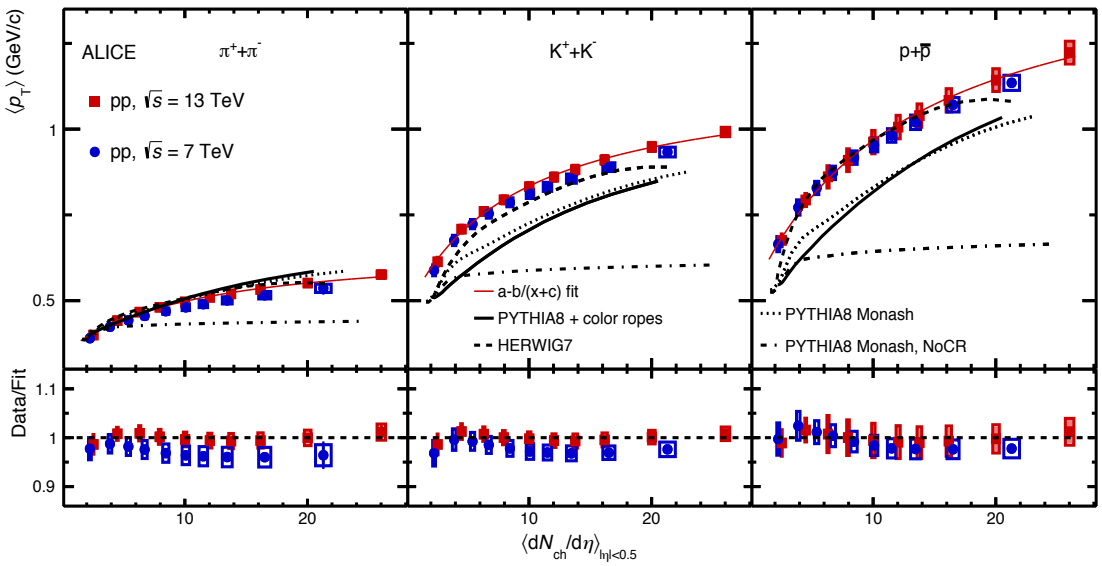

Fig. 4.13 (Upper panels) The $\langle p_{\mathrm{T}} \rangle$ of π, K and p as a function of multiplicity in pp collisions at $\sqrt{s} = 13$ TeV are compared with the results of lower energy pp collisions as well as with different MC event generators. The solid line represents the $a - \frac{b}{(\langle \mathrm{d}N_{\mathrm{ch}}/\mathrm{d}\eta \rangle + c)}$ fit of pp 13 TeV data. (Lower panels) The ratios of $\langle p_{\mathrm{T}} \rangle$ in different collisions energies to the fitted line.

Moreover, the prediction of different Monte Carlo models such as the HERWIG7, PYTHIA8 Monash with colour reconnection and PYTHIA8 with colour ropes are also shown in Fig. 4.13. From the figure, it could be observed that all the models provide a very good description of the pions $\langle p_{\mathrm{T}} \rangle$ evolution with charged-particle multiplicity. These three models are tuned to describe the $\langle p_{\mathrm{T}} \rangle$ of charged particles, and hence, a good description of pions $\langle p_{\mathrm{T}} \rangle$ is expected as they are the most abundant particles produced in hadronic collisions. On the contrary, $\langle p_{\mathrm{T}} \rangle$ of kaons and protons are well described by the HERWIG7 model only, while PYTHIA8 with colour ropes and PYTHIA8 with colour reconnection model underestimate the $\langle p_{\mathrm{T}} \rangle$ in the whole multiplicity range studied. Furthermore, it is also observed that the PYTHIA8 Monash model without colour reconnection could not describe the evolution of $\langle p_{\mathrm{T}} \rangle$ with multiplicity for all the identified particles.

The p_{T}-integrated K/π and p/π yields ratios for pp collisions at $\sqrt{s} = 13$ TeV are plotted in Figs. 4.14(a) and 4.14(b) respectively and are then compared with the already published results of the pp, p-Pb and Pb-Pb collisions system at the different centre-of-mass energies [19, 11, 17]. From the figure, the K/π ratio is observed to increase with increasing charged-particle multiplicity from low to high multiplicity pp collisions. A similar increase has also been observed in the p-Pb and Pb-Pb collisions, where such an increase in the K/π ratio with increasing multiplicity can be well described by the enhanced production of strange quarks in the medium or due to a reduced canonical suppression of strangeness production in larger freeze-out volumes [17, 11]. On the other hand, the p/π ratio measurement is almost independent of the multiplicity classes studied for pp collisions. However, for Pb-Pb colliding system, the p/π ratio indicates a decreasing trend, which is expected due to annihilation of baryon-antibaryon in the hadronic phase [203–209]. Furthermore, it is evident that both the particle ratios follow a common trend from low multiplicity pp to p-Pb and then up to central Pb-Pb collisions, independent of the size of the colliding systems and collisions centre-of-mass energy.

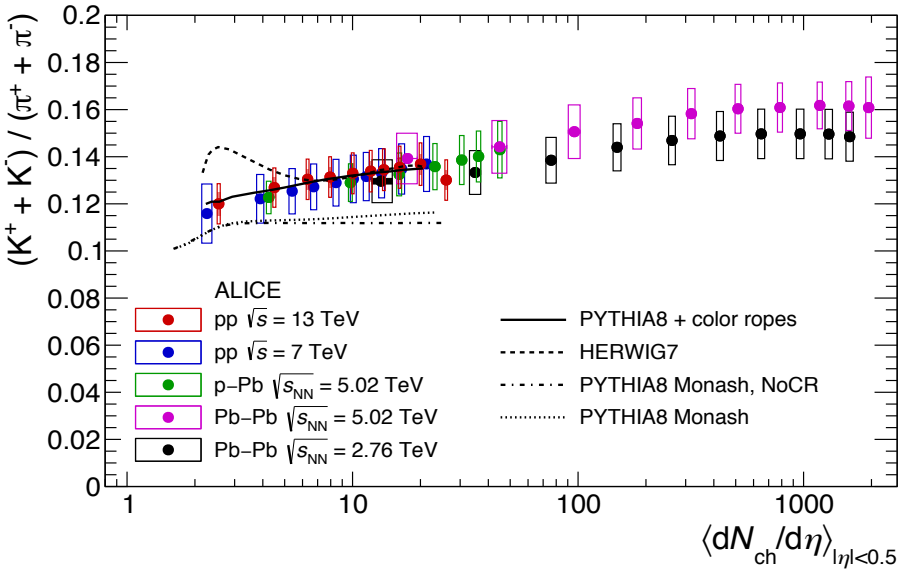

(a)

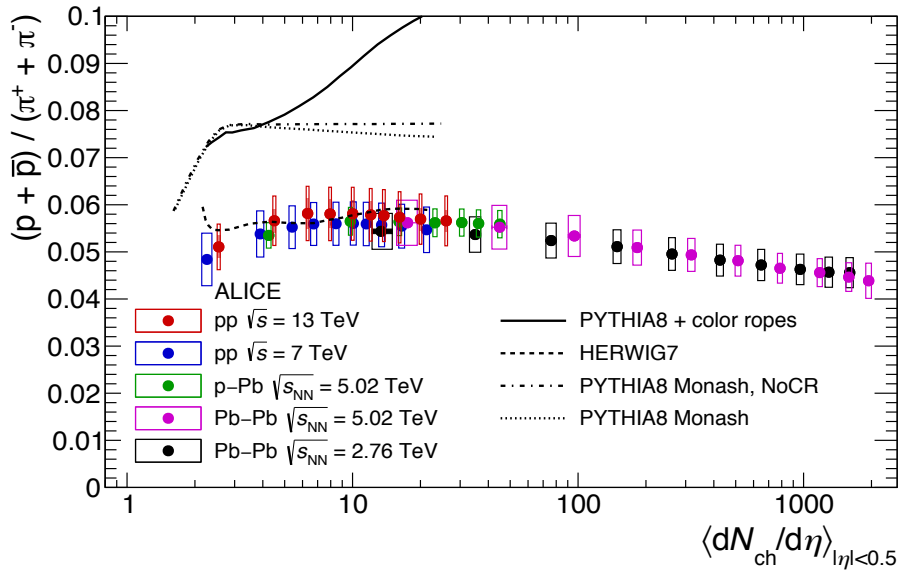

(b)

Fig. 4.14 p_T-integrated (a) K/π and (b) p/π yields ratios as a function of charged-particle multiplicity in pp collisions at $\sqrt{s} = 13$ TeV are compared with the results of the lower energy pp, p-Pb and Pb-Pb collisions. The prediction from different Monte Carlo event generators are also shown.

The Monte Carlo predictions for the K/π and p/π yields ratios in pp collisions are also shown in Fig. 4.14(a) and 4.14(b), respectively. The PYTHIA8 with the colour ropes model seems to describe the evolution of the K/π ratio with increasing multiplicity very well. The HERWIG7 model is also found to describe the K/π ratio quite well for all the multiplicity classes except for the very low multiplicity class, where a peak-like structure could be observed in the ratio of the yields. The PYTHIA8 Monash prediction with and without colour reconnection seems to underestimate the measured data results. On the other hand, for the p/π ratio, the HERWIG7 can describe the ratio quite well in the measured multiplicity classes, whereas, all the version of the PYTHIA8 overestimates the p/π ratio. Moreover, PYTHIA8 with colour ropes predict an increase in the p/π ratio with increasing charged-particle multiplicity, which could be attributed to the enhanced production of strange and di-quark during the rope fragmentation.

Furthermore, the p_{T}-integrated yields of pions provide the reference measurements for different strange and multi-strange hadrons. Therefore, the availability of yields of the strange and multi-strange hadrons [186] offers the opportunity to investigate the relative abundances of the hyperons to pions. The yields ratios of K^0_s, Λ, Ξ, and Ω to π as a function of charged-particle multiplicity for pp collisions at $\sqrt{s} = 13$ TeV are shown in Fig. 4.15 and are compared with the results of the lower energy pp, p-Pb and Pb-Pb collisions at the LHC [20, 17, 11]. As observed in lower energy pp collisions [20], a significant enhancement in the strange and multi-strange particle production could also be seen with increasing charged-particle multiplicity in pp collisions at $\sqrt{s} = 13$ TeV. This behaviour is reminiscent of that observed in lower energy pp and p-Pb collisions, considering the values of the ratio and their evolution with multiplicity [20, 18]. This thesis studies reveal no significant dependence on the centre-of-mass energy for pp collisions at the LHC energies. Moreover, all the results of Figs. 4.14 and 4.15 indicate that the hydrochemistry of the particles at the LHC energies

scaled with the final-state charged-particle multiplicity density rather than the collisions energy or colliding systems.

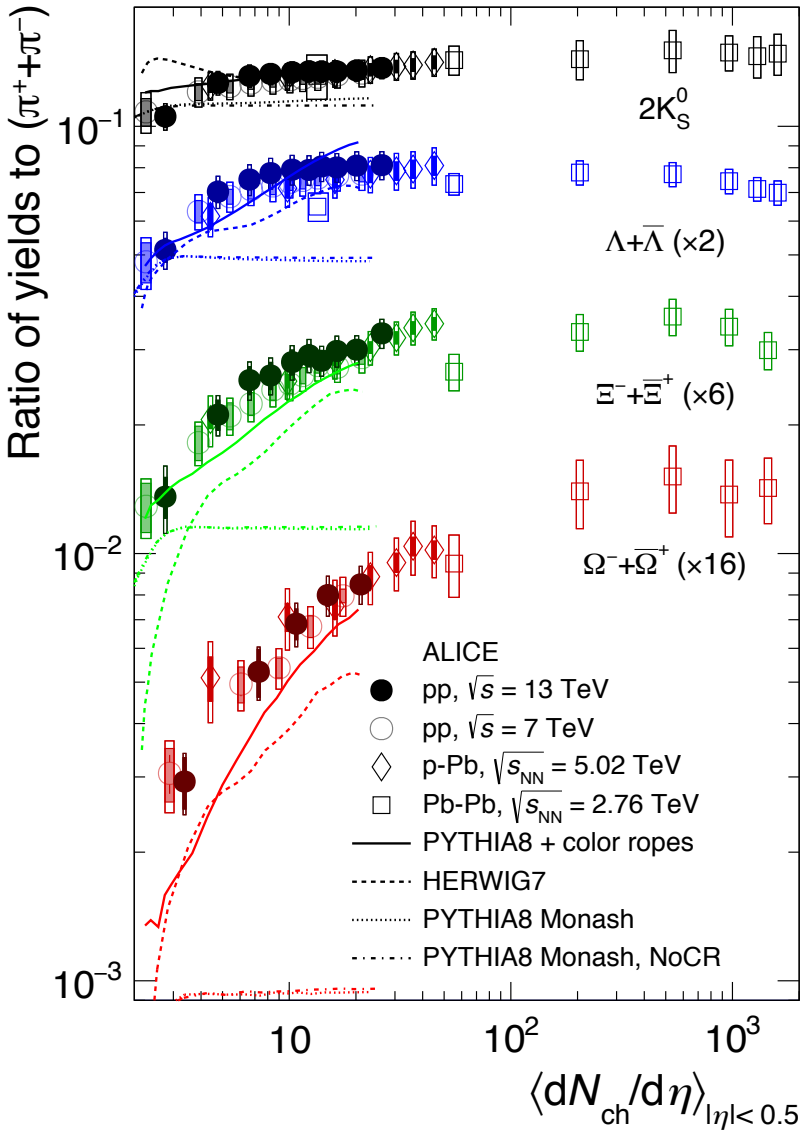

Fig. 4.15 p_T-integrated yields ratios of K^0_s/π, Λ/π, Ξ/π and Ω/π as a function of multiplicity in pp collisions at $\sqrt{s} = 13$ TeV are compared with the results of lower energy pp, p-Pb and Pb-Pb collisions. Prediction from different Monte Carlo event generator are also shown.

The prediction of yields ratios of different particles w.r.t pions for different Monte Carlo (MC) models are also shown in Fig. 4.15. The PYTHIA8 Monash with and without colour reconnection is unable to describe all the particle ratios evolution with charged-particle

multiplicity. On the other hand, PYTHIA8 with the colour ropes quantitatively predict the enhancement of strange and multi-strange baryon production with increasing charged-particle multiplicity. The most significant quantitative difference could be observed for the Ω/π ratio in the low multiplicity class, whereas, the predictions for the Ξ/π ratios are seen to be in good agreement. The prediction of the Λ/π ratios shows an increasing trend in the studied multiplicity classes, but overestimate the ratios at the highest multiplicity. Further, the HERWIG7 model with baryonic ropes qualitatively predicts the enhancement of strange and multi-strange baryon production with increasing charged-particle multiplicity. The Λ/π ratios are well described by HERWIG7, whereas, the low multiplicity classes of Ξ/π ratios and all the Ω/π ratios show the largest difference than the data results. Overall, the description of the hadrons to pions ratios results with all the MC models get worse for the particles with larger strangeness content and therefore, require further tuning of the studied MC generators.

4.4 Summary

The π, K and p production measurement as a function of charged-particle multiplicity in pp collisions at $\sqrt{s} = 13$ TeV has been performed in this chapter. The studied p_{T} spectra of the identified charged hadrons at low p_{T} becomes harder with increasing multiplicity, and the effect is more pronounced for heavier particles like protons, similar to those observed for the heavy-ion collisions with hydrodynamical evolution. At high p_{T} (> 8 GeV/c), the spectral shape of the particles become independent of the multiplicity class considered as predicted by the pQCD calculation [195]. Moreover, the average transverse momentum of the particles are also studied, and a similar mass-dependent hardening as observed in the p_{T} spectra could be seen. The hardening of the $\langle p_{\mathrm{T}} \rangle$ with increasing charged-particle multiplicity is observed to describe by the PYTHIA8 with colour ropes, PYTHIA8 Monash with colour reconnection

and HERWIG7 MC models. All the three models provide a good quantitative description of the pions $\langle p_{\mathrm{T}} \rangle$, whereas, the HERWIG7 only qualitatively describes the $\langle p_{\mathrm{T}} \rangle$ of K and p.

The p_{T}-differential K/π ratio shows no evolution with increasing charged-particle multiplicity, whereas, for the p/π ratio, a depletion at low p_{T}, an enhancement at the intermediate p_{T} and a constant behaviour at the high p_{T} could be observed. The measured particle ratios in pp collisions at $\sqrt{s} = 13$ TeV are consistent with those measured at pp collisions at $\sqrt{s} = 7$ TeV. The predictions of different MC models describe the evolution of the p_{T}-differential K/π and p/π ratios with multiplicity in some p_{T} bins, while none of them could provide a consistent description of the data in all p_{T} bins.

The p_{T}-integrated hadrons to pions ratios as a function of the charged-particle multiplicity shows no evolution with the centre-of-mass energy and the measurement performed at pp collisions at $\sqrt{s} = 13$ TeV are compatible with the results available at pp, p-Pb and Pb-Pb collisions at $\sqrt{s_{NN}} = 7$, 5.02 and 2.76 TeV, respectively. These results indicate that the chemical composition of primary hadrons at the LHC energies scales with charged-particle multiplicity rather than collisions energy or colliding system. A comparison with the different MC generator shows that the PYTHIA8 with colour ropes provide the best description for the (multi-)strange hadron, but overestimate the value for the p/π ratio. The HERWIG7 also describes the evolution of the ratios with multiplicity but underestimate the values of Ξ/π and Ω/π ratios. None of the event generators can provide a consistent quantitative evolution of the measured hadrons to pions ratios with multiplicity in pp collisions at $\sqrt{s} = 13$ TeV. Further, the prediction of the hadrons to pions ratios with the charged-particle multiplicity of different MC generator becomes worse for the particles with larger strangeness content and therefore, require further tuning of the studied MC generators.

5

Dynamical fluctuation in charged particles emission spectra of high multiplicity pp collision at the LHC energies

5.1 Introduction

Ultra-relativistic nucleus-nucleus collisions provide the unique opportunity to study the properties of the matter formed during collisions. Moreover, understanding the particle

production mechanism is also one of the primary goals of high energy A+A and h+h collisions. A characteristic feature of primary charged particles produced in any such collision is that they often exhibit large fluctuation in the number densities of particles over the pseudorapidity space. Such fluctuation is much larger than the statistical fluctuations arising due to finiteness of the yield of particles produced in a collision. In the pseudorapidity distribution spectra, these fluctuations manifest themselves as peaks and valleys in narrow domains of pseudorapidity space. Such anomalous fluctuation resulting in a 'spike' like structure in single-particle density distribution spectrum is often used to investigate if the nuclear matter has undergone phase transition during the process of evolution of a collision [32–34]. Further, a study on such fluctuation is also important from the point of view that such anomalous spatial fluctuation may arise because of the possible formation of a significant number of mini-jets as a result of semi-hard parton-parton interactions or gluon bremsstrahlung [23–25].

To gather any meaningful information about the particle production mechanism, it is therefore important to disentangle and analyze these anomalous fluctuations, arising out of some dynamical processes, from that of noise arising due to the finite number of available particles in the final state. The scaled factorial moment (SFM) technique, as proposed by Bialas and Peschanski [23], is found to be a useful mathematical tool that separates the dynamical fluctuation from the mixture of the two. According to this prescription, a power-law growth of the averaged scaled factorial moments ($\langle F_q \rangle$) with the decrease of the phase space bin width (δw), or otherwise, the number of bins M into which the entire phase space is divided, that is, $\langle F_q \rangle \propto (M)^{\alpha_q}$ is referred to as intermittency and thus indicates the presence of the contribution of the dynamical fluctuation in the data sample. Intermittency, in turn, is found to be related with self-similarity and fractality of emission spectra as well as the particle emitting source [210]. The exponent α_q of the power law, called intermittency index, is connected with anomalous dimension d_q ($= D - D_q$) through the relation $d_q = \alpha_q/(q-1)$,

where D is the ordinary topological dimension of the space into which the fractal objects are embedded, and D_q is the generalized q^{th} order Renyi dimension [211, 26]. Knowledge of order dependence of d_q is helpful to make comments on the fractal nature of emission spectra and in turn on particle production mechanism and associated phase transition, if any.

Indications of the existence of a new state of matter where quarks and gluons are considered as the degrees of freedom and generally known as the quark-gluon plasma (QGP), have been provided for A+A collisions by previous studies at the CERN Super Proton Synchrotron (SPS) [3] and the Relativistic Heavy-Ion Collider (RHIC) [4–10] and then at CERN Large Hadron Collider (LHC) [11–14]. On the other hand, in small systems like pp collisions, with a few available partons for the collisions, no such phase transition is expected and is traditionally considered as the reference system for the heavy-ion collision studies. Due to early thermalisation, it also remains doubtful if the matter formed in such collisions exhibits collective-like behaviour as observed in heavy-ion collisions [212]. However, with the increased energy for the proton-proton colliding system at the LHC, the high multiplicity pp events reach multiplicity comparable to proton-nucleus and nucleus-nucleus collisions [20]. Recent experimental measurements in pp collisions show that the flow-like effects do exist in high multiplicity pp events as well, indicating collective behaviour in such a small system [20]. Thus, systematic studies on various observable of high multiplicity pp events have become essential for a better understanding of the dynamics of such collisions.

5.2 Computing facility for generation of the Monte Carlo events

In this thesis, for the studies of dynamical fluctuations in pp collisions, PYTHIA Monte Carlo event generated data have been used. Some detailed information about the PYTHIA event generator is given in Section 5.3. As the focus of this investigation is on the high-

multiplicity pp collisions and the production cross-sections for such events are very small, a large amount of data needs to be generated. For this purpose, the High-Performance Computing Cluster (HPCC) facility available at the Nuclear and Radiation Physics Research Laboratory (NRPRL) has been used.

The HPCC facility consists of one master server, and three compute servers. The master server of the HPCC is coupled with the compute servers for parallel computation. This master blade server consists of 24 nodes, and all of them are reserved for operating software. The compute 1, 2 and 3 servers contain 24 nodes (48 threads), 12 nodes (24 threads) and 24 nodes (48 threads), respectively. Therefore, the total number of available threads in the server is 120, and all of them can be used for parallel computation. These servers operate through CentOS7.6 operating system (OS). The Rocks Cluster Distribution having version 7.0 is implemented in the master server. For parallel computation in the compute nodes, jobs are submitted via Sun Grid Engine (SGE). Apart from generating events and computation, for storing a large amount of generated sets of data, an external hard-disk having the total storage capacity of (4 TB $\times$ 4 =) 16 TB is used. The complete HPCC facility with the external storage system is shown in Fig. 5.1.

5.3 PYTHIA Monash event generator

The PYTHIA Monte Carlo event generator is a general-purpose perturbative-QCD (pQCD) based event generator. It uses a factorised perturbative expansion for the hard parton-parton interaction, combined with parton showers and details models for hadronisation and multiple parton interactions. The various step involves for the generation of events in PYTHIA are described as follows:

Fig. 5.1 The HPCC facility available at the NRPRL along with the external hard-drive and UPS facility is shown.

1. At first, two beams of the particle come towards each other. These particles are characterised by a set of the parton distribution function, and they define the partonic substructure in terms of energy sharing and flavour composition.

2. The partons from each of the beam can now start off a sequence of branching, such as $q \rightarrow qg$, which build up an initial-state shower.

3. An incoming parton from each of the shower interact via hard process, where the numbers of outgoing partons are then produced. The number limited to two in PYTHIA and the nature of this process determines the main characteristics of the event.

4. The hard process may produce short-lived resonances, like the Z^0, $W^{\pm}$ gauge bosons. These then decay to normal partons, which has a close association with the hard process.

5. The outgoing partons may branch as well to build up the final-state showers.

6. Other than the hard process, the remaining partons of the incoming beam may also interact via the semi-hard process.

7. Once a shower initiator from a beam particle is taken out, a beam remnant is left behind. Now, this beam remnant may have some internal structure and a net colour charge that relates it to the rest of the final state.

8. The colour confinement mechanism of QCD ensures that the outgoing partons are not observable; instead, they fragment into a colour neutral hadrons.

9. Different produced hadrons in the above-described interactions are unstable and therefore, they decay to stable hadrons.

5.4 Motivation for the study of dynamical fluctuation in PYTHIA-generated high-multiplicity pp collisions

The PYTHIA event generator has been extensively used to describe the pp collisions data and is found to be quite successful in explaining various experimental results of pp collisions at the LHC energies [36, 35, 37]. Different parameters of the existing PYTHIA model have been improved or tuned from time to time to describe the data well. In PYTHIA Monash version, the parameters are tuned in such a way that a better description of the experimental data at the LHC energies $\sqrt{s} = 7$ and 13 TeV could be achieved [149]. Complete details of the PYTHIA event generator are available in Refs. [149, 213]. In this work, an attempt has been made with the PYTHIA Monash generated data to study, within ALICE acceptance, the non-statistical fluctuation of single-particle density distribution spectrum in the light of scaled factorial moment (SFM) for pp collisions at the LHC energies $\sqrt{s} = 2.76$, 7 and 13 TeV.

Apart from the previously described various mechanism in PYTHIA, colour reconnection (CR), a string fragmentation model, has also been implemented. In this mechanism, the final partons are considered to be colour connected in such a way that the total string length becomes as short as possible [214]. It has been reported recently that CR mechanism in PYTHIA can mimic the effect of collective-like behaviour, such as a mass-dependent rise in $\langle p_{\mathrm{T}} \rangle$ with multiplicity, bump in baryon to meson ratio at intermediate p_{T} etc. as observed in heavy-ion collisions [150, 11]. Such behaviour is attributed to the fact that due to CR, partons from two independent interactions select a preferred pseudo-rapidity (η) and azimuthal (ϕ) angle of emissions giving rise to boost in p_{T} and higher-order flow. Since, an increase in the scaled factorial moment with the decrease of phase space bin width is considered to be an indication of the presence of large fluctuation in the data sample, which in turn is related with the phase transition and particle production mechanism, in this work, an attempt has

also been made to find if colour reconnection has any significant role to play on intermittency and other related observables of nuclear collisions.

The approximate number of the event generated using the PYTHIA Monash (default) Monte Carlo (MC) event generator for pp collisions at $\sqrt{s} = 2.76$, 7, and 13 TeV are 87×10^6, 70×10^6, and 32×10^6, respectively.

5.5 The Scaled Factorial Moments Technique

The technique of the scaled factorial moment estimation is a well established mathematical tool of high energy nuclear collision studies and is described in details in a number of works [23–30]. However, in this thesis, for completeness of the chapter only, some of the relevant steps are described hereunder.

Let us consider the distribution of the primary charged particles in the pseudorapidity [$\eta = -\ln\tan(\theta/2)$] space. Let $\Delta\eta$ be the overall interval of the space, and n is the total number of particles in an event within $\Delta\eta$. If the overall interval is divided into M equal parts, we get bins of smaller width $\delta\eta = \Delta\eta$/M, and if the number of particles falling within m^{th} such bin is n_m, then $n = \sum n_m$, where the summation runs over m from m = 1 to M. The factorial moment (f_q) of order q can now be calculated from the m^{th} bin as [215]:

$$f_q = n_m(n_m-1)\cdots(n_m-q+1) \tag{5.1}$$

Such moments for a particular bin is first calculated for all events and then averaged over all events. This average moment is then calculated for all bins and again averaged over all bins. This method of averaging procedure is called the vertical averaging [23, 29, 215].

On the other hand, if the factorial moments is first calculated for a bin and then averaged over all bins and this averaged moments is then calculated for all events and again averaged over all events, then this method of estimation of scaled factorial moments is called horizontal

averaging [23, 25, 26, 29]. While the technique of vertical averaging takes accounts of the dynamical fluctuation in event space, the horizontal averaging takes account of the non-statistical fluctuation in phase space of an event.

The expression for the vertically averaged scaled factorial moment is given by:

$$\langle F_q \rangle = \frac{1}{M} \sum_{m=1}^{M} \frac{1}{N} \sum_{i=1}^{N} \frac{n_m(n_m-1)\cdots(n_m-q+1)}{\langle n_m \rangle^q} \tag{5.2}$$

and the horizontally averaged scaled factorial moments is expressed as:

$$\langle F_q \rangle = \frac{1}{N} \sum_{i=1}^{N} M^{q-1} \sum_{m=1}^{M} \frac{n_m(n_m-1)\cdots(n_m-q+1)}{\langle n \rangle^q} \tag{5.3}$$

Where N is the total number of events in the data sample.

Here, it is worth mentioning that the horizontal scaled factorial moment technique has the limitation of its dependence on the shape of the single-particle density distribution spectra. However, the shape dependence of the horizontally averaged SFM can be eliminated by converting the distribution of the particles in pseudorapidity space to a distribution of a new cumulative variable $\chi(\eta)$, defined as [216, 217, 22, 218]:

$$\chi(\eta) = \frac{\int_{\eta_{min}}^{\eta} \rho(\eta) d\eta}{\int_{\eta_{max}}^{\eta_{min}} \rho(\eta) d\eta} \tag{5.4}$$

In $\chi(\eta)$ space, the density distribution spectrum would be perfectly flat.

For power law type dependence of $\langle F_q \rangle$ on M, i.e. if $\langle F_q \rangle \propto (M)^{\alpha_q}$, a plot of $\ln\langle F_q \rangle$ vs. lnM should be a straight line with the slope as the exponent of the power law.

$$\alpha_q = \frac{\Delta ln \langle F_q \rangle}{\Delta ln M} \tag{5.5}$$

α_q, called the intermittency index, is related to the anomalous fractal dimension d_q $(= D - D_q)$ through the relation:

$$d_q = \frac{\alpha_q}{q-1} \tag{5.6}$$

An order invariance of d_q refers to monofractality whereas an increase of d_q with q refers to the multifractal nature of the emission spectra [211, 26].

5.6 Results and discussions

The pseudorapidity distributions of the primary charged particles within the acceptance of ALICE detector, for both minimum bias (MB) and high multiplicity ($N_{ch} > 50$ for 2.76 TeV and $N_{ch} > 60$ for 7 and 13 TeV) (HM) pp collisions at $\sqrt{s} = 2.76$, 7 and 13 TeV with the present set of generated data are shown in Figs. 5.2(a) and 5.2(b) respectively and are compared with the existing experimental results of ALICE Collaboration for INEL>0 [35, 219]. From these figures, it is found that the pseudorapidity distributions of MC generated events agrees well with the experimental data for the studied region of $|\eta| < 0.8$. It is therefore believed that further analysis of our generated data using the scaled factorial moment technique might be of some significance.

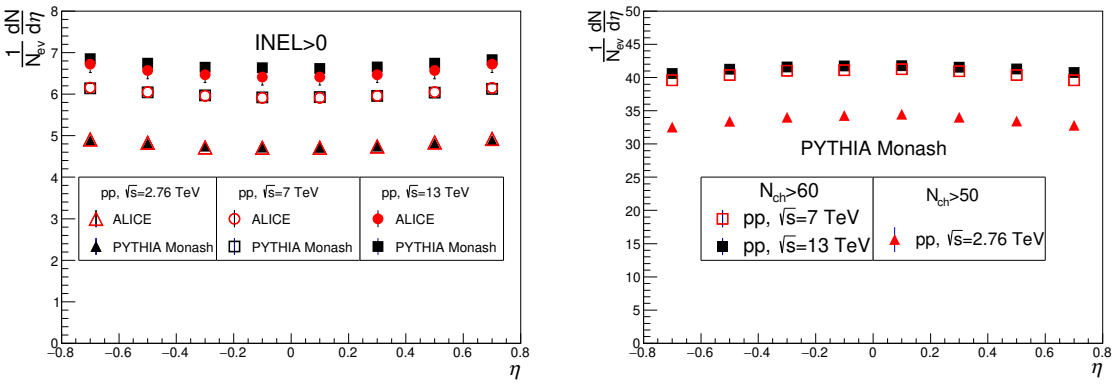

(a) Minimum bias pp collisions (b) High multiplicity pp collisions

Fig. 5.2 Pseudorapidity distribution of the primary charged particles for PYTHIA Monash (default) generated data (a) compared with experimental data of ALICE in minimum bias pp collisions [35, 219] and (b) in high multiplicity pp events at $\sqrt{s}$ = 2.76, 7 and 13 TeV.

Fig. 5.3 represents the same distributions of Figs. 5.2(a) and 5.2(b), but in $\chi(\eta)$ space for the generated sets of data only for MB and HM pp events of $\sqrt{s} = 2.76$, 7 and 13 TeV. It could be readily seen from Fig. 5.3 that, as expected, the various distributions of Figs. 5.2(a) and 5.2(b) become perfectly flat in $\chi(\eta)$ space.

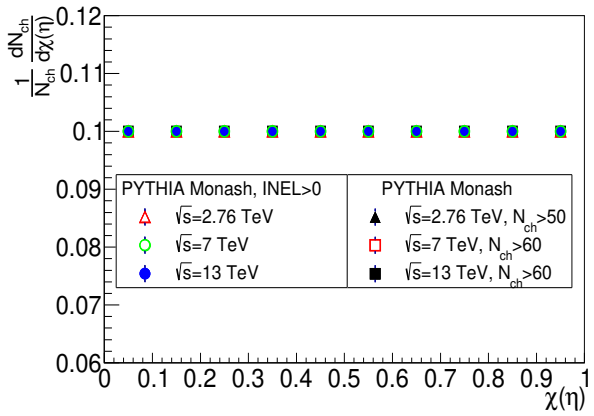

Fig. 5.3 $\chi(\eta)$ distribution of the primary charged particles produced in MB and HM pp event at $\sqrt{s}$ = 2.76, 7 and 13 TeV with PYTHIA Monash (default) generated data.

The horizontally averaged scaled factorial moments $\langle F_q \rangle$ for different order q = $2-5$ for minimum bias pp collisions at $\sqrt{s} = 2.76$, 7 and 13 TeV have been estimated for $\chi(\eta)$ space using Eq. (5.3) and plotted against the number of phase space bin M in log-log scale and is shown in Fig. 5.4(a). The same amount of events are generated using a random number (RAN) generator with values lying between 0 and 1 and the estimated $\ln\langle F_q \rangle$ vs. lnM are plotted in the same Fig. 5.4(a). No significant rise in $\ln\langle F_q \rangle$ against lnM could be seen for both MB and the random number generated data giving no indication of the presence of any dynamical fluctuation in the emission spectra of primary particles of MB events in $\chi(\eta)$ space.

In Fig. 5.4(b), the $\ln\langle F_q \rangle$ against lnM plot is shown for the high-multiplicity pp collisions at $\sqrt{s} = 2.76$, 7 and 13 TeV. The solid green lines represent the straight-line fit of the data points. The straight-line fitting is done keeping the correlation coefficient value $R^2 = 0.99$. The errors shown in these plots are statistical errors only. It could be readily seen from

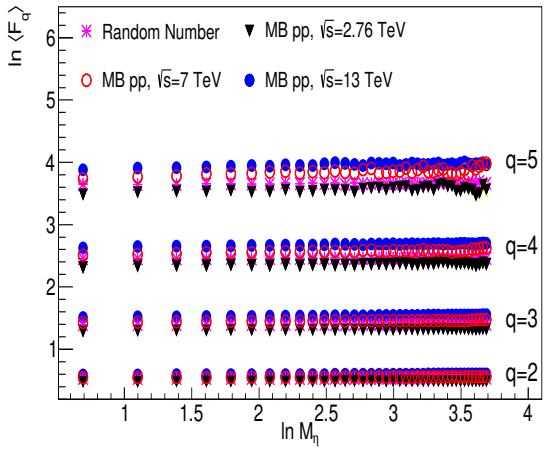

(a)

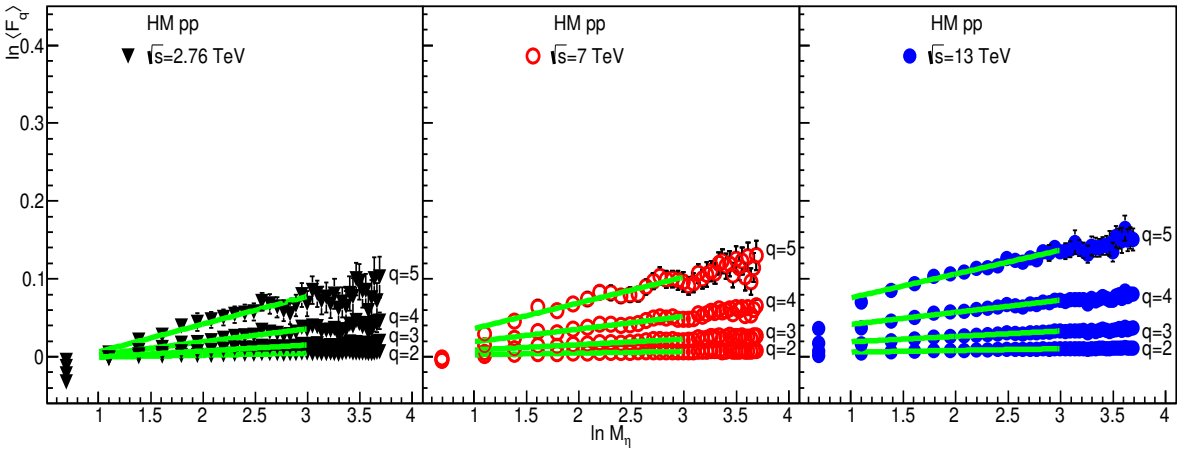

(b)

Fig. 5.4 $\ln\langle F_q\rangle$ vs. lnM plots for moments q = 2 – 5 for (a) RAN, MB pp collisions and (b) HM pp collisions at $\sqrt{s} = 2.76$, 7 and 13 TeV in one-dimensional $\chi(\eta)$ space with PYTHIA Monash (default) generated data.

the plot that $\ln\langle F_q \rangle$ increases linearly with the increase of lnM, and the increase is more pronounced for the higher moments. This behaviour is a clear indication of the presence of intermittency and multi-particle correlation in pseudorapidity space in the emission spectra of PYTHIA Monash (default) generated primary particles of high multiplicity pp events at $\sqrt{s} = 2.76$, 7 and 13 TeV.

The intermittent pattern in the emission source of the particle in high energy nuclear collisions may be different in different phase space, depending on the nature of the emission spectra. To realise the (a)symmetric nature of the intermittent pattern in pp collisions at the LHC energies, the same analysis has also been carried out in one-dimensional azimuthal (ϕ) space.

The azimuthal angle distributions of the primary charged particles within the acceptance of ALICE detector, for both MB and HM pp collisions at $\sqrt{s} = 2.76$, 7 and 13 TeV with the PYTHIA generated sets data are shown in Figs. 5.5(a) and 5.5(b) respectively. These ϕ distributions are then converted to $\chi(\phi)$ value as done for η distributions. As the plot of $\chi(\phi)$ looks the same as that of $\chi(\eta)$ (Fig. 5.3), the $\chi(\phi)$ distributions for different types of event classes are not shown here.

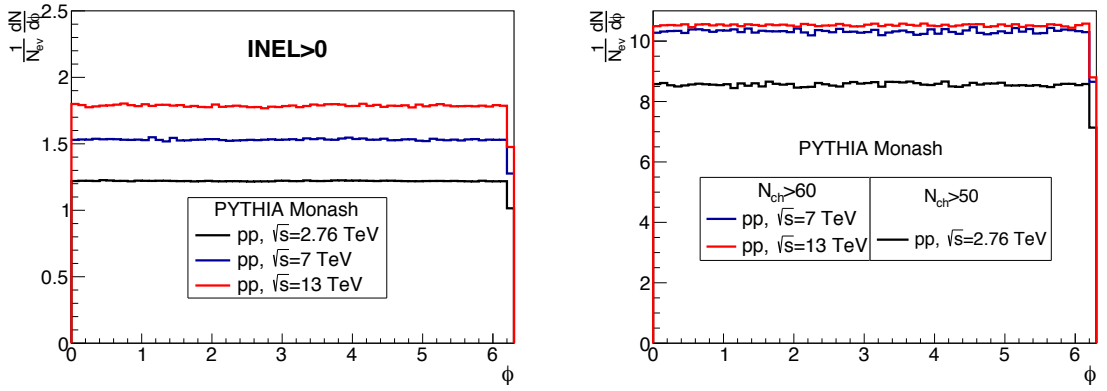

(a) Minimum bias pp collisions

(b) High multiplicity pp collisions

Fig. 5.5 Azimuthal angle distribution of the primary charged particles for PYTHIA Monash (default) generated data (a) in minimum bias and (b) in high multiplicity pp events at $\sqrt{s}$ = 2.76, 7 and 13 TeV.

The $\ln\langle F_q\rangle$ has also been estimated for one-dimensional $\chi(\phi)$ space using Eq. (5.3) for q = $2-5$ in both minimum bias and high multiplicity pp collisions at $\sqrt{s} = 2.76$, 7 and 13 TeV and are plotted against lnM as shown in Figs. 5.6(a) and 5.6(b) respectively. A small rise in $\ln\langle F_q\rangle$ against lnM is evident from Fig. 5.6(a) for moments q = 4 and 5 in MB pp collisions. On the other hand, from Fig. 5.6(b) for HM pp events, a clear increase in the $\ln\langle F_q\rangle$ against lnM could be observed for q $= 2-5$. The intermittency index α_q, for the high multiplicity pp events of different energies, estimated from the straight-line fit of the data points (lnM = 1.0 to 3.0) in $\chi(\eta)$ and $\chi(\phi)$ spaces, are respectively found to be same within the statistical error, and therefore the values corresponding to $\sqrt{s} = 13$ TeV are only listed in Table. 5.1. From the obtained values of the α_q, the emission of particles is found to be more intermittent in $\chi(\phi)$ space than $\chi(\eta)$space.

Table 5.1 The values of the intermittency index α_q in high multiplicity pp events at $\sqrt{s} = 13$ TeV for different moments q in $\chi(\eta)$ and $\chi(\phi)$ spaces.

q	Intermittency index (α_q) for $\sqrt{s} = 13$ TeV		R^2
	$\chi(\eta)$ space	$\chi(\phi)$ space	
2	0.0022 ± 0.0004	0.0202 ± 0.0005	0.99
3	0.0070 ± 0.0008	0.066 ± 0.0010	0.99
4	0.016 ± 0.0014	0.150 ± 0.0019	0.99
5	0.031 ± 0.0029	0.291 ± 0.0038	0.99

Furthermore, the intermittent behaviour that occurs in higher dimensional space may disappear or saturate at small phase space intervals in one-dimensional space. This is believed to happen due to the reduction of fluctuation by the averaging process in lower-dimensional projection. This is reported out by Ochs [31]. Therefore, the study of fluctuation in higher dimensional space has become significantly important, particularly for the MB pp collisions.

To study the dynamical fluctuation in two-dimensional pseudorapidity-azimuthal $(\eta-\phi)$ space, the one-dimensional $\chi(\eta)$ and $\chi(\phi)$ distributions have been mapped into a two-dimensional $\chi(\eta-\phi)$ distribution as shown in Fig. 5.7. The two-dimensional $\chi(\eta-\phi)$ space is now successively divided into $M_i \times M_i$ bins of equal width $\delta\chi_\eta \times \delta\chi_\phi$ where $i = 1$

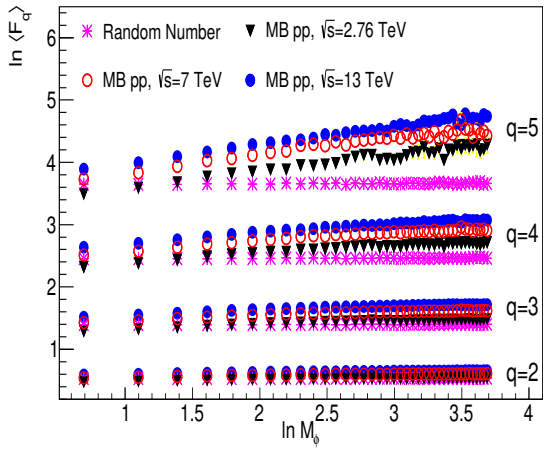

(a)

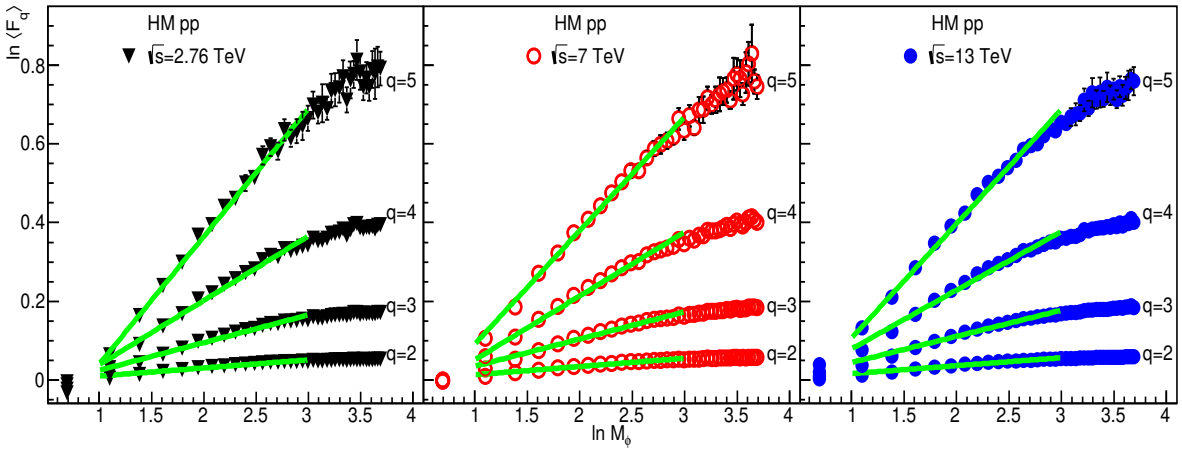

(b)

Fig. 5.6 $\ln\langle F_q\rangle$ vs. lnM plots for moments q = 2 – 5 for (a) RAN, MB pp collisions and (b) HM pp collisions at $\sqrt{s} = 2.76$, 7 and 13 TeV in one-dimensional $\chi(\phi)$ space with PYTHIA Monash (default) generated data.

to 10. The numbers of particles in each square bin are counted, and its corresponding scaled factorial moments (SFM) are estimated. Finally, the obtained SFM are averaged over all bins and all events to obtain $\langle F_q \rangle$ for $M = M_i \times M_i = 2 \times 2 = 4$, say [28, 22].

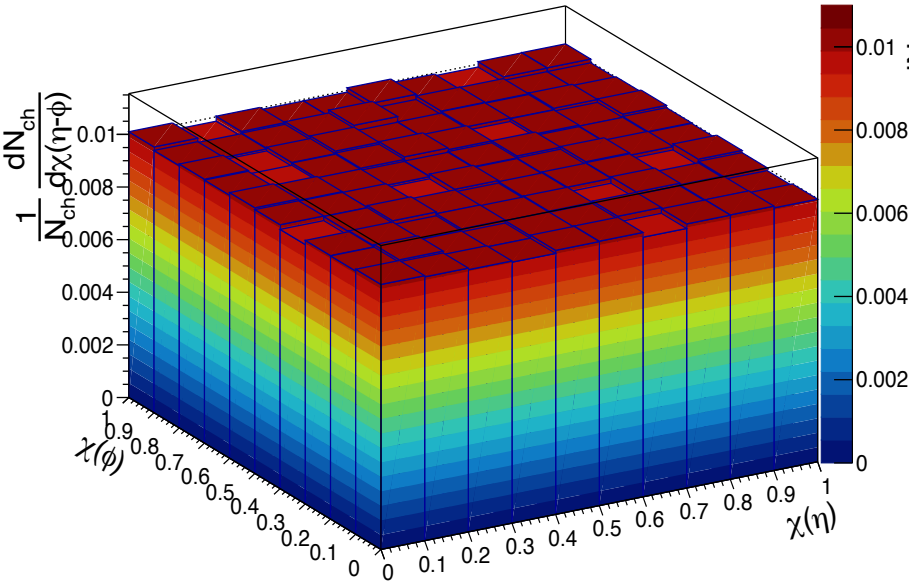

Fig. 5.7 $\chi(\eta - \phi)$ distribution of the primary charged particles produced in HM pp event at $\sqrt{s}$ = 13 TeV with PYTHIA Monash (default) generated data.

The $\ln\langle F_q \rangle$ estimated for the two-dimensional $\chi(\eta - \phi)$ space is plotted against lnM for different order q = $2-5$ for minimum bias and high multiplicity pp collisions at $\sqrt{s} = 2.76$, 7 and 13 TeV are shown in Figs. 5.8(a) and 5.8(b) respectively. From the two-dimensional analysis, a weak intermittent type of emission could now be seen for MB pp events for all the studied energies, as shown in Fig. 5.8(a). For all the three energies, the intermittency index α_q, within the statistical error, are respectively found to be same for MB and HM pp events, and therefore, the values corresponding to $\sqrt{s} = 13$ TeV are only listed in Table. 5.2.

The anomalous dimension d_q has been estimated using the Eq. (5.6) for MB pp events in $\chi(\eta - \phi)$ space and for high multiplicity pp events in $\chi(\eta)$, $\chi(\phi)$ and $\chi(\eta - \phi)$ spaces at $\sqrt{s} = 13$ TeV. The variations of d_q with the order of the moments q are shown in Fig. 5.9.

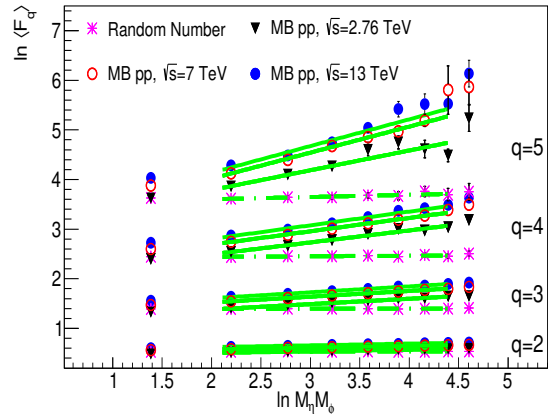

(a)

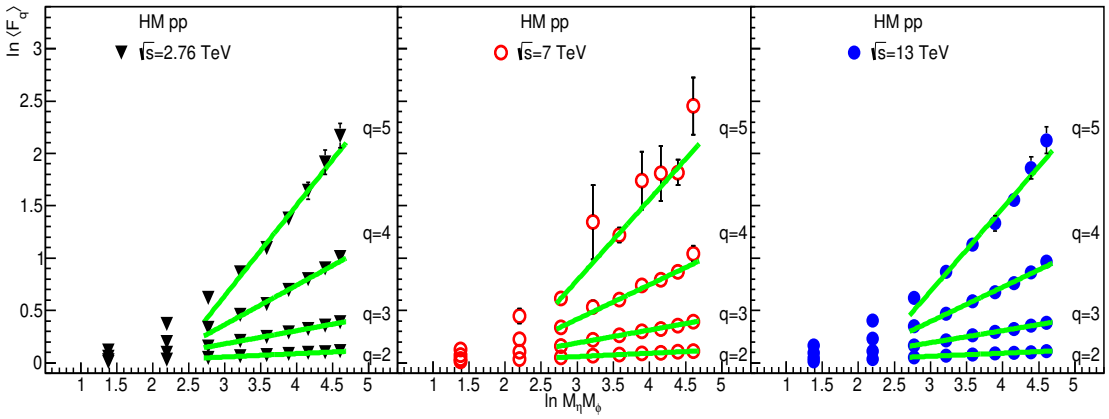

(b)

Fig. 5.8 $\ln\langle F_q\rangle$ vs. lnM plots for moments q = 2 – 5 for (a) RAN, MB pp collisions and (b) HM pp collisions at $\sqrt{s} = 2.76$, 7 and 13 TeV in two-dimensional $\chi(\eta - \phi)$ space with PYTHIA Monash (default) generated data.

Table 5.2 The values of the intermittency index α_q in minimum bias and high multiplicity pp collisions at $\sqrt{s} = 13$ TeV for different moments q in $\chi(\eta - \phi)$ space.

q	Intermittency index (α_q) for $\sqrt{s} = 13$ TeV $\chi(\eta - \phi)$ space		R^2
	Minimum bias	High multiplicity	
2	0.034 ± 0.002	0.029±0.001	0.99
3	0.119 ± 0.004	0.116±0.002	0.99
4	0.276 ± 0.012	0.330±0.008	0.99
5	0.538 ± 0.034	0.794±0.027	0.99

The dotted (MB) and solid (HM) lines in the figure are drawn to guide the eyes only. From the figure, an increase in d_q with the order of the moment q could be observed for MB pp events in the two-dimensional $\chi(\eta-\phi)$ space and high multiplicity pp events in all the $\chi(\eta)$, $\chi(\phi)$ and $\chi(\eta-\phi)$ spaces. The increase is found to be more pronounced in $\chi(\eta-\phi)$ space than that of $\chi(\eta)$, $\chi(\phi)$ spaces. Such an increase of d_q with q indicates the presence of multifractal behaviour in the emission spectra of the particles of MB and HM pp events, which could be attributed to cascading mechanism of particles production in such pp collisions [23–25].

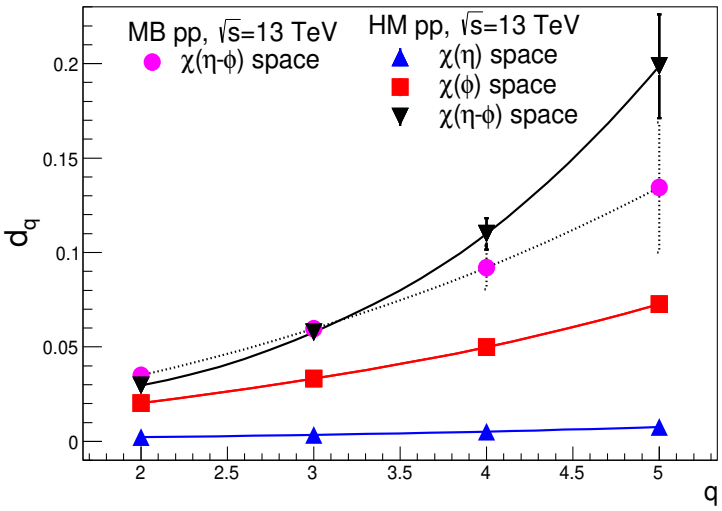

Fig. 5.9 Variation of d_q against q for high multiplicity pp event at $\sqrt{s} = 13$ TeV in $\chi(\eta)$, $\chi(\phi)$ and $\chi(\eta-\phi)$ spaces with PYTHIA Monash (default) generated data.

Bialas and Zalewski [220] reported that the intermittent behaviour in the final state particles in the ultra-relativistic collisions might also be a projection of non-thermal phase transition that occurs during the evolution of the collisions which in turn would be responsible for the occurrence of the anomalous events. The presence of a non-thermal phase transition is expected to have a minimum value of coefficient λ_q at some value of $q = q_c$ [220–223], where λ_q is related to α_q through the relation as given in the following Eq. (5.7).

$$\lambda_q = \frac{\alpha_q + 1}{q} \tag{5.7}$$

The value of q_c need not necessarily be an integer and the region satisfying the condition $q < q_c$ may be dominated by many small fluctuations whereas, the region $q > q_c$ contains rarely occurring large fluctuation.

The variations of λ_q against q in different spaces for MB ($\chi(\eta-\phi)$) and HM ($\chi(\eta)$, $\chi(\phi)$ and $\chi(\eta-\phi)$) pp events at $\sqrt{s} = 13$ TeV are shown in Fig. 5.10. λ_q is found to decrease monotonically with q for MB pp events, thereby, ruling out any possibility of occurrence of non-thermal phase transition like behaviour in such collisions. However, it is interesting to note for HM pp events that, though the λ_q value for one-dimensional $\chi(\eta)$ and $\chi(\phi)$ spaces decreases monotonically with q, a clear minimum in λ_q, estimated from two-dimensional analysis, could be observed at $q = q_c = 4$. The observation of a clear minimum in λ_q at $q = q_c = 4$ is indicative of a non-thermal phase transition like behaviour in high multiplicity pp events.

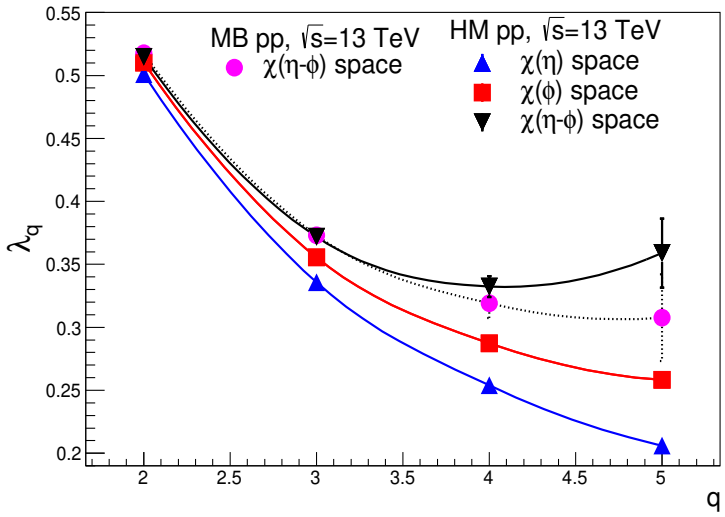

Fig. 5.10 Variation of λ_q against q for high multiplicity pp event at $\sqrt{s} = 13$ TeV in $\chi(\eta)$, $\chi(\phi)$ and $\chi(\eta-\phi)$ spaces with PYTHIA Monash (default) generated data.

Colour reconnection (CR) mechanism implemented in PYTHIA is a string fragmentation model where final partons are considered to be colour connected in such a way that the total string length becomes as short as possible [214]. The fragmentation of two independent interactions selects a preferred pseudorapidity minimising $\Delta\eta$. Such an effect might give rise large fluctuation in narrow pseudorapidity space.

Colour reconnection in PYTHIA is introduced through a parameter called reconnection range RR. In default PYTHIA Monash model, RR is taken to be equal to 1.8. To investigate the effect of colour reconnection in our scaled factorial moments estimation in pp data, a new set of (16.6×10^{6}) pp events has been generated by switching off (RR = 0.0) the colour reconnection mechanism at $\sqrt{s} = 2.76$, 7 and 13 TeV and the same analyses have been carried out for the high multiplicity pp events. For such events, as the values of the observed intermittency index and other derived quantities, within statistical error, is found to be same in respective spaces for $\sqrt{s} = 2.76$, 7 and 13 TeV, the results of the highest studied energy will only be discussed hereafter. The obtained results for $\ln\langle F_q\rangle$ against lnM in $\chi(\eta)$, $\chi(\phi)$ and $\chi(\eta-\phi)$ spaces in high multiplicity pp events at $\sqrt{s} = 13$ TeV are shown Figs. 5.11(a), 5.11(b), and 5.11(c) respectively and are compared with the results of our default (RR = 1.8) PYTHIA data. A significant decrease in the strength of the intermittency could readily be observed from these figures for moments $q = 2-5$ for CR off data set.

From the above observation, it is evident that colour reconnection plays a significant role in the observed intermittency in the PYTHIA Monash (default) generated data set at $\sqrt{s} = 2.76$, 7 and 13 TeV. For further confirmation of the effect of CR on the observed intermittent behaviour, the RR parameter has been changed to 3.0, and a new set of 43.5×10^{6} data has been generated again for pp collisions at $\sqrt{s} = 13$ TeV.

The $\ln\langle F_q\rangle$ against lnM plots for different moments for high multiplicity pp collisions at $\sqrt{s} = 13$ TeV with RR = 3.0 are shown in Figs. 5.12(a), 5.12(b) and 5.12(c) for $\chi(\eta)$, $\chi(\phi)$ and $\chi(\eta-\phi)$ spaces respectively and compared with the results of the default (RR = 1.8)

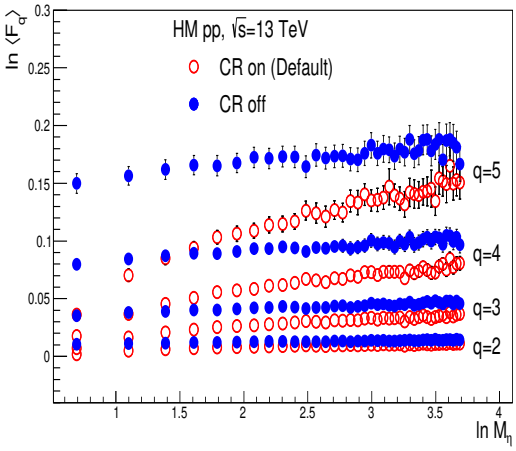

(a) $\chi(\eta)$ space

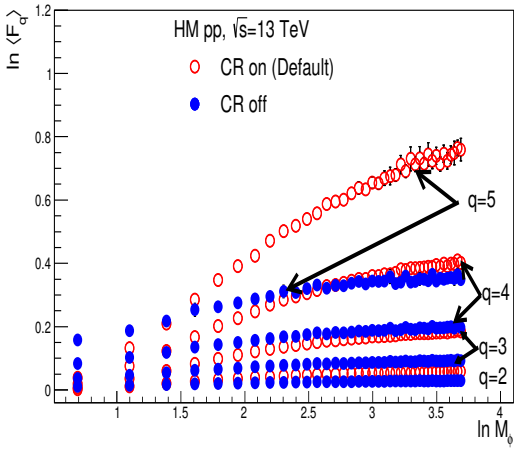

(b) $\chi(\phi)$ space

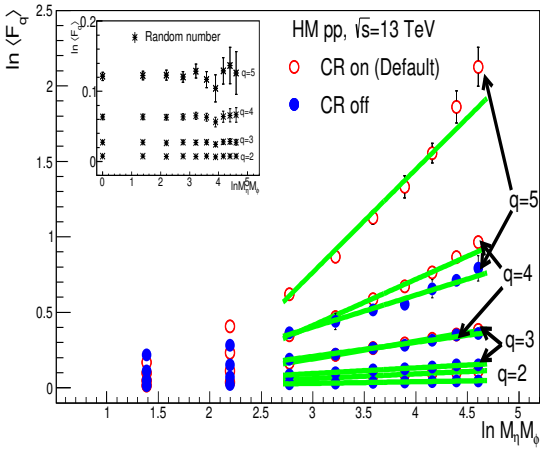

(c) $\chi(\eta-\phi)$ space

Fig. 5.11 $\ln\langle F_q\rangle$ vs. lnM for moments q = 2 – 5 for high multiplicity pp events at $\sqrt{s} = 13$ TeV in (a) $\chi(\eta)$, (b) $\chi(\phi)$ and (c) $\chi(\eta-\phi)$ spaces for PYTHIA Monash generated data with CR on (RR = 1.8) and CR off (RR = 0.0). Inset plot in (c) shows the $\ln\langle F_q\rangle$ vs. lnM for random number.

PYTHIA Monash generated data set. Here also, the solid green lines represent the straight-line fit of the data points, and the fitting is done keeping $R^2 = 0.99$. From these figures, a sharp increase in the values of $\ln\langle F_q\rangle$ against lnM is clearly evident for RR = 3.0 than that of the default one. This behaviour confirms that the colour reconnection mechanism plays a significant role on the observed intermittent type of emission of primary charged particles of our PYTHIA Monash generated sets of data of pp collisions.

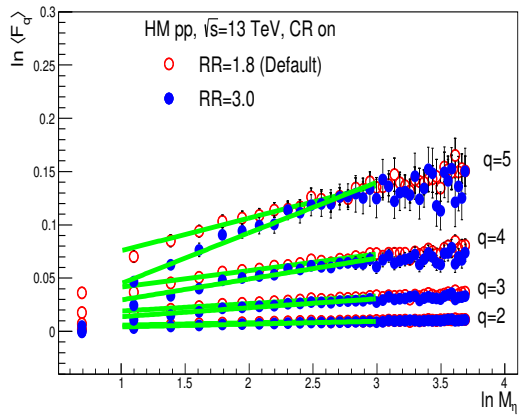

(a) $\chi(\eta)$ space

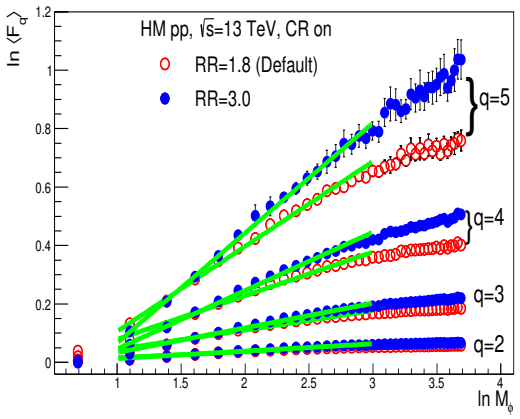

(b) $\chi(\phi)$ space

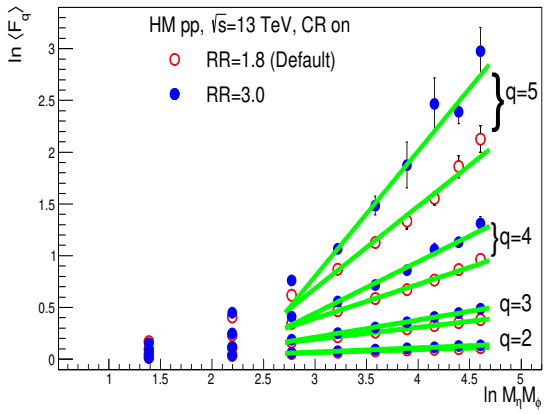

(c) $\chi(\eta-\phi)$ space

Fig. 5.12 $\ln\langle F_q\rangle$ vs. lnM plots for moments q = $2-5$ for high multiplicity pp events at $\sqrt{s} = 13$ TeV in (a) $\chi(\eta)$, (b) $\chi(\phi)$ and (c) $\chi(\eta-\phi)$ spaces for PYTHIA Monash generated data with RR = 1.8 and 3.0.

The anomalous dimension d_q and the coefficient λ_q, estimated using Eqs. (5.6) and (5.7) respectively for RR = 3.0 for $\chi(\eta)$, $\chi(\phi)$ and $\chi(\eta-\phi)$ spaces are plotted against q in Figs. 5.13(a), 5.13(b) respectively and compared with the estimated values with RR = 0.0 and 1.8 (default) PYTHIA Monash generated data. Though a significant change in the values of d_q could be observed with the order of the moments q (Fig. 5.13(a)) for RR = 1.8 and 3.0, not much change in d_q with q could be observed for RR = 0.0. Further, it is interesting to note from Fig. 5.13(b) that, whereas for RR = 0.0 data, no minimum could be seen in λ_q vs. q plot, the minimum in λ_q is found to be shifted towards lower values of $q = q_c = 3.65$ for RR = 3.0. Such behaviour confirms that for data set RR = 1.8 (default) and RR = 3.0, a non-thermal phase transition like behaviour is conspicuous in the studied pp events.

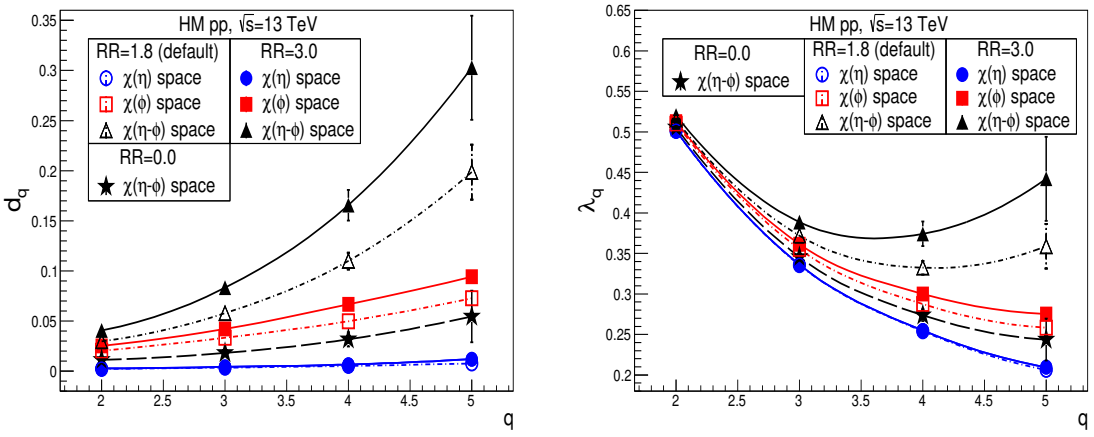

(a) d_q vs. q

(b) λ_q vs. q

Fig. 5.13 Variation of (a) d_q against q and (b) λ_q against q for high multiplicity pp event at $\sqrt{s} = 13$ TeV for PYTHIA Monash generated data with RR = 0.0 in $\chi(\eta-\phi)$ space and with RR = 1.8 and 3.0 in $\chi(\eta)$, $\chi(\phi)$ and $\chi(\eta-\phi)$ spaces.

5.7 Summary

A clear intermittent pattern in the emission spectra of the primary charged particles produced in high-multiplicity pp events at the LHC energies of $\sqrt{s} = 2.76$, 7, and 13 TeV could be seen in one-dimensional pseudorapidity (η), azimuthal (ϕ), and two-dimensional pseudorapidity-azimuthal ($\eta - \phi$) spaces with the PYTHIA Monash (default) generated MC data. On the other hand, little (ϕ, $\eta - \phi$ spaces) or no (η space) such signature of intermittency could be seen with the same sets of data for the minimum-bias pp collisions. In the high-multiplicity pp events, the intermittency index α_q is observed to increase with the increase of the order of the moments q in all the three $\chi(\eta)$, $\chi(\phi)$, and $\chi(\eta - \phi)$ spaces. Further, the values of α_q for the various order of the moment q are found to be most in $\chi(\eta - \phi)$ space and least in $\chi(\eta)$ space. No centre of mass energy dependence in the strength of intermittency index could be seen for the studied systems (pp at $\sqrt{s} = 2.76$, 7, and 13 TeV). Estimation of anomalous dimension d_q and its variation with the order of the moment q suggests a multifractal nature of emission spectra of high-multiplicity pp events and is attributed to the particle production through the cascading mechanism. The coefficient λ_q decreases monotonically with the increase of q, and no minimum value of λ_q is evident in the λ_q vs. q plot in $\chi(\eta)$ and $\chi(\phi)$ spaces. On the other hand, a clear minimum value of λ_q at $q = q_c = 4$ is evident in $\chi(\eta - \phi)$ space and is indicative of the occurrence of nonthermal phase transition like behaviour in the studied high-multiplicity pp events. The region $q < q_c$ is dominated by many small fluctuations, whereas the region $q > q_c$ contains rarely occurring large fluctuations. With colour reconnection off (RR = 0.0) in PYTHIA, a small rise in $\ln\langle F_q \rangle$ vs. $\ln M$ for higher values of q could be observed in high-multiplicity pp events in $\chi(\eta - \phi)$ space. With the increase of reconnection range (RR), the controlling parameter of CR, a significant increase in the intermittent behaviour could be observed in comparison to default (RR = 1.8) and RR = 0.0 PYTHIA data [Figs. 5.14(a), 5.14(b), and 5.14(c)]. Moreover, the position of the λ_q minimum is found to decrease ($q = q_c = 3.65$) with the increase of colour reconnection

parameter (RR = 3.0). No such minimum in λ_q could be seen with CR off (RR = 0.0). Thus, from this study, it is evident that the colour reconnection mechanism in PYTHIA has a significant effect on the observed intermittency and hence on the nonthermal phase transition like behaviour in the studied high-multiplicity events of pp collisions.

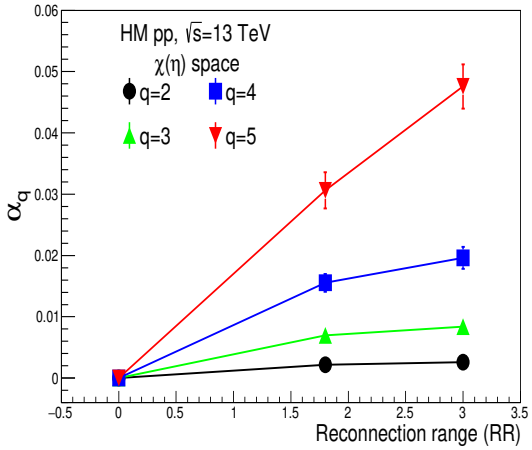

(a) $\chi(\eta)$ space

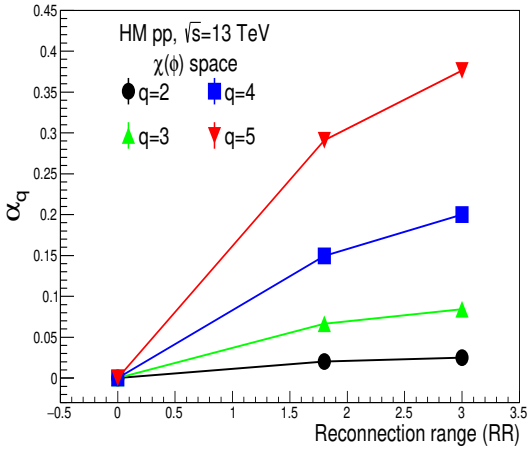

(b) $\chi(\phi)$ space

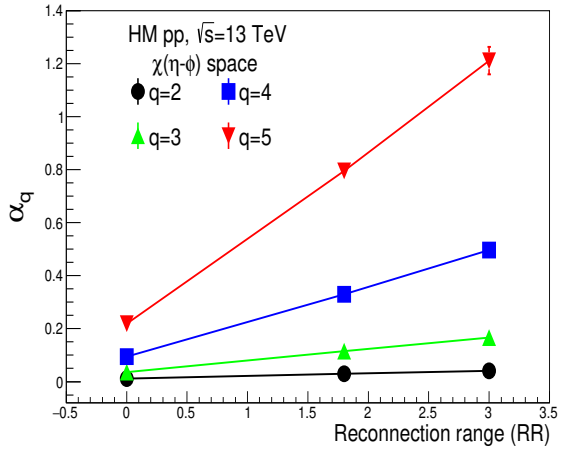

(c) $\chi(\eta-\phi)$ space

Fig. 5.14 Variation of intermittency index ϕ_q against reconnection range (RR) for q = 2 – 5 in (a) $\chi(\eta)$, (b) $\chi(\phi)$ and (c) $\chi(\eta-\phi)$ spaces in high multiplicity PYTHIA Monash generated pp events at $\sqrt{s} = 13$ TeV.

6

Summary

6.1 Summary

In this investigation, measurement of π, K and p production for various charged-particle multiplicity in pp collisions at $\sqrt{s} = 13$ TeV has been performed with the ALICE Time of Flight (TOF) detector. The TOF is a large-area gaseous detector built using the Multi-Gap Resistive Plate Chambers (MRPC). It identifies particles via measurement of their flight time from the collisions point to the detector. The statistical unfolding method has been applied on the time-difference distribution between the experimental time of flight (TOF) and the expected time of flight of a particle to estimate particles raw yields, as shown in Fig. 6.1. This

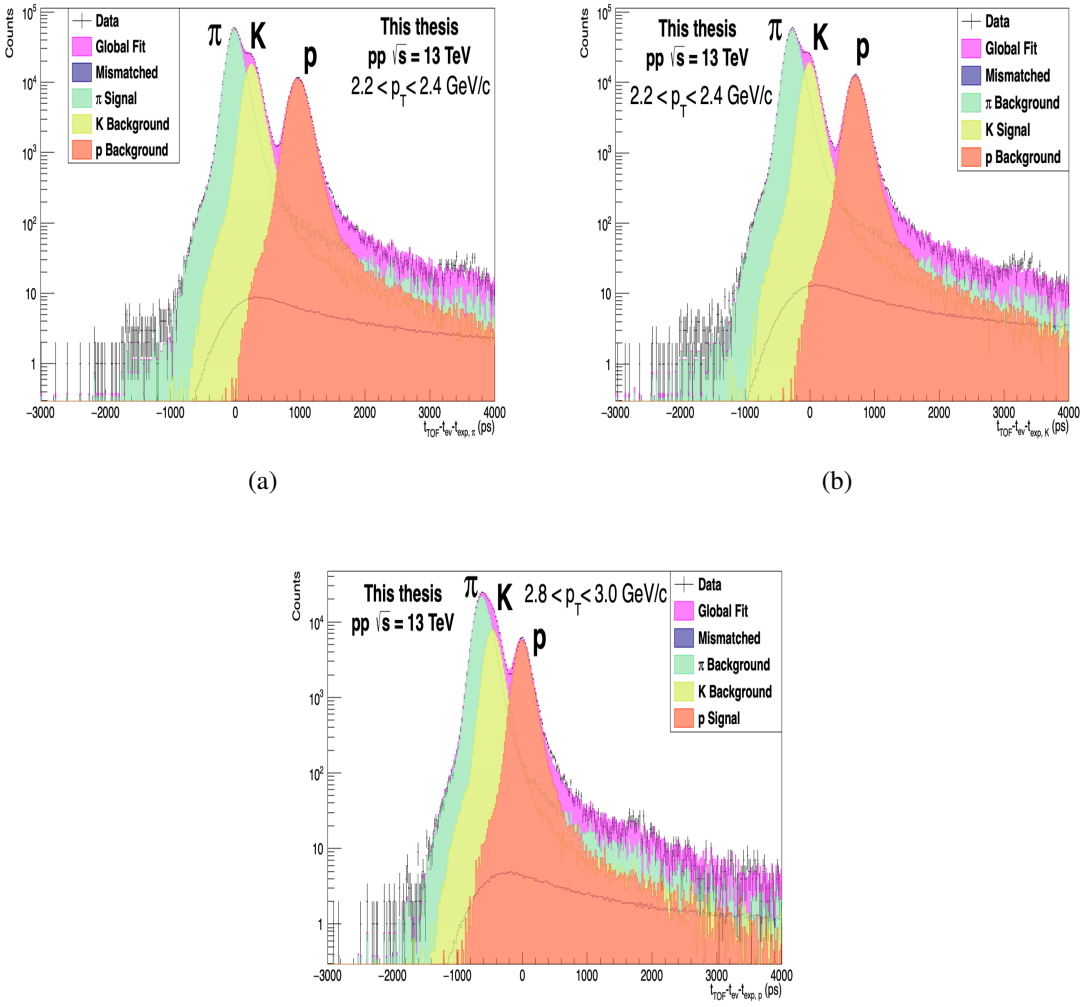

Fig. 6.1 Fit examples of (a) pions, (b) kaons and (c) protons to extract the raw yields in some p_{T} bins for minimum bias pp collisions. The templates for the three type of particles are shown in a different colour. The mismatched template is shown in the blue line, and the total fit is represented by magenta colour. The peak corresponding to the zero time difference is the correct template for that particle selected with the rapidity cut of $|y|<0.5$.

particle identification method provides the opportunity to identify pions, kaons and protons in the p_{T} range 0.7 to 4 GeV/c, 0.6 to 3 GeV/c and 0.9 to 4 GeV/c, respectively. Different correction factors such as the track reconstruction efficiency, TPC-TOF matching efficiency and feed-down correction factors are estimated for each particle. These correction factors are then applied in the raw p_{T} spectra to obtain the final corrected p_{T} spectra of identified charged-particles in different multiplicity classes. Then, various sources of systematic uncertainty related to the TOF detector and other sources are estimated. Further, the TOF detector's measurements are combined with the analysis of the ITSsa, TPC-TOF, rTPC and kinks to obtain the p_{T} spectra of the identified particles in an extended p_{T} region.

The p_{T} spectra of studied identified charged particles become harder with increasing multiplicity, and the effect is more pronounced for heavier particles like protons than comparatively lighter particles like pions and kaons, as observed from Fig. 6.2. These behaviour are qualitatively similar to those observed in the p-Pb and Pb-Pb collisions at lower LHC energies. In the heavy-ion collisions, such effects are consistent with the picture of the hydrodynamical evolution of the system formed after the collisions [11]. At high p_{T} (> 8 GeV/c), the spectral shape of different particles, as shown in Fig. 6.2, become independent of the studied multiplicity class, as predicted by the pQCD calculation [195]. The $\langle p_{\mathrm{T}} \rangle$ measurement of pions, kaons and protons, as shown in Fig. 6.3, also show multiplicity and mass-dependent hardening with increasing multiplicity similar to those observed for the p_{T} spectra. From the model point of view, the evolution of the $\langle p_{\mathrm{T}} \rangle$ with increasing multiplicity is found to be described by the PYTHIA8 with colour ropes, PYTHIA8 Monash with colour reconnection and HERWIG7 MC model. All these models describe the $\langle p_{\mathrm{T}} \rangle$ of pions very well, whereas $\langle p_{\mathrm{T}} \rangle$ of K and p are qualitatively explained by the HERWIG7 only.

The p_{T}-differential K/π ratio shows no modification with increasing charged-particle multiplicity whereas, a depletion at the low p_{T}, an enhancement at the intermediate p_{T} and saturation at the high p_{T} could be observed in the p/π ratio, as shown in Fig. 6.4. For the

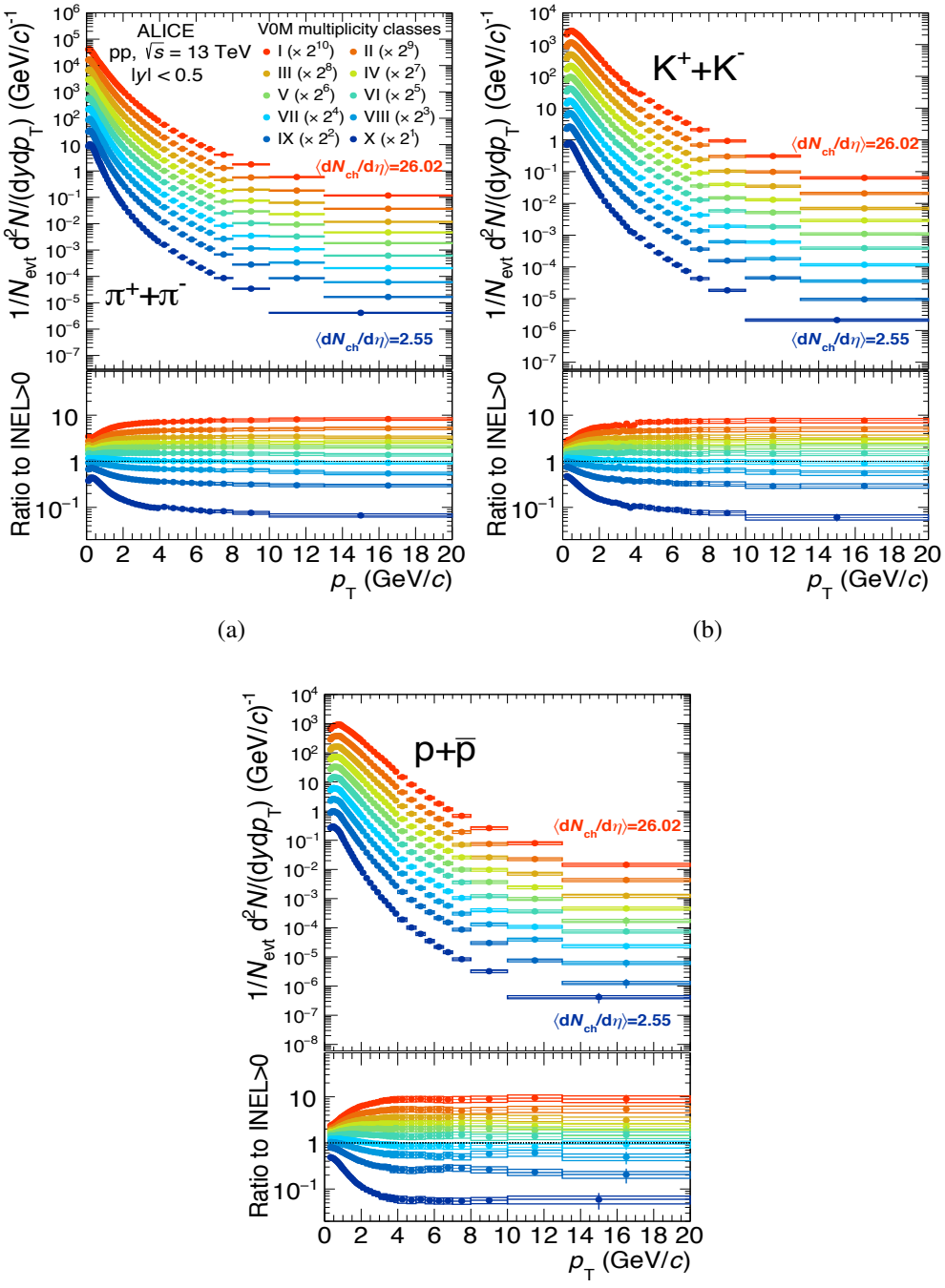

Fig. 6.2 Final p_{T} spectra of (a) pions, (b) kaons and (c) protons in different V0M multiplicity classes. Spectra are scaled by powers of 2 for better visibility. The corresponding ratios to INEL>0 spectra are shown in the bottom panels of each figure.

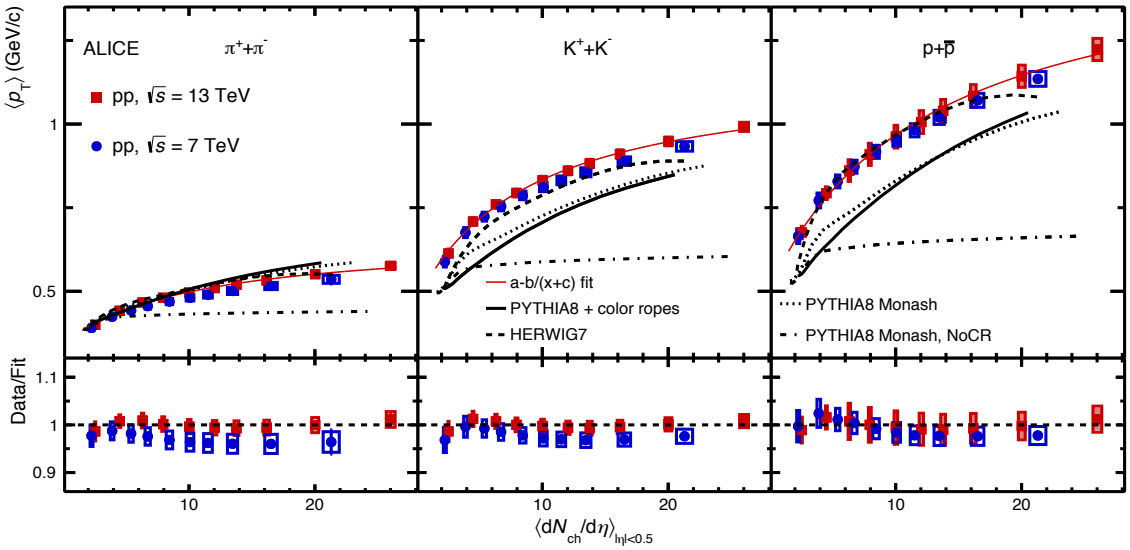

Fig. 6.3 (Upper panels) The $\langle p_{\mathrm{T}} \rangle$ of π, K and p as a function of multiplicity in pp collisions at $\sqrt{s} = 13$ TeV are compared with the results of lower energy pp collisions as well as with different MC event generators. The solid line represents the $a - \frac{b}{(\langle \mathrm{d}N_{\mathrm{ch}}/\mathrm{d}\eta \rangle + c)}$ fit of pp 13 TeV data. (Lower panels) The ratios of $\langle p_{\mathrm{T}} \rangle$ in different collisions energies to the fitted line.

central Pb-Pb collisions, such effects in the p/π ratio could be described by a collectively expanding source or hadronisation via recombination of quarks in the plasma phase [11]. The measured particle ratios in pp collisions at $\sqrt{s} = 13$ TeV are consistent with those measured at pp collisions at $\sqrt{s} = 7$ TeV. Predictions from the HERWIG7 MC events generator can provide a good description of the evolution of the K/π and p/π ratios with increasing multiplicity within 1-2 standard deviations in low and intermediate p_{T} ranges. However, PYTHIA8 model with colour reconnection provides only a qualitative description of the evolution of the p/π ratios with multiplicity and overestimate the values of the ratio in the low and high p_{T}. Without CR in PYTHIA, the evolution of both the particle ratios with multiplicity cannot be described. Moreover, PYTHIA8 with colour ropes model can describe the K/π and p/π ratios qualitatively at low and intermediate p_{T}, respectively, but overestimate the p/π ratio at low p_{T}.

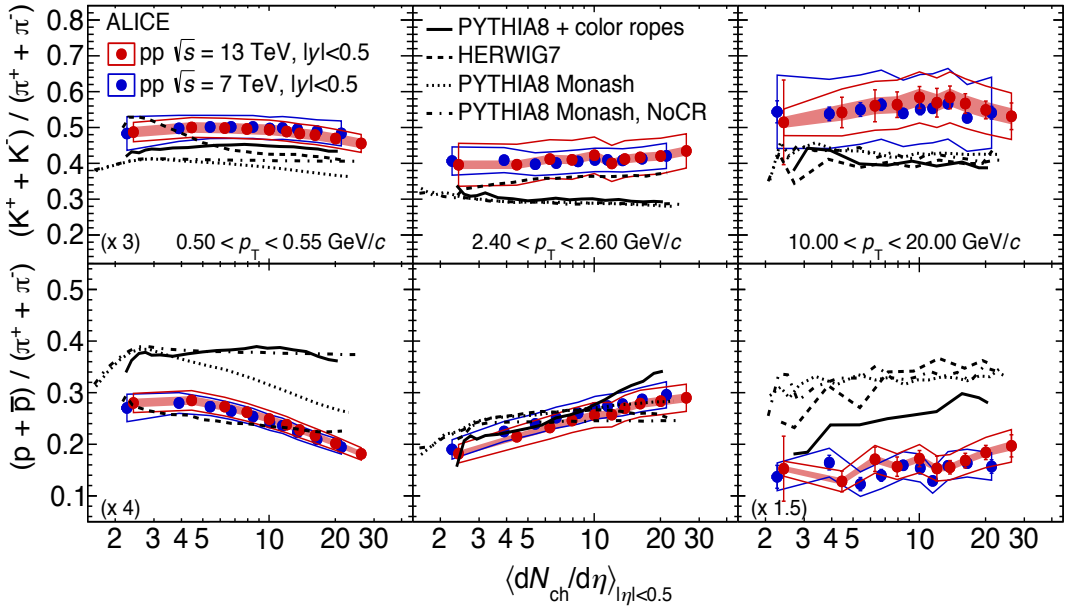

Fig. 6.4 K/π and p/π ratios as a function of charged-particle multiplicity at low, intermediate and high p_{T} bins are compared with the lower energy pp collisions. Predictions from various Monte Carlo event generators are also shown.

From Figs. 6.5(a) and 6.5(b), it could be seen that the p_{T}-integrated K/π and p/π yields ratios as a function of the charged-particle multiplicity show no modification with the centre of mass energy. The K/π ratio shows an increasing behaviour with increasing multiplicity similar to those observed for the lower energy pp, p-Pb and Pb-Pb collisions. Such an enhancement in the heavy-ion system can be described by enhanced production of the strange particle in the plasma phase or reduced canonical suppression of strangeness production in larger freeze-out volumes [17, 11]. The p/π ratio, on the contrary, is almost independent of the studied multiplicity classes for pp collisions. However, for Pb-Pb collisions, a decreasing behaviour in the p/π ratio is evident, which is expected due to annihilation of baryon and anti-baryon in the hadronic phase [203–209]. Both the particle ratios follow a universal trend independent of the colliding system's size and energy. From the model point of view, the evolution of the K/π ratio with increasing multiplicity can be described by the PYTHIA with colour ropes model. The HERWIG7 model can also describe the K/π ratio quite well, except for the very low multiplicity class, where a peak-like structure is evident in the yields ratio

with the model data. The PYTHIA8 Monash prediction with and without colour reconnection are found to underestimate results obtained with the experimental data. For the p/π ratio, the HERWIG7 can describe the evolution of the ratio with multiplicity quite well. However, predictions with all PYTHIA8 versions overestimate the p/π ratio. Moreover, PYTHIA8 with colour ropes predicts an increasing behaviour in the p/π ratio with increasing charged-particle multiplicity. These type of effect could be attributed to the enhanced production of di-quark during the rope fragmentation.

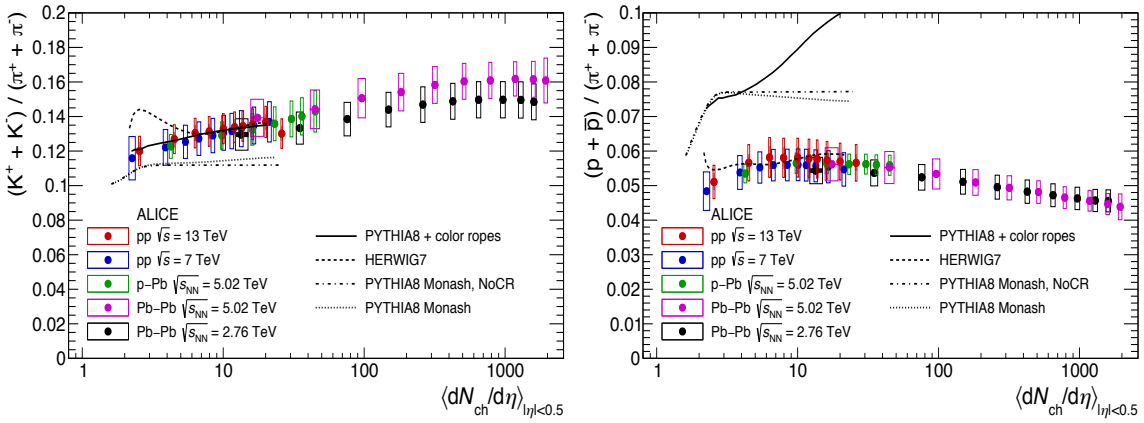

(a) (b)

Fig. 6.5 p_{T}-integrated yields ratios of (a) K/π and (b) p/π as a function of charged-particle multiplicity in pp collisions at $\sqrt{s} = 13$ TeV are compared with the results of the lower energy pp, p-Pb and Pb-Pb collisions. The prediction from different Monte Carlo event generators are also shown.

The p_{T}-integrated yields ratios of different hadrons to pions as a function of the charged-particle multiplicity is shown in Fig. 6.6. Here also, the particle ratios show no modification with the centre of mass energy. The measurement performed in pp collisions at $\sqrt{s} = 13$ TeV are comparable to those available at the lower energy pp, p-Pb and Pb-Pb collisions. These results suggest that, at the LHC energies, the chemical composition of primary hadrons scales with charged-particle multiplicity rather than colliding system or energy. The MC event generator PYTHIA8 with colour ropes provide the best description for the (multi-)strange hadron, but unable to describe the p/π ratio well. The HERWIG7 model can describe the

evolution of K^0_S/π, and Λ/π ratios with increasing multiplicity but, underestimate the values of the Ξ/π and Ω/π ratios.

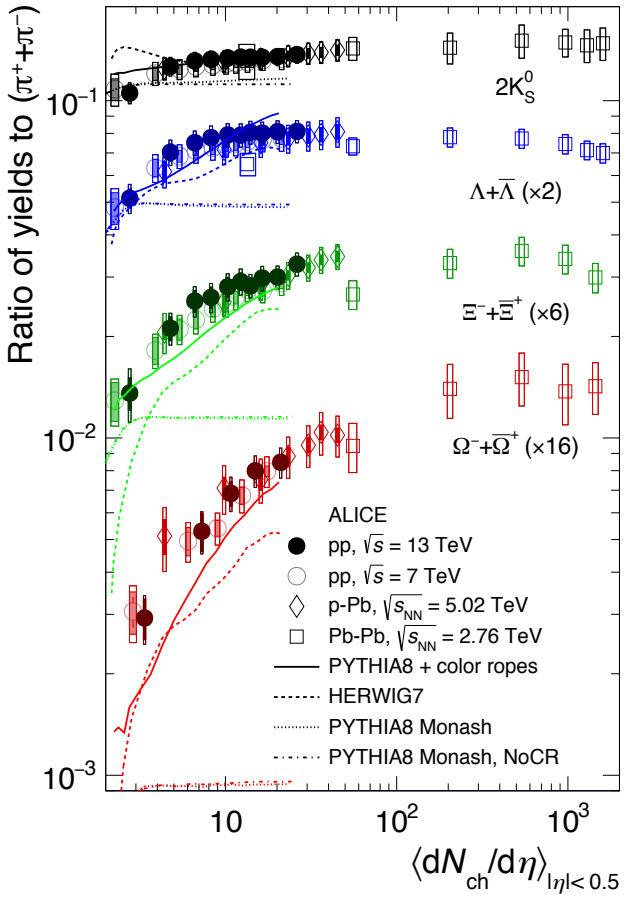

Fig. 6.6 p_T-integrated yields ratios of K^0_s/π, Λ/π, Ξ/π and Ω/π as a function of multiplicity in pp collisions at $\sqrt{s} = 13$ TeV are compared with the results of lower energy pp, p-Pb and Pb-Pb collisions. Prediction from different Monte Carlo event generator are also shown.

Apart from characterising the medium formed in the collisions, another important aspect of such collisions studies is to understand the various mechanisms of particle production. Correlated emission of particles resulting fluctuations in the number density of emitted particles in phase-space bin is believed to arise due to different underlying processes of particle production such as - cascading mechanism, two- & three-particle hadronic decay, collective flow, Bose-Einstein correlations etc. Moreover, correlated emission of particles produced in the collisions results in preferential emission over some phase-space of pseudo-

rapidity (η), azimuthal angle (ϕ), transverse momentum (p_{T}) or any combination of these resulting non-statistical fluctuations in the single-particle density spectra. Since numbers of particles produced in the pp collisions at the LHC energies are comparable to peripheral Pb-Pb collisions, studies on dynamical fluctuations in high-multiplicity pp collisions at the LHC energies becomes significantly important. Moreover, the PYTHIA Monash Monte Carlo model is found to describe the results of the pp experimental data at the LHC energies very well. Thus, investigations on dynamical fluctuations in these high-multiplicity pp events generated with PYTHIA are performed to understand the particle production mechanism better. Several mathematical tools are available that can be applied to disentangle dynamical fluctuations to have insight into the collisions dynamics and particle production mechanisms. In this work, non-statistical fluctuations in the charged particle emission spectra are investigated using the Scaled Factorial Moment (SFM) technique in the high-multiplicity as well as on minimum bias pp event. An intermittent pattern in the emission spectra of the primary charged particle produced in the high-multiplicity pp events of $\sqrt{s} = 2.76$, 7, and 13 TeV could be observed in one-dimensional pseudorapidity (η), azimuthal (ϕ), and two-dimensional pseudorapidity-azimuthal ($\eta - \phi$) analyses (Fig. 6.7). On the contrary, no such intermittent pattern could be observed in the minimum bias pp collisions at the LHC energies. The intermittency indices α_q are observed to increase with increasing order of the moments q in all three $\chi(\eta)$, $\chi(\phi)$, and $\chi(\eta - \phi)$ spaces of the high-multiplicity pp events. The strength of the intermittency indices is found to be higher for the 2D $\chi(\eta - \phi)$ space and least in 1D $\chi(\eta)$ space. Further, intermittency indices show no centre-of-mass energy dependence for the studied systems, i.e. pp at $\sqrt{s} = 2.76$, 7, and 13 TeV.

The anomalous dimensions d_q, which is the difference between the topological and generalised qth order Renyi dimension, are observed to increase with the increase in the order of the moment q in all three spaces. Such increasing behaviour of d_q with q suggest a multi-fractal nature of emission spectra of high-multiplicity pp events and is indicative of

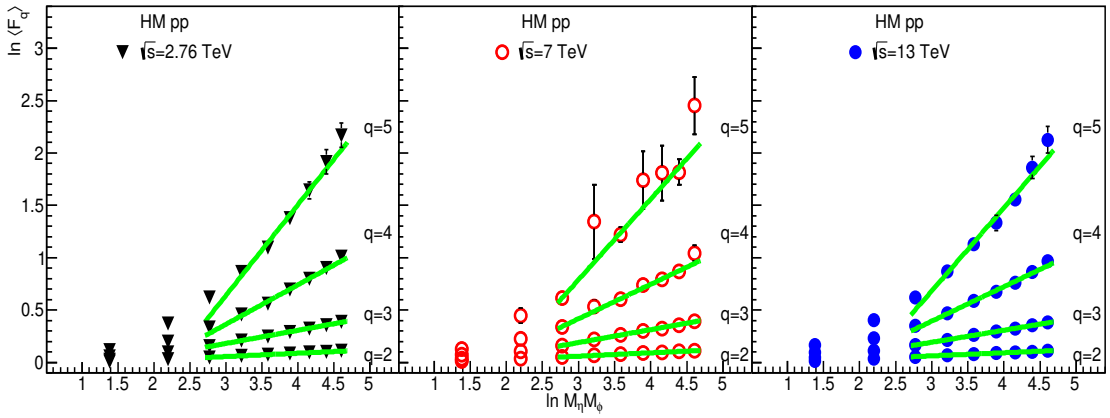

Fig. 6.7 $\ln\langle F_q\rangle$ vs. lnM plots for moments q = 2 – 5 for HM pp collisions at $\sqrt{s} = 2.76$, 7 and 13 TeV in two-dimensional $\chi(\eta-\phi)$ space with PYTHIA Monash (default) generated data.

the particle production through cascading mechanism. Moreover, studies on the parameter $\lambda_q = \frac{\alpha_q+1}{q}$ provide information about the amount of fluctuations in particles density spectra. The λ_q vs q plot show a clear minimum value of λ_q at $q = q_c = 4$ in $\chi(\eta-\phi)$ space and hence indicates the occurrence of nonthermal phase transition like behaviour in the studied high-multiplicity pp events. The region $q < q_c$ is dominated by many small fluctuations, whereas the region $q > q_c$ contains rarely occurring large fluctuations. Further, with the increase of reconnection range (RR), the controlling parameter of colour reconnection (CR), a significant increase in the intermittent behaviour could be observed in comparison to default (RR = 1.8) and RR = 0.0 PYTHIA data [Figs. 6.8(a), 6.8(b), and 6.8(c)]. Also, the values of anomalous dimensions are found to be more than the default PYTHIA Monash results as shown in Fig. 6.9. Moreover, the position of the minimum value of λ_q is observed to decrease ($q = q_c = 3.65$) with the increase of colour reconnection parameter (RR = 3.0) as shown in Fig. 6.10. When the CR mechanism is switched off (RR = 0.0) in PYTHIA, no such minimum in λ_q could be seen. Therefore, from this investigation, it is conspicuous that the colour reconnection mechanism, implemented in PYTHIA, gives rise to the strongly correlated emission of particles in the studied high-multiplicity pp events. Also, CR has a

significant effect on the observed intermittency and hence on the nonthermal phase transition like behaviour in the studied high-multiplicity events of pp collisions.

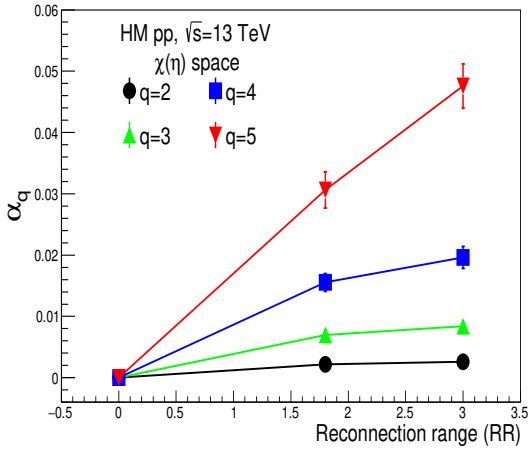

(a) $\chi(\eta)$ space

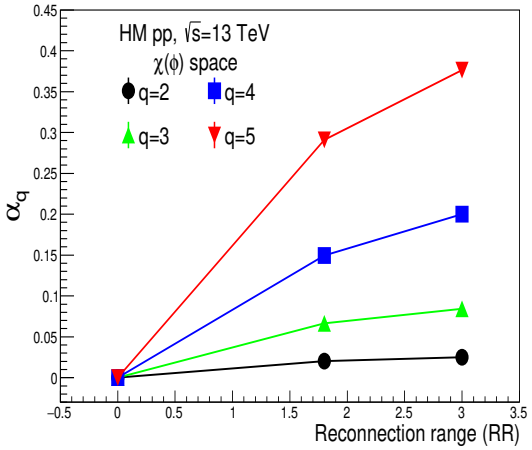

(b) $\chi(\phi)$ space

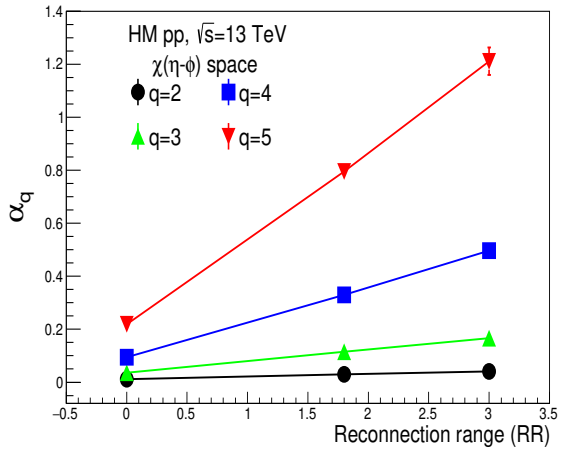

(c) $\chi(\eta-\phi)$ space

Fig. 6.8 Variation of intermittency index ϕ_q against reconnection range (RR) for q = $2-5$ in (a) $\chi(\eta)$, (b) $\chi(\phi)$ and (c) $\chi(\eta-\phi)$ spaces in high multiplicity PYTHIA Monash generated pp events at $\sqrt{s} = 13$ TeV.

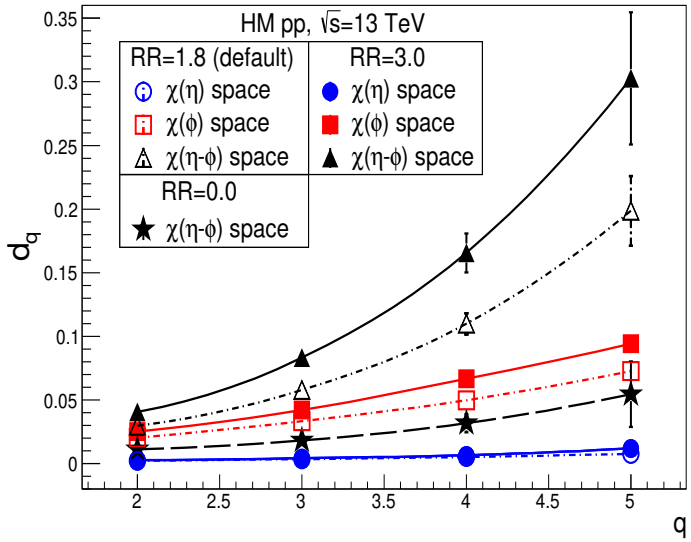

Fig. 6.9 Variation of (a) d_q against q for high multiplicity pp event at $\sqrt{s} = 13$ TeV for PYTHIA Monash generated data with RR = 0.0 in $\chi(\eta - \phi)$ space and with RR = 1.8 and 3.0 in $\chi(\eta)$, $\chi(\phi)$ and $\chi(\eta - \phi)$ spaces.

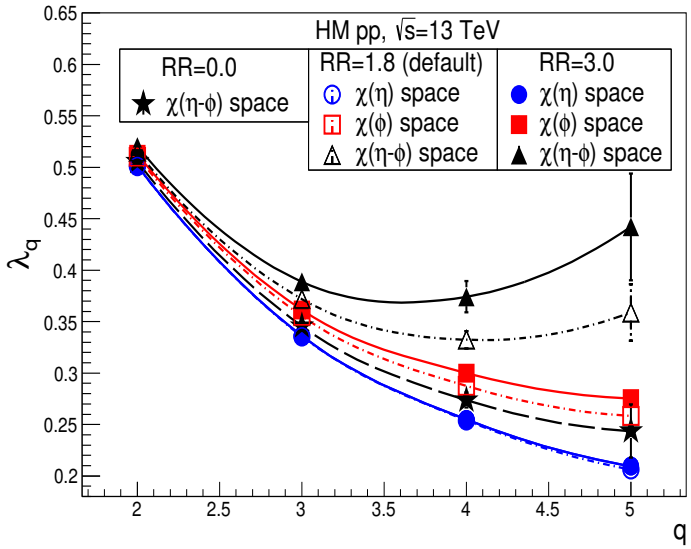

Fig. 6.10 Variation of λ_q against q for high multiplicity pp event at $\sqrt{s} = 13$ TeV for PYTHIA Monash generated data with RR = 0.0 in $\chi(\eta - \phi)$ space and with RR = 1.8 and 3.0 in $\chi(\eta)$, $\chi(\phi)$ and $\chi(\eta - \phi)$ spaces.

References

[1] P. Braun-Munzinger and J. Stachel. The quest for the quark–gluon plasma. *Nature*, 448:302, 2007.

[2] J. W. Harris and B. Müller. THE SEARCH FOR THE QUARK-GLUON PLASMA. *Ann. Rev. Nucl. Part. Sci.*, 46(1):71–107, 1996.

[3] U. Heinz and M. Jacob. Evidence for a New State of Matter: An Assessment of the Results from the CERN Lead Beam Programme. *nucl-th/0002042*, 2000.

[4] I. Arsene et al. (BRAHMS Collaboration). Quark–gluon plasma and color glass condensate at RHIC? The perspective from the BRAHMS experiment. *Nucl. Phys. A*, 757:1 – 27, 2005.

[5] K. Adcox et al. (PHENIX Collaboration). Formation of dense partonic matter in relativistic nucleus–nucleus collisions at RHIC: Experimental evaluation by the PHENIX Collaboration. *Nucl. Phys. A*, 757:184 – 283, 2005.

[6] B. Back et al. (PHOBOS Collaboration). The PHOBOS perspective on discoveries at RHIC. *Nucl. Phys. A*, 757:28 – 101, 2005.

[7] J. Adams et al. (STAR Collaboration). Experimental and theoretical challenges in the search for the quark–gluon plasma: The STAR Collaboration's critical assessment of the evidence from RHIC collisions. *Nucl. Phys. A*, 757:102 – 183, 2005.

[8] E. Shuryak. What RHIC experiments and theory tell us about properties of quark–gluon plasma? *Nucl. Phys. A*, 750:64 – 83, 2005.

[9] P. Huovinen and P. V. Ruuskanen. Hydrodynamic Models for Heavy Ion Collisions. *Ann. Rev. Nucl. Part. Sci.*, 56:163–206, 2006.

[10] B. Muller and J. L. Nagle. Results from the Relativistic Heavy Ion Collider. *Ann. Rev. Nucl. Part. Sci.*, 56:93–135, 2006.

[11] B. Abelev et al. (ALICE Collaboration). Centrality dependence of π, K, and p production in Pb-Pb collisions at $\sqrt{s_{NN}} = 2.76$ TeV. *Phys. Rev. C*, 88:044910, 2013.

[12] J. Adam et al. (ALICE Collaboration). Centrality dependence of the nuclear modification factor of charged pions, kaons, and protons in Pb-Pb collisions at $\sqrt{s_{NN}} = 2.76$ TeV. *Phys. Rev. C*, 93:034913, 2016.

[13] J. Adam et al. (ALICE Collaboration). Pseudorapidity dependence of the anisotropic flow of charged particles in Pb–Pb collisions at $\sqrt{s_{NN}} = 2.76$ TeV. *Phys. Lett. B*, 762:376 – 388, 2016.

[14] B. Abelev et al. (ALICE Collaboration). Elliptic flow of identified hadrons in Pb-Pb collisions at $\sqrt{s}_{\mathrm{NN}} = 2.76$ TeV. *JHEP*, 06:190, 2015.

[15] D. de Florian, M. Epele, R. J. Hernández-Pinto, R. Sassot, and M. Stratmann. Parton-to-kaon fragmentation revisited. *Phys. Rev. D*, 95:094019, May 2017.

[16] B. Abelev et al. (ALICE Collaboration). Long-range angular correlations on the near and away side in p–Pb collisions at $\sqrt{s_{NN}}$ =5.02 TeV. *Phys. Lett. B*, 719(1):29 – 41, 2013.

[17] B. Abelev et al. (ALICE Collaboration). Multiplicity dependence of pion, kaon, proton and lambda production in p–Pb collisions at $\sqrt{s_{NN}}$ = 5.02 TeV. *Phys. Lett. B*, 728:25 – 38, 2014.

[18] J. Adam et al. (ALICE Collaboration). Multi-strange baryon production in p-Pb collisions at $\sqrt{s_{NN}} = 5.02$ TeV. *Phys. Lett. B*, 758:389 – 401, 2016.

[19] S. Acharya et al. (ALICE Collaboration). Multiplicity dependence of light-flavor hadron production in pp collisions at $\sqrt{s} = 7$ TeV. *Phys. Rev. C*, 99:024906, 2019.

[20] J. Adam et al. (ALICE Collaboration). Enhanced production of multi-strange hadrons in high-multiplicity proton–proton collisions. *Nature Physics*, 13:535 – 539, 2017.

[21] A. Bialas. Intermittency '90. *Nucl. Phys. A*, 525:345 – 360, 1991.

[22] M. I. Adamovich et al. (EMU01 Collaboration). On intermittency in heavy-ion collisions and the importance of γ-conversion in a multi-dimensional intermittency analysis. *Nucl. Phys. B*, 388:3 – 30, 1992.

[23] A. Bialas and R. Peschanski. Moments of rapidity distributions as a measure of short-range fluctuations in high-energy collisions. *Nucl. Phys. B*, 273:703 – 718, 1986.

[24] W. Ochs and J. Wosiek. Intermittency and jets. *Phys. Lett. B*, 214(4):617 – 620, 1988.

[25] A. Bialas and R. Peschanski. Intermittency in multiparticle production at high energy. *Nucl. Phys. B*, 308(4):857 – 867, 1988.

[26] B. Bhattacharjee. Signature of intermittent behavior in the emission spectra of target associated particles from ^{84}Kr–AgBr interactions at 0.95 GeV/A. *Nucl. Phys. A*, 748:641 – 648, 2005.

[27] D. H. Zhang et al. Evidence of intermittent fluctuation of target residue in ^{84}Kr–AgBr interactions at 1.7 AGeV. *Radiat. Meas.*, 43:S258 – S261, 2008.

[28] P. Mali, A. Mukhopadhyay, and G. Singh. Self-affine two dimensional intermittency in ^{28}Si–Ag/Br interaction at 14.5 A GeV. *Acta Phys. Pol. B*, 43:463, 2012.

[29] Yi-Long Xie et al. Scaling properties of multiplicity fluctuations in heavy-ion collisions simulated by AMPT model. *Nucl. Phys. A*, 920:33 – 44, 2013.

[30] S. Bhattacharyya et al. A study of pion fluctuation and correlation in heavy-ion collisions. *Eur. Phys. J. A*, 52:301, 2016.

[31] W. Ochs. The importance of phase space dimension in the intermittency analysis of multi hadron production. *Phys. Lett. B*, 247(1):101 – 106, 1990.

[32] L. V. Hove. Two problems concerning hot hadronic matter and high energy collisions (Equilibrium formation, plasma deflagration). *Z. Phys. C*, 21:93 – 98, 1983.

[33] M. Gyulassy et al. Deflagrations and detonations as a mechanism of hadron bubble growth in supercooled quark-gluon plasmas. *Nucl. Phys. B*, 237:477 – 501, 1984.

[34] R. C. Hwa. A proposed analysis of multiplicity fluctuations in high-energy heavy-ion collisions. *Phys. Lett. B*, 201(1):165 – 168, 1988.

[35] J. Adam et al. (ALICE Collaboration). Charged-particle multiplicities in proton–proton collisions at $\sqrt{s}$ = 0.9 to 8 TeV. *Eur. Phys. J. C*, 77:33, 2017.

[36] S. Acharya et al. (ALICE Collaboration). Charged-particle multiplicity distributions over a wide pseudorapidity range in proton-proton collisions at $\sqrt{s}$ = 0.9, 7, and 8 TeV. *Eur. Phys. J. C*, 77:852, 2017.

[37] B. Abelev et al. (ALICE Collaboration). Multiplicity dependence of the average transverse momentum in pp, p–Pb, and Pb–Pb collisions at the LHC. *Phys. Lett. B*, 727:371 – 380, 2013.

[38] D. J. Griffiths. *Introduction to elementary particles*. Physics textbook. Wiley, New York, NY, 2008.

[39] https://www.quantumdiaries.org/2014/03/14/the-standard-model-a-beautiful-but-flawed-theory/.

[40] A. Salam and J. C. Ward. Electromagnetic and weak interactions. *Phys. Lett.*, 13:168–171, 1964.

[41] S. Weinberg. A Model of Leptons. *Phys. Rev. Lett.*, 19:1264–1266, Nov 1967.

[42] S. L. Glashow, J. Iliopoulos, and L. Maiani. Weak Interactions with Lepton-Hadron Symmetry. *Phys. Rev. D*, 2:1285–1292, Oct 1970.

[43] M. Tanabashi et al. Review of Particle Physics. *Phys. Rev. D*, 98(3):030001, 2018.

[44] P. W. Higgs. Broken Symmetries and the Masses of Gauge Bosons. *Phys. Rev. Lett.*, 13:508–509, Oct 1964.

[45] F. Englert and R. Brout. Broken Symmetry and the Mass of Gauge Vector Mesons. *Phys. Rev. Lett.*, 13:321–323, Aug 1964.

[46] G. S. Guralnik, C. R. Hagen, and T. W. B. Kibble. Global Conservation Laws and Massless Particles. *Phys. Rev. Lett.*, 13:585–587, Nov 1964.

[47] P. W. Higgs. Spontaneous Symmetry Breakdown without Massless Bosons. *Phys. Rev.*, 145:1156–1163, May 1966.

[48] G. Aad et al. (ATLAS Collaboration). Observation of a new particle in the search for the Standard Model Higgs boson with the ATLAS detector at the LHC. *Phys. Lett. B*, 716(1):1 – 29, 2012.

[49] S. Chatrchyan et al. (CMS Collaboration). Observation of a new boson at a mass of 125 GeV with the CMS experiment at the LHC. *Phys. Lett. B*, 716(1):30 – 61, 2012.

[50] D. H. Perkins. *Introduction to High Energy Physics*. Cambridge University Press, 4 edition, 2000.

[51] D. J. Gross and F. Wilczek. Ultraviolet Behavior of Non-Abelian Gauge Theories. *Phys. Rev. Lett.*, 30:1343–1346, Jun 1973.

[52] D. J. Gross and F. Wilczek. Asymptotically Free Gauge Theories. I. *Phys. Rev. D*, 8:3633–3652, Nov 1973.

[53] D. J. Gross and F. Wilczek. Asymptotically free gauge theories. II. *Phys. Rev. D*, 9:980–993, Feb 1974.

[54] H. D. Politzer. Reliable Perturbative Results for Strong Interactions? *Phys. Rev. Lett.*, 30:1346–1349, Jun 1973.

[55] L. J. Boya and C. Rivera. On the Scales of Masses in Elementary Particles. *Phys. Part. Nucl.*, 42:800–811, 2011.

[56] S. Bethke. α_s 2002. *Nucl. Phys. Proc. Suppl.*, 121:74–81, 2003.

[57] S. Sarkar, H. Satz, and B. Sinha. The physics of the quark-gluon plasma. *Lect. Notes Phys.*, 785:pp.1–369, 2010.

[58] K. G. Wilson. Confinement of quarks. *Phys. Rev. D*, 10:2445–2459, Oct 1974.

[59] F. Karsch, E. Laermann, and A. Peikert. The pressure in 2, 2+1 and 3 flavour QCD. *Phys. Lett. B*, 478(4):447 – 455, 2000.

[60] F. Karsch. Lattice results on QCD thermodynamics. *Nucl. Phys. A*, 698:199–208, 2002.

[61] P. Braun-Munzinger and J. Wambach. Colloquium: Phase diagram of strongly interacting matter. *Rev. Mod. Phys.*, 81:1031–1050, Jul 2009.

[62] A. Aprahamian et al. Reaching for the horizon: The 2015 long range plan for nuclear science. 10 2015.

[63] A. Bazavov et al. (HotQCD Collaboration). Chiral and deconfinement aspects of the QCD transition. *Phys. Rev. D*, 85:054503, Mar 2012.

[64] U. W. Heinz. The Little bang: Searching for quark gluon matter in relativistic heavy ion collisions. *Nucl. Phys. A*, 685:414–431, 2001.

[65] J. Berges and K. Rajagopal. Color superconductivity and chiral symmetry restoration at nonzero baryon density and temperature. *Nucl. Phys. B*, 538:215–232, 1999.

[66] M. Buballa. NJL model analysis of quark matter at large density. *Phys. Rept.*, 407:205–376, 2005.

[67] D. Keane. The Beam Energy Scan at the Relativistic Heavy Ion Collider. *J Phys.: Conf. Ser.*, 878:012015, jul 2017.

[68] J. Bartke. *Introduction to relativistic heavy ion physics*. 11 2009.

[69] B. Betz. Jet Propagation and Mach-Cone Formation in (3+1)-dimensional Ideal Hydrodynamics. Master thesis, 10 2009.

[70] A. Alkin. Phenomenology of charged-particle multiplicity distributions. *Ukr. J. Phys.*, 62(9):743, 2017.

[71] M. L. Miller, K. Reygers, S. J. Sanders, and P. Steinberg. Glauber Modeling in High-Energy Nuclear Collisions. *Ann. Rev. Nucl. Part. Sci.*, 57(1):205–243, 2007.

[72] J. D. Bjorken. Highly relativistic nucleus-nucleus collisions: The central rapidity region. *Phys. Rev. D*, 27:140–151, Jan 1983.

[73] K. Aamodt et. al (ALICE Collaboration). Charged-Particle Multiplicity Density at Midrapidity in Central Pb-Pb Collisions at $\sqrt{s_{NN}} = 2.76$ TeV. *Phys. Rev. Lett.*, 105:252301, Dec 2010.

[74] R. Nouicer. Systematics of Global Observables in Cu+Cu and Au+Au Collisions at RHIC Energies. *AIP Conference Proceedings*, 842(1):86–88, 2006.

[75] B. Alver et. al (PHOBOS Collaboration). System Size, Energy, and Centrality Dependence of Pseudorapidity Distributions of Charged Particles in Relativistic Heavy-Ion Collisions. *Phys. Rev. Lett.*, 102:142301, Apr 2009.

[76] S. V. Afanasiev et. al (NA49 Collaboration). Energy dependence of pion and kaon production in central Pb+Pb collisions. *Phys. Rev. C*, 66:054902, Nov 2002.

[77] T. Anticic et. al (NA49 Collaboration). Energy and centrality dependence of deuteron and proton production in Pb + Pb collisions at relativistic energies. *Phys. Rev. C*, 69:024902, Feb 2004.

[78] R. Pasechnik and M. Šumbera. Phenomenological Review on Quark–Gluon Plasma: Concepts vs. Observations. *Universe*, 3(1):7, 2017.

[79] G. Roland, K. Šafařík, and P. Steinberg. Heavy-ion collisions at the LHC. *Prog. Part. Nucl. Phys.*, 77:70 – 127, 2014.

[80] E. Schnedermann, J. Sollfrank, and U. Heinz. Thermal phenomenology of hadrons from 200A GeV S + S collisions. *Phys. Rev. C*, 48:2462–2475, Nov 1993.

[81] U. Heinz. Concepts of Heavy-Ion Physics. *arXiv:hep-ph/0407360*, 2004.

[82] E. Schnedermann, J. Sollfrank, and U. Heinz. Thermal phenomenology of hadrons from 200A GeV S+S collisions. *Phys. Rev. C*, 48:2462–2475, Nov 1993.

[83] B. Abelev et. al (STAR Collaboration). Systematic measurements of identified particle spectra in pp, $d+\mathrm{Au}$, and $\mathrm{Au}+\mathrm{Au}$ collisions at the STAR detector. *Phys. Rev. C*, 79:034909, 2009.

[84] M. Lisa et. el (EOS Collaboration). Radial Flow in $\mathrm{Au}+\mathrm{Au}$ Collisions at $E = (0.25-1.15)\,A$ GeV. *Phys. Rev. Lett.*, 75:2662–2665, Oct 1995.

[85] W. Reisdorf et. al (FOPI Collaboration). Systematics of central heavy ion collisions in the 1 A GeV regime. *Nucl. Phys. A*, 848(3):366 – 427, 2010.

[86] C. Alt et. al (NA49 Collaboration). Bose-Einstein correlations of $\pi^-\pi^-$ pairs in central Pb+Pb collisions at $20A, 30A, 40A, 80A$, and $158A$ GeV. *Phys. Rev. C*, 77:064908, Jun 2008.

[87] B. Abelev et. al (STAR Collaboration). Identified particle production, azimuthal anisotropy, and interferometry measurements in $\mathrm{Au}+\mathrm{Au}$ collisions at $\sqrt{s_{NN}} = 9.2$ GeV. *Phys. Rev. C*, 81:024911, Feb 2010.

[88] B. Abelev et. al (ALICE Collaboration). Pion, Kaon, and Proton Production in Central Pb-Pb Collisions at $\sqrt{s_{\mathrm{NN}}}$=2.76 TeV. *Phys. Rev. Lett.*, 109:252301, Dec 2012.

[89] A. Andronic. An overview of the experimental study of quark-gluon matter in high-energy nucleus-nucleus collisions. *Int. J. Mod. Phys.*, A29:1430047, 2014.

[90] B. I. Abelev et. al (STAR Collaboration). Identified Baryon and Meson Distributions at Large Transverse Momenta from $\mathrm{Au}+\mathrm{Au}$ Collisions at $\sqrt{s_{NN}} = 200$ GeV.

[91] R. J. Fries, B. Müller, C. Nonaka, and S. A. Bass. Hadronization in Heavy-Ion Collisions: Recombination and Fragmentation of Partons. *Phys. Rev. Lett.*, 90:202303, May 2003.

[92] V. Greco, C. M. Ko, and P. Lévai. Parton Coalescence and the Antiproton/Pion Anomaly at RHIC. *Phys. Rev. Lett.*, 90:202302, May 2003.

[93] S. Wheaton and J. Cleymans. THERMUS: A Thermal model package for ROOT. *Comput. Phys. Commun.*, 180:84–106, 2009.

[94] A. Andronic, P. Braun-Munzinger, and J. Stachel. Thermal hadron production in relativistic nuclear collisions: The Hadron mass spectrum, the horn, and the QCD phase transition. *Phys. Lett. B*, 673:142–145, 2009. [Erratum: Phys. Lett. B 678,516(2009)].

[95] G. Torrieri et al. SHARE: Statistical hadronization with resonances. *Comput. Phys. Commun.*, 167:229–251, 2005.

[96] J. Letessier and J. Rafelski. Strangeness chemical equilibration in a quark-gluon plasma. *Phys. Rev. C*, 75:014905, 2007.

[97] G. Kestin and U. Heinz. Hydrodynamic radial and elliptic flow in heavy-ion collisions from AGS to LHC energies. *Eur. Phys. J. C*, 61(4):545–552, Jun 2009.

[98] J. Y. Ollitrault. Anisotropy as a signature of transverse collective flow. *Phys. Rev. D*, 46:229–245, 1992.

[99] R. Nouicer. New state of nuclear matter: Nearly perfect fluid of quarks and gluons in heavy-ion collisions at RHIC energies. *Eur. Phys. J. Plus*, 131(3):70, Mar 2016.

[100] A. M. Poskanzer and S. A. Voloshin. Methods for analyzing anisotropic flow in relativistic nuclear collisions. *Phys. Rev. C*, 58:1671–1678, Sep 1998.

[101] J. Adams et al. (STAR Collaboration). Multi-strange baryon elliptic flow in Au + Au collisions at $\sqrt{s_{\rm NN}} = 200$ GeV. *Phys. Rev. Lett.*, 95:122301, 2005.

[102] J. Adams et al. (STAR Collaboration). Particle type dependence of azimuthal anisotropy and nuclear modification of particle production in Au + Au collisions at $\sqrt{s_{\rm NN}} = 200$ GeV. *Phys. Rev. Lett.*, 92:052302, 2004.

[103] B. B. Abelev et al. (ALICE Collaboration). Elliptic flow of identified hadrons in Pb-Pb collisions at $\sqrt{s_{\rm NN}} = 2.76$ TeV. *JHEP*, 06:190, 2015.

[104] S. Acharya et al. (ALICE Collaboration). Investigations of Anisotropic Flow Using Multiparticle Azimuthal Correlations in pp, $p-$Pb, Xe-Xe, and Pb-Pb Collisions at the LHC. *Phys. Rev. Lett.*, 123:142301, Oct 2019.

[105] V. Khachatryan et al. Evidence for collectivity in pp collisions at the LHC. *Phy. Lett. B*, 765:193–220, 2017.

[106] J. Rafelski and B. Müller. Strangeness Production in the Quark-Gluon Plasma. *Phys. Rev. Lett.*, 48:1066–1069, 1982.

[107] P. Koch, B. Müller, and J. Rafelski. Strangeness in relativistic heavy ion collisions. *Phys. Rep.*, 142(4):167 – 262, 1986.

[108] E. Andersen et. al (WA97 Collaboration). Strangeness enhancement at mid-rapidity in Pb–Pb collisions at 158 A GeV/c. *Phys. Lett. B*, 449(3):401 – 406, 1999.

[109] F. Antinori et. al (NA57 Collaboration). Enhancement of hyperon production at central rapidity in 158 A G*e*V/c Pb-Pb collisions. *J. Phys. G*, 32(4):427, 2006.

[110] B. Abelev et. al (STAR Collaboration). Energy and system size dependence of phi meson production in Cu+Cu and Au+Au collisions. *Phys. Lett. B*, 673:183–191, 2009.

[111] B. Abelev et. al (ALICE Collaboration). Multi-strange baryon production at mid-rapidity in Pb-Pb collisions at $\sqrt{s_{NN}} = 2.76$ TeV. *Phys. Lett. B*, 728:216 – 227, 2014.

[112] A. Tounsi, A. Mischke, and K. Redlich. Canonical aspects of strangeness enhancement. *Nucl. Phys. A*, 715:565c – 568c, 2003. Quark Matter 2002.

[113] S. Hamieh, K. Redlich, and A. Tounsi. Canonical description of strangeness enhancement from p-A to Pb-Pb collisions. *Phys. Lett. B*, 486:61–66, 2000.

[114] C. W. Fabjan et al. (ALICE Collaboration). ALICE: Physics performance report, volume II. *J. Phys.*, G32:1295–2040, 2006.

[115] M. Stephanov, K. Rajagopal, and E. Shuryak. Event-by-event fluctuations in heavy ion collisions and the QCD critical point. *Phys. Rev. D*, 60:114028, Nov 1999.

[116] L. Stodolsky. Temperature Fluctuations in Multiparticle Production. *Phys. Rev. Lett.*, 75:1044–1045, Aug 1995.

[117] J. Adams et al. (STAR Collaboration). Incident energy dependence of pt correlations at RHIC. *Phys. Rev. C*, 72:044902, 2005.

[118] S. Gavin. Traces of Thermalization from p_t Fluctuations in Nuclear Collisions. *Phys. Rev. Lett.*, 92:162301, Apr 2004.

[119] E. G. Ferreiro, F. del Moral, and C. Pajares. Transverse momentum fluctuations and percolation of strings. *Phys. Rev. C*, 69:034901, Mar 2004.

[120] M. Rybczynski, Z. Wlodarczyk, and G. Wilk. Possible signal for critical point in hadronization process. *Acta Phys. Polon. B*, 35:819–836, 2004.

[121] M. H. Thoma and M. Gyulassy. Quark damping and energy loss in the high temperature QCD. *Nucl. Phys. B*, 351(3):491 – 506, 1991.

[122] E. Braaten and M. H. Thoma. Energy loss of a heavy fermion in a hot QED plasma. *Phys. Rev. D*, 44:1298–1310, Aug 1991.

[123] Xi. Wang and M. Gyulassy. hijing: A Monte Carlo model for multiple jet production in pp, pA, and AA collisions. *Phys. Rev. D*, 44:3501–3516, Dec 1991.

[124] M. Gyulassy and Xi. Wang. Multiple collisions and induced gluon bremsstrahlung in QCD. *Nucl. Phys. B*, 420(3):583 – 614, 1994.

[125] Xi. Wang, M. Gyulassy, and M. Plümer. Landau-Pomeranchuk-Migdal effect in QCD and radiative energy loss in a quark-gluon plasma. *Phys. Rev. D*, 51:3436–3446, Apr 1995.

[126] R. Baier et al. Induced gluon radiation in a QCD medium. *Phys. Lett. B*, 345(3):277 – 286, 1995.

[127] R. S. Bhalerao. Relativistic heavy-ion collisions. In *Proceedings, 1st Asia-Europe-Pacific School of High-Energy Physics (AEPSHEP): Fukuoka, Japan, October 14-27, 2012*, pages 219–239, 2014.

[128] K. Aamodt et al. (ALICE Collaboration). Suppression of charged particle production at large transverse momentum in central Pb–Pb collisions at $\sqrt{s_{NN}} = 2.76$ TeV. *Phys. Lett. B*, 696(1):30 – 39, 2011.

[129] J. Adams et al. (STAR Collaboration). Evidence from $d+$Au Measurements for Final-State Suppression of High-p_T Hadrons in Au$+$Au Collisions at RHIC. *Phys. Rev. Lett.*, 91:072304, Aug 2003.

[130] T. Matsui and H. Satz. J/ψ Suppression by Quark-Gluon Plasma Formation. *Phys. Lett. B*, 178:416–422, 1986.

[131] M. C. Abreu et al. (NA50 Collaboration). J/ψ and Drell-Yan cross-sections in Pb-Pb interactions at 158 GeV/c per nucleon. *Phys. Lett. B*, 410(2):327 – 336, 1997.

[132] M. C. Abreu et al. (NA50 Collaboration). Anomalous J/ψ suppression in Pb-Pb interactions at 158 GeV/c per nucleon. *Phys. Lett. B*, 410(2):337 – 343, 1997.

[133] A. Adare et al. (PHENIX Collaboration). J/ψ Production versus Centrality, Transverse Momentum, and Rapidity in Au + Au Collisions at $\sqrt{s_{NN}} = 200$ GeV. *Phys. Rev. Lett.*, 98:232301, Jun 2007.

[134] B. Abelev et al. (ALICE Collaboration). J/ψ Suppression at Forward Rapidity in Pb-Pb Collisions at $\sqrt{s_{\rm NN}} = 2.76$ TeV. *Phys. Rev. Lett.*, 109:072301, Aug 2012.

[135] A. Andronic, P. Braun-Munzinger, K. Redlich, and J. Stachel. Evidence for charmonium generation at the phase boundary in ultra-relativistic nuclear collisions. *Phys. Lett. B*, 652(5):259 – 261, 2007.

[136] R. L. Thews, M. Schroedter, and J. Rafelski. Enhanced J/ψ production in deconfined quark matter. *Phys. Rev. C*, 63:054905, Apr 2001.

[137] B. Abelev et al. (ALICE Collaboration). Centrality, rapidity and transverse momentum dependence of J/ψ suppression in Pb–Pb collisions at $\sqrt{s_{NN}}$ =2.76 TeV. *Phys. Lett. B*, 734:314 – 327, 2014.

[138] J. Alam, S. Raha, and B. Sinha. Electromagnetic probes of quark gluon plasma. *Phys. Rep.*, 273(5):243 – 362, 1996.

[139] K. Reygers. Direct-photon production in heavy-ion collisions from SPS to RHIC energies. *Eur. Phys. J. C*, 43(1):393–398, Aug 2005.

[140] L. Bhattacharya, R. Ryblewski, and M. Strickland. Photon production from a nonequilibrium quark-gluon plasma. *Phys. Rev. D*, 93:065005, Mar 2016.

[141] M. M. Aggarwal et al. (WA98 Collaboration). Observation of Direct Photons in Central 158 *A* GeV $Pb+Pb$ Collisions. *Phys. Rev. Lett.*, 85:3595–3599, Oct 2000.

[142] J. Adam et. al (ALICE Collaboration). Direct photon production in Pb-Pb collisions at $\sqrt{s_{\rm NN}} = 2.76$ TeV. *Phys. Lett. B*, 754:235–248, 2016.

[143] R. Rapp. Signatures of thermal dilepton radiation at ultrarelativistic energies. *Phys. Rev. C*, 63:054907, Apr 2001.

[144] S. Chatrchyan et al. (CMS Collaboration). Observation of long-range, near-side angular correlations in p-Pb collisions at the LHC. *Phys. Lett. B*, 718(3):795 – 814, 2013.

[145] J. Adams et al. (STAR Collaboration). Distributions of Charged Hadrons Associated with High Transverse Momentum Particles in pp and Au + Au Collisions at $\sqrt{s_{NN}} = 200$ GeV. *Phys. Rev. Lett.*, 95:152301, Oct 2005.

[146] A. Adare et al. (PHENIX Collaboration). System Size and Energy Dependence of Jet-Induced Hadron Pair Correlation Shapes in Cu + Cu and Au + Au Collisions at $\sqrt{s_{NN}} = 200$ and 62.4 GeV. *Phys. Rev. Lett.*, 98:232302, Jun 2007.

[147] B. Alver et al. (PHOBOS Collaboration). System size dependence of cluster properties from two-particle angular correlations in Cu + Cu and Au + Au collisions at $\sqrt{s_{NN}} = 200$ GeV. *Phys. Rev. C*, 81:024904, Feb 2010.

[148] S. Chatrchyan et al. (CMS Collaboration). Centrality dependence of dihadron correlations and azimuthal anisotropy harmonics in Pb-Pb collisions at $\sqrt{s_{NN}} = 2.76$ TeV. *Eur. Phys. J. C*, 72(5):2012, May 2012.

[149] P. Skands, S. Carrazza, and J. Rojo. Tuning PYTHIA 8.1: The Monash 2013 tune. *Eur. Phys. J. C*, 74:3024, 2014.

[150] A. O. Velasquez et al. Color Reconnection and Flowlike Patterns in pp Collisions. *Phys. Rev. Lett.*, 111:042001, 2013.

[151] K. Aamodt et al. (ALICE Collaboration). The ALICE experiment at the CERN LHC. *J. Instr.*, 3(08):S08002–S08002, 2008.

[152] F. Carminati et al. (ALICE Collaboration). ALICE: Physics performance report, Volume I. *J. Phys. G*, 30(11):1517–1763, 2004.

[153] CERN, Report on the 19th September incident at the LHC. 2008.

[154] OPEN-PHO-ACCEL-2016-013, https://cds.cern.ch/record/2225847?ln=en.

[155] A. Tauro. ALICE Schematics. *General Photo*, May, 2017.

[156] G. Dellacasa et al. (ALICE Collaboration). ALICE technical design report of the Inner Tracking System (ITS). 1999.

[157] G. Dellacasa et al. (ALICE Collaboration). ALICE: Technical design report of the Time Projection Chamber. 2000.

[158] J. Alme et al. (ALICE Collaboration). The ALICE TPC, a large 3-dimensional tracking device with fast readout for ultra-high multiplicity events. *Nucl. Instrum. Meth.*, A622:316–367, 2010.

[159] A. Kalweit. Production of light flavor hadrons and anti-nuclei at the LHC. *PhD thesis*, 2012.

[160] K. Nakamura et al. Review of Particle Physics, 2010-2011. Review of Particle Properties. *J. Phys. G*, 37(7A):075021, 2010.

[161] P. Cortese et al. (ALICE Collaboration). ALICE transition-radiation detector: Technical Design Report. *CERN-LHCC-2001-021*, 2001.

[162] G. Dellacasa et al. (ALICE Collaboration). ALICE technical design report of the Time-Of-Flight system (TOF). *CERN-LHCC-2000-012*, 2000.

[163] G. Dellacasa et al. (ALICE Collaboration). ALICE technical design report of the Photon Spectrometer (PHOS). *CERN-LHCC-99-04*, 1999.

[164] S. Beole et al. (ALICE Collaboration). ALICE technical design report: Detector for High Momentum PID. *CERN-LHCC-98-19*, 1998.

[165] L. Molnar. The ALICE HMPID detector ready for collisions at the LHC. *Nuclear Instruments and Methods in Physics Research Section A: Accelerators, Spectrometers, Detectors and Associated Equipment*, 595(1):27 – 30, 2008.

[166] P. Cortese et al. (ALICE Collaboration). ALICE electromagnetic calorimeter technical design report. *CERN-LHCC-2008-014, CERN-ALICE-TDR-014*, 2008.

[167] G. Dellacasa et al. (ALICE Collaboration). ALICE technical design report: Photon multiplicity detector (PMD). *CERN-LHCC-99-32, CERN-OPEN-2000-184*, 1999.

[168] P. Cortese et al. (ALICE Collaboration). ALICE technical design report on forward detectors: FMD, T0 and V0. *CERN-LHCC-2004-025*, 2004.

[169] ALICE technical design report of the dimuon forward spectrometer. *CERN-LHCC-99-22*, 1999.

[170] G. Dellacasa et al. (ALICE Collaboration). ALICE technical design report of the zero degree calorimeter (ZDC). *CERN-LHCC-99-05*, 1999.

[171] A. Fernández et al. (ALICE Collaboration). ACORDE a Cosmic Ray Detector for ALICE. *Nucl. Instrum. Meth.*, A572:102–103, 2007.

[172] C. W. Fabjan et al. (ALICE Collaboration). ALICE trigger data-acquisition high-level trigger and control system: Technical Design Report. *CERN-LHCC-2003-062*, 2004.

[173] http://alice-offline.web.cern.ch/.

[174] ROOT: An object-oriented data analysis framework. *https://root.cern.ch*.

[175] P. Billoir, R. Frühwirth, and M. Regler. Track element merging strategy and vertex fitting in complex modular detectors. *Nuclear Instruments and Methods in Physics Research Section A: Accelerators, Spectrometers, Detectors and Associated Equipment*, 241(1):115 – 131, 1985.

[176] P. Billoir. Track fitting with multiple scattering: A new method. *Nucl. Instrum. Meth. Phys. Res.*, 225(2):352 – 366, 1984.

[177] R. Frühwirth. Application of Kalman filtering to track and vertex fitting. *Nuclear Instruments and Methods in Physics Research Section A: Accelerators, Spectrometers, Detectors and Associated Equipment*, 262(2):444 – 450, 1987.

[178] P. Saiz et al. (ALICE Collaboration). AliEn—ALICE environment on the GRID. *Nuclear Instruments and Methods in Physics Research Section A: Accelerators, Spectrometers, Detectors and Associated Equipment*, 502(2):437 – 440, 2003. Proceedings of the VIII International Workshop on Advanced Computing and Analysis Techniques in Physics Research.

[179] P. Cortese et al. (ALICE Collaboration). ALICE: Physics performance report, volume I. *J. Phys.*, G30:1517–1763, 2004.

[180] J. Adam et al. (ALICE Collaboration). ALICE luminosity determination for pp collisions at $\sqrt{s} = 13$ TeV. *ALICE-PUBLIC-2016-002*, Jun 2016.

[181] R. Brun et al. *GEANT 3: user's guide Geant 3.10, Geant 3.11; rev. version*. CERN, Geneva, 1987.

[182] R. Brun et al. GEANT Detector Description and Simulation Tool. *CERN-W5013, CERN-W-5013, W5013, W-5013*, 1994.

[183] S. Agostinelli et al. (GEANT4 Collaboration). GEANT4: A Simulation toolkit. *Nucl. Instrum. Meth.*, A506:250–303, 2003.

[184] A. Ferrari et al. FLUKA: A multi-particle transport code (Program version 2005). *CERN-2005-010, SLAC-R-773, INFN-TC-05-11*, 2005.

[185] B. Abelev et al. (ALICE Collaboration). Performance of the ALICE Experiment at the CERN LHC. *Int. J. Mod. Phys.*, A29:1430044, 2014.

[186] S. Acharya et al. (ALICE Collaboration). Multiplicity dependence of (multi-)strange hadron production in proton-proton collisions at $\sqrt{s}$ = 13 TeV. *Eur. Phys. J. C*, 80(2):167, 2020.

[187] S. Acharya et. al (ALICE Collaboration). The ALICE definition of primary particles. *ALICE-PUBLIC-2017-005*, Jun 2017.

[188] J. Adam et al. (ALICE Collaboration). Determination of the event collision time with the ALICE detector at the LHC. *Eur. Phys. J. Plus*, 132(2):99, Feb 2017.

[189] S. Baker and R. D. Cousins. Clarification of the use of CHI-square and likelihood functions in fits to histograms. *Nucl. Instrum. Meth. Phys. Res.*, 221(2):437 – 442, 1984.

[190] B. Guerzoni. Identified primary hadron spectra with the TOF detector of the ALICE experiment at LHC. *PhD thesis*, 2012.

[191] J. Adam et al. (ALICE Collaboration). Measurement of pion, kaon and proton production in proton–proton collisions at $\sqrt{s} = 7$ TeV. *Eur. Phys. J. C*, 75(5):226, 2015.

[192] https://twiki.cern.ch/twiki/bin/viewauth/ALICE/AliDPGtoolsTrackSystematicUncertaintyBookkeping.

[193] S. Acharya et al. (ALICE Collaboration). Charged-particle production as a function of multiplicity and transverse spherocity in pp collisions at $\sqrt{s} = 5.02$ and 13 TeV. *Eur. Phys. J. C*, 79(10):857, 2019.

[194] J. Adam et at. (ALICE Collaboration). Multiplicity dependence of charged pion, kaon, and (anti)proton production at large transverse momentum in p–Pb collisions at $\sqrt{s}$ =5.02 TeV. *Phys. Lett. B*, 760:720 – 735, 2016.

[195] S. Kretzer. Fragmentation functions from flavor-inclusive and flavor-tagged e^+e^- annihilations. *Phys. Rev. D*, 62:054001, 2000.

[196] M. Bahr et al. Herwig++ Physics and Manual. *Eur. Phys. J. C*, 58:639–707, 2008.

[197] J. Bellm et al. Herwig 7.0/Herwig++ 3.0 release note. *Eur. Phys. J. C*, 76(4):196, 2016.

[198] C. Flensburg, G. Gustafson, and L. Lönnblad. Inclusive and exclusive observables from dipoles in high energy collisions. *JHEP*, 2011(8):103, 2011.

[199] C. Bierlich et al. Effects of overlapping strings in pp collisions. *JHEP*, 2015(3):148, 2015.

[200] C. Bierlich et al. The Angantyr model for heavy-ion collisions in PYTHIA8. *JHEP*, 2018(10):134, 2018.

[201] C. Tsallis. Possible Generalization of Boltzmann-Gibbs Statistics. *J. Statist. Phys.*, 52:479–487, 1988.

[202] B. I. Abelev et al. (STAR Collaboration). Strange particle production in $p+p$ collisions at $\sqrt{s} = 200$ GeV. *Phys. Rev. C*, 75:064901, Jun 2007.

[203] S. Acharya et al. (ALICE Collaboration). Production of charged pions, kaons, and (anti-)protons in Pb-Pb and inelastic pp collisions at $\sqrt{s_{NN}}$ = 5.02 TeV. *Phys. Rev. C*, 101(4):044907, 2020.

[204] I. A. Karpenko, Y. M. Sinyukov, and K. Werner. Uniform description of bulk observables in the hydrokinetic model of $A+A$ collisions at the BNL Relativistic Heavy Ion Collider and the CERN Large Hadron Collider. *Phys. Rev. C*, 87:024914, Feb 2013.

[205] F. Becattini et al. Hadron Formation in Relativistic Nuclear Collisions and the QCD Phase Diagram. *Phys. Rev. Lett.*, 111:082302, Aug 2013.

[206] J. Steinheimer, J. Aichelin, and M. Bleicher. Nonthermal p/π Ratio at LHC as a Consequence of Hadronic Final State Interactions. *Phys. Rev. Lett.*, 110:042501, Jan 2013.

[207] F. Becattini et al. Hadronization conditions in relativistic nuclear collisions and the QCD pseudo-critical line. *Phys. Lett. B*, 764:241 – 246, 2017.

[208] A. Andronic et al. The thermal proton yield anomaly in Pb-Pb collisions at the LHC and its resolution. *Phys. Lett. B*, 792:304–309, 2019.

[209] R. Stock et al. The QCD Phase Diagram from Statistical Model Analysis. *Nucl. Phys. A*, 982:827–830, 2019.

[210] I. Sarcevic and H. Satz. Self-similar multihadron production at high energies. *Phys. Lett. B*, 233(1):251 – 255, 1989.

[211] P. Lipa and B. Buschbeck. From strong to weak intermittency. *Phys. Lett. B*, 223:465 – 469, 1989.

[212] A. Bzdak, B. Schenke, P. Tribedy, and R. Venugopalan. Initial-state geometry and the role of hydrodynamics in proton-proton, proton-nucleus, and deuteron-nucleus collisions. *Phys. Rev. C*, 87:064906, 2013.

[213] T. Sjöstrand, S. Mrenna, and P. Skands. PYTHIA 6.4 physics and manual. *JHEP*, 05:026, 2006.

[214] G. Gustafson. Deflagrations and detonations as a mechanism of hadron bubble growth in supercooled quark-gluon plasmas. *Acta Phys. Pol. B*, 40:1981, 2009.

[215] B. Bhattacharjee et al. On the emission of fast and slow target fragments from ^{84}Kr–AgBr interactions at 0.95 GeV/A. *Radiat. Meas.*, 36:291 – 294, 2003.

[216] A. Bialas and M. Gazdzicki. A new variable to study intermittency. *Phys. Lett. B*, 252(3):483 – 486, 1990.

[217] M. K. Ghosh and A. Mukhopadhyay. Erraticity analysis of particle production in $^{32}\mathrm{S} - \mathrm{Ag/Br}$ interaction at 200 $A\mathrm{GeV}/c$. *Phys. Rev. C*, 68:034907, 2003.

[218] W. Shaoshun and W. Zhaomin. Chaotic behavior of multiparticle production in pp collisions at 400 GeV/c. *Phys. Rev. D*, 57:3036–3039, 1998.

[219] J. Adam et al. (ALICE Collaboration). Pseudorapidity and transverse-momentum distributions of charged particles in proton–proton collisions at $\sqrt{s}$ = 13 TeV. *Phys. Lett. B*, 753:319 – 329, 2016.

[220] A. Bialas and K. Zalewski. Phase structure of self-similar multiparticle systems and experimental determination of intermittency parameters. *Phys. Lett. B*, 238:413 – 416, 1990.

[221] R. Peschanski. INTERMITTENCY IN PARTICLE COLLISIONS. *Int. J. Mod. Phys. A*, 06(21):3681–3722, 1991.

[222] R. Peschanski. On the existence of a non-thermal phase transition in multi-particle production. *Nucl. Phys. B*, 327(1):144–156, 1989.

[223] Ph. Brax and R. Peschanski. Multifractal analysis of intermittency and phase transitions in multiparticle dynamics. *Nucl. Phys. B*, 346(1):65–83, 1990.

A

List of Publications

REFERRED JOURNAL PAPERS

1. "Multiplicity dependence of π, K and p production in pp collisions at $\sqrt{s} = 13$ TeV" − S. Acharya, ... B. Bhattacharjee, ... **P. Sarma**, *et al.* (ALICE Collaboration) (**Paper committee members:** Vytautas Vislavicius, Ivan Ravasenga, **Pranjal Sarma**, Paraskevi Ganoti, Omar Varquez Rueda)

   European Physical Journal C 20: 693 (2020)

   doi: https://doi.org/10.1140/epjc/s10052-020-8125-1

2. "Color reconnection as a possible mechanism of intermittency in the emission spectra of charged particles in PYTHIA-generated high-multiplicity pp collisions at energies available at the CERN Large Hadron Collider"

   – **Pranjal Sarma** and Buddhadeb Bhattacharjee

   Physical Review C 99, 034901 (2019)

   doi: 10.1103/PhysRevC.99.034901

BOOK CHAPTER

1. "Collectivity in small system"

   Pranjal Sarma and Buddhadeb Bhattacharjee

   A chapter in **"A book on selected research topics in Physics Research, Volume: I, 2021"**

   Published by: **The Physical Society, Department of Physics, Gauhati University**

   ISBN: **9789390919642**

REFEREED CONFERENCE PAPERS

1. "Identified particle production as a function of multiplicity in proton–proton collisions at $\sqrt{s} = 7$ TeV using the ALICE detector"

   Pranjal Sarma on behalf of the ALICE Collaboration

   Proceeding of the DAE Symposium on Nuclear Physics 62 818 (2017)

2. "Multiplicity dependence of π, K and p production in pp collisions at $\sqrt{s} = 13$ TeV with ALICE at the LHC"

   Pranjal Sarma on behalf of the ALICE Collaboration

   Proceeding of the DAE Symposium on Nuclear Physics 64 702 (2019)

ANALYSIS NOTE (ALICE INTERNAL)

1. "Production of pions, kaons and protons in pp collisions at $\sqrt{s} = 13$ TeV as a function of multiplicity"
   Paraskevi Ganoti, Yasser Corrales Morales, Ivan Ravasenga, **Pranjal Sarma**, Omar Varquez Rueda and Vytautas Vislavicius
   ALICE-ANA-2018-4718

PARTICIPATION IN CONFERENCE/SCHOOL

1. "JETSCAPE Summer online school" held in University of Tennessee, USA during 13-24th July 2020.

2. **Poster** presentation at "27$^{\text{th}}$ International Conference on Ultra-relativistic Nucleus-Nucleus Collisions (Quark Matter 2018)" held in Venezia Lido, Venice, Italy during 13-19$^{\text{th}}$ May 2018.

3. **Oral** presentation at "62$^{\text{nd}}$ DAE-BRNS Symposium on Nuclear Physics" held in Thapar Univeristy, Patiala, India during 20-24$^{\text{th}}$ December 2017.

4. "11$^{\text{th}}$ SERC School on Experimental High-Energy Physics" held in NISER, Bhubaneswar, India during 07-27$^{\text{th}}$ November 2017.

5. **Poster** presentation at "17$^{\text{th}}$ International Conference on Strangeness in Quark Matter (SQM 2017)" held in Utrecht University, Utrecht, The Netherlands during 10-15$^{\text{th}}$ July 2017.

6. **Oral** presentation at "10$^{\text{th}}$ Biennial National Conference on Physics Academy of North East" held in St' Anthony College, Meghalaya, India during 10-12$^{\text{th}}$ November 2016.

European Organization for Nuclear Research
Organisation européenne pour la recherche nucléaire

Dr. Luciano Musa
CERN, Experimental Physics (EP)
ALICE Experiment Spokesperson

Mail address:
CERN, EP Department
CH-1211 GENEVE 23
Switzerland

Telephone : +4175 4113119
e-mail : luciano.musa@cern.ch

Geneva, 8th July 2020

To Whom It May Concern,

Pranjal Sarma is a member of the ALICE Collaboration since April 2015. During that time, he has given several contributions to the physics analysis, as member of the Physics Working Group that studies the production of Light Flavour hadrons (PWG-LF), as well as to the operation of the experiment.

More in detail, Pranjal Sarma has carried out the analysis of pp collisions data at sqrt(s) = 13 TeV to identify pions, kaons and protons as a function of multiplicity,using the ALICE Time-of-Flight (TOF) detector. He is also one of the authors of the analysis note entitled "**Production of pions, kaons and protons in pp collisions at** sqrt(s) = **13 TeV as a function of multiplicity**", and one of the members of the paper committee on **"Multiplicity dependence of π, K, and p production in pp collisions at sqrt(s)= 13 TeV".**

The **ALICE Collaboration** as no objections to allowing him to include the results from the aforementioned contributions in his thesis.

Yours sincerely,

Luciano Musa
ALICE Collaboration Spokesperson

EUROPEAN ORGANIZATION FOR NUCLEAR RESEARCH

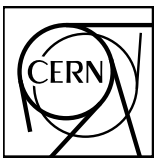

ALICE-ANA-2018-4718
March 5, 2020

Production of pions, kaons and protons in pp collisions at $\sqrt{s}$ = 13 TeV as a function of multiplicity

Paraskevi Ganoti[1], Yasser Corrales Morales[2], Ivan Ravasenga[3], Pranjal Sarma[4], Vytautas Vislavicius[5], Omar Vázquez Rueda[5]

1. National and Kapodistrian University of Athens, School of Science, Department of Physics
2. Sezione INFN, Torino (Italy)
3. Dipartimento DISAT del Politecnico and Sezione INFN, Torino (Italy)
4. Department of Physics, Gauhati University, Guwahati, India
5. Lund University Department of Physics/Division of Particle Physics, Sweden

Email: paraskevi.ganoti@cern.ch; yasser.corales.morales@cern.ch; ivan.ravasenga@cern.ch; pranjal.sarma@cern.ch; vytautas.vislavicius@cern.ch

Abstract

In this document we describe the analysis details to measure the production of charged pions, kaons and (anti)protons in pp collisions at $\sqrt{s} = 13$ TeV as a function of multiplicity from hundreds of MeV/c up to 6 GeV/c combining different particle identification techniques: Inner Tracking System (ITS), Time Projection Chamber (TPC), Time Of Flight (TOF). In addition, kaon production from kink decay topology is also included.
The identified particle transverse momentum spectra (p_{T}) are used to extract the integrated yield, the mean p_{T}, the kaon-to-pion and proton-to-pion ratios. Moreover the data are compared to the Blast-Wave model extracting the temperature of the kinetic freeze-out and the average of the transverse velocity distribution.
The results are finally compared to the ones obtained in ALICE with other colliding systems and energies.

Eur. Phys. J. C (2020) 80:693
https://doi.org/10.1140/epjc/s10052-020-8125-1

THE EUROPEAN PHYSICAL JOURNAL C

Regular Article - Experimental Physics

Multiplicity dependence of π, K, and p production in pp collisions at $\sqrt{s} = 13$ TeV

ALICE Collaboration[*]

CERN, 1211 Geneva 23, Switzerland

Received: 11 March 2020 / Accepted: 7 June 2020

Abstract This paper presents the measurements of $\pi^{\pm}$, $\mathrm{K}^{\pm}$, p and $\overline{\mathrm{p}}$ transverse momentum (p_{T}) spectra as a function of charged-particle multiplicity density in proton–proton (pp) collisions at $\sqrt{s} = 13$ TeV with the ALICE detector at the LHC. Such study allows us to isolate the center-of-mass energy dependence of light-flavour particle production. The measurements reported here cover a p_{T} range from 0.1 to 20 GeV/c and are done in the rapidity interval $|y| < 0.5$. The p_{T}-differential particle ratios exhibit an evolution with multiplicity, similar to that observed in pp collisions at $\sqrt{s} = 7$ TeV, which is qualitatively described by some of the hydrodynamical and pQCD-inspired models discussed in this paper. Furthermore, the p_{T}-integrated hadron-to-pion yield ratios measured in pp collisions at two different center-of-mass energies are consistent when compared at similar multiplicities. This also extends to strange and multi-strange hadrons, suggesting that, at LHC energies, particle hadrochemistry scales with particle multiplicity the same way under different collision energies and colliding systems.

1 Introduction

The unprecedented energies available at the Large Hadron Collider (LHC) provide unique opportunities to investigate the properties of strongly-interacting matter. Particle production at large transverse momenta (p_{T}) is well-described by perturbative Quantum Chromodynamics (pQCD). The soft regime ($p_{\mathrm{T}} \lesssim 2$ GeV/c), in which several collective phenomena are observed in proton-proton (pp), proton-lead (p–Pb), and heavy-ion (A–A) collisions, is not calculable from first principles of QCD. Instead, in order to describe bulk particle production in A–A collisions, one usually relies on hydrodynamic and thermodynamic modelling, which assumes the system to be in kinetic and chemical equilibrium [1,2]. On the other hand, the description of low-p_{T} particle spectra in smaller systems such as pp collisions is often based on phenomenological modelling of multi-partonic interactions (MPI) and color reconnection (CR) [3,4] or overlapping strings [5].

Recent reports on the enhancement of (multi)strange hadrons [6], double-ridge structure [7,8], non-zero v_2 coefficients [9], mass ordering in hadron p_{T} spectra, and characteristic modifications of baryon-to-meson ratios [10] suggest that collective phenomena are present at the LHC energies also in p–Pb collisions. This is further extended to even smaller systems, such as pp collisions at $\sqrt{s} = 7$ TeV, where similar observations have been reported in high multiplicity events, indicating that the collective effects are not characteristic of heavy-ion collisions only. Furthermore, a continuous transition of light-flavor hadron-to-pion ratios as a function of charged-particle multiplicity density $\mathrm{d}N_{\mathrm{ch}}/\mathrm{d}\eta$ from pp to p–Pb and then to Pb–Pb collisions was found [11–13]. The observed similarities suggest the existence of a common underlying mechanism determining the chemical composition of particles produced in these three collision systems.

Results from pp [11] and p–Pb [10] collisions indicate that particle production scales with $\mathrm{d}N_{\mathrm{ch}}/\mathrm{d}\eta$ independent of the colliding system. Measurements reported in previous multiplicity-dependent studies have considered different colliding systems, each at a different center-of-mass energy. In this work, we extend the existing observations by performing a detailed study of pp collisions at $\sqrt{s} = 13$ TeV. A similar study has been reported by the CMS Collaboration, albeit in a limited p_{T} range [14]. Thanks to the availability of Run 2 data from the LHC, for the first time, in pp collisions, we can disentangle the effect of center-of-mass energy from the multiplicity dependence of $\pi^{\pm}$, $\mathrm{K}^{\pm}$and p ($\overline{\mathrm{p}}$) production in a wide p_{T} range.

In this paper, we report on the multiplicity dependence of the production of primary $\pi^{\pm}$, $\mathrm{K}^{\pm}$and p ($\overline{\mathrm{p}}$) at $\sqrt{s} = 13$ TeV. Particles are considered as primary if their mean proper decay length $c\tau$ is larger than 1 cm and they are created in the collision (including products of strong and electro-

See Appendix A for the list of collaboration members.

[*] e-mail: alice-publications@cern.ch

Published online: 01 August 2020

R. P. Pezzi[70], S. Piano[59], M. Pikna[13], P. Pillot[114], O. Pinazza[33,53], L. Pinsky[125], C. Pinto[27], S. Pisano[10,51], D. Pistone[55], M. Płoskoń[79], M. Planinic[98], F. Pliquett[68], S. Pochybova[145,a], M. G. Poghosyan[95], B. Polichtchouk[90], N. Poljak[98], A. Pop[47], S. Porteboeuf-Houssais[134], V. Pozdniakov[75], S. K. Prasad[3], R. Preghenella[53], F. Prino[58], C. A. Pruneau[143], I. Pshenichnov[62], M. Puccio[33], J. Putschke[143], L. Quaglia[25], R. E. Quishpe[125], S. Ragoni[110], S. Raha[3], S. Rajput[100], J. Rak[126], A. Rakotozafindrabe[137], L. Ramello[31], F. Rami[136], S. A. R. Ramirez[44], R. Raniwala[101], S. Raniwala[101], S. S. Räsänen[43], R. Rath[49], V. Ratza[42], I. Ravasenga[89], K. F. Read[95,130], A. R. Redelbach[38], K. Redlich[84,f], A. Rehman[21], P. Reichelt[68], F. Reidt[33], X. Ren[6], R. Renfordt[68], Z. Rescakova[37], K. Reygers[103], V. Riabov[97], T. Richert[80,88], M. Richter[20], P. Riedler[33], W. Riegler[33], F. Riggi[27], C. Ristea[67], S. P. Rode[49], M. Rodríguez Cahuantzi[44], K. Røed[20], R. Rogalev[90], E. Rogochaya[75], D. Rohr[33], D. Röhrich[21], P. S. Rokita[142], F. Ronchetti[51], E. D. Rosas[69], K. Roslon[142], A. Rossi[28,56], A. Rotondi[139], A. Roy[49], P. Roy[109], O. V. Rueda[80], R. Rui[24], B. Rumyantsev[75], A. Rustamov[86], E. Ryabinkin[87], Y. Ryabov[97], A. Rybicki[118], H. Rytkonen[126], O. A. M. Saarimaki[43], S. Sadhu[141], S. Sadovsky[90], K. Šafařík[36], S. K. Saha[141], B. Sahoo[48], P. Sahoo[48], R. Sahoo[49], S. Sahoo[65], P. K. Sahu[65], J. Saini[141], S. Sakai[133], S. Sambyal[100], V. Samsonov[92,97], D. Sarkar[143], N. Sarkar[141], P. Sarma[41], V. M. Sarti[104], M. H. P. Sas[63], E. Scapparone[53], J. Schambach[119], H. S. Scheid[68], C. Schiaua[47], R. Schicker[103], A. Schmah[103], C. Schmidt[106], H. R. Schmidt[102], M. O. Schmidt[103], M. Schmidt[102], N. V. Schmidt[68,95], A. R. Schmier[130], J. Schukraft[88], Y. Schutz[33,136], K. Schwarz[106], K. Schweda[106], G. Scioli[26], E. Scomparin[58], M. Šefčík[37], J. E. Seger[15], Y. Sekiguchi[132], D. Sekihata[132], I. Selyuzhenkov[92,106], S. Senyukov[136], D. Serebryakov[62], E. Serradilla[71], A. Sevcenco[67], A. Shabanov[62], A. Shabetai[114], R. Shahoyan[33], W. Shaikh[109], A. Shangaraev[90], A. Sharma[99], A. Sharma[100], H. Sharma[118], M. Sharma[100], N. Sharma[99], S. Sharma[100], A. I. Sheikh[141], K. Shigaki[45], M. Shimomura[82], S. Shirinkin[91], Q. Shou[39], Y. Sibiriak[87], S. Siddhanta[54], T. Siemiarczuk[84], D. Silvermyr[80], G. Simatovic[89], G. Simonetti[33], B. Singh[104], R. Singh[85], R. Singh[100], R. Singh[49], V. K. Singh[141], V. Singhal[141], T. Sinha[109], B. Sitar[13], M. Sitta[31], T. B. Skaali[20], M. Slupecki[126], N. Smirnov[146], R. J. M. Snellings[63], C. Soncco[111], J. Song[125], A. Songmoolnak[115], F. Soramel[28], S. Sorensen[130], I. Sputowska[118], M. Spyropoulou-stassinaki[83], J. Stachel[103], I. Stan[67], P. Stankus[95], P. J. Steffanic[130], E. Stenlund[80], D. Stocco[114], M. M. Storetvedt[35], L. D. Stritto[29], A. A. P. Suaide[121], T. Sugitate[45], C. Suire[61], M. Suleymanov[14], M. Suljic[33], R. Sultanov[91], M. Šumbera[94], V. Sumberia[100], S. Sumowidagdo[50], S. Swain[65], A. Szabo[13], I. Szarka[13], U. Tabassam[14], S. F. Taghavi[104], G. Taillepied[134], J. Takahashi[122], G. J. Tambave[21], S. Tang[6,134], M. Tarhini[114], M. G. Tarzila[47], A. Tauro[33], G. Tejeda Muñoz[44], A. Telesca[33], L. Terlizzi[25], C. Terrevoli[125], D. Thakur[49], S. Thakur[141], D. Thomas[119], F. Thoresen[88], R. Tieulent[135], A. Tikhonov[62], A. R. Timmins[125], A. Toia[68], N. Topilskaya[62], M. Toppi[51], F. Torales-Acosta[19], S. R. Torres[36,120], A. Trifiro[55], S. Tripathy[49,69], T. Tripathy[48], S. Trogolo[28], G. Trombetta[32], L. Tropp[37], V. Trubnikov[2], W. H. Trzaska[126], T. P. Trzcinski[142], B. A. Trzeciak[36,63], T. Tsuji[132], A. Tumkin[108], R. Turrisi[56], T. S. Tveter[20], K. Ullaland[21], E. N. Umaka[125], A. Uras[135], G. L. Usai[23], M. Vala[37], N. Valle[139], S. Vallero[58], N. van der Kolk[63], L. V. R. van Doremalen[63], M. van Leeuwen[63], P. Vande Vyvre[33], D. Varga[145], Z. Varga[145], M. Varga-Kofarago[145], A. Vargas[44], M. Vasileiou[83], A. Vasiliev[87], O. Vázquez Doce[104,117], V. Vechernin[112], E. Vercellin[25], S. Vergara Limón[44], L. Vermunt[63], R. Vernet[7], R. Vértesi[145], L. Vickovic[34], Z. Vilakazi[131], O. Villalobos Baillie[110], G. Vino[52], A. Vinogradov[87], T. Virgili[29], V. Vislavicius[88], A. Vodopyanov[75], B. Volkel[33], M. A. Völkl[102], K. Voloshin[91], S. A. Voloshin[143], G. Volpe[32], B. von Haller[33], I. Vorobyev[104], D. Voscek[116], J. Vrláková[37], B. Wagner[21], M. Weber[113], A. Wegrzynek[33], S. C. Wenzel[33], J. P. Wessels[144], J. Wiechula[68], J. Wikne[20], G. Wilk[84], J. Wilkinson[10,53], G. A. Willems[114], E. Willsher[110], B. Windelband[103], M. Winn[137], W. E. Witt[130], Y. Wu[128], R. Xu[6], S. Yalcin[77], Y. Yamaguchi[45], K. Yamakawa[45], S. Yang[21], S. Yano[137], Z. Yin[6], H. Yokoyama[63], I.-K. Yoo[17], J. H. Yoon[60], S. Yuan[21], A. Yuncu[103], V. Yurchenko[2], V. Zaccolo[24], A. Zaman[14], C. Zampolli[33], H. J. C. Zanoli[63], N. Zardoshti[33], A. Zarochentsev[112], P. Závada[66], N. Zaviyalov[108], H. Zbroszczyk[142], M. Zhalov[97], S. Zhang[39], X. Zhang[6], Z. Zhang[6], V. Zherebchevskii[112], D. Zhou[6], Y. Zhou[88], Z. Zhou[21], J. Zhu[6,106], Y. Zhu[6], A. Zichichi[10,26], G. Zinovjev[2], N. Zurlo[140]

[1] A.I. Alikhanyan National Science Laboratory (Yerevan Physics Institute) Foundation, Yerevan, Armenia
[2] Bogolyubov Institute for Theoretical Physics, National Academy of Sciences of Ukraine, Kiev, Armenia
[3] Department of Physics and Centre for Astroparticle Physics and Space Science (CAPSS), Bose Institute, Kolkata, India
[4] Budker Institute for Nuclear Physics, Novosibirsk, Russia
[5] California Polytechnic State University, San Luis Obispo, CA, USA
[6] Central China Normal University, Wuhan, China
[7] Centre de Calcul de l'IN2P3, Villeurbanne, Lyon, France
[8] Centro de Aplicaciones Tecnológicasy Desarrollo Nuclear (CEADEN), Havana, Cuba
[9] Centro de Investigación y de Estudios Avanzados (CINVESTAV), Mexico City and Mérida, Mexico
[10] Centro Fermi-Museo Storico della Fisica e Centro Studi e Ricerche "Enrico Fermi', Rome, Italy
[11] Chicago State University, Chicago, IL, USA

[12] China Institute of Atomic Energy, Beijing, China
[13] Faculty of Mathematics, Physics and Informatics, Comenius University Bratislava, Bratislava, Slovakia
[14] COMSATS University Islamabad, Islamabad, Pakistan
[15] Creighton University, Omaha, NE, USA
[16] Department of Physics, Aligarh Muslim University, Aligarh, India
[17] Department of Physics, Pusan National University, Pusan, Republic of Korea
[18] Department of Physics, Sejong University, Seoul, Republic of Korea
[19] Department of Physics, University of California, Berkeley, CA, USA
[20] Department of Physics, University of Oslo, Oslo, Norway
[21] Department of Physics and Technology, University of Bergen, Bergen, Norway
[22] Dipartimento di Fisica dell'Università 'La Sapienza' and Sezione INFN, Rome, Italy
[23] Dipartimento di Fisica dell'Università and Sezione INFN, Cagliari, Italy
[24] Dipartimento di Fisica dell'Università and Sezione INFN, Trieste, Italy
[25] Dipartimento di Fisica dell'Università and Sezione INFN, Turin, Italy
[26] Dipartimento di Fisica e Astronomia dell'Università and Sezione INFN, Bologna, Italy
[27] Dipartimento di Fisica e Astronomia dell'Università and Sezione INFN, Catania, Italy
[28] Dipartimento di Fisica e Astronomia dell'Università and Sezione INFN, Padua, Italy
[29] Dipartimento di Fisica 'E.R. Caianiello' dell'Università and Gruppo Collegato INFN, Salerno, Italy
[30] Dipartimento DISAT del Politecnico and Sezione INFN, Turin, Italy
[31] Dipartimento di Scienze e Innovazione Tecnologica dell'Università del Piemonte Orientale and INFN Sezione di Torino, Alessandria, Italy
[32] Dipartimento Interateneo di Fisica 'M. Merlin' and Sezione INFN, Bari, Italy
[33] European Organization for Nuclear Research (CERN), Geneva, Switzerland
[34] Faculty of Electrical Engineering, Mechanical Engineering and Naval Architecture, University of Split, Split, Croatia
[35] Faculty of Engineering and Science, Western Norway University of Applied Sciences, Bergen, Norway
[36] Faculty of Nuclear Sciences and Physical Engineering, Czech Technical University in Prague, Prague, Czech Republic
[37] Faculty of Science, P.J. Šafárik University, Košice, Slovakia
[38] Frankfurt Institute for Advanced Studies, Johann Wolfgang Goethe-Universität Frankfurt, Frankfurt, Germany
[39] Fudan University, Shanghai, China
[40] Gangneung-Wonju National University, Gangneung, Republic of Korea
[41] Department of Physics, Gauhati University, Guwahati, India
[42] Helmholtz-Institut für Strahlen- und Kernphysik, Rheinische Friedrich-Wilhelms-Universität Bonn, Bonn, Germany
[43] Helsinki Institute of Physics (HIP), Helsinki, Finland
[44] High Energy Physics Group, Universidad Autónoma de Puebla, Puebla, Mexico
[45] Hiroshima University, Hiroshima, Japan
[46] Hochschule Worms, Zentrum für Technologietransfer und Telekommunikation (ZTT), Worms, Germany
[47] Horia Hulubei National Institute of Physics and Nuclear Engineering, Bucharest, Romania
[48] Indian Institute of Technology Bombay (IIT), Mumbai, India
[49] Indian Institute of Technology Indore, Indore, India
[50] Indonesian Institute of Sciences, Jakarta, Indonesia
[51] INFN, Laboratori Nazionali di Frascati, Frascati, Italy
[52] INFN, Sezione di Bari, Bari, Italy
[53] INFN, Sezione di Bologna, Bologna, Italy
[54] INFN, Sezione di Cagliari, Cagliari, Italy
[55] INFN, Sezione di Catania, Catania, Italy
[56] INFN, Sezione di Padova, Padua, Italy
[57] INFN, Sezione di Roma, Rome, Italy
[58] INFN, Sezione di Torino, Turin, Italy
[59] INFN, Sezione di Trieste, Trieste, Italy
[60] Inha University, Incheon, Republic of Korea
[61] Institut de Physique Nuclèaire d'Orsay (IPNO), Institut National de Physique Nuclèaire et de Physique des Particules (IN2P3/CNRS), Universitè de Paris-Sud, Université Paris-Saclay, Orsay, France
[62] Institute for Nuclear Research, Academy of Sciences, Moscow, Russia

Color reconnection as a possible mechanism of intermittency in the emission spectra of charged particles in PYTHIA-generated high-multiplicity *pp* collisions at energies available at the CERN Large Hadron Collider

Pranjal Sarma* and Buddhadeb Bhattacharjee†
Nuclear and Radiation Physics Research Laboratory, Department of Physics, Gauhati University, Guwahati, Assam - 781014, India

(Received 14 November 2018; published 1 March 2019)

Nonstatistical fluctuation in pseudorapidity (η), azimuthal (ϕ), and pseudorapidity-azimuthal (η–ϕ) distribution spectra of primary particles of PYTHIA Monash (default) generated pp events at $\sqrt{s} = 2.76$, 7, and 13 TeV have been studied using the scaled factorial moment technique. A weak intermittent type of emission could be realized for minimum-bias (MB) pp events in $\chi(\eta$–$\phi)$ space and a much stronger intermittency could be observed in high-multiplicity (HM) pp events in all $\chi(\eta)$, $\chi(\phi)$, and $\chi(\eta$–$\phi)$ spaces at all the studied energies. For HM pp events, at a particular energy, the intermittency index α_q is found to be largest in two-dimensional $\chi(\eta$–$\phi)$ space and least in $\chi(\eta)$ space, and no center of mass energy dependence of α_q could be observed. The anomalous dimensions d_q are observed to be increased with the order of the moment q, suggesting a multifractal nature of the emission spectra of various studied events. While, the coefficient λ_q is found to decrease monotonically with the order of the moment q for two-dimensional analysis of MB pp events as well as for one-dimensional analysis of HM pp events, a clear minimum in λ_q values could be observed from the two-dimensional HM pp data analysis. For PYTHIA Monash generated sets of data, the strength of the intermittency is found to vary significantly with the variation of the strength of the color reconnection (CR) parameter, i.e., reconnection range RR, for RR = 0.0, 1.8 and 3.0, thereby, establishing a strong connection between the CR mechanism and the observed intermittent type of emission of primary charged particles of the studied high-multiplicity pp events.

DOI: 10.1103/PhysRevC.99.034901

I. INTRODUCTION

Understanding the particle production mechanism is one of the primary goals of high-energy $A + A$ and $h + h$ collisions. A characteristic feature of primary charged particles produced in any such collision is that they exhibit fluctuation in particle number densities over the pseudorapidity space. Such fluctuation is much larger than the statistical fluctuations arising due to the finiteness of the yield of particles produced in a collision. In the pseudorapidity distribution spectra, these fluctuations manifest themselves as peaks and valleys in narrow domains of pseudorapidity space. Such anomalous fluctuation resulting in a "spike" like structure in single-particle density distribution spectrum is often used to examine if the nuclear matter has undergone a phase transition during the evolution of a collision [1–3]. Further, a study on such a fluctuation is also important from the point of view that such anomalous spatial fluctuations may arise due to many mini-jets that might have been formed as a result of semi-hard parton-parton interactions or gluon bremsstrahlung [4–6].

To gather any meaningful information about the particle production mechanism, it is therefore important to disentangle and analyze these anomalous fluctuations arising out of some dynamical processes, from that of noise arising due to the finite number of available particles in the final state. The scaled factorial moment (SFM) technique, as proposed by Bialas and Peschanski [4], is found to be a useful mathematical tool that separates the dynamical fluctuation from the mixture of the two. According to this prescription, a power law growth of the averaged scaled factorial moment ($\langle F_q \rangle$) with the decrease of the phase-space bin width (δw), or otherwise, the number of bins M into which the entire phase space is divided, that is, $\langle F_q \rangle \propto (M)^{\alpha_q}$, is referred to as intermittency and thus indicates the presence of the contribution of the dynamical fluctuation in the data sample. Intermittency, in turn, is found to be related to self-similarity and fractality of emission spectra as well as the particle emitting source [7]. The exponent α_q of the power law, called the intermittency index, is connected with the anomalous dimension d_q ($= D - D_q$) through the relation $d_q = \alpha_q/(q - 1)$, where D is the ordinary topological dimension of the space into which the fractal objects are embedded and D_q is the generalized qth-order Renyi dimension [8,9]. Knowledge of order dependence of d_q is helpful to make comments on the fractal nature of emission spectra and in turn on the particle production mechanism and associated phase transition, if any.

Indications of the existence of a new state of deconfined matter, called quark-gluon plasma (QGP), have been provided

*pranjal.sarma@cern.ch
†Corresponding author: buddhadeb.bhattacharjee@cern.ch